Effects of Increasing Surface Reflectivity on Urban Climate, Air Quality and Heat-Related Mortality

Zahra Jandaghian

A Thesis

in

The Department of

Building, Civil and Environmental Engineering

Presented in the Partial Fulfillment of the Requirements

For the Degree of

Doctor of Philosophy (Building Engineering) at

Concordia University

Montreal, Quebec, Canada

September 2018

CONCORDIA UNIVERSITY
SCHOOL OF GRADUATE STUDIES

This is to certify that thesis prepared

By: Zahra Jandaghian
Entitled: Effects of Increasing Surface Reflectivity on Urban Climate,
          Air Quality and Heat-Related Mortality

and submitted in partial fulfillment of the requirements for the degree of

        Doctor of Philosophy (Building Engineering)

complies with the regulations of the University and meets the accepted standards with respect to originality and quality.

Signed by the final examining committee:

_____ Chair
  Dr. Adam Krzyzak

_____ External Examiner
  Dr. David J. Sailor

_____ External to Program
  Dr. Damon H. Matthews

_____ Examiner
  Dr. Fariborz Haghighat

_____ Examiner
  Dr. Fuzhan Nasiri

_____ Thesis Supervisor
  Dr. Hashem Akbari

_____

Approved by

_____
  Dr. Fariborz Haghighat   Chair of Department of Graduate Program Director

25 October 2018
Date of Defense

_____
      Dr. Amir Asif   Dean, Gina Cody School of Engineering and Computer Science

Abstract

**The Effects of Increasing Surface Reflectivity on Urban Climate, Air Quality
and Heat-Related Mortality**

Zahra Jandaghian, Ph.D.
Concordia University, 2018

This dissertation investigates the effects of increasing surface reflectivity (ISR) on urban climate, air quality, and heat-related mortality and some of the details of simulations and modelling. Meteorological and photochemical models are applied to assess the benefits of albedo enhancement in the Greater Montreal Area (GMA, Quebec) in Canada and Sacramento (California), Houston (Texas) and Chicago (Illinois) in the United State.

Mesoscale models are comprised of physical parameterizations (cumulus, microphysics, planetary boundary layer, radiation, and land-surface) that need to be carefully selected to predict weather conditions. A proper simulation platform is essential to have a better understanding of the effects of UHI and its mitigation strategy on urban climate and air quality for environmental policymakers. The sensitivity of near surface air temperature, wind speed, relative humidity and precipitation to different physical models was evaluated by applying the WRF for Greater Montreal Area, Canada for the period 9–11 August 2009. A combination of WDM6 as microphysics estimation, Grell 3D for cumulus scheme, MYJ as planetary boundary layer and RRTMG as radiation scheme, resulted in the least error compared to the measurements. Thus, this combination is suggested as an appropriate platform for urban climate simulations and heat island mitigation strategy in Greater Montreal Area. Increasing the surface albedo of roofs, walls, and pavements from 0.2 to 0.65, 0.60, and 0.45, respectively, resulted in a decrease in 2-m air temperature by 0.2°C in a rainy day and by 0.7 in a sunny day, a slight increase in 10-m wind speed, a decrease in relative humidity by 3%, and a decrease in precipitation by 0.2 mm/day across the domain.

The proper physical parameterizations for Montreal were applied to investigate the effects of increasing surface reflectivity on meteorological parameters (air temperature, wind speed, relative humidity, and dew point temperature), heat stress indices (National Weather Service – Heat Index, apparent temperature, Canadian Humid Index, and Discomfort Index), and heat-related deaths. The simulation domain was the Greater Montreal Area. The simulations were conducted during the

2005 and 2011 heat wave periods. Heat-related mortality correlations were developed for Montreal. The beneficial contributions of albedo enhancement were a decrease in temperature by 0.8ºC, an increase in relative humidity by 2%, an increase in dew point temperature by 0.4ºC, a slight increase in wind speed, and a decrease in heat-related mortality by 3.2%. Increasing surface reflectivity could save seven lives and improve the level of comfort for urban dwellers.

To assess the effects of increasing surface reflectivity on mitigating urban heat islands and improving air quality, simulations were carried out over a larger geographical area (North America with horizontal resolution of 12km) within nested domains as urban areas (Sacramento in California, Houston in Texas, and Chicago in Illinois with horizontal resolution of 2.4km) in a two-way nested approach by online coupling of chemistry package with the solver of WRF (WRF-Chem). The 2-way nested approach provided an integrated simulation setup to capture the full impacts of meteorological and photochemical reactions and decrease the uncertainties associated with scale separation and grid resolution. The Lin, Goddard, Rapid Radiative Transfer Model, Mellor-Yamada-Janjic and Grell-Devenyi ensemble schemes are respectively selected for microphysics, shortwave radiation, longwave radiation, planetary boundary layer and cumulus parameterization. For anthropogenic and biogenic emission estimations, the models of the United States National Emission Inventory for 2011 (US-NEI11) and Model of Emissions of Gases and Aerosols from Nature (MEGAN) are respectively simulated for the inner domains. The Modal Aerosol Dynamics Model for Europe and Regional Atmospheric Chemistry Mechanism (RACM) are applied to estimate the effects of aerosols on radiation processes and hydrological cycles in the atmosphere and to estimate the gas-phase reactions. Photolysis frequencies are calculated by the Fast_J model scheme. Increasing surface albedo resulted a decrease in air temperature by 2-3ºC in urban areas of these three cities. Albedo enhancement resulted in a slight increase in wind speed; an increase in relative humidity (3%) and dew point temperature (0.3ºC) during simulation period. Increasing urban reflectivity led to a decrease in $PM_{2.5}$ and O_3 concentrations by 2-4μg/m^3 and 4-8 ppb in urban areas of these three cities based on their locations. Sacramento showed a larger reduction in ozone concentration as a result of larger decrease in air temperature because of the heat island mitigation strategy.

The two-way nested approach was employed to investigate the effects of albedo enhancement on aerosol-radiation-cloud (ARC) interactions over the Greater Montreal Area during the 2011 heat wave period. The third domain of simulation covers the GMA with the horizontal resolution of

800m. Four sets of simulations with and without aerosol estimations and convective parameterizations were carried out to explore the direct, semi-direct and indirect effects of aerosols. The physical and chemical parameterizations are modified to be coupled with the Model for Simulating Aerosol Interactions with Chemistry (MOSAIC) aerosol scheme and the Carbon Bond Mechanism (CBM-Z) gas phase chemistry scheme. The Morrison double-moment scheme and the Mellor-Yamada-Janjic scheme are selected as microphysics and planetary boundary layer options, respectively. The Grell-Devenyi ensemble scheme and the rapid radiative transfer model are respectively used for cumulus parameterization and shortwave and longwave radiations. The US-NEI11 and MEGAN are applied to calculate the anthropogenic and biogenic emission estimation, respectively. The Fast-J is used for the photolysis scheme in WRF-Chem. Aerosols cause a decrease in shortwave radiation reaching to the ground (20 Wm^{-2}) and thus reduces the radiation budget (25 Wm^{-2}). The albedo enhancement induced a decrease in air temperature by nearly 0.5℃ in Montreal during heat wave period. The relative humidity and water mixing ratio also decreased by 0.5 g/kg and 3%, respectively. Increasing surface reflectivity led to a decrease of 8-h ozone concentrations by 2ppb across the GMA. Reducing temperature induced a reduction in planetary boundary layer height, which reduced the advection and diffusion of pollutants. Hence, reducing planetary boundary layer height increases the pollutant concentrations and assists the O_3 and NO reaction rates to produce NO_2. The fine particulate matter also decreased by nearly 3 $\mu g/m^3$ in GMA during simulation period. An increase of albedo led to a net decrease of radiative flux into the ground and therefore a decrease of convective cloud formation.

The comparisons between simulated air temperature using WRF and WRF-Chem with measurements indicated that both models predict the temperature reasonably well. The modeling results indicated that each of these four cities (Montreal, Sacramento, Houston, Chicago) across North America can benefit from increasing surface reflectivity. But, the extent to which surface modification can improve urban climate and air quality effectively depends on meteorology, geography, scale, topography, morphology, land use patterns, the emission rates and mixture of biogenic and anthropogenic pollutants, baseline albedo fraction distribution, and the potential for surface modification in that specific city.

Acknowledgements

First and foremost, I would like to express my sincere gratitude and heartful appreciation to my supervisor, *Professor Hashem Akbari*, for his continuous guidance, wisdom, and great support. His breadth of experience helped me through countless challenges. This research is owed to his intellectual inputs, moral encouragement and selfless commitment to conveying his knowledge to a fare-thee-well. I am, and will always be, grateful for the invaluable advices, knowledge and time he devoted during this research. The legacy of his excellent work as an advisor will shape my professional career for years to come.

I would also like to sincerely thank my dissertation committee, *Prof. Fariborz Haghighat*, *Prof. Damon Matthews*, *Prof. Fuzhan Nasiri* and *Prof. David Sailor (Arizona State University)* for their interest in my work and their valuable inputs, insightful comments and precious time.

When I first joined the Heat Island Group at Concordia, there were a number of students whose assistance, guidance, and mentorship were essential to setting my scientific groundwork. I appreciate their time and most importantly, their friendship. Special thanks to *Dr. Ali G. Touchaei* for his valuable discussions.

There are several collaborators and support staff to whom I extend my biggest thanks. I thank *Mr. Sylvain Belanger* for his computational maintenance at Concordia. I would also like to thank the staff at Calculquebec, especially *Dr. Daniel Stubbs* for providing computational facilities for my simulations.

Second to the last, I wish to express my warmest appreciation and love to my family. I wholeheartedly thank my parents -*Effat Javadi and Mohammad Jandaghian*- who have contributed the most to my life and made many sacrifices. Thank you for serving as role models and giving me perspective and constant reminders to maintain life balance. Big thanks to my wonderful brothers -Taha and Mojtaba- by playing in childhood, we learnt how to always have fun and be happy and support each other to pursue our dreams. Big thanks to my lovely sisters-in-low -Mahdiyeh and Elaheh- you bring more joy and beauty to our lives. Here, I would also wish to thank the loveliest and compassionate grandma in the world, *Akram*. Your legacy as being kind, motivated, thankful, hardworking throughout life will always remain with us. You are so much missed.

Last, but the most, I am deeply thankful to my loving husband and best friend, *Ehsan Saadatfar*. Your patience, continuous encouragement and kindness have always upheld me. Thank you for your love, immense support and thoughtful advices. I am very grateful for all you have provided me over these years. I cannot express my feelings and gratitude into words.

Dedication

To my beloved parents, *Effat and Mohammad*

To my lovely husband and best friend, *Ehsan*

Contribution

Article Title: Sensitivity Analysis of Physical Parameterizations in WRF for Urban Climate Simulations and Heat Island Mitigation in Montreal
Authors: Zahra Jandaghian, Ali G. Touchaei, Hashem Akbari
Article Status: Published in Urban Climate. doi:10.1016/j.uclim.2017.10.004 The content of this paper is used in chapter **4**.

Article Title: The Effects of Increasing Surface Reflectivity on Heat-Related Mortality in Greater Montreal Area
Authors: Zahra Jandaghian, Hashem Akbari
Article Status: Published in Urban Climate. doi.org/10.1016/j.uclim.2018.06.002 The content of this paper is used in chapter **5**.

Article Title: Effects of Increasing Surface Reflectivity on Urban Climate and Air Quality: A Detailed Study for Sacramento, Houston, and Chicago
Authors: Zahra Jandaghian, Hashem Akbari
Article Status: Published in Climate. doi:10.3390/cli6020019 The content of this paper is used in chapter **6**.

Article Title: Effects of Increasing Surface Reflectivity on Aerosol-radiation-cloud Interactions
Authors: Zahra Jandaghian, Hashem Akbari
Article Status: To be submitted The content of this paper is used in chapter **7**.

Conference presentations: SEP

- Zahra Jandaghian, Hashem Akbari. "Effects of Increasing Surface Reflectivity on Urban Climate and Air Quality over North America", *4th International Conference on Building, Energy, Environment*, 4-5 February 2018, Melbourne, Australia

- Zahra Jandaghian, Hashem Akbari. "The Effects of Aerosol-radiation-cloud Interactions on Air Quality over North America during Heatwave Period" *6th International Conference on Climate Change Adaptation*, 16-17 September 2017, University of Toronto, Canada

- Zahra Jandaghian, Hashem Akbari. "Urban Heat Island and Human Health", *4th International Conference on Countermeasures to Urban Heat Island,* 30-31 May and 1 June 2016, National University of Singapore, Singapore

Table of Contents

List of Figures

List of Tables

List of Symbols & Abbreviations

English Symbols

C_R	Heat Capacity of Roof (J m^{-3} K^{-1})
C_W	Heat Capacity of Wall (J m^{-3} K^{-1})
C_G	Heat Capacity of Ground (J m^{-3} K^{-1})
C_M	The value of each parameter from simulations
C_O	Observations from weather or air quality stations
f_{urb}	Urban fraction (Fraction)
g	Gravitational Acceleration (m/s)
GFX	Ground Heat Flux (Wm^{-2})
HFX	Sensible Heat Flux (Wm^{-2})
LH	Latent Heat Flux (Wm^{-2})
mb	millibar
P_{surf}	dry hydrostatic surface pressure (millibar)
P_{top}	dry hydrostatic pressure at model top (millibar)
$P_{station}$	station pressure (millibar)
ppb	part per billion
Q2	Actual mixing ratio (%)
Q_{WMR}	water mixing ratio (g $_{water}$ /kg $_{dry\ air}$)
$Q_{C_{WMR}}$	cloud water mixing ratio (g $_{water}$ /kg $_{dry\ air}$)
$Q_{R_{WMR}}$	rain water mixing ratio (g $_{water}$ /kg $_{dry\ air}$)
$Q_{V_{WMR}}$	water vapor mixing ratio (g $_{water}$ /kg $_{dry\ air}$)
RB	Radiative Balance (Wm^{-2})

Greek Symbols

α_R	Surface Albedo of Roof (Fraction)
α_W	Surface Albedo of Wall (Fraction)
α_G	Surface Albedo of Ground (Fraction)
α_i	Constant value in heat-related mortality calculations
ε_R	Surface Emissivity of Roof
ε_W	Surface Emissivity of Wall
ε_G	Surface Emissivity of Ground

λ_R	Thermal Conductivity of Roof (J m^{-1}s^{-1} K^{-1})
λ_W	Thermal Conductivity of Wall (J m^{-1}s^{-1} K^{-1})
λ_G	Thermal Conductivity of Ground (J m^{-1}s^{-1} K^{-1})
Z_{0R}	Roughness Length for momentum over Roof (m)
Z_{0G}	Roughness Length for momentum over Ground (m)
Z_{0W}	Roughness Length for momentum- Wall (m)

Abbreviations

AC-SDE	Aerosol-Cloud Semi-Direct Effect
AGL	Above Ground Level
ALA	American Lung Association
AH	Absorbed Heat (Wm^{-2})
ALBEDO	Albedo scenario
AOD	Aerosol Optical Depth
AQS	Air Quality System
ARC	Aerosol-Radiation-Cloud
ARC-IDE	Aerosol-Radiation-Cloud Indirect Effect
AR-DE	Aerosol-Radiation Direct Effect
AT	Apparent Temperature (ºC)
AC	Air Conditioning
AVHRR	Advanced Very High-Resolution Radiometer
BASE	Base case scenario
BEM	Building Energy Model
BEP	Building Effect Parameterization
BETA	Thermal efficiency of heat exchanger
BouLac	Bougeault- Lacarrere
CASTNET	Clean Air Status and Trend Network
CBM	Carbon Bond Mechanism
CCN	Cloud Condensation Nuclei
CD	Consecutive Days
CFC	Chlorofluorocarbon
CFD	Computational Fluid Dynamic

CAM	Compliance Assurance Monitoring Model
CMAQ	Community Multiscale Air Quality Modeling System
CHI	Canadian Humid Index
CEHA	Canadian Environmental Health Atlas
CSUMM	Colorado State Urban Meteorological Model
CASTNET	Clean Air Status and Trend Network
CTRL	Control scenario
COP	Coefficient of performance of AC conditioning
DI	Discomfort Index
DPT	Dew Point Temperature (^{o}C)
DIS	Day In Sequences
DT	Dry Tropical
DP	Dry Polar
DM	Dry Moderate
EPA	Environmental Protection Agency
GMA	Greater Montreal Area
GFS	Global Forecast System
GAPTEM	Comfort range of indoor temperature (k)
GAPHUM	Comfort humidity of AC systems (kg/kg)
HRM	Heat-Related Mortality
HI	heat indices
HSEQUIP_SCALE_FACTOR	Peak Heat Generated by Equipment (Wm^{-2})
IPCC	Intergovernmental Panel on Climate Change
ISR	Increasing Surface Reflectivity
JJA	June, July, August
LBNL	Lawrence Berkeley National Laboratory
LSM	Land-Surface Model
LST	Local Standard Time (hr)
LULC	Land Use/Land Cover
LW	Long Wave Radiation (Wm^{-2})
MADE	Modal Aerosol Dynamics Model for Europe
MAE	Mean Absolute Error
MB	Mean Bias
MAE	Mean Absolute Error

MBE	Mean Bias Error
ME	Mean Error
MP	Moist Polar
MM	Moist Moderate
MT	Moist Tropical
MT+	Moist Tropical+
MEGAN	Model of Emissions of Gases and Aerosols from Nature
ML-UCM	Multi-Layer of the Urban Canopy Model
MM5	Fifth-generation NCAR/Penn State Mesoscale Model
MOSAIC	Model for Simulating Aerosol Interactions with Chemistry
MT	Moist Tropical
MT+	Moist Tropical Plus
MYJ	Mellor-Yamada-Janjic
NARR	North American Regional Reanalysis
NBE	Normalized Bias Error
NCAR	National Center for Atmospheric Research
NCEP	National Center for Environmental Prediction
NOAA	National Oceanic and Atmospheric Administration
NOAH-LSM	NOAH- Land Surface Model
NSSL	National Severe Storm Laboratory
NWP	Numerical Weather Prediction
NWS-HI	National Weather Service – Heat Index
NMA	Mean Absolute Error
NMB	Normalized Mean Bias
NME	Normalized Mean Error
PBLH	Planetary Boundary Layer Height (m)
P	Pressure (millibar)
PWIN	Coverage area fraction of windows in the walls of the buildings
RADM2	Regional Acid Deposition Model Version 2
RACM	Regional Atmospheric Chemistry Mechanism
RRTMG	Rapid Radiative Transfer Model
RANS	Reynolds Averaged Navier-Stokes equations
RB	Radiative Budget (Wm^{-2})
RH2	2-m Relative Humidity (%)

RMSE	Root Mean Square Error
RRTM	Rapid Radiative Transfer Model
SIA	Secondary Inorganic Aerosol
SYN	Synergistic
SL-UCM	Single Layer Urban Canopy Model
SOA	Secondary Organic Aerosols
SORGAM	Secondary ORGanic Aerosol Model
SSA	Single Scattering Albedo
SSC	Spatial Synoptic Classification
SVP	Saturated Vapor Pressure
SMR	saturated mixing ratio
SW	Short Wave Radiation (Wm^{-2})
SWDOWN	Downward Shortwave Radiation (Wm^{-2})
T2	2-m air temperature (ºC)
TR	Transition
TOS	Time of Season
TKE	Turbulent Kinetic Energy
TARGHUM	Target Humidity of AC systems (kg/kg)
TARGTEMP	Target Temperature of AC systems (K)
UBL	Urban Boundary Layer
UCM	Urban Canopy Model
USCB	United States Census Bureau
UHI	Urban Heat Island
US-NEI11	US National Emission Inventory-2011
UAM	Urban Airshed Model
UMM	Urbanized Mesoscale Model
UTC	Universal Time Coordinate
USGS	US Geographical System
VOC	Volatile Organic Compound
WBGT	Wet Bulb Global Temperature (K)
WPS	WRF Pre-processing System
WRF	Weather Research Forecasting
WRF-Chem	Weather Research and Forecasting model with Chemistry
WS10	10-m Wind Speed (m/s)

WHO	World Health Organization
WSM6	WRF Single-Moment 6-class
WDM6	WRF Double-Moment 6-class Scheme
WMR	Water Mixing Ratio ($g_{water}/kg_{dry\ air}$)
YSU	Yonsei University scheme

Definitions of the terminologies used in the thesis

Terminology	Definition
Albedo	The portion of the incident radiation that is reflected by a surface
ALBEDO Scenario	The albedo of roofs, walls, and roads are assumed to be 0.65, 0.60, and 0.45, respectively in this scenario
Aerosol-Radiation-Cloud interactions	The direct, semi-direct and indirect effects of aerosols and the interaction of aerosols with radiation and cloud in the atmosphere
CTRL Scenario	The albedo of roofs, walls, and roads are assumed to be 0.2
Cumulus Model	Considers the cloud convection in the domain
Dry Polar (DP) of air mass classification	From polar regions. Associated with the lowest temperatures and clear, dry conditions
Dry Moderate (DM) of air mass classification	Includes mild and dry air
Dry Tropical (DT) of air mass classification	Represents the hottest and driest conditions at any location with sunny, clear skies
Day In Sequence (DIS) for heat-related mortality calculation	It is a day during heat wave period for an offensive weather type (day 1= 1 and day 3= 3)
High-intensity residential areas (class 32) of the Urban Canopy Model	An urban area with vegetation coverage under 20%
Industrial/commercial areas (class 33) of the Urban Canopy Model	includes infrastructure and highly developed areas not classified as residential
Low-intensity residential (class 31) of the Urban Canopy Model	includes areas with a mixture of built-up structures and vegetation (for 20–70% of land cover)
Land-surface Model	Estimates the physical processes as heat & moisture on the land
Multi-layered Urban Canopy Model (ML-UCM)	The ML-UCM is a part of the land-surface parameterization to predict the heat and moisture fluxes from canopies to atmosphere
Microphysics Model	Estimates the processes of transforming water in the atmosphere
Model of Emissions of Gases and Aerosols from Nature (MEGAN)	MEGAN estimates the time resolved gridded BVOC emission estimation in mole/km^2/hr. It is designed for regional and global emission modeling and has a base resolution of 1 km
Mean Bias Error (MBE)	MBE is an indication of underestimation or overestimation of a parameter. $\text{MBE} = \frac{1}{N}\sum_1^N (C_M - C_O)$, C_O are modeled and observed concentrations, respectively and N is the total number of model and observation pairs.
Mean Absolute Error (MAE)	MAE is a natural metric to evaluate the performance of the model (absolute differences between measurement and simulations). $\text{MAE} = \frac{1}{N}\sum_1^N |C_M - C_O|$ C_M and C_O are modeled and observed concentrations, respectively and N is the total number of model and observation pairs.
Moist Polar (MP) of air mass classification	Typically, cool, humid, and cloudy conditions
Moist Moderate (MM) of air mass classification	Warmer and more humid than MP
Moist Tropical (MT) of air mass classification	Represent hottest and most humid weather type. Skies are partly cloudy in the summer because of instability and convection
Moist Tropical+ (MT+) of air mass classification	Extreme subset of MT, in which morning and afternoon apparent temperature are above the MT
Planetary boundary layer model	Accounts for the change in near surface wind distribution & determine vertical exchanges of heat, moisture & momentum
Root Mean Square Error (RMSE)	RMSE is a standard deviation of the residuals. Residuals are a measure of how far from the regression line data points are. RMSE is a measure of how spread out these residuals are. $\text{RMSE} = \left[\frac{1}{N}\sum_1^N (C_M - C_O)^2\right]^{1/2}$ C_M and C_O are modeled and observed concentrations, respectively and N is the total number of model and observation pairs.
Radiation Model	Determines different radiation processes in the atmosphere and at surface
Transition (TR) of air mass classification	Days in which one weather type yields to another
Time Of Season (TOS) for heat-related mortality calculation	The day of simulation during summertime (June, July and August) (1 = 1st of June and 32 = 1st of July, and so on until the end of August)

Two-way nested approach	Online coupling of the chemistry package with the solver of the meteorological model and simulating over a larger geographical area within a nested domain as an urban area
Urban Canopy Models (UCMs)	Provides more accurate feedbacks on urban areas for surface layer and planetary boundary layer schemes

Chapter 1
Introduction

Cities cover about 2% of the Earth`s land and account for 60–80% of energy use (Akbari et al., 2015). Half of the world`s population live in urban areas and this number is expected to increase to 70% by 2050 (IPCC, 2014). The growth of urbanization leads to changes in land use/land cover. In urban areas, human activities consume energy and release anthropogenic heat. Thus, the temperatures in urban areas are typically higher than in their surroundings. This phenomenon is called urban heat island (UHI). UHI causes an increase in cooling energy consumption (Akbari and Konopacki, 2005), and in air pollutants emissions (Akbari et al., 2001). UHI deteriorates air quality, endangers human health, increases mortality (Kosatsky et al., 2005) and changes the urban ecosystem (Kayleigh et al., 2013).

To reduce the adverse effects of UHI, various adaptation and mitigation strategies are considered. Adaptation requires the adjustment of urban inhabitants to modify their way of living. Mitigation implies direct intervention into the system to identify problems and to reduce negative aspects. The mitigation strategies of the UHI include but are not limited to: increasing surface reflectivity (ISR) (roofs, walls and pavements), increasing greenery spaces (shade trees), and decreasing anthropogenic heat emissions. These strategies lead to a decrease in air temperature and temperature-dependent atmospheric chemistry that controls photochemical reaction rate of production and destruction of ozone. The consequences of applying these methods result in a decrease in cooling energy demand in summertime (Akbari et al., 2001) with partially offsetting increases in heating demand in winter (Touchaei et al., 2016). In addition, surface modifications will improve urban climate and air quality. Table 1.1 presents the potential effects of these mitigation strategies.

Table 1.1. UHI mitigation strategies and their impacts

Mitigation strategies	Impacts
Increasing surface reflectivity	- Decrease surface, air and apparent temperature - Decrease anthropogenic and biogenic emissions rate - Decrease temperature-dependent photochemical reaction rate - Decrease planetary boundary layer height
Increasing greenery spaces	- Decrease surface, air and radiant temperature - Decrease biogenic emissions rate - Increase deposition of pollutants - Increase evapotranspiration, cooling and shading - Increase volatile organic compounds (VOCs)
Decreasing anthropogenic heat emissions	- Decrease air and apparent temperatures - Decrease the rate of anthropogenic emission

Increasing surface reflectivity (ISR) is a verifiable, measurable and repeatable heat island mitigation strategy. ISR decreases urban temperatures and photochemical reaction rates and enhances human health and comfort (Akbari and Kolokotsa, 2016; Taha, 2008). The albedo in urban areas ranges from 0.1 to 0.2. It can be increased to 0.6 by the use of high-reflective materials on roofs, walls, and pavements (Akbari et al., 2001; Akbari and Kolokotsa, 2016). The effects of surface modifications on urban climate and atmospheric conditions have been investigated in various regions and episodes (Salamanca and Martilli, 2012; Fallmann et al., 2014; Touchaei et al., 2016). More detail is presented in Chapter 2.

Meteorological and photochemical models have been developed to predict urban climate and air quality. The interaction between meteorology and atmospheric chemistry is complicated. Meteorology has its effects on atmospheric chemistry through temperature, cloud formation, precipitation, radiation, wind speed and direction, and planetary boundary layer (PBL) height. Chemical interactions in the atmosphere influence meteorology through aerosol, ozone, NOx, CO and VOCs. Land surface properties also affect natural emission and dry deposition (Seinfeld and Pandis, 2012). A model is required to capture the full impacts of meteorological processes and photochemical interactions in the atmosphere and at the surface.

The online Weather Research and Forecasting Model (WRF) (Skamarock et al., 2005) is applied to simulate the meteorological processes in the atmosphere. The WRF is a non-hydrostatic mesoscale numerical weather prediction (NWP) system. Mesoscale models are comprised of many physical parameterizations to predict the weather condition. The WRF can be coupled with the urban canopy models (UCMs). The UCM is a part of the land-surface parameterization to predict

the heat and moisture fluxes from canopies to atmosphere. In addition, the WRF can be coupled with a chemistry package (WRF-Chem) to simulate meteorological quantities and air pollution concentrations simultaneously (Grell et al., 2005). The components of air quality are consistent with the meteorological components within the same transport scheme, grid and physics schemes and time steps. Chapter 3 explains these models.

1.1. Problem Statement

High temperatures increase the rate of heat-related mortality in urban areas and cause 12,000 deaths worldwide annually (McMichaeland et al., 2004). UHI intensity and duration cause an increase in morbidity and mortality (Nitschke et al., 2011; Wang et al., 2012; Jenkins et al., 2014; Horton et al., 2014; Hajat et al., 2010; Harlan et al., 2006; Harlan and Ruddell 2011). Yet the effects of UHI mitigation strategies have not been investigated in relation to the rate of heat-related deaths in urban areas. Here, the effects of increasing surface reflectivity are investigated on heat-related mortality during heat wave periods.

The UHI impact on urban climate and air quality is typically studied through a one-way approach at local, regional and global scales (Arnfield, 2003; Ban-Weiss et al., 2015; Taha 2008 and 2009; Salamanca et al., 2012; Li and Bou-Zeid 2014; Bhati and Mohan 2016). The meteorological processes and photochemical reactions in the urban atmosphere magnify the UHI effects. These interactions in the urban environment cause changes in regional climate. The changes in the regional atmosphere affect local pollution. Thus, a two-way nested simulation approach is required to capture the full impacts of these processes, from the regional scale through the local scale. Here, the effects of increasing surface reflectivity on urban climate and air quality are investigated over a larger geographical area within nested domains as urban areas in a two-way nested simulation approach.

Atmospheric aerosols affect the radiative balance of the Earth-Atmosphere system by scattering and absorbing the incoming solar radiation directly and by influencing cloud formation and precipitation indirectly (IPCC 2013; Zhang et al., 2014 and 2008). The atmospheric aerosols have been closely linked with modification of radiation budgets and cloud systems (Fan et al., 2013). The effects of albedo enhancement have not been investigated on aerosol direct (aerosol-radiation), semi-direct (aerosol-cloud), and indirect (aerosol-radiation-cloud) interactions in the atmosphere. This dissertation investigates the effects of heat island and increasing surface reflectivity on the

interactions of aerosols, radiation and clouds in the atmosphere in urban area.

The Weather Research and Forecasting Model (WRF) (Skamarock et al., 2005) is used. The WRF includes parameterizations for microphysics, cumulus, planetary boundary layer, radiation, and land surface model. Analyzing the sensitivity of meteorological parameters (e.g., air temperature, wind speed and relative humidity) to a different set of parameterizations enables researchers to select the most accurate model platform for urban climate simulations. In previous studies the effects of UHI and its mitigation strategies have been investigated applying the WRF model (Salamanca et al., 2012; Li and Bou-Zeid, 2014; Bhati and Mohan, 2016). Previous efforts are mostly performed using coarse grid cells, because of limitation in computational resources. But, the fine-resolution grid spacing provides more detailed information on the spatial variation of the air temperature in urban areas. In this study, sensitivity analyses of physical parameterizations in WRF are also performed to develop a proper platform for urban climate simulations.

1.2. Research Objectives

The main aim is to investigate the effects of increasing surface reflectivity on heat-related mortality, urban climate and air quality. For these purposes, four objectives are defined. The research objectives and a brief explanation to accomplish them are stated as follows.

1st objective: *Develop a platform for urban climate simulation and heat island mitigation strategy*

Mesoscale models are comprised of physical parameterizations (cumulus, microphysics, planetary boundary layer, radiation, and land-surface) that need to be carefully selected to predict weather conditions. The physical processes can be selected based on a set of sensitivity analyses. A proper simulation platform is essential to have a better understanding of the effects of UHI and its mitigations strategy on urban climate and air quality for environmental policymakers. Twenty sets of simulations are conducted. A variety of WRF options are used to investigate the sensitivity of air temperature, wind speed, relative humidity and precipitation to the choice of the model ensemble. The simulation domain is the Greater Montreal Area. The simulation period includes sunny and rainy conditions in summer 2009.

2nd objective: *Investigate the effects of urban heat island and its mitigation strategy on heat-related mortality*

The proper physical parameterizations are applied to achieve the second goal. The effects of extreme heat events and increasing surface reflectivity are investigated on meteorological parameters (air temperature, wind speed, relative humidity, and dew point temperature), heat stress indices (National Weather Service – Heat Index, apparent temperature, Canadian Humid Index, and Discomfort Index) and heat-related deaths. The non-accidental mortality data is used for the period of June, July, and August from Canadian Vital Statistics data bases at Statistics Canada. Heat-related mortality correlations are developed. The simulation domain is the Greater Montreal Area. The simulation period includes two heat wave events in 2005 and 2011.

3rd objective: *Develop a two-way nested simulation approach to assess the effects of urban heat island and its mitigation strategy on urban climate and air quality*

A two-way nested simulation approach is developed and applied over a larger geographical area through local scales such as urban areas. This approach provides an integrated simulation setup to capture the full impacts of meteorological processes and photochemical interactions in the atmosphere. The effects of surface modification are investigated on meteorological parameters (air temperature, wind speed, dew point temperature and relative humidity) and air quality components (ozone, fine particulate matters, nitrogen dioxide and $PM_{2.5}$ subspecies). The simulation domain is over North America with a focus on three cities: Sacramento, California; Houston, Texas; and Chicago, Illinois. The simulations cover the 2011 heat wave period.

4th objective: *Investigate the effects of heat island mitigation strategy on aerosol-radiation-cloud interactions in the urban atmosphere*

Increasing surface reflectivity affects the aerosol-radiation, aerosol-cloud and aerosol-radiation-cloud interactions. An approach is developed to calculate the radiation budget and water mixing ratio in the atmosphere and at the surface. Four scenarios are defined to separate the impacts of aerosol-radiation from aerosol-cloud interactions. The two-way nested simulation approach is applied to analyze the direct, semi-direct and indirect effects of aerosols on urban climate and air quality. These simulations predict the interaction of aerosols, meteorology, chemistry and radiation in a fully interactive manner. The simulation domain covers North America through the Greater Montreal Area, during the 2011 heat wave period.

1.3. Limitations and Assumptions

At the heart of this research, there are several limitations and assumptions. Limitations include data processing and computer resources. Data processing includes collecting, categorizing, validating, and extracting reliable data. Computer resources are required with sufficient memory capacity and fast processing in order to compile, couple and carry on various simulations in a timely manner.

Assumptions include urban characteristics and simulations approaches. Urban areas are categorized in three groups: 1) low intensity residential, 2) high intensity residential and 3) industrial and commercial ones. In each category, building properties are considered to be similar. Proportions of roofs, pavements, and vegetation in each grid cell are assumed to be constant and the same as other grids in the same urban category. The simulations and analyses are based on the assumptions that the population density and urban structure over the domain is homogenous. The simulations are conducted to cover heat wave periods. Simulation of the entire year can reveal more detailed information on the annual effects of the mitigation strategy. In addition, the atmospheric layer is assumed to be heterogeneous in these modeling. The results of this dissertation are region-specific.

1.4. Research Significance

The effects of heat island and its mitigation strategies have already been reported in previous studies on specific locations and episodes (Arnfield, 2003; Ban-Weiss et al., 2015; Taha, 2008 and 2009; Salamanca et al., 2012; Li and Bou-Zeid, 2014; Bhati and Mohan, 2016). But, there are many aspects of these strategies that need attention. For example, the effects of heat island mitigation strategies on heat-related mortality have not been investigated. Here, an algorithm is defined to estimate the effects of increasing surface reflectivity on heat-related deaths.

The other contribution is to provide a two-way nested approach to enable the researcher to analyze the effects of surface modifications on urban climate and air quality over a larger geographical area through regional and local scales such as urban areas. Another contribution is to prepare an approach to investigate the effects of increasing surface albedo on aerosols interactions, radiative budgets and the hydrological cycle in the atmosphere and at the surface.

1.5. Thesis Structure

Chapter 2 presents a literature review of the current state of knowledge and its shortcomings. Chapter 3 provides a description of the simulation tools and methodologies. Chapter 4, 5, 6 and 7, respectively discuss the results of the four objectives: sensitivity analysis of physical parameterizations in WRF for urban climate simulations and heat island mitigation strategy, the effects of increasing surface reflectivity on heat-related mortality, effects of increasing surface albedo on urban climate and air quality over a large geographical area within nested domain as urban areas, and effects of increasing surface reflectivity on aerosol-radiation-cloud interactions in the atmosphere and at the surface. Chapter 8 addresses the research conclusions, contributions, and future work. Appendix A presents the "namelist.input" of each task of this dissertation. The theory of the aerosol interactions in the atmosphere is presented in Appendix B. Appendix C shows the National Weather Service – Heat Index chart.

Chapter 2
Literature Review

Surface and air temperatures are typically higher in urban areas compared to their surroundings and cause the formation of urban heat island (UHI) (Akbari et al., 2016; Taha 1997; Oke, 1987; Roth et al., 1989). The UHI depends upon urban characteristics (the type of urban materials), heat emissions from anthropogenic sources (such as buildings, transportations, industrial processes and human metabolism), and population density (Akbari et al., 2015; Akbari et al., 2016; Taha, 2008; Wilby, 2007). Summertime UHI reduces indoor-outdoor thermal comfort and increases cooling energy demand. UHI increases the temperature-sensitive emissions from biogenic and anthropogenic sources. High temperature accelerates the photochemical reaction rates and increases the formation and concentrations of tropospheric ozone.

Mitigation strategies are applied to reduce the effects of UHI in urban areas. These strategies include but are not limited to: increasing surface reflectivity (roofs, walls and pavements), increasing greenery spaces, and controlling the source of anthropogenic heat in urban areas (Akbari et al., 2016; Akbari, 1992; Taha, 2008). Increasing surface reflectivity (ISR) is a verifiable, measurable, and repeatable strategy to mitigate the impacts of UHI on regional, urban and global scales (Akbari et al., 2001 and 2009; Arnfield, 2003; Ban-Weiss et al., 2015; Taha, 2008 and 2009; Taha et al., 1997). Meteorological and photochemical models are applied to investigate the effects of heat island and its mitigation strategy on urban climate and air quality. Table 2.1 summarizes some of these studies.

The present chapter aims to prepare a brief background of the existing literature to investigate the effects of UHI and increasing surface reflectivity on urban climate, air quality and heat-related mortality. Section 2.1 presents the effects of UHI and its mitigation strategy on heat-related mortality (HRM) and human health. Section 2.2 explains the effects of UHI and ISR on urban climate and air quality. Section 2.3 summarizes the meteorological and photochemical simulations

applied in this research. A concluding statement regarding the objectives of this thesis is addressed in Section 2.4.

Table 2.1. Summary of the effects of increasing surface reflectivity on urban climate from previous studies

Reference	Model Used	Albedo changes	Effects of increasing surface reflectivity
Taha (2008)	MM5 & CAM	roof, wall, pavement albedo increased by 0.1, 0.25, 0.08, respectively	surface and air temperature decreased by up to 10ºC and 3ºC in Sacramento during summer time
Santamouris et al., 2012	CFD	surface albedo in a park increased by 0.12	surface temperature decreased by up to 12ºC during a typical summer day in Athens
Millstein D. & Menon S., 2011	WRFV3.2	roof & pavement albedo increased by 0.25 & 0.15 over US	summer afternoon temperature in urban locations reduced by 0.11-0.53ºC
Georgescu et al., 2012	WRFV3.2	surface albedo increased to 0.88 under maximum expansion scenario in Sun Corridor	average air temperature decreased by 0.83, 0.77 & 0.7ºC in Spring, Summer, & Fall, respectively
Georgescu et al., 2014	WRFV3.2	cool roofs in urban areas over the US under urban expansion scenario increased by 0.8	average air temperature decreased in all urban areas by up to 2ºC in Mid-Atlantic & California
Zhou Y. et al., 2010	WRFV3.3	urban albedo is doubled and tripled	air temperature decreased by 2.5ºC in Atlanta
Oleson et al., 2010	CAM	roof albedo increased by 0.58	air temperature decreased by 0.6
Fallmann et al., 2014	WRFV3.6	surface albedo increased by 0.7	2-m air temperature and ozone concentrations decreased by nearly 0.5 °C and 5–8% in urban areas of Stuttgart during the 2003 heat wave period
Salamanca & Martilli, 2012	WRFV3.2	roof and road albedo increased by 0.45 & 0.35	urban temperature decreased by 1.5–2 °C during hot summer days in Madrid
Taha et al., 2015	WRF & CMAQ	roof, wall, and pavement albedo increased by 0.4, 0.1, and 0.2, respectively	surface and air temperature decreased by up to 7 °C and 2–3 °C, respectively, ozone decreased by up to 5–11 ppb during the daytime
Touchaei et al., 2016	WRF-Chem	roof, wall and road albedo increased by 0.45, 0.40, and 0.25, respectively	air temperature, ozone & fine particulate matters concentrations decreased by up to 0.7 °C, 0.2 ppb, and 1.8 μg/m^3, respectively during the 2005 heat wave period in Greater Montreal Area, Canada

MM5: fifth-generation of Mesoscale Model; CAM: Compliance Assurance Monitoring Model; CFD: Computational Fluid Dynamic; CMAQ: Community Multiscale Air Quality Modeling System

2.1. Effects of Urban Heat Island and Its Mitigation Strategy on Heat-Related Deaths

Heat-related mortality can be magnified in urban areas because of the urban heat island effects. Climate change can also exacerbate extreme heat events and the duration of high temperature (IPCC, 2014). High temperature intensity and duration cause an increase in morbidity and mortality (Nitschke et al., 2011; Wang et al., 2012; Jenkins et al., 2014; Horton et al., 2014; Hajat et al., 2010; Harlan et al., 2006 and 2011).

Health impacts range from heat exhaustion to heat stress, kidney failure and heart attacks (WHO, 2010; Matzarakis and Nastos, 2011). Heat-related mortality occurs mostly in vulnerable sections of the society such as elderly, homeless, and socially disadvantaged people (Vandentorren

et al., 2006; Vaneckova et al., 2010; Peng et al., 2011, Cusack et al., 2011; Yardley et al., 2011; Buchina et al., 2015). Much of the excess mortality is related to cardiovascular, cerebrovascular and respiratory causes and is concentrated in the elderly (Åström et al., 2011; Bunker et al., 2016).

The combination of climate change, urban heat island and heat wave leads to higher daytime temperatures, causing heat stress for urban dwellers. The extreme heat event analyses indicate that urban heat island plays an important role in premature urban mortality (Conti et al., 2005). Heat island effects air temperature, humidity, wind speed, radiation, and air pollution (Fischer et al., 2012). Epidemiological and statistical studies indicate a positive correlation between extreme ambient temperature and mortality during summer, particularly among elderly and women (McGeehin et al., 2001; Diaz et al., 2002; O'Neill et al., 2003, 2005 and 2009).

People living in urban environments are at greater risk than those in rural areas (Diaz et al., 2002). Inner urban environments, with high thermal mass and low ventilation, absorb and retain heat and can amplify the rise in temperature. Mortality is related to daytime temperature, humidity, heat wave duration, and nighttime low temperatures. Anderson and Bell (2009) estimate an increment in death by 4.5% per degree Celsius in heat wave intensity and 0.4% per day in heat wave duration. Zanobetti et al. (2008 and 2014) used mortality data across the United States and found that mortality increases by 3.6% per °C increase in temperature. Basu (2009) and Basu and Samet (2002) evaluated the relationship between mortality rate and temperature and found that mortality rate increased 4.6% per °C rise in apparent temperature (representing the combined effects of air temperature and relative humidity).

McMichael et al. (2006) presented the results of an investigation on the relation between temperature and mortality in eleven cities of the eastern United States. They defined a U-shaped relationship between the number of daily deaths and daily temperature. The study illustrates that mortality rates rise as temperatures reach beyond the upper and lower thresholds of human comfort. Figure 2.1 shows that by 2050, the number of heat-related deaths will increase more compared to cold-related deaths.

The indirect impacts of the UHI on human health occur through its effects on increasing photochemical reaction rates, which produce more ozone, thus worsening air quality. Air pollution affects the respiratory, circulatory, and olfactory systems. The effect is to aggravate pre-existing diseases or to degrade health status. The CO, NO_2 and O_3 effects on health are well documented (Conti et al., 2005). In high temperature, the ability of the circulatory system to transport O_2 will

be reduced and the aggregation of cardiovascular disease increased if a person is exposed to CO over a long period. Human exposure to NO_2 causes an increase in respiratory pathogens, and the exposure to O_3 causes a decrement in pulmonary function, with increased coughing, chest discomfort and risk of asthma attack (Conti et al., 2005).
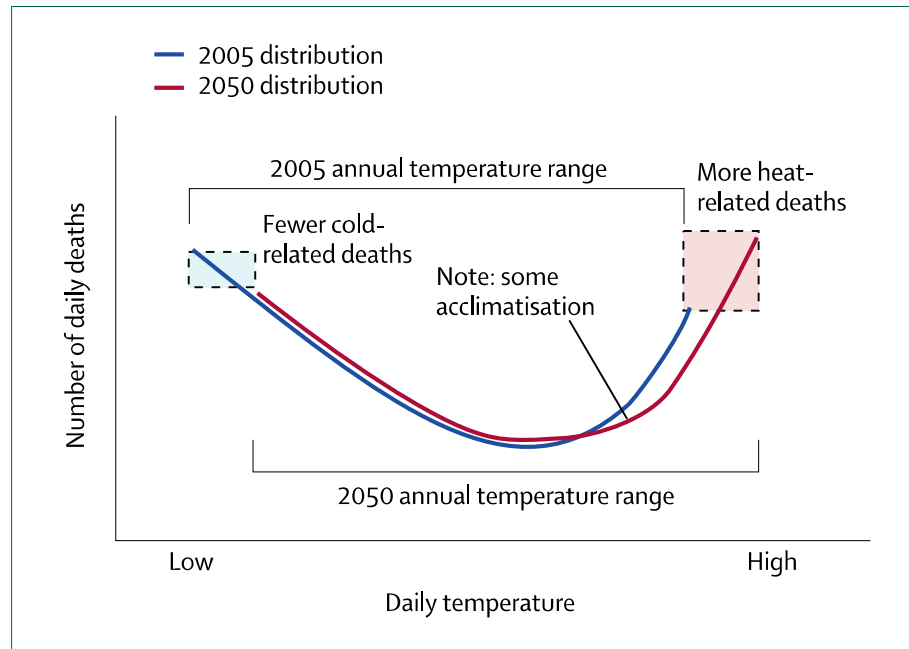
Figure 2.1. The effect of an increase in average annual temperature on temperature-related deaths (After McMichael et al., 2006)

In addition, high temperature has adverse effects on human mental health (Williams et al., 2012). People with mental disorders are more vulnerable to the high temperature (Cusack et al., 2011) and pre-existing mental and physical ailments can be exacerbated (Cusack et al., 2011). People may have trouble sleeping during hot summer periods and this in return can lead to fatigue and a lack of concentration, in turn leading to accidents (Sakka et al., 2012). There are also social issues associated with high temperature, such as the increase in crime and domestic violence (PwC, 2011). Doherty and Clayton (2011) attributed these issues such as increased homicide and suicide to the psychological impacts of climate change. Huang et al., (2011) found that the land surface temperature is statistically correlated with high poverty and low education as well as higher crime level.

High temperature can also increase the demand for fresh water and decrease the quality of water. Wetz and Yoskowitz (2013) pointed out that heat waves affect the water quality in terms of

nutrients and organic matter. The degraded water quality will consequently affect human health. In addition, access to reliable water service presents one of the social risks associated with heat wave events (Yardley et al., 2011). Extreme heat can lead to damage the urban water infrastructure such as pipelines, which can interrupt water services. The quality of water, especially drinking water, affects the health condition of human beings significantly.

The heat–health relationship has been investigated using a wide range of weather metrics such as temperature, relative humidity, solar radiation, barometric pressure, and wind speed (Barnett et al., 2010; Zhang et al., 2014). But there is still no universal standard metric for heat exposure. Furthermore, the impacts of high temperature on human health may vary according to geographical location (Zhang et al., 2014). Another important factor deserving attention is the consideration of high temperature in relation to age, gender, education, social, economic and cultural aspects.

The effects of high temperature on mortality is based on data collection and statistical analysis. Applying the statistical data alone cannot reflect the effects of any adaptation or mitigation strategies on heat-related health and deaths. Thus, developing a proper approach to estimate the effects of high temperature and its mitigation strategies will assist the estimation of heat-related mortality rates. Therefore, to have a proper understanding of the effects of heat wave events and heat island mitigation strategy on heat-related deaths, a meteorological simulation needs to be applied. Meteorological simulation deals with complex interactions between the meteorological parameters (e.g., temperature, wind, moisture, etc.) and urban morphology. Results can be used by decision-makers to make policies to improve lives of urban dwellers.

The effects of increased surface reflectivity on heat-related mortality has been investigated in a few studies. Kalkstein et al. (2013) showed that the UHI mitigation strategies in the District of Columbia contribute to a 7% reduction in the total number of heat-related mortality. The effects of UHI mitigation strategies were investigated in health-debilitating air masses in four cities across the US (Detroit, Los Angeles, New Orleans and Philadelphia). The heat-related deaths decreased by an average of 5 to 10% in these cities (Kalkstein and Sheridan, 2003). The results of another study by Kalkstein (1999) showed that a 1-2 °C reduction in outdoor temperature could reduce mortality by 10–20% in Washington.

One objective of this dissertation is to investigate the effects of urban heat island and increasing surface reflectivity on heat-related mortality in the Greater Montreal Area, Canada. The intention is to apply meteorological simulations to define heat-related mortality correlations.

2.2. Effects of Urban Heat Island and Increasing Surface Reflectivity on Urban Climate and Air Quality

The urban heat island phenomenon intensifies the effects of meteorological and chemical parameters in the urban atmosphere. UHI increases the photochemical reaction rates and pollutant emissions from biogenic and anthropogenic sources. UHI causes an increase in cooling energy demands, thus producing more pollutants from fossil fuel combustion. In addition, high temperature leads to smog formation and increased ozone concentrations in urban areas. Ozone has a close interaction with meteorological parameters (temperature, cloud, radiation, wind speed) as well as chemical parameters (NOx, CO, VOCs). Ozone is a photochemical pollutant. O_3 reactions take place in the presence of sunlight and involve volatile organic compounds (VOC) and oxides of nitrogen (NOx). It is formed during daytime and destroyed during the night within complex chemical reaction chains. The ozone concentration increases during periods with hot, sunny and calm conditions and thus negatively affects the air quality in urban areas (Seinfeld & Pandis, 2012). The heat island also intensifies the processes of ozone formation in the urban environment. Thus, the effects of UHI mitigation strategies on temperature and ozone concentrations need to be investigated.

The UHI impacts on urban climate and air quality are typically studied through a one-way approach at local, regional and global scales (Arnfield, 2003; Ban-Weiss et al., 2015; Taha, 2008 and 2009; Salamanca et al., 2012; Li and Bou-Zeid, 2014; Bhati and Mohan, 2016). In these studies, the interaction between regional atmosphere and local climate is neglected. The one-way approach cannot simulate the complete interactions between urban climate and air quality. The meteorological processes and photochemical reactions in the urban atmosphere magnify the UHI effects. These interactions in the urban environment cause changes in regional climate. The changes in regional atmosphere affect local pollution. A two-way nested approach provides an integrated simulation setup to capture the full impacts of meteorological processes and photochemical interactions in the atmosphere. This approach decreases the uncertainties associated

with scale separation and grid resolution. In addition, this method reveals more details of the effects of surface modifications on urban climate and regional air quality.

Another important factor that affects air quality in urban areas is aerosols. Aerosols affect the radiative balance of the Earth-Atmosphere system by scattering and absorbing the incoming solar radiation directly and by influencing cloud formation and precipitation indirectly (IPCC 2013; Zhang et al., 2014 and 2008). The aerosols impact cloud properties by convective potential energy such as radiation, relative humidity and wind shear (Fan et al., 2013). The evaporative cooling of water bodies during daytime is recognized to modulate the influence of aerosols on the processes of convective systems (Tao et al., 2011). Aerosols also act as cloud condensation nuclei (CCN) and may impact the life-time, albedo, and precipitation of cloud systems, through a complex interaction between cloud micro-physics and dynamics (Chen et al., 2011; Archer-Nicholls et al., 2015). There are two opposite effects of aerosol on cloud formation and precipitation because of aerosol radiative properties and CCN potentials: aerosols reduce the downward solar radiation to the ground, decreasing sensible heat fluxes to evaporate water and thus lessening precipitation; or absorbing solar radiation and gain heat and enhancing the convective clouds formation, thus increasing precipitation (Kluser et al., 2008; Levin and Brenguier, 2009; Koren et al., 2005; Fan et al., 2013). But current understanding of aerosol effects on the radiative budget and hydrological cycle of the climate system is still inadequate at the fundamental level. Some uncertainties also exist in aerosol estimation because of their heterogeneous distribution and complex interactions with radiation and clouds in the atmosphere (IPCC AR5, 2013).

Increasing surface albedo results in reflecting more short wave radiation and decreasing air temperature and photochemical reaction rates (Akbari et al., 2001 and 2009; Arnfield, 2003; Ban-Weiss et al., 2015; Taha, 2008 and 2009; Taha et al., 2000; Salamanca et al., 2012; Li and Bou-Zeid., 2014; Bhati and Mohan., 2016). By increasing surface reflectivity (ISR), Taha (2008) found 2 ºC decrease in maximum air temperature in urban areas in California. Similar results were found in Greece (Synnefa et al., 2008) and New York City (Lynn et al., 2009). Taha (2015) found 3 ºC and 5–10 ppb decreases in air temperature and ozone concentrations respectively in Sacramento. Salamanca and Martilli (2012) have shown that a higher albedo decreases urban temperature by 1.5–2 ºC during hot summer days in Madrid. Fallmann et al. (2013 and 2014) showed that increasing surface albedo led to a decrease in 2-m air temperature and ozone concentrations, by 0.5 ºC and 5–8 % respectively, in urban areas of Stuttgart during the 2003 heat wave period. Taha et

al. (2015) found that by increasing surface albedo, the air temperature was reduced by 2–3°C in Sacramento and the ozone concentrations decreased by up to 5–11 ppb during the daytime. The results of increasing albedo in Houston showed a reduction in temperature by up to 3.5 °C (Taha, 2008).

Few studies have also addressed the effects of albedo enhancement on a global scale. Akbari et al. (2012) found that by increasing roofs' (0.25) and pavements' (0.15) albedos, the total radiative forcing will decrease by 0.044 Wm^{-2}. Menon et al. (2010) found an increase of 0.5 Wm^{-2} in total outgoing radiation over global land area with albedo enhancement in urban areas (0.1). Oleson et al. (2010) found a decrease of 0.8 to 1.2 °C of urban heat island by increasing roof albedo (0.9).

Most previous studies have used a one-way simulation (climate simulations first, followed by air quality simulations). This approach does not provide a feedback of the atmospheric pollutants on the climate. *One objective of this dissertation is to develop a two-way nested approach to simulate the full impacts of meteorological processes and photochemical reactions on urban climate and air quality*. This approach provides an integrated simulation setup to investigate the effects of UHI and its mitigation strategy over a larger geographical area through urban areas. Increasing surface albedo may induce impacts on the hydrological cycle and radiative budget in the atmosphere. Yet, the effect of surface modification on aerosol-radiation-cloud interactions has not been investigated. Thus, it is necessary to illustrate the effects of heat island mitigation strategy on aerosols through case studies at different scales with a proper simulation tool. The model is required to combine the nonlinear effects of aerosols and simulate the interaction of aerosols, meteorology, chemistry and radiation in a fully interactive manner. *Another objective of this dissertation is to develop an approach to investigate the effects of UHI and albedo enhancement on aerosols' direct, semi-direct and indirect effects in the atmosphere and at the surface.*

2.3. Meteorological and Photochemical Models to Investigate the Effects of UHI and ISR on Heat-Related Mortality, Urban Climate and Air Quality

The meteorological and photochemical prediction models have been developed in response to the increased concerns regarding the effects of urban climate and air quality on human health. To investigate the effects of urban heat island and increasing surface reflectivity on urban climate, the NCAR Weather Research and Forecasting Model (WRF) (Skamarock et al., 2005) is applied to simulate the meteorological processes in the atmosphere. The online WRF is a non-hydrostatic

mesoscale numerical weather prediction (NWP) system. Mesoscale models are comprised of many physical parameterizations (cumulus, microphysics, planetary boundary layer, radiation, and land-surface) that have been used to predict the weather condition (WRF User Guide, 2014). In addition, the urban canopy models (UCMs) are used to represent the urban areas for more accurate estimation of air temperature, wind speed, relative humidity, surface temperature, and shortwave and longwave radiation. Urban areas are considered as a part of the land-surface parameterization to predict the heat and moisture fluxes from land to atmosphere.

Analyzing the sensitivity of meteorological parameters (e.g., air temperature, wind speed and relative humidity) to a different set of parameterizations (i.e., model ensemble) enables researchers to select the most accurate model platform for urban climate simulations. In previous studies the effects of UHI and its mitigation strategies have also been investigated applying the WRF model (Salamanca et al., 2012; Li and Bou-Zeid, 2014; Bhati and Mohan, 2016). Previous efforts in urban climate simulations are mostly performed using coarse grid cells, because of limitation in computational resources. In recent years, with further advancement of supercomputers and parallel processing, an approach with fine-resolution (sub-kilometer) grid cells has become a new trend (Marta-Almeida et al., 2016; Zheng et al., 2016; Touchaei et al., 2016). The fine-resolution grid spacing provides more detailed information on the spatial variation of the air temperature; hence, the selected model ensemble should be compatible with the selected technique. The results of these simulations are compared with the measurements obtained from weather stations and aircraft observations. The sensitivity analyses of physical parameters are based on the comparison between a predicted variable and the observed value from weather stations. *The other objective of this dissertation is to develop an appropriate platform for urban climate simulations and heat island mitigation strategy.*

To investigate the effects of UHI and ISR on air quality, the WRF model needs to be coupled with a chemistry package (WRF-Chem) to simulate meteorological quantities and air quality simultaneously (Grell et al., 2005). WRF-Chem has several physical and chemical parameterizations (Skamarock et al., 2008). The component of air quality is consistent with the meteorological ones within the same transport scheme, grid and physics schemes, and time steps. The spatial and temporal aspects of the WRF-Chem application have been analysed in many studies through one-way approaches, in local, regional or global scales (Ahmadov et al., 2012; Chuang et al., 2011; Misenis and Zhang, 2010; Zhang et al., 2012; Yahya et al., 2014; Tessum et al., 2015).

Another intention is to apply a two-way nested approach in WRF-Chem over a larger geographical area through regional and local scales such as urban areas. The morphological, thermal, and micro-scale properties of the urban canopy are considered by coupling WRF-Chem with a multi-layer of the Urban Canopy Model (ML-UCM) (Martilli et al., 2002).

The WRF-Chem model considers a variety of coupled physical and chemical processes such as transport, deposition, emission, chemical transformation, aerosol interactions, photolysis and radiation. Thus, to investigate the effects of UHI and ISR on aerosol-radiation-cloud (ARC) interactions in the atmosphere, the online-coupled WRF-Chem is applied to provide such interactive opportunities (Grell et al., 2005, 2013 and 2014). WRF-Chem has been employed in a wide range of studies and is capable of simulating the interactions among various atmospheric processes and meteorological components and air quality (Grell and Baklanov, 2011; Baklanov et al., 2014; Fast et al., 2012; Gao et al., 2011; Qian et al., 2009; Zhang et al., 2010). Saide et al. (2012) and Yang et al. (2011) evaluated the WRF-Chem simulations of aerosol-cloud-precipitation interactions over the Southeast Pacific for one month. The comparisons with measurements and satellite data indicated that the model performed reasonably well in predicting aerosols and clouds. Fast et al. (2006) investigated the treatment of aerosol optical properties in WRF-Chem and evaluated the simulation results using data collected during clear sky periods in the 2000 Texas Air Quality Study. Zhang (2008) applied WRF-Chem over eastern Texas in August 2000 to show that the presence of aerosols causes a decrease in temperature by up to 0.18 ℃ near the surface and an increase by up to 0.16 ℃ at the top of planetary boundary layer (~30 km). Zhang et al. (2014) represented a decrease of 0.22–0.59 mm/day in domain-wide mean precipitation over eastern Texas. Aerosols have a significant impact on climate state (Jacobson, 2002; Chung and Seinfeld, 2005; H. Liao et al., 2009) and future climate changes with regard to mitigation strategies employment (Brasseur and Roeckner, 2005). *The other goal of this dissertation is to investigate the effects of UHI and ISR on aerosols' direct (aerosol-radiation), semi-direct (aerosol-cloud), and indirect (aerosol-radiation-cloud) interactions in the atmosphere.*

2.4. Concluding Statement of Literature Review: Effects of Increasing Surface Reflectivity on Heat-Related Mortality, Urban Climate and Air Quality

This chapter reviewed the literature in several areas that pertain to the topic of the present research. The research gaps are identified here and addressed further in the following chapters. The

conclusions of the literature review with respect to investigations of the effects of increasing surface reflectivity on heat-related mortality, urban climate and air quality are summarized in the following statements:

- The urban heat island phenomenon has adverse effects on urban climate and air quality. UHI increases photochemical reaction rates, increases cooling energy demands, endangers human health and increases heat-related mortality.

- Increasing surface reflectivity (ISR) decreases urban temperatures, decreases photochemical reaction rates, decreases cooling energy demands in buildings during summertime, and improves air quality and human health and comfort.

- The impacts of high temperature on mortality are significant. Yet, there is no correlation between the effects of heat island and its mitigation strategy on heat-related deaths.

- There is a close relation between UHI, urban morphology and atmospheric science. To have a better understanding of the UHI effects on urban climate and air quality for environmental policymakers, a proper simulation platform is essential for further simulations and analyses.

- Most analyses regarding the effects of UHI and its mitigation strategy have focused on a one-way simulation approach. Instead, a two-way nested approach is required to capture the full impacts of meteorological processes and photochemical reactions on urban climate and air quality.

- The effects of urban heat island and increasing surface albedo have not been investigated on aerosol interactions, radiative budget and hydrological cycle of the climate system. Thus, a simulation approach is required to combine these nonlinear effects of aerosols and to simulate the aerosols-radiation-cloud interactions in the atmosphere in a fully interactive manner.

The applied methodology and simulation approaches to address the objectives of this thesis are presented in Chapter 3.

Chapter 3
Methodology

The main objectives of this dissertation are to investigate the effects of increasing surface reflectivity on urban climate, air quality and heat-related mortality. These objectives are accomplished by the following tasks:

- developing a platform for urban climate simulation and heat island mitigation strategy;
- investigating the effects of urban heat island and its mitigation strategy on heat-related mortality;
- developing a two-way nested simulation approach to assess the effects of urban heat island and increasing surface reflectivity on urban climate and air quality; and
- investigating the effects of heat island and increasing surface albedo on aerosol-radiation-cloud interactions.

Section 3.1 introduces the simulation approaches to achieve these tasks including: meteorological and photochemical models, a setup procedure, preparation to perform simulations, and evaluation of model performance. Section 3.2 explains applied methodology to develop an appropriate platform for urban climate simulation and heat island mitigation strategy. Section 3.3. addresses the approaches to estimate the effects of increasing urban albedo on heat-related mortality. Section 3.4. describes the methods to investigate the effects of increasing solar reflectance on urban climate and air quality within a two-way nested simulation approach. Section 3.5 provides the procedure to estimate the effects of increasing surface albedo on aerosol-radiation-cloud interactions in the atmosphere.

3.1. Meteorological and Photochemical Simulations

Meteorological models use surface characteristics (land use / land cover) and initial and boundary conditions to solve a set of conservation equations, simulate the advection and diffusion of pollutants, and predict meteorological conditions (namely air temperature, moisture, wind speed, etc.). Photochemical models use the meteorological conditions and air pollutants' emission estimations (from biogenic and anthropogenic sources) to simulate emission, transformation and dispersion of pollutants and predict air quality conditions (namely ozone, nitrogen dioxide, carbon monoxide, etc.). Figure 3.1. shows the meteorological and photochemical models' interactions.
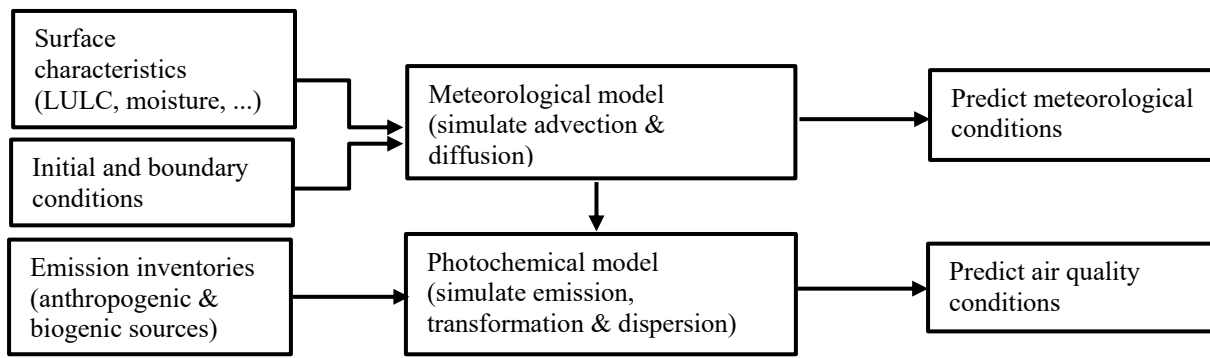
Figure 3.1. Meteorological and photochemical models' interactions (LULC= Land Use/Land Cover)

3.1.1. Simulation Models: WRF, WRF-Chem, ML-UCM

The online Weather Research and Forecasting model (WRF) considers a variety of meteorological and physical parameterizations (cumulus, microphysics, planetary boundary layer, radiation, and land-surface) to predict weather conditions. The WRF is a mesoscale numerical weather prediction (NWP) system which is fully compressible (deals with flows having significant changes in fluid density) and non-hydrostatic (the vertical momentum equation is solved). WRF can be coupled with chemical parameterizations (Chem) to simulate the meteorological quantities and air pollution concentrations simultaneously (Grell et al., 2005). Coupling the WRF with a chemistry package enables researchers to simulate chemical processes (transport, deposition, emission, chemical transformation, aerosol interactions, photolysis and radiation) to predict air quality conditions. The component of air quality is consistent with the meteorological components within the same transport scheme, grid and physics schemes, and time steps. In addition, the multi-layered Urban Canopy Model (ML-UCM) can be coupled with the meteorological and photochemical models. The ML-UCM is a part of the land-surface parameterization to predict the

heat and moisture fluxes from canopies to atmosphere. The UCM represents the urban areas for more accurate estimation of air temperature, wind speed, relative humidity, precipitation, and shortwave and longwave radiation.

Figure 3.2. shows the flowchart of WRF with chemistry package and urban canopy model for urban climate and air quality simulations. The terrestrial data and weather gridded data are obtained from North America Regional Reanalysis (NARR). The pre-processing of WRF (called WPS) is used to define the domain and period of simulation and interpolates the NARR data into the domain of interest. With WRF there are physical parametrizations to solve a set of conservation equations and predict meteorological conditions. The chemical boundary conditions are defined by simulations that predict the anthropogenic and biogenic emission estimations. The chemistry package is used to estimate the aerosol interactions, photolysis rates, gas-phase reactions, and wet and dry depositions of chemical components. A brief description of WRF, chemistry package and urban canopy model is presented below. A more detailed explanation can be found in the WRF User Guide 2018.
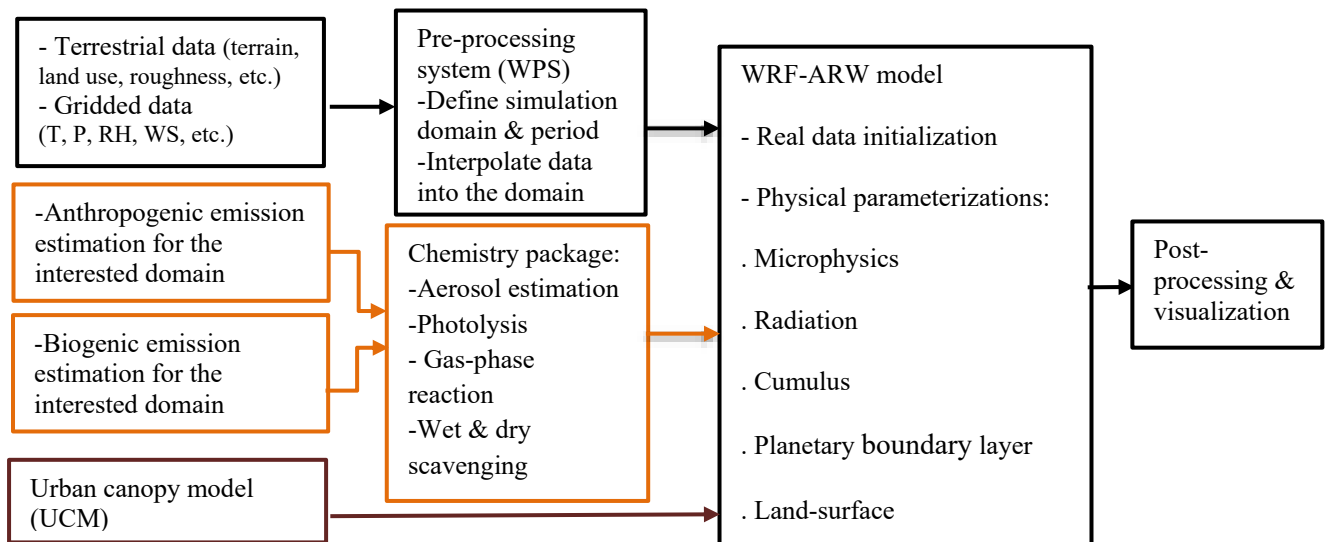
Figure 3.2. Flowchart of WRF coupled with chemistry package (green color) and urban canopy model (brown color) (T= air temperature, P= pressure, RH=relative humidity, WS=wind speed, WPS=weather pre-processing system, UCM=urban canopy model, WRF=weather research & forecasting model, ARW=advanced research WRF)

Figure 3.3 shows the simulation approach to accomplish the multiple goals of this study, including preparation, processes and achievements. The preparation includes compiling and coupling of models and simulation steps (defining domain and period of simulation and collecting

input data and measurements data). The processes refer to WRF, WRF-Chem, UCM simulations, and anthropogenic and biogenic emission estimations. In addition, data analysis is a main part of the process, including comparing the simulation results with measurements and comparing different scenarios. The consequences of these approaches are to: 1) develop a platform for urban climate simulations and heat island mitigation strategy; 2) develop an algorithm to estimate heat-related mortality; 3) provide a two-way nested approach to simulate urban climate and air quality; 4) define an approach to estimate the effects of surface modification on aerosol-radiation-cloud interactions in the atmosphere. These procedures are explained in the following figure.
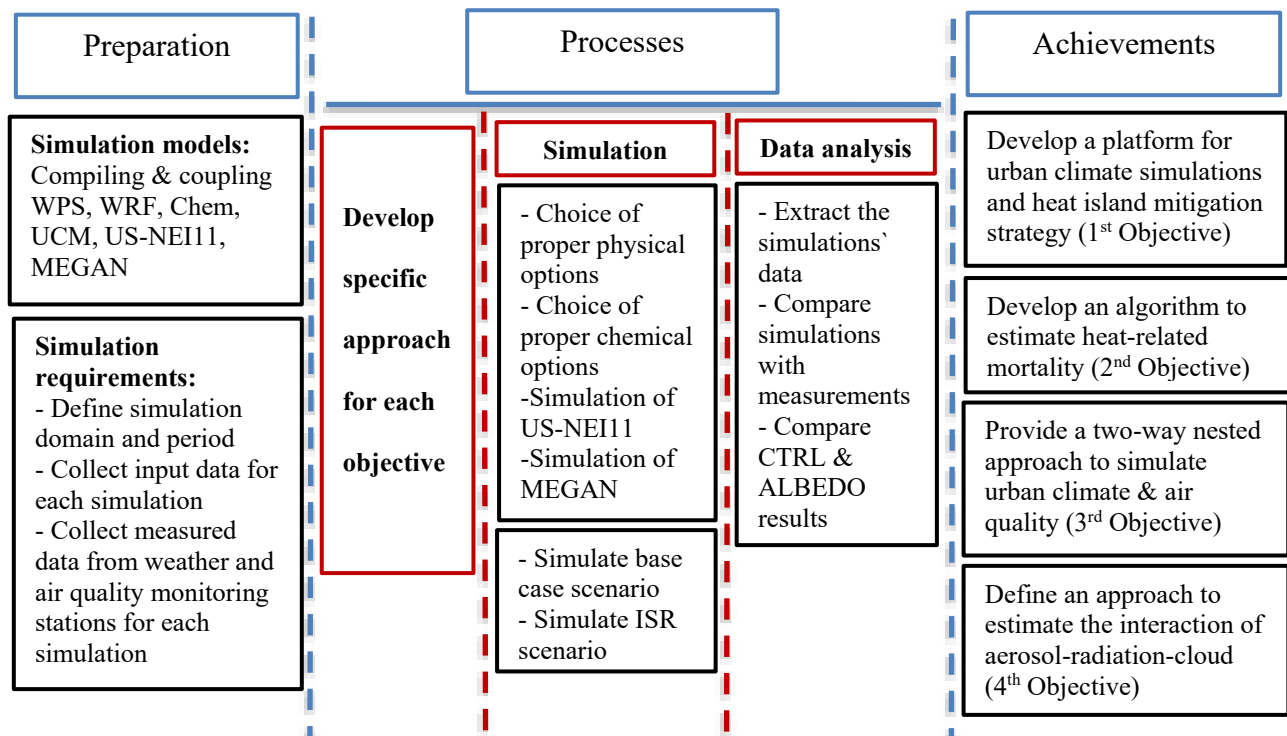
Figure 3.3. Simulation approaches: preparation, processes and achievements (WPS=weather pre-processing system, WRF=weather research & forecasting model, WRF with chemistry=WRF-Chem, UCM=urban canopy model, US-NEI11=United States National Emission Inventory 2011, MEGAN= Model of Emissions of Gases and Aerosols from Nature, CTRL=control case, ALBEDO= albedo enhancement, ISR=increasing surface reflectivity)

3.1.2. Preparation of Simulation Models and Requirements

3.1.2.1. Compiling and Coupling of Simulation Models

WRF simulations require significant preparation and computer resources. At the onset, one should make sure that the computer has sufficient memory capacity and a fast processing system

in order to compile, couple and carry out various simulations in a timely manner. Here, the North America-caluculquebec cluster is used to perform each simulation. The first step to start simulations is to compile and couple the WRF Preprocessing System (WPS), WRF Data Assimilation (WRF-DA) and Advanced Research WRF Solver (ARW-WRF).

➢ **WRF Preprocessing System (WPS)**

This program is used primarily for real-data simulations. Its functions include: 1) defining simulation domains; 2) interpolating terrestrial data (such as terrain, land use, and soil types) to the simulation domain; and 3) interpolating meteorological data to the simulation domain.

➢ **WRF Data Assimilation (WRF-DA)**

This program is used to inject observations into the interpolated analyses created by WPS. It can also be used to update the WRF model's initial conditions when the model is run in cycling mode. It is based on an incremental variational data assimilation technique and has both 3D-Var and 4D-Var capabilities.

➢ **Advanced Research WRF Solver (ARW-WRF)**

This is the key component of the modeling system, which is composed of several initialization programs for real-data simulations. The key features of the WRF model include: 1) fully compressible, nonhydrostatic equations with hydrostatic option; 2) regional and global applications; 3) mass-based terrain-following coordinates; 4) vertical grid-spacing which can vary with height; 5) Runge-Kutta 2nd and 3rd order time integration options; 6) scalar-conserving flux form for prognostic variables; 7) 2nd to 6th order advection options (horizontal and vertical); 8) monotonic transport and positive-definite advection option for moisture, scalar, tracer, and TKE (Turbulent Kinetic Energy); and 9) full physics options for land-surface, planetary boundary layer, atmospheric and surface radiation, microphysics and cumulus convection. Figure 3.4 shows the steps to compile and run WPS and WRF. Table 3.1 summarizes the description of these steps.
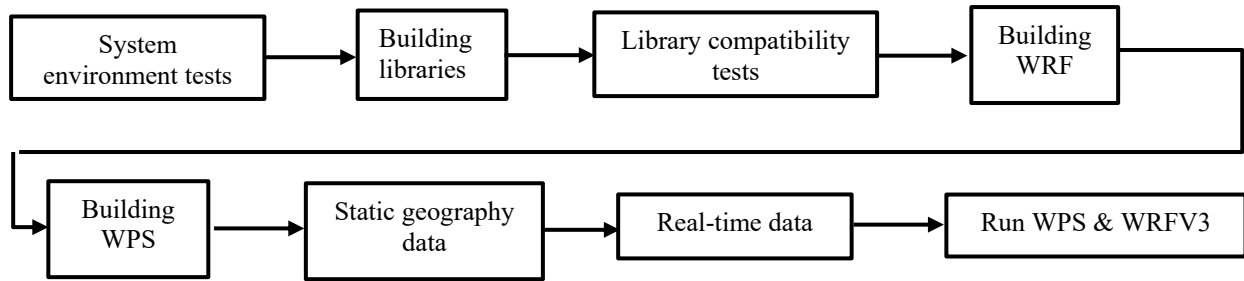
Figure 3.4. Steps to compile and run the WPS and WRF models

Table 3.1. Description of the steps to compile and run the WPS and WRF models

Steps to compile & run WPS & WRF models	Description
System environment tests	It is important to have required compiler as gfortran. The WRF build system has scripts as the top level for the user interface as well.
Building libraries	There are various libraries that should be installed for example netcdf and Jasper. These libraries must be installed with the same compilers as will be used to install WRF and WPS.
Library compatibility tests	These tests are essential to verify that the libraries are able to work with the compilers that are to be used for the WPS and WRF builds.
Building WRFV3	After ensuring that all libraries are compatible with the compilers, one can now prepare to build WRFV3. First, the tar file should be downloaded from verified source and unpacked in the preferred directory. Then, a configuration file should be created to compile. The compiler is selected to be serially or in parallel.
Building WPS	After building the WRF model, WPS program needs to be built. A tar file containing the WPS source code, is downloaded and unpacked. Then the WPS is compiled to be compatible with WRF. If the compilation is successful, there should be three executables in the WPS top-level directory, that are linked to their corresponding directories.
Static geography data	To initiate a real-data case, the domain's physical location on the globe and the static information for that location must be created. This requires a data set that includes such fields as topography and land use categories. These data need to be downloaded and un-compressed.
Real-Time data	For real-data cases, the WRF model requires up-to-date meteorological information for both an initial condition and lateral boundary conditions. This meteorological data is traditionally a file that is provided by a previously run external model or analysis. For a semi-operational set-up, the meteorological data is usually sourced from a global model, which permits locating the WRF model's domains anywhere on the globe. The National Centers for Environmental Prediction (NCEP) run the Global Forecast System (GFS) model four times daily.
Run WPS & WRFV3	First, the WPS is executed by modifying its name-list to reflect information that is required for the particular simulation. The geogrid will match the geographical data and define the simulation domain. The ungird unpack necessary data regarding the simulation period. The met-gird interpolate the weather and terrestrial data on the domain of interest. To simulate the WRF, the name-list needs to be modified. The data provided by WPS, should be connected and linked to the run directory.

18

➢ **System Environment Tests**

It is important to have "gfortran", "gcc" and "cpp" compilers. In addition to the compilers required to manufacture the WRF executables, the WRF build system has scripts as the top level for the user interface—namely, "csh", "perl", and "sh".

➢ **Building Libraries**

There are various libraries that should be installed including: "mpich", "netcdf", "Jasper", "libpng", and "zlib". These libraries must be installed with the same compilers as will be used to install WRF and WPS.

➢ **Library Compatibility Tests**

Once the target machine is able to make "Fortran" and "C" executables, after the "NetCDF" and "MPI" libraries are constructed, two additional small tests are required to emulate the WRF code's behavior. It is essential to verify that the libraries are able to work with the compilers that are to be used for the WPS and WRF builds. These tests are for "Fortran+ C+ NetCDF" and "Fortran + C + NetCDF + MPI".

➢ **Building WRFV3**

After ensuring that all libraries are compatible with the compilers, one can now prepare to build WRFV3. First, the tar file should be downloaded from a verified source (NCAR) and unpacked in the preferred directory. Then, a configuration file should be created to compile. The compiler is selected to be serial or in parallel. For parallel, which is for real case simulations, there are three options: "smpar", "dmpar" and "dm+sm". The "dmpar" is the best option; it has fewer errors and is more compatible with other programming languages. To check whether it was successful, the executable files—namely, "wrf.exe", "real.exe", "ndown.exe", and "tc.exe"—need to be checked.

➢ **Building WPS**

After building the WRF model, WPS program needs to be built. A tar file containing the WPS source code is downloaded and unpacked. Then the WPS is compiled to be compatible with WRF.

If the compilation is successful, there should be three executables in the WPS top-level directory, which are linked to their corresponding directories—namely, "geogrid", "ungrib", and "metgrid".

➢ **Static Geography Data**

To initiate a real-data case, the domain's physical location on the globe and the static information for that location must be created. This requires a data set that includes such fields as topography and land use categories. These data need to be downloaded and un-compressed.

➢ **Real-Time Data**

For real-data cases, the WRF model requires up-to-date meteorological information for both an initial condition and lateral boundary conditions. This meteorological data is traditionally a Grib file that is provided by a previously run external model or analysis. For a semi-operational setup, the meteorological data is usually sourced from a global model, which permits locating the WRF model's domains anywhere on the globe. The National Centers for Environmental Prediction (NCEP) run the Global Forecast System (GFS) model four times daily (initializations valid for 0000, 0600, 1200, and 1800 UTC). This is a global, isobaric, 0.5-degree latitude/longitude, forecast data set that is freely available, and is usually accessible +4h after the initialization time period. A single data file needs to be acquired for each requested time period.

➢ **Run WPS & WRFV3**

First, the WPS is executed by modifying its "namelist.wps" to reflect information that is required for the particular simulation. The "geogrid.exe" will match the geographical data and define the simulation domain. The "ungird.exe" unpacks necessary data regarding the simulation period. The "metgird.exe" interpolates the weather and terrestrial data in the domain of interest. To simulate the WRF, the "namelist.input" needs to be modified. The data provided by WPS should be connected and linked to the run directory. First, the "real.exe" is executed and then the "WRF.exe". The "error.rsl" file needs to be checked for any errors. If the execution was successful, then the required data should be extracted and analysed. The physical parameterizations used in WRF includes: planetary boundary layer, shortwave and long wave radiation, microphysics, cumulus and land-surface schemes. A brief description is presented in Section 3.2.4.

➢ **Run WPS & WRFV3**

First, the WPS is executed by modifying its "namelist.wps" to reflect information that is required for the particular simulation. The "geogrid.exe" will match the geographical data and define the simulation domain. The "ungird.exe", unpack necessary data regarding the simulation period. The "metgird.exe", interpolate the weather and terrestrial data on the domain of interest. To simulate the WRF, the "namelist.input" needs to be modified. The data provided by WPS, should be connected and linked to the run directory. First, the "real.exe" is executed and then the "WRF.exe". The "error.rsl" file needs to be checked for any errors. If the execution was successful, then the required data should be extracted and analysed. The physical parameterizations used in WRF includes: planetary boundary layer, shortwave and long wave radiation, microphysics, cumulus and land-surface schemes. A brief description is presented in section 3.2.4.

3.1.2.2. Coupling the WRF with the Urban Canopy Model (UCM)

Urban Canopy Models (UCMs) can provide more accurate feedbacks on urban areas for surface layer and planetary boundary layer schemes. There are three types of UCMs within WRF: slab (bulk), single-layer (SL), and multi-layer (ML). The urban canopy model consists of sensible heat fluxes from roofs, walls and roads and aggregates them into the exchange of momentum and energy between the urban surface and atmosphere. Surface temperatures are calculated from the upward long wave radiation. Wind shear calculations allow for increased roughness, shadowing from buildings and characteristic radioactive properties within street canyons. Thermal properties of building materials and anthropogenic heat generated by human activities are considered as well (Chen et al., 2011).

A multi-layer of the urban canopy model (ML-UCM) represents the 3-dimentional nature of urban surfaces and interacts with the planetary boundary layer. In the ML-UCM, the effects of walls (as vertical surfaces) and roofs and roads (as horizontal surfaces) are considered in terms of momentum, turbulent kinetic energy and potential temperature.

3.1.2.3. Compiling and Coupling the Chemistry Package with WRF

The chemistry package is downloaded from NCAR and unpacked in the "run" directory of WRF. The "GFortran", "C" and "NetCDF" programming languages are used to compile the chemistry package with the solver of the WRF. The air quality component of the model is fully consistent with the meteorological component, having the same transport, grid, and physics

schemes with the same time steps. WRF-Chem considers a variety of chemical processes including dry deposition, aerosol and photolysis estimations. Dry deposition is defined based on the surface of the soil and the plants' resistances and is simulated within suitable schemes in WRF-Chem. The surface resistance depends on the diffusion coefficient, the reactivity, and water solubility of the reactively trace gas. By changing the land use input data, these schemes have to be adapted accordingly. To estimate the photolysis rate, the Fast-J model in the chemistry package is an accurate and fast algorithm to evaluate the effect of cloud, aerosol and ozone on photolysis rate (Wild et al., 2000). The model solves the multi-reflection in the atmosphere using exact scattering phase function and optical depths to predict the photolytic intensities. For model stability, wet scavenging, cloud chemistry, sub-grid aqueous chemistry, and aerosols radiation feedback need to be activated in the solver of WRF-Chem.

> **Emission Estimations**

Modeling of the chemical composition of the atmosphere requires preliminary information about initial emissions of chemical compounds within the modeling domain. Emission inventories describe the amount of pollutants discharged into the atmosphere. For anthropogenic emission estimation, the United States National Emission Inventory for 2011 (US-NEI-11) is used. The US-NEI-11 is installed. The simulation domain and episode are defined by modifying its name-list file. The US-NEI contains the anthropogenic emission for the contiguous 48 states of the US, southern Canada and northern Mexico in 4-km spatial resolution. This inventory is designed for regional scale and photochemical models that require emission data for NOx, VOC, CO, SO_2, NH_3, $PM_{2.5}$, and PM_{10}. Emissions have been split into point and area sources. The model results are then transferred to the programming language that can be read by the solver of the WRF-Chem. Figure 3.5 shows the steps to estimate the anthropogenic emissions with NEI-2011.
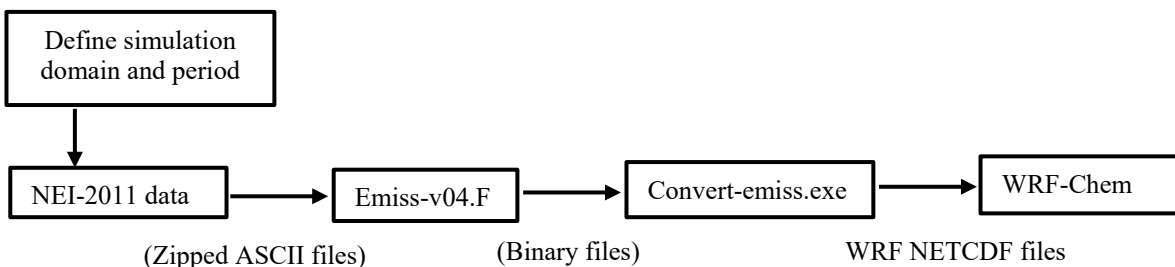
Figure 3.5. The US-NEI11 simulation approach to estimate anthropogenic emissions

For biogenic emission estimation, the Model of Emissions of Gases and Aerosols from Nature (MEGAN) is used. MEGAN estimates the time resolved gridded BVOC emission estimation in mole/km^2/hr. MEGAN is designed for regional and global emission modeling and has a base resolution of 1 km. MEGAN estimates the 134 chemical species including isoprene, monoterpenes, oxygenated compounds, nitrogen oxide and so on. The calculation of emissions in MEGAN is defined based on emission factor, leaf area index factor, temperature response factor, leaf age factor, soil moisture factor, production within the plant canopy. The model results need to be transferred to the programming language that can be read by the solver of WRF-Chem. Figure 3.6 shows the MEGAN approach to estimate biogenic emissions in the interested domain.
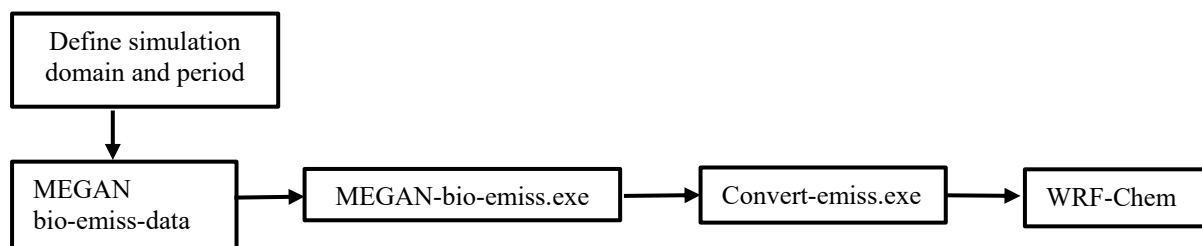
Figure 3.6. The MEGAN simulation approach to estimate biogenic emission

> **Aerosols Estimations in WRF-Chem**

There are several options in the chemistry package to estimate the aerosols' interactions in the atmosphere—namely, bulk, sectional, and modal. The model treatment of aerosols is shown in Figure 3.7. The emissions parameters from various sectors are the main source of aerosols in the urban atmosphere. The aerosol chemistry is estimated by gas phase chemistry model. The atmospheric conditions affect aerosol nucleation and coagulation. Thus, the aerosol chemistry is changing in time. The changes are calculated by aqueous phase chemistry, cloud microphysics, and wet and dry depositions. In addition, aerosol affects the hydrological cycle by wet scavenging and being activated in the aqueous phase chemistry (e.g., in cloud formation and precipitation). Aerosols also affect the radiation budget in the atmosphere through their effects on shortwave and longwave radiation processes in the atmosphere and at the land surface.
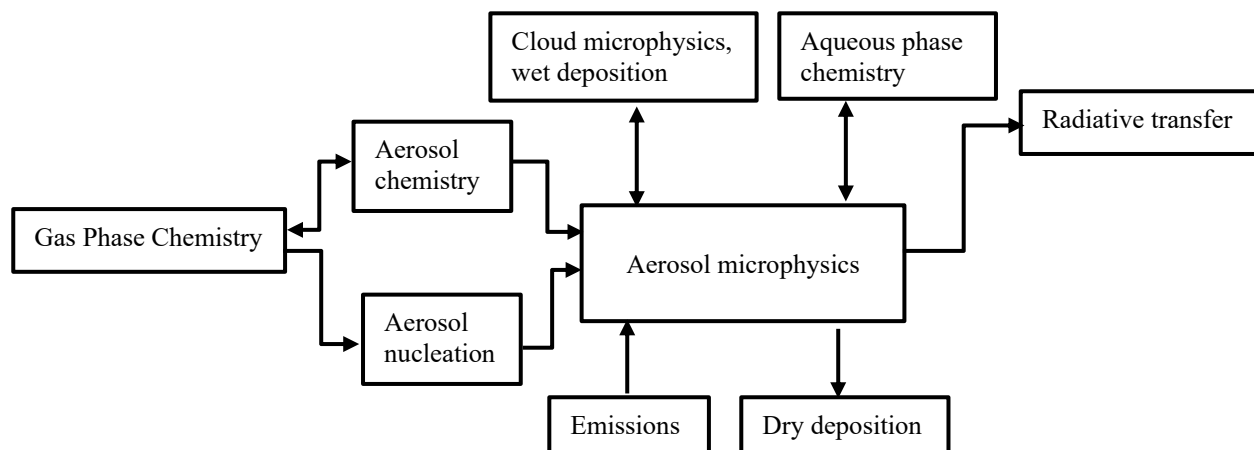
Figure 3.7. Model treatment of aerosol estimations and interactions with other physical and chemical options in WRF-Chem

3.1.2.5. Preparation of Simulation Requirements

For each objective, the simulation domain and period are different, thus the input data differ also. The simulations are conducted with the initial and boundary conditions obtained from the North American Regional Reanalysis (NARR) for the specific domain and episode. These data are then interpolated to the domain of interest by simulating WPS. The evaluation of the model performance is conducted by comparing the simulation results with measurements obtained from weather and air-quality monitoring stations across the domain. A more detailed explanation regarding each objective follows.

3.1.3. Simulations Scenarios and Evaluation of Model Performance

3.1.3.1. Simulations of Control Case and Increasing Surface Reflectivity

Two sets of simulations are conducted with different scenarios for each objective: the base case condition that the albedo of roofs, walls, and roads are assumed to be 0.2 (hereafter referred to as CTRL); and the increasing surface reflectivity scenario where the albedo of roofs, walls, and roads is increased (hereafter referred to as ALBEDO). The changes to gridded ALBEDO can be calculated as: surface albedo enhancement (roofs, walls, and roads) × fraction of urban area per grid cell.

Three different urban categories are defined within WRF urban canopy models. Low-intensity residential (class 31) includes areas with a mixture of built-up structures and vegetation (for 20–70% of land cover). High-intensity residential areas (class 32) have vegetation coverage under

24

20%. Industrial/commercial areas (class 33) include infrastructure and highly developed areas not classified as residential (USGS 2014). To investigate the effects of albedo enhancement, the albedo of roofs, walls, and roads are increased from 0.2 to 0.65, 0.60, and 0.45, respectively. The α_R, α_W and α_G represent surface albedo of roofs, walls, and roads, respectively, and are modified in the URBPARM.TBL. Table 3.2 is located in the "run" directory of the WRF and represents urban canopy parameters. The changes are shown in bold. With these modifications, the effects of increasing surface reflectivity are investigated on urban climate and air quality in a specific domain and period of simulation by comparing the ALBEDO results with the CTRL results.

Table 3.2. urban canopy parameters in URBPARM.TBL in WRFV3.6.1

Parameters	Unit	Specific value for		
		Low-intensity residential	High-intensity residential	Industrial /commercial
F_{urb} (Urban Fraction)	Fraction	0.5	0.9	0.95
C_R & C_W (Heat Capacity of Roof & Wall)	J m^{-3} K^{-1}	1.0E6	1.0E6	1.0E6
C_G (Heat Capacity of Ground)	J m^{-3} K^{-1}	1.4E6	1.4E6	1.4E6
λ_R & λ_W (Thermal Conductivity of Roof & Wall)	J m^{-1}s^{-1} K^{-1}	0.67	0.67	0.67
λ_G (Thermal Conductivity of Ground)	J m^{-1}s^{-1} K^{-1}	0.4004	0.4004	0.4004
α_R (Surface Albedo of Roof)	**Fraction**	**0.65**	**0.65**	**0.65**
α_W (Surface Albedo of Wall)	**Fraction**	**0.60**	**0.60**	**0.60**
α_G (Surface Albedo of Ground)	**Fraction**	**0.45**	**0.45**	**0.45**
ε_R & ε_W (Surface Emissivity of Roof & Wall)	-	0.90	0.90	0.90
ε_G (Surface Emissivity of Ground)	-	0.95	0.95	0.95
Z_{0R} & Z_{0G} (Roughness Length for momentum over Roof & Ground)	m	0.01	0.01	0.01
Z_{0W} (Roughness Length for momentum- Wall)	m	0.0001	0.0001	0.0001
PWIN (Coverage area fraction of windows in the walls of the buildings)	-	0.2	0.2	0.2
BETA (Thermal efficiency of heat exchanger)	-	0.75	0.75	0.75
Air Conditioning Switch (On=1)		1	1	1
COP (Coefficient of performance of AC conditioning)	-	3.5	3.5	3.5
TARGTEMP (Target T of AC systems)	K	297	298	298
GAPTEM (Comfort range of indoor temperature)	K	0.5	0.5	0.5
TARGHUM & GAPHUM (Target & Comfort humidity of AC systems)	kg/kg	0.005	0.005	0.005
HSEQUIP_SCALE_FACTOR (Peak Heat Generated by Equipment)	W/m^2	36	20	16

3.1.3.2. Evaluation of Model Performance

The performance and accuracy of the simulation results are quantitatively based on a series of metrics estimations (Boylan and Russell, 2006). The mean bias error (MBE), mean absolute error (MAE), and the root mean square error (RMSE) of the meteorological parameters are calculated. Mean bias error (MBE) is the indication of underestimation (negative value) or overestimation (positive value) of the predicted meteorological variables compared to the measurements (Eq. 1).

Mean absolute error (MAE) represents the absolute error in simulation and is known as a natural metric to evaluate the performance of a model (Walcott, 2005) (Eq. 2). Root mean square error (RMSE) is a more rigorous indicator for model assessment (Eq. 3).

$$MBE = \frac{1}{N}\sum_{1}^{N}(C_M - C_O) \tag{Eq. 1}$$

$$MAE = \frac{1}{N}\sum_{1}^{N}|C_M - C_O| \tag{Eq. 2}$$

$$RMSE = \sqrt{\frac{\sum_{1}^{N}(C_M - C_O)^2}{N}} \tag{Eq. 3}$$

Where C_M and C_O are modelled and observed data, and N is the number of model and observation pairs in hours.

3.2. Develop a Platform for Urban Climate Simulation and Heat Island Mitigation Strategy

Parameterization is a simple way of representing physical processes such as cloud formation and precipitation. Mesoscale models are comprised of many parameterizations that are used for predicting the weather condition. The model ensemble for urban climate simulation includes parameterizations for microphysics, cumulus, planetary boundary layer (PBL), radiation, land surface, and urban canopy. Characterizing the meteorological parameters (e.g., air temperature, wind speed, relative humidity and precipitation) to a different set of parameterizations (i.e., model ensemble) enables researchers to select the proper model platform for urban climate simulations. Figure 3.8 shows the simulation approach to accomplish this objective. A brief description is presented for each step in the following sections. Box A refers to explanations in Section 3.1.2, and box B shows the accomplishments and endpoints of this objective.
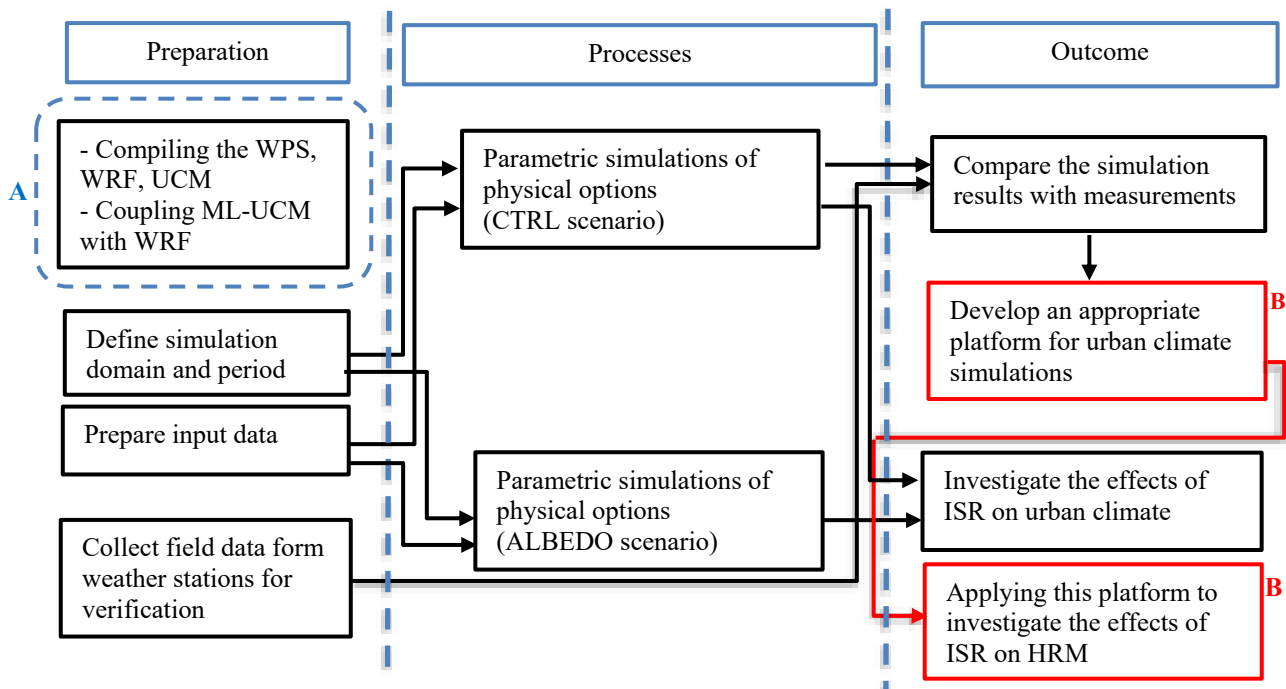
Figure 3.8. The simulation approach to prepare an appropriate platform for urban climate assessment (ISR=increasing surface reflectivity, HRM= heat-related mortality, CTRL= base case simulations, ALBEDO= increasing urban albedo)

3.2.1. Defining Simulation Domain and Period

The simulation domain is the Greater Montreal Area (GMA) that is centered at the ~45.5ºN and ~73.6ºW. The horizontal domain of the simulations is composed of four two-way nested domains with 37×22, 43×34, 91×61, and 145×91 grid points, and a grid sizes of 9, 3, 1 and 0.333 km × km, respectively. The vertical coordinate eta is calculated by $((P - P_{top})/(P_{surf} - P_{top})$; where P is the dry hydrostatic pressure at each corresponding level, P_{surf} is dry hydrostatic surface pressure, and P_{top} is a constant dry hydrostatic pressure at model top). The vertical resolution includes 51 vertical layers from the surface to a fixed pressure of ~100 mb (~16 km AGL). The selected simulation period starts with a clear sky condition (9th of August) and ends with a rainy condition (11th of August). The summer days are selected because results are used to evaluate the effect of urban heat island mitigation strategy (increasing surface reflectivity). Figure 3.9 shows the simulation domains based on USGS land use categories.

<div style="text-align:center">Domain 1 (grid size: 9 km × km)</div>

<div style="text-align:center">Domain 2 (grid size: 3 km × km)</div>

<div style="text-align:center">Domain 3 (grid size: 1 km × km)</div>

<div style="text-align:center">Domain 4 (grid size:0.333 km × km)</div>
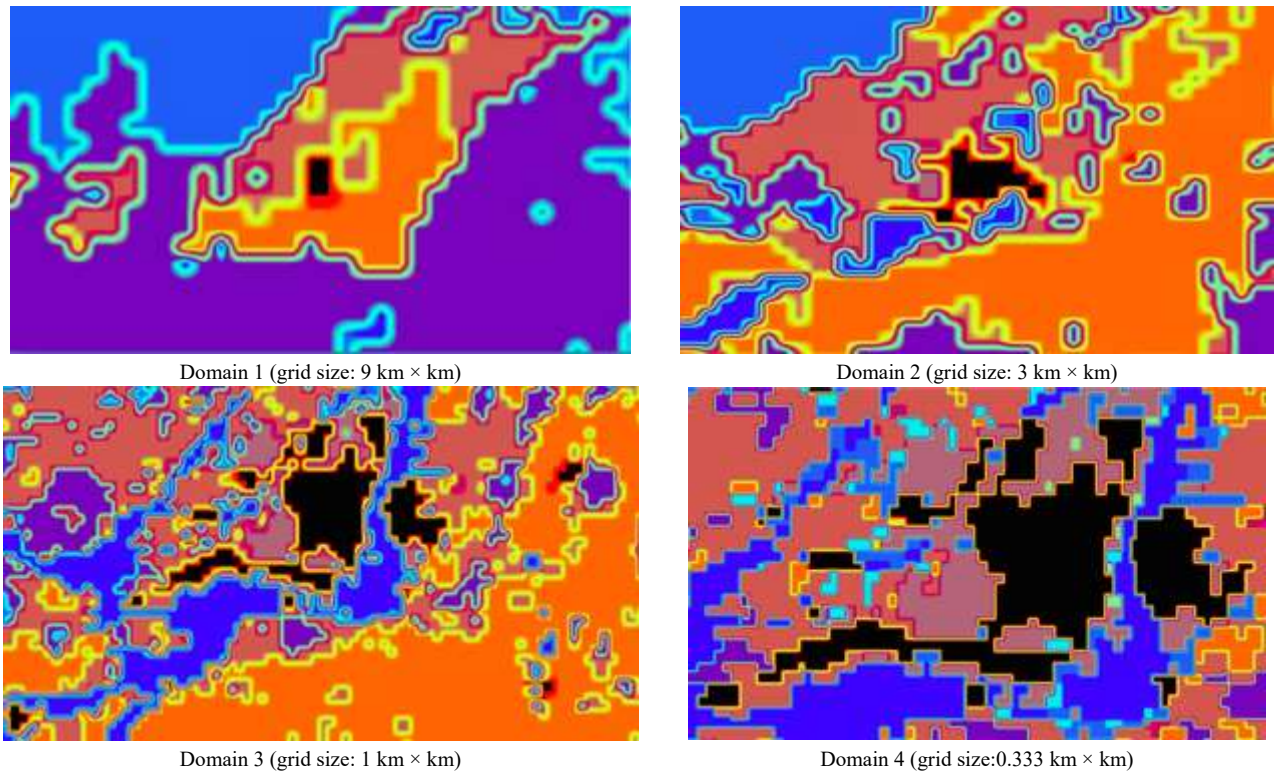
Figure 3.9. Simulation domains (grid sizes of domain 1: 9 km × km, domain 2: 3 km × km, domain 3: 1 km × km, domain 4: 0.333 km × km). Black refers to urban and build-up and cropland/woodland, the blue and purple refer to water bodies

3.2.2. Preparation of Input Data for Simulations

The simulations were conducted with the initial and boundary conditions obtained from the North American Regional Reanalysis (NARR). A vertical resolution of 51eta level is defined to take full advantages of the urban parameterizations. Land Use/Land Cover (LULC) data was derived from the USGS 24-category data set. Advanced Very High-Resolution Radiometer (AVHRR) measures the background surface albedo (Csiszar and Gutman 1999). The other physical parameterizations are explained in section 3.2.4. The positive-define advections of moisture, scalars and turbulent kinetic energy is activated to maintain model stability. Each simulation begins at 0000 UTC (LST= UTC - 4h) of the previous day of each period. The first 28h is considered as a spin up period.

3.2.3. Collection of Local Meteorological Data to Evaluate Model Performance

To evaluate the simulations performances, the meteorological parameters namely: the 2-m air temperature (T2), 10-m wind speed (WS10), 2-m relative humidity (RH2), and precipitation are collected from seven weather stations (McTavish (MT), Pierre Elliott Trudeau Intl (PET), St-Hubert (SH), Ste-Anne-de-Bellevue (SAB), Varennes (VA), Mirabel (MI), and Ste-Clothilde (SC))

across the Greater Montreal Area for the 9th to 11th of August 2009. Figure 3.10 and Table 3.3 present their geographical locations.

Figure 3.10. The location of weather stations in Greater Area of Montreal

Table 3.3. Weather stations in Greater Montreal Area with their locations (Latitude, Longitude, and Elevation)

Signs	Station Name	Station Code	Latitude (N)	Longitude (W)	Elevation (m)
▲	McTavish	MT	45.50	-73.58	73
▲	Pierre Elliott Trudeau	PET	45.47	-73.75	36
▲	St-Hubert	SH	45.52	-73.42	27
▲	Ste-Anne-de-Bellevue	SAB	45.42	-73.92	39
▲	Varennes	VA	45.72	-73.38	18
▲	Mirabel	MI	45.67	-74.03	82
▲	Ste-Clothilde	SC	45.17	-73.68	53

3.2.4. Parametric Simulations of Physical Options

The physical parameterizations need to be carefully selected to predict weather conditions. The physical processes can be selected based on a set of sensitivity analysis. A proper simulation platform is essential to have a better understanding of the effects of UHI and its mitigations strategy on urban climate and air quality for environmental policy makers. Table 3.4 presents the simulation set-ups with different options on parametrizations. The options that are used for each physical model are presented in the parenthesis. The options for all domains are the same, except the cumulus model that is not activated for the 4th domain and the ML-UCM that is only activated for the 4th domain. A land surface model (LSM) is used for all these model ensembles. LSM provides information on momentum, heat and moisture fluxes on land points by using atmospheric feedback of other schemes in a simulation. LSM updates surface variables (e.g., the ground temperature, soil temperature profile, soil moisture profile, snow cover, and canopy properties) in each iteration step as independent variables. A brief description of other physical parameterizations is provided in the

following.

Table 3.4. Simulation set-ups with different options on parameterization of microphysics, cumulus, PBL, and radiation

	Microphysics	Cumulus	PBL	Radiation
S01	WDM (16)[1]	Simplified Arakawa-Schubert (4)[2]	MYJ (2)[3]	RRTMG (4)
S02	WDM (16)	Betts-Miller-Janjic (2)[5]	MYJ (2)	RRTMG (4)
S03	WDM (16)	Grell 3D (5)[6]	BouLac PBL (8)[7]	RRTMG (4)
S04	WDM (16)	Grell 3D (5)	MYJ (2)	Dudhia (1)[8]
S05	Eta (5)[9]	Grell 3D (5)	MYJ (2)	RRTMG (4)
S06	WDM (16)	Grell 3D (5)	MYJ (2)	RRTMG (4)
S07	WDM (16)	Grell-Freitas (3)[10]	MYJ (2)	RRTMG (4)
S08	Goddard (7)[11]	Grell 3D (5)	MYJ (2)	RRTMG (4)
S09	WDM (16)	Kain-Fritsch (1)[12]	MYJ (2)	RRTMG (4)
S10	Lin (2)[13]	Grell 3D (5)	MYJ (2)	RRTMG (4)
S11	Milbrandt-Yau (9)[14]	Grell 3D (5)	MYJ (2)	RRTMG (4)
S12	Morrison (10)[15]	Grell 3D (5)	MYJ (2)	RRTMG (4)
S13	NSSL (17)[16]	Grell 3D (5)	MYJ (2)	RRTMG (4)
S14	NSSL with CCN (18)	Grell 3D (5)	MYJ (2)	RRTMG (4)
S15	WDM (16)	New Simplified Arakawa-Schubert (14)[17]	MYJ (2)	RRTMG (4)
S16	SBU-YLin (13)[18]	Grell 3D (5)	MYJ (2)	RRTMG (4)
S17	Thompson (8)[19]	Grell 3D (5)	MYJ (2)	RRTMG (4)
S18	WDM (16)	Tiedtke (6)[20]	MYJ (2)	RRTMG (4)
S19	WSM (6)[21]	Grell 3D (5)	MYJ (2)	RRTMG (4)
S20	WDM (16)	Zhang-McFarlane (7)22	MYJ (2)	RRTMG (4)

[1] Lim and Hong, (2010), [2] Pan and Wu., (1995), [3] Janjic (1994), [4] Iacono et al. (2008),[5] Janjic (1990), [6] Grell (1993), and Grell and Devenyi (2002), [7] Bougeault and Lacarrere, (1989), [8] Dudhia (1989), and Mlawer et al. (1997), [9] NOAA, (2001), [10] Grell and Freitas (2014), [11] Tao et al. (1989), [12] Kain (2004), [13] Lin (1983), [14] Milbrandt and Yau, (2005a), and Milbrandt and Yau, (2005b), [15] Morrison et al. (2009), [16] Mansellet al. (2010), [17] Han and Pan (2011), [18] Lin and Colle (2011), [19] Thompson et al. (2008), [20] Tiedtke (1989), and Zhang et al. (2011), [21] Hong and Lim, (2006), [22] Zhang and McFarlane, (1995)

3.2.4.1. Selection of Appropriate Microphysics Options

Microphysics models determine the process of transforming water from one form (rain, snow, graupel, vapor) to another. In general, water vapor creates cloud water and cloud ice to shape snow, graupel (soft hail or snow pellets) and rain. The main equations governing the processes are conservation of momentum, energy, and mass of water in the cloud, rain, snow, and other forms of precipitation. Table 3.5 presents a brief description of different schemes of microphysics in WRF. Detailed explanation follows.

Table 3.5. Parameterization schemes of microphysics model in WRF

Scheme	Description
Lin	Applies conservation equation for the mass of water to the combination of cloud ice, cloud water, and water vapor. Conservation of mass is also applied to snow, rain, and hail mixing ratios. It predicts source and sink terms of snow, hail and rain
SBU-YLin	Has accurate prediction of ice and snow
Eta	Considers six species of water, mixed phase of rain and snow for temperature of more than -10ºC
WRF Single-Moment 6-class (WSM6)	Has more accurate dependency of snow to temperature, calculate ice nuclei number concentration, and has a new algorithm to consider the auto-conversion of cloud water to rain
WRF Double-Moment 6-class (WDM6)	Considers mixing ratio and number concentration as independent variables. It calculates the number concentration of cloud, rain, and cloud condensation nuclei
Thompson	Predicts the mixing ratios of five hydrometeors and the number concentration of cloud ice. It predicts the saturation adjustment, vapor deposition, sublimation, and evaporation
Morrison	Considers five species of water and predicts mixing ratio. Concentrations are calculated from the specified size distribution and the predicted mixing ratio
National Severe Storms Laboratory (NSSL)	Considers lightning in microphysical models to understand the charging processes of hydrometeors and evolution of storms
Goddard	Uses a saturation adjustment scheme as a function of liquid water and ice saturation values to calculate the amount of condensation and deposition of cloud water and cloud ice
Milbrandt-Yau	Uses gamma size distribution and predicts the shape parameter in prognostic equations

> **Lin Sscheme**

Lin developed and improved the microphysics models by adding the effect of snow and its related processes (Lin et al. 1983). Conservation equation for the mass of water is applied to the combination of cloud ice, cloud water, and water vapor. Conservation of mass is also applied to snow, rain, and hail mixing ratios. Parameterization of microphysics models predicts source and sink terms of snow (ice crystal aggregation, accretion (increase), sublimation, and melting), hail (snow crystal aggregation, accretion, raindrop freezing, sublimation, and melting), and rain (auto-conversion, accretion, freezing and melting, and evaporation) in the mass conservation equations. This model is improved for fine resolutions and is implemented in WRF by Chen et al. (2002).

> **SBU-YLin Scheme**

Lin et al. (2011) proposed a new model with more accurate prediction of riming intensity of ice and snow. They reduced the number of variables and conversion processes compare with Lin et al. (1983) to get a more computationally efficient parameterization.

> **Eta Scheme**

Eta model (NOAA, 2001) is a parameterization of microphysics processes that improves previous model of NCEP (Zhao et al., 1997a; 1997b). The model considers six species of water (water vapor, cloud ice or cloud water, ice, snow, graupel, and sleet). Moreover, the model can consider mixed

31

phase of rain and snow for temperature of more than -10ºC. Temperature range specifies the presence of cloud water (>0 ºC), cloud ice (< -15ºC), or the chance for either of them.

> **WRF Single-Moment 6-class (WSM6) Scheme**

WRF Single-Moment 6-class (WSM6) scheme (Hong and Lim, 2006) is the improved version of previous parameterizations proposed by Hong et al. (2004). Many modifications were performed to have a realistic model: 1) more accurate dependence of snow to temperature, 2) advanced model for calculating ice nuclei number concentration, and 3) new algorithm for auto-conversion of cloud water to rain.

> **WRF Double-Moment 6-class (WDM6) Scheme**

WDM6 (Lim and Hong, 2010) is the double-moment version of WSM6 (Hong and Lim, 2006). In the double-moment scheme both mixing ratio and number concentration are considered as independent variables. This model calculates the number concentration of cloud, rain, and cloud condensation nuclei. Numbers of cloud and rain drops are an exponential function of their size. The interception is a function of mixing ratio and temperature. This assumption significantly changes the number of small size raindrops.

> **Thompson Scheme**

Thompson scheme predicts the mixing ratios of five hydrometeors (cloud water, rain, cloud ice, snow, and graupel) and the number concentration of cloud ice (Thompson et al., 2008). The model predicts the saturation adjustment, vapor deposition, sublimation, and evaporation.

> **Morrison Scheme**

Morrison double-moment scheme (Morrison 2009) considers five species (cloud droplets, cloud ice, snow, rain, and graupel). The velocity components and the perturbation of potential temperature, geopotential, and surface pressure of dry air, along with water vapor mixing ratio, and the different cloud microphysics variables are used in a set of prognostic equations to predict the mixing ratio. The number concentrations are calculated from the specified size distribution and the predicted mixing ratio.

> **National Severe Storms Laboratory (NSSL) Scheme**

The NSSL scheme has the capability of considering lightning in microphysical models (Mansell et al., 2010) to understand the charging processes of hydrometeors and evolution of storms. Two independent moments, mass mixing ratio and number concentration of cloud droplets, rain, ice crystals, snow, and graupel is predicted by the model.

➢ **Goddard Scheme**

Tao et al. (1989) proposed a saturation adjustment scheme as a function of liquid water and ice saturation values to calculate the amount of condensation and deposition of cloud water and cloud ice. The scheme is a single-moment microphysical model that can predict the mixing ratio of different hydrometeors.

➢ **Milbrandt-Yau Scheme**

Milbrandt-Yau scheme uses gamma size distribution (Milbrandt and Yau, 2005a; 2005b) and the radar reflectivity is added to predict the shape parameter in prognostic equations.

3.2.4.2. Selection of Appropriate Cumulus Options

Cumulus parameterizations consider the effect of convective air movement outside clouds on up drafting and down drafting of clouds (Grell and Devenyi, 2002). Inclusion of the cumulus model affects the vertical heat and moisture fluxes in a column of air above individual grids. In addition, some models are able to predict the cloud and precipitation tendencies. All WRF options estimate the convective component of surface rainfall. In general, the models have three parts; 1) trigger function to identify the convection, 2) flux equations for mass and/or momentum and/or energy, 3) the closure assumptions. Table 3.6 presents a brief description of different schemes of cumulus in WRF. Detailed explanation follows.

Table 3.6. Parameterization schemes of cumulus model in WRF

Scheme	Description
Simplified Arakawa-Schubert	Considers the mass and energy balance in clouds. Surface rainfall is parameterized in the moisture balance equation
Betts-Miller-Janjic	Considers convective mixing and keeps the total enthalpy unchanged in the deep convection profile. Predicts the shallow clouds to consider the effect of atmospheric stability on the temperature profile
Grell 3D	Divides parameterizations into dynamic control and feedback. It accounts for both entrainment rate and detrainment rate in the steady state plume equation
Grell-Freitas	Predicts the cloud convection in high-resolution grid size simulations
Kain-Fritsch	Uses the vertical momentum conservation equation to capture instabilities
New Simplified Arakawa-Schubert	Uses turbulent diffusion-based approach and considers the convection-induced pressure gradient forcing in momentum equation
Tiedtke	Considers the eddy transport of energy in prognostic equations
Zhang-McFarlane	Modifies the cumulus parameterization in the Canadian Climate Center General Circulation Model by considering the exchange of unstable air change with adjacent layers

➢ **Simplified Arakawa-Schubert Scheme**

A simple set of equations considers the mass and energy balance in clouds (Pan and Wu., 1995). High energy parcels are assumed to move upward to reach a level of free convection. The percentage of the parcels at a point below the cloud is specified to determine the entrainment rate

and it was assumed that the parcel will lose the energy in the cloud. In this model surface rainfall is also parameterized in the moisture balance equation.

 ➢ **Betts-Miller-Janjic Scheme**

Janjic (1994) modified the earlier version of a cumulus parameterization by adding convective mixing to the thermodynamically driven process and keeping the total enthalpy unchanged in the deep convection profile. Additionally, for shallow clouds, which are identified by a jump in relative humidity, a positive change in entropy change is conditionally added to the equations. To predict the shallow clouds, the humidity profile plays an important role and it was modified to consider the effect of atmospheric stability on the temperature profile.

 ➢ **Grell 3D Scheme**

This model divides parameterizations into dynamic control and feedback (Grell, 1993; Grell and Devenyi, 2002). The dynamic control governs the effect of convection by the environment. The feedback parameterization determines the adjustment of the environment by the convection. Grell 3D Scheme accounts for both entrainment rate and detrainment rate in the steady state plume equation. The model uses the updraft and downdraft mass flux to calculate normalized mass flux, normalized condensation and evaporation profiles, moist static energy, and liquid water content.

 ➢ **Grell-Freitas Scheme**

The Grell-Freitas scheme predicts the cloud convection in high-resolution grid size simulations (Grell and Freitas, 2014). The model limited the number of ensembles in Grell 3D scheme to optimize the calculation time in numerical weather prediction simulations.

 ➢ **Kain-Fritsch Scheme**

Kain-Fritsch scheme is a new version based on the Lagrange approach mass flux parameterization. It uses the vertical momentum conservation equation to capture instabilities (Kain, 2004). The model calculates the decay of the convective available potential energy of cloud convection. The outputs are temperature, water vapor mixing ratio, and cloud water mixing ratio tendencies. The model also estimates the surface rainfall.

 ➢ **New Simplified Arakawa-Schubert Scheme**

Han and Pan (2011) developed the New Simplified Arakawa-Schubert scheme using turbulent diffusion-based approach and considering the convection-induced pressure gradient forcing in momentum equation. A finite entrainment and detrainment rates for heat, moisture, and momentum

was specified. To avoid excessive grid-scale precipitation by depleting more instability in deep convection, cumulus convection was modified to be stronger and deeper.

➢ **Tiedtke Scheme**

Tiedtke (1989) proposed a mass flux-based model that considers the eddy transport of energy in prognostic equations. In addition to updraft and downdraft of clouds, a penetrative convection closure was parameterized for deep convection. Shallow convection is governed by the same turbulent moisture flux as of penetrative convection for near surface layers.

➢ **Zhang-McFarlane Scheme**

This model modifies the cumulus parameterization in the Canadian Climate Center General Circulation Model by considering the exchange of unstable air change with adjacent layers (Zhang and McFarlane, 1995). The formulation is based on the mass flux of hydrometeors along with their energy conservation.

3.2.4.3. Selection of Appropriate Planetary Boundary Layer (PBL) Options

Planetary boundary layer (PBL) is responsible for vertical flux exchange in the whole column of air in a grid cell (Pielke, 2002). PBL quantifies the influence of momentum, heat and moisture fluxes in the vertical sub-grid terms. In mesoscale models, PBL is divided into three sub-layers. The viscous layer goes from the ground to the height of surface roughness where fluxes of heat, moisture, and other constituents are experimentally estimated based on the von Karman constant and friction velocity. The surface layer and transition layer are the two other parts of PBL and they can be estimated as a function of height (Pielke, 2002). Urban surfaces are heterogeneous surfaces and the parameterization is based on more complex methods. Table 3.7 presents a brief description of different schemes of PBL in WRF. Detailed explanation follows.

Table 3.7. Parameterization schemes of planetary boundary layer models in WRF

Scheme	Description
Mellor-Yamada-Janjic (MYJ)	Considers the viscous sublayer above water bodies and a turbulent layer above the water sublayer and lands
Bougeault- Lacarrere (BouLac)	Calculates the TKE in a prognostic equation as a function of vertical molecular dissipation, mass flux, horizontal velocity, and heat

➢ **Mellor-Yamada-Janjic (MYJ) Scheme**

Janjic (1994) considers the viscous sublayer above water bodies and a turbulent layer above the water sublayer and lands. In addition, the model calculates TKE (Turbulent Kinetic Energy) above turbulent layer to reduce the spin up time for the model (Janjic, 2002). MYJ (Mellor-Yamada-

Janjic) has the minimum bias for different urban categories, about 0°C for industrial category and high-density residential category and about 1°C for low-density residential category. Thermal roughness length affects the surface temperature during the day, and the surface temperature during the night is strongly related to the choice of PBL.

➢ **Bougeault- Lacarrere (BouLac) Scheme**

This model calculates the TKE (Turbulent Kinetic Energy) in a prognostic equation as a function of vertical molecular dissipation, mass flux, horizontal velocity, and heat (Bougeault and Lacarrere, 1989).

3.2.4.4. Selection of Appropriate Radiation Options

Radiation parameterization determines the energy balance of the domain. The surface of the domain (e.g., urban surface) can receive shortwave energy from the sun or longwave energy from the sky. Urban surfaces absorb part of the energy and reflect the rest, while emitting longwave radiation. The amount of energy that strikes the surface is a function of sky condition and solar zenith angle. The energy exchange on the surface is well discussed by Liou (1980), and a different algorithm with a different level of complexity has been developed to quantify it (ASHRAE, 2007; Duffie and Beckman, 2006; Iqbal, 1983). Incoming solar radiation and emitted longwave radiation from the ground varies through different mechanisms in the atmosphere. In a clear sky, part of the sunlight energy on top of the atmosphere is absorbed by different tracer gases (e.g., ozone, water vapor, etc.) and the rest reaches the ground. However, cloudy and polluted sky increases the absorption by increasing the normal optical thickness of the air layer (Liou, 1980). The part of the radiation reflected from the ground goes through the same process. The longwave radiation that is emitted from the surface of the earth and gases are absorbed by the atmosphere or transmitted.

3.2.5. Analyses of Physical Parameterizations in WRF

Data analysis are comprised of two parts: compare the simulation results with measurements (model performance evaluation) and compare the results of two simulations (CTRL scenario with ALBEDO scenario). The parameters that are directly extracted from the simulation results are 2-m air temperature (T2, K), precipitation (RAINNC, mm), horizontal and vertical wind speed (U10, V10, m/s), and mixing ratio (amount of water vapor in the air) (Q2, %). Other parameters are calculated as presented in Table 3.8 namely 10-m wind speed (WS10, m/s) and 2-m relative humidity (RH2, %).

Table 3.8. WRF output parameters and calculations to obtain other parameters

Parameters to be calculated	Calculations	
10-m wind speed (m/s) (U10, V10)	$\sqrt{(U10)^2 + (V10)^2} = WS(m/s)$	U10 = horizontal wind speed V10 = vertical wind speed
Mixing ratio (Q2) to estimate the 2-m relative humidity (%)	$SVP = 6.11 \times 10^{\left(\frac{7.5 \times T2}{237.3 + T2}\right)}$ $SMR = 621.97 \dfrac{SVP}{(P_{station} - SVP)}$ $RH = \dfrac{Q2}{SMR} \times 100$	SVP = saturated vapor pressure SMR = saturated mixing ratio $P_{station}$ = station pressure (millibar) T2 = 2-m air temperature (ºC)

The physical parameterizations in the solver of WRF need to be carefully selected to predict weather conditions. Proper physical options for meteorological simulations enable environmental policy makers to have a better understanding of the effects of heat island and its mitigations strategy on urban climate and air quality. For Greater Montreal Area (GMA), an appropriate platform is developed based on the city`s specific location and weather conditions. This platform is verified by comparing the simulations results with measurements and thus further is applied to perform other objectives such as assessing the effects of heat island and increasing surface reflectivity on heat-related mortality in Greater Montreal Area. In addition, it provides a good understanding of each physical parametrizations in WRF and their impacts on meteorological parameters in cold climate.

3.3. Heat-Related Mortality Estimation

Heat-related mortality (HRM) can be magnified in urban areas because of the urban heat island (UHI) effects. UHI intensity and duration cause an increase in mortality. To fight the heat island effects, increasing urban albedo is applied. To investigate the effects of increasing surface reflectivity (ISR) on heat-related deaths, a meteorological simulation is used. An algorithm is defined to estimate the effects of high temperature on HRM. Figure 3.11 shows the simulation approach to estimate the effects of urban heat island and increasing surface reflectivity on heat-related mortality. Box A refers to explanations in Section 3.1.2, and box B shows the accomplishments of this objective.

3.3.1. Defining Simulation Domain and Period

The simulation domain is Greater Montreal Area centered at the ~45.5º N and ~73.6º W. The horizontal domain of the simulations is composed of four two-way nested domains with 37×22, 43×34, 91×61, and 145×91 grid points, and a grid spacing of 9, 3, 1 and 0.333 km x km,

respectively. Figure 3.12 shows the simulation domain and land use/ land cover of domain 4. The simulations are conducted during the 2005 (10th -12th July) and the 2011 (20th – 23rd July) heat wave events. Table 3.9 presents the maximum air temperature recorded on each day of the simulation. Figure 3.13 shows the maximum and minimum temperatures for the summer (June, July, August (JJA)) for GMA in 2005 and 2011.
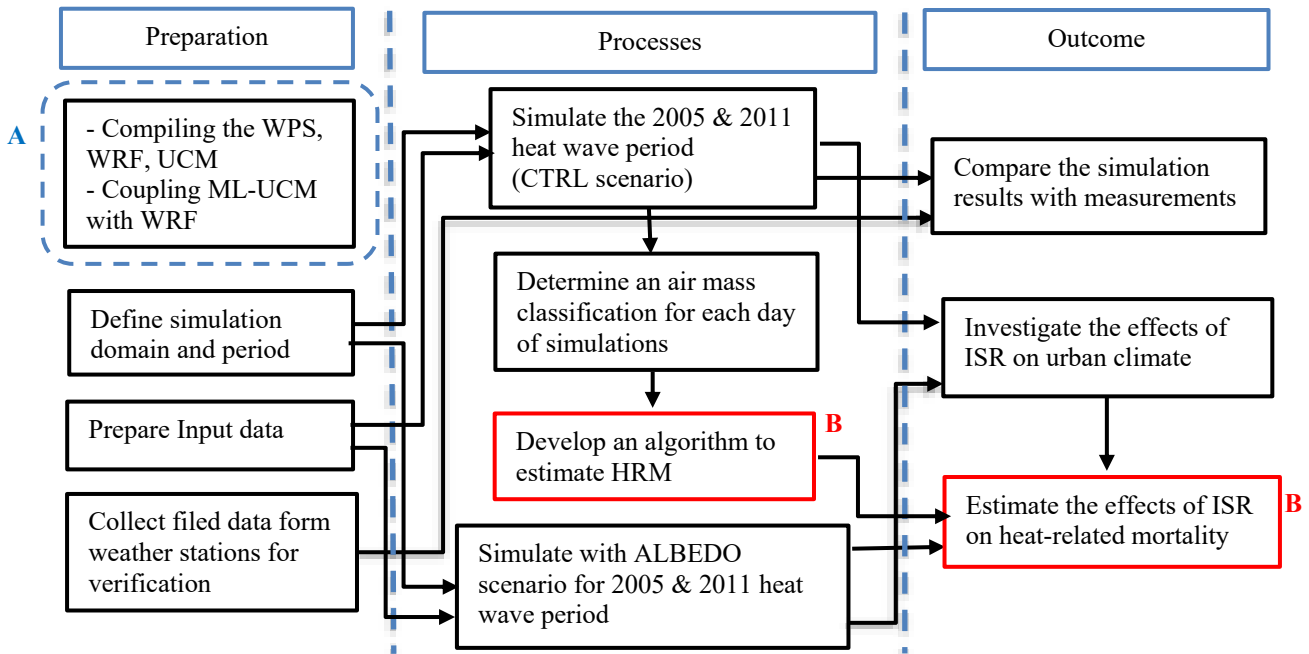
Figure 3.11. Simulation approach to estimate the effects of increasing surface reflectivity on heat-related mortality (ISR=increasing surface reflectivity, HRM= heat-related mortality, CTRL= base case simulations, ALBEDO= increasing urban albedo)
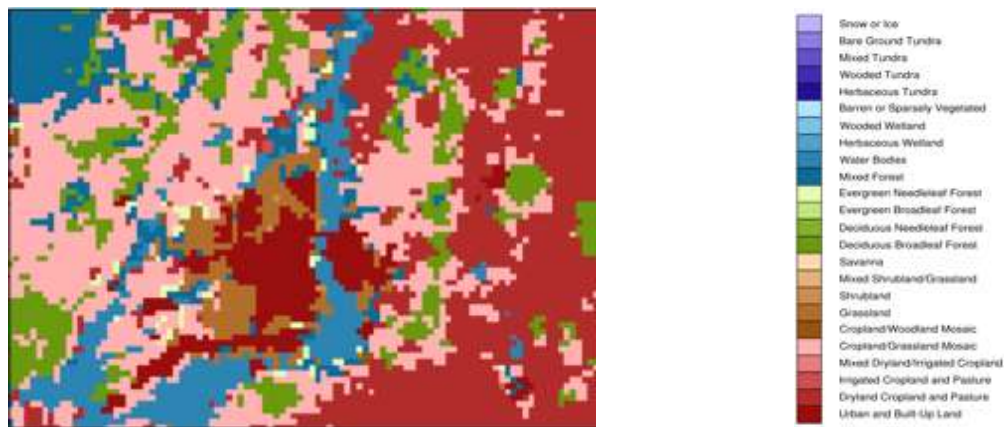
Figure 3.12. Simulation domain and Land Use Land Cover (LULC) of GMA

Table 3.9. Maximum air temperature measured in four weather stations over GMA in 2005 and 2011heat wave periods (McTavish (MT), Pierre Elliott Trudeau Intl (PET), St-Hubert (SH), St-Anne-de-Bellevue (SAB))

Heat wave periods	July 2005	Max temperature (ºC)			
		MT	PET	SH	SAB
July 2005	10th	31.6	31.5	31.1	30.8
	11th	32.3	32.8	31.5	32.2
	12th	30.6	30.6	30.7	30.3
	July Average T (ºC)	**26.9**	**27.3**	**27.0**	**27.1**
July 2011	21th	34.9	35.6	36.0	34.7
	22nd	31.3	31.9	32.6	32.2
	23rd	31.6	32.6	32.6	31.9
	July Average T (ºC)	**28.3**	**28.5**	**29.0**	**28.5**

Figure 3.13. Maximum and minimum temperatures for the summer (June, July, August (JJA)) for GMA in 2005 and 2011

39

3.3.2. Preparation of Input Data for Simulations

The simulations were conducted with the initial and boundary conditions obtained from the North American Regional Reanalysis (NARR). A vertical resolution of 51eta level is defined to take full advantages of the urban parameterizations. The proper physical parameterizations of the 1st objective is used to simulate the CTRL and ALBEDO cases of the 2005 and 2011 heat wave period over Greater Montreal Area. The positive-define advections of moisture, scalars and turbulent kinetic energy is activated to maintain model stability. Each simulation begins at 1200 UTC (LST= UTC - 4h) of the previous day of each period. The first 24h is considered as a spin up period.

3.3.3. Collection of Local Meteorological Data to Evaluate Model Performance

To evaluate the simulations performances, the meteorological parameters namely: 2-m air temperature (T2), 10-m wind speed (WS10), relative humidity (RH), and dew point temperature (DPT) are collected from four weather stations (McTavish (MT), Pierre Elliott Trudeau Intl (PET), St-Hubert (SH), Ste-Anne-de-Bellevue (SAB)) across the Greater Montreal Area for two heat wave period in 2005 and 2011. Table 3.3 presents their geographical locations.

3.3.4. Analyses of Meteorological and Heat Stress Indices Parameters

The parameters that are directly extracted from the simulation results are the 2-m air temperature (T2, K), dew point temperature (DPT, K), horizontal and vertical wind speed (U10, V10, m/s), and water mixing ratio (Q2, %). Other parameters are calculated as presented in Table 3.10—namely, 10-m wind speed (WS10), 2-m relative humidity (RH2), and three heat stress indices: apparent temperature (AT), Canadian Humid Index (CHI), and Discomfort Index (DI). The parameters that are analysed for the two heat wave periods are T2, WS10, RH2, DPT, AP, CHI, DI, and the National Weather Service Heat Index (NWS-HI). The NWS-HI is a measurement to show how hot it feels when RH2 is factored in with the actual T2. The NWS-HI is extracted from the Heat Index Chart (Appendix C).

Table 3.10. WRF output variables and calculation to obtain other parameters

WRF output variables	Calculations	
2-m air temperature (K) [T2] T2(K) – 273.15 = T2(ºC)	$CHI = T2 + \left(0.55 \times (VP - 10)\right)$	Canadian Humid Index VP = vapor pressure (millibar)
	$DI = T2 - \left(0.55 \times (1 - 0.01RH)\right) \times (T2 - 14.5)$	Discomfort Index
10-m wind speed (m/s) [U10, V10]	$\sqrt{(U10)^2 + (V10)^2} = WS(m/s)$	U10 = horizontal wind speed V10 = vertical wind speed
Actual mixing ratio [Q2] to estimate the 2-m relative humidity (%)	$SVP = 6.11 \times 10^{\left(\frac{7.5 \times T2}{237.3 + T2}\right)}$ $SMR = 621.97 \dfrac{SVP}{(P_{station} - SVP)}$ $RH = \dfrac{Q2}{SMR} \times 100$	SVP = saturated vapor pressure SMR = saturated mixing ratio $P_{station}$= station pressure (millibar)
Dew point temperature (K) (TH2) TH2(K) – 273.15 = TH2(ºC)	$AT = 23.2 + 0.55T2 + 0.003DPT^2 - 0.2DPT$	Apparent temperature DPT=dew point temperature (ºC)

3.3.5. Considering Air Mass Classification

Three indicators are applied to translate the effects of extreme heat events and the potential of increasing surface reflectivity on heat-related mortality rates: air mass type, air temperature, and apparent temperature changes for each day during heat wave periods. The air temperature and apparent temperature are calculated based on simulation results. As this research focuses on heat, the summer period of June, July and August (JJA) in the Greater Montreal Area (GMA) is being analysed. In another study, Vanos et al. (2014) classified weather types into Spatial Synoptic Classification (SSC) (Sheridan, 2002) for 12 cities in Canada. The air mass classifications are presented in Table 3.11. The meteorological data applied to classify weather types into SSC was collected from airport weather stations maintained by the Meteorological Service of Canada. They estimated the heat-related mortality based on daily non-accidental mortality data that were collected across the city's metropolitan area from the Canadian Vital Statistics databases at Statistics Canada over 20 years (1981–2000). Table 3.12 represents the GMA specific air mass classification, the summertime frequencies (JJA, %), and heat-related mortality (Vanos et al., 2014; Martel B et al., 2010). The number of deaths related to each air mass classification is estimated based on the rate above the mean anomalous daily mortality in Montreal per 100,000 people. The Statistics Canada Census estimated the population of Montreal as 3,824,221 people in 2011. The Dry Moderate (DM) weather type, that includes mild and dry air in the summer season, is the most common type in the Greater Montreal Area. The highest rate of mortality in the GMA during summer periods corresponds to the hotter and more humid air mass type (MT+), while the dry tropical condition (DT) places second (Vanos et al., 2014). Figure 3.14 shows the number of deaths

corresponding to each synoptic weather type during summertime (JJA). The Canadian Environment Health Atlas (CEHA) estimates that in Montreal 121 people die each year because of high temperature. This number is subject to a number of limitations: 1) it is not categorized on a daily basis; 2) it does not reflect people's age, sex, or economic, social or education status, or whether they had any health issues before; 3) it does not show whether summer death is only because of heat or is a combination of intense heat and air quality degradation.

Table 3.11. Air mass types in the Spatial Synoptic Classifications (Sheridan, 2002)

Air Mass	Definition
Dry Polar (DP)	From polar regions. Associated with the lowest temperatures and clear, dry conditions
Dry Moderate (DM)	Includes mild and dry air
Moist Polar (MP)	Typically, cool, humid, and cloudy conditions
Moist Moderate (MM)	Warmer and more humid than MP
Transition (TR)	Days in which one weather type yields to another
Moist Tropical (MT)	Represent hottest and most humid weather type. Skies are partly cloudy in the summer because of instability and convection
Moist Tropical+ (MT+)	Extreme subset of MT, in which morning and afternoon apparent temperature are above the MT
Dry Tropical (DT)	Represents the hottest and driest conditions at any location with sunny, clear skies

Table 3.12. Summertime mortality rate for GMA within five weather types (1981–2000): weather type frequency for JJA and relative mortality (the averaged anomalous number of heat-related death above baseline value for mean daily mortality). The standard deviation is presented. [Mortality rate per 100,000 people, calculated based on Statistics Canada 2011 Census as 3,824,221 people in GMA] (Source: Vanos et al., 2014)

Synoptic weather category	Frequency (%)	Deaths	SD	~ Number of deaths based on 2011 Census
DM	32.2	1.96	$\pm$0.36	75
DT	1.30	2.27	$\pm$0.53	87
MM	24.0	1.95	$\pm$0.36	75
MT	22.0	2.13	$\pm$0.42	81
MT+	4.40	2.38	$\pm$0.59	91
TR	16.1	0	0	0

Dry Moderate (DM): mild and dry air; Dry Tropical (DT): the hottest and driest conditions; Moist Moderate (MM): warmer and more humid conditions; Moist Tropical (MT): warm and very humid; Moist Tropical Plus (MT+): hotter and more humid subset of MT; Transition (TR): days in which one weather type yields to another (Source: Sheridan, 2002)
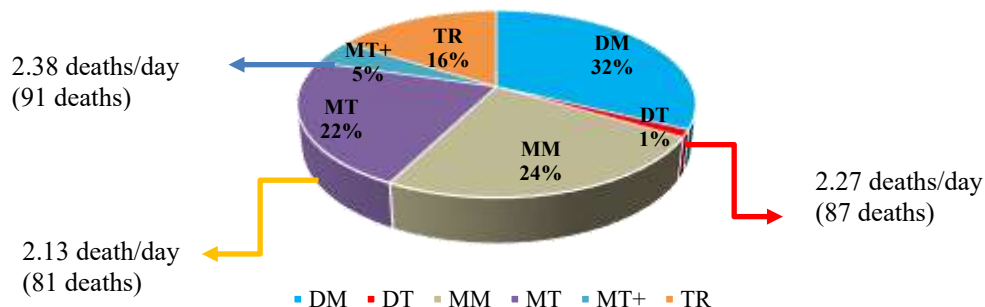
Figure 3.14. The number of deaths corresponding to each synoptic weather type during summer time (JJA). Dry Moderate (DM): mild and dry air; Dry Tropical (DT): the hottest and driest conditions; Moist Moderate (MM): warmer and more humid conditions; Moist Tropical (MT): warm and very humid; Moist Tropical Plus (MT+): hotter and more humid subset of MT; Transition (TR): days in which one weather type yields to another (Source: Sheridan, 2002)

3.3.6. Estimation of Heat- Related Mortality

Air mass type, air temperature and apparent temperature changes for each day are applied to translate the effects of extreme heat events and the potential of increasing surface reflectivity on heat-related mortality during heat wave periods. The steps to estimate heat-related mortality are presented in Figure 3.15. To estimate the heat-related mortality for the domain of interest during the 2005 and 2011 heat wave periods, first the previous correlations (as presented in Table 3.13) are analysed. Three of these correlations, in the cities with the same air mass classifications as the Greater Montreal Area (New York and the District of Columbia) are selected.

Table 3.13. Mortality calculation for summer time in various locations per 100,000 population (DT=dry tropical, MT= moist tropical, MT+= moist tropical plus, DIS = day in sequence during for an offensive weather type (day 1= 1 and day 3= 3), TOS= time of season (1 = 1st of June and 32 = 1st of July, and so on until the end of August), AT=apparent temperature)

No.	City	Air mass classifications	Heat-related mortality correlations (HRM$_d$)
1	New York		$-4.394 + 8.343$ DIS $- 0.082$ TOS $+ 0.33$ AT (1)
2	Philadelphia	For all air mass	$-1.625 + 0.835$ DIS $- 0.018$ TOS $+ 0.086$ AT (2)
3	St. Louis	classifications	$0.023 - 0.012$ TOS $+ 0.13$ AT (3)
4	Detroit	(Kalkstein et al., 2007)	$-0.653 + 3.183$ DIS (4)
5	Washington, D.C.		$1.538 + 0.281$ DIS $- 0.006$ TOS $+ 0.065$ AT (5)
6	District of Columbia	DT air mass	$-13.197 + 1.07$ DIS $- 0.066$ TOS $+ 0.612$ AT (6)
7	(Kalkstein et al., 2013)	MT & MT+ air masses	$8.168 - 0.016$ TOS $+ 0.301$ AT (7)
8	Chicago	DT & MT air masses	$-26.74 + 4.62$ DIS $+ 0.777$ AT (8)
9	(Hayhoe et al., 2009)	For other air mass types	$-7.8 + 0.266$ AT (9)

Two categories are considered regarding the air mass classifications for heat-related mortality estimation: dry tropical (DT) and moist tropical / moist tropical plus (MT/MT+). Since the heat-related deaths corresponding to the frequency of DT are significant, the positive weighting factor for the day in sequences (DIS) is only defined for this air mass category. The DIS factor means that for each consecutive day within the DT area, the estimated mortality increases by 1.07. Another weighting factor in this calculation is apparent temperature, 0.339, derived from the effects of temperature (T2) and dew point temperature (DPR). The other factor is time of season (TOS), derived from Kalkstein et al.'s (2013) HRM correlations for DT and MT/MT+ in the District of Columbia. Accordingly, the daily heat-related mortality calculation for Dry Tropical (DT) that represents the hottest and driest condition is Equation 4:

$$HRM_D = -4.32 + 1.07DIS - 0.066TOS + 0.339 \, AT \qquad \text{(Eq. 4)}$$

and for Moist Tropical (MT) and Moist Tropical Plus (MT+) that represent very warm and humid condition is Equation 5:

$$HRM_D = 2.70 - 0.016TOS + 0.339AT \qquad \text{(Eq. 5)}$$

Table 3.14. The parameters to estimate HRM in GMA during the 2005 and 2011 heat wave period (DT=dry tropical, MT= moist tropical, MT+= moist tropical plus, DIS= day in sequence, TOS= time of season, AT=apparent temperature)

Air mass	Data	AT	TOS	DIS
MT/MT+	11-Jul-2005	35.3	42	0
	21-Jul-2011	35.4	52	0
	22-Jul-2011	34.8	53	0
DT	10-Jul-2005	32.2	41	1
	12-Jul-2005	34.8	43	3
	23-Jul-2011	35.2	54	3

Figure 3.16 and 3.17 respectively present the algorithms to find the constant value for daily HRM for the MT/MT+ and DT air mass classifications. The heat-related mortality correlations (Table 3.9) are programmed and applied one by one to find the proper constant value. This constant value represents the weather condition in the domain of interest. For HRM calculations, the data in Table 3.14 is used. Table 3.14 shows the apparent temperature, time of season, and day in sequences during this period.

To calculate the constant value, two algorithms are applied for two air mass classifications: DT and MT/MT+. The algorithm starts from the first equation in the HRM calculations. flowchart and the input data as AT, TOS and DIS are applied. the daily heat-related mortality is estimated. If the rate of daily HRM is between 1 and 4, then the number of HRM will be used to find the constant value of this calculation for the GMA. If not, the estimation of this calculation will be terminated, and the next calculation will be initiated.

The rate of daily HRM (1 to 4) is used because of the heat-related deaths estimated by the Canadian Environment Health Atlas (CEHA). They estimated that 121 people die in Montreal because of high temperature annually. This calculation assumes that during the weekend, people may travel to cooler areas. Thus, people will have less exposure to high temperature. In August and June, the weather is more pleasant because of windy conditions with less humidity. Hence, the only month that perfectly reflects the effects of heat island as well as heat wave is July in the GMA. By these assumptions, every day in July, at least 1 person and at most 4 people will die because of high temperature. The constant value as ai will be estimated from the daily HRM calculation in Montreal. Finally, the ai will be averaged and then divided by 4.51, which is the sum of MT and MT+, or deaths per day during these two air mass classifications (see Table 3.9). This algorithm will be performed for each day (11th of July 2005, 21st and 22nd of July 2011). The same approach

is performed to estimate the HRM for DT air mass condition. The differences are in the input data, in the HRM correlation, and in that the average number is divided by 2.27 (see Table 3.9).

```
┌─────────────────────────────────────────────────────────────────┐
│   Collecting measured data from weather stations (T2, WS10, RH,    │
│         DPT, AP) regarding the 2005 & 2011 heatwave events         │
│                    in the domain of interest                       │
└─────────────────────────────────────────────────────────────────┘
                                │
                                ▼
┌─────────────────────────────────────────────────────────────────┐
│   Collecting the verified heat-related mortality data from         │
│                       previous studies                             │
└─────────────────────────────────────────────────────────────────┘
                                │
                                ▼
┌─────────────────────────────────────────────────────────────────┐
│   Identifying air mass classification for the summer period        │
│                  (JJA) from previous studies                       │
└─────────────────────────────────────────────────────────────────┘
                                │
                                ▼
┌─────────────────────────────────────────────────────────────────┐
│   Simulating the meteorological model for the 2005 & 2011          │
│                       heatwave events                              │
└─────────────────────────────────────────────────────────────────┘
                                │
                                ▼
┌─────────────────────────────────────────────────────────────────┐
│   Categorizing each day during heatwave period into an air mass    │
│   classification based on simulation results (T2, WS10, RH, DPT,   │
│   AP). The focus is on two air mass classifications: DT & MT/MT+   │
└─────────────────────────────────────────────────────────────────┘
                                │
                                ▼
┌─────────────────────────────────────────────────────────────────┐
│   Estimating the heat-related correlations from previous studies   │
│                          (Table 3.9)                               │
└─────────────────────────────────────────────────────────────────┘
                                │
                                ▼
┌─────────────────────────────────────────────────────────────────┐
│   The heat-related calculation is:                                 │
│       HRM_d = C_1 + C_2 DIS + C_3 TOS + C_4 AT                     │
│   HRM_D = heat-induced mortality on daily basis                    │
│   DIS = day in sequence during for an offensive weather type       │
│   TOS = time of season                                             │
│   AT = apparent temperature                                        │
│   The constant C_1 to C_4 are city specific and air mass type      │
└─────────────────────────────────────────────────────────────────┘
```

The heat-related calculation is:

$$HRM_d = C_1 + C_2 DIS + C_3 TOS + C_4 AT$$

HRM_D = heat-induced mortality on daily basis
DIS = day in sequence during for an offensive weather type (day 1= 1 and day 3= 3)
TOS = time of season (1 = 1st of June and 32 = 1st of July, and so on until the end of August)
AT = apparent temperature at a specific time of the day in that location
The constant C_1 to C_4 are city specific and air mass type specific

Defining an algorithm to derive the constant values from other correlations in previous studies

Employing simulation results (AT), time of season and day in sequence to find constant parameters for two air mass classifications (DT & MT/MT+)

Estimating the HRM in GMA during the 2005 and 2011 heat waves

Figure 3.15. Steps to calculate heat-related mortality

45

Start

Select TOS, DIS, AT from Table 3.14

n=0, i =0

HRM equations from Table 3.13

n= n+1

Select Equation n

Calculate HRM$_i$

If 1< HRM$_i$ <4   NO

YES

i= i+1

Print HRM$_i$

$a_i = \mathrm{HRM}_i + 0.016\mathrm{TOS} - 0.339\,\mathrm{AT}$

Save a_i

If n<N   NO

YES

Print a_i, i= 1, I

$Avg\ a = -\left(\frac{\sum a_i}{I}\right)/4.51$

Print a

Stop
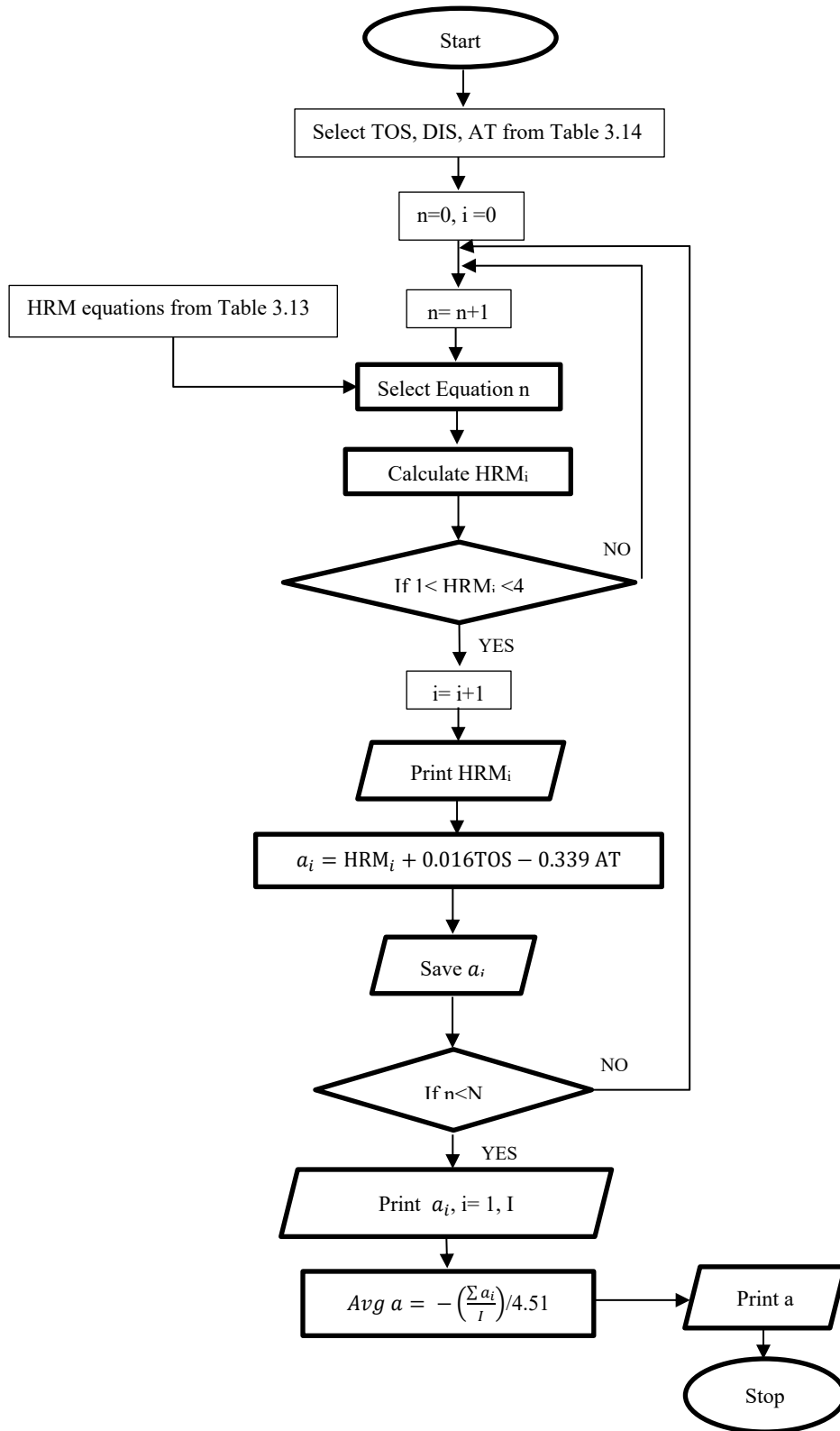
Figure 3.16. HRM-algorithm to find the constant value (a) for HRM corresponding to the MT/MT+ air mass classification for each day of simulations (the number 4.51 is the sum of MT/MT+ frequency in JJA in GMA)
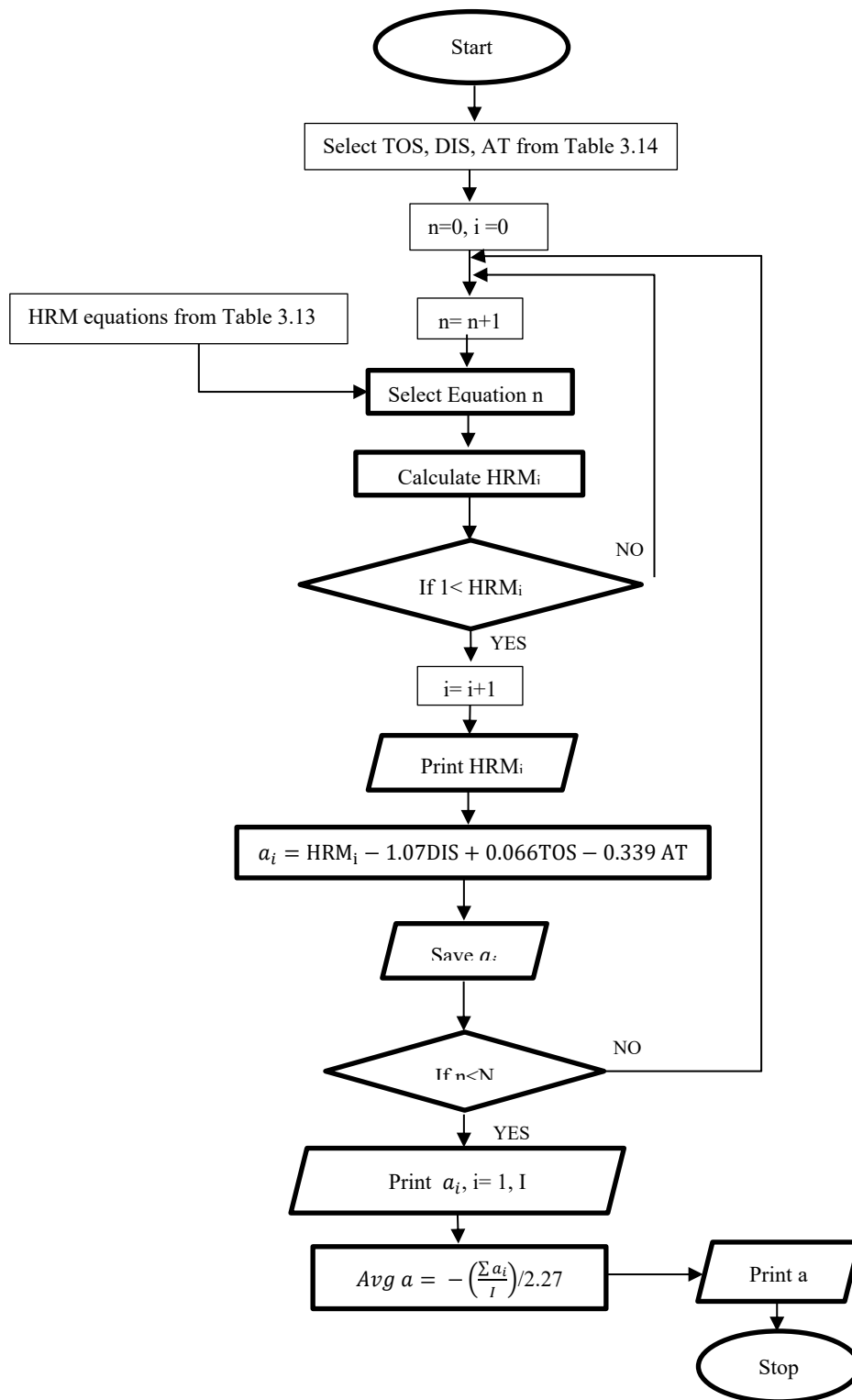
Figure 3.17. HRM-algorithm to find the constant value (a) for HRM corresponding to the DT air mass classification (the number 2.27 is the DT frequency in JJA in GMA

There are a number of HRM correlations that have been developed to estimate the effects of high temperature on the rate of deaths in several cities across the globe, except in cold climate cities such as the Greater Montreal Area. In addition, the effects of increasing surface reflectivity on reducing heat mortality rate has not been investigated in the GMA. Thus, the meteorological simulations are performed to investigate the effects of heat island and its mitigation strategy on meteorological parameters and heat stress indices during two heat wave periods. The achievements of this study are not limited to only comparing the effects of increasing surface reflectivity on the aforementioned parameters, but they are also extended further and lead to defining algorithms to develop HRM correlations for two main air mass classifications in the GMA. The developed HRM algorithms can assist other researchers and policymakers to estimate the effects of any other mitigation strategies for heat-related deaths in the GMA. The study illuminates the essential steps to take before modifying these correlations or defining new ones. The air quality degradation can also be a cause of heat-related death because of increasing the temperature-dependent photochemical reaction rates and increasing emissions from pollutant sources in the urban area. Thus, further analysis of the effects of high temperature on air quality needs to be carried out by photochemical models such as WRF-Chem.

3.4. Simulations of Urban Climate and Air Quality within a Two-way Nested Approach

Previous studies focused on a one-way simulation approach to investigate the effects of UHI and its mitigation strategy on urban climate and air quality. But a two-way nested approach provides an integrated simulation setup and captures the full impacts of meteorological processes and photochemical reactions. This method can be applied over a larger geographical area through regional and local scales such as urban areas. Thus, it reduces the uncertainties associated with scale separation and grid resolution to investigate the effects of UHI and surface modifications on urban climate and air quality. The WRF-Chem is used to consider a variety of coupled physical and chemical processes such as transport, deposition, emission, chemical transformation, aerosol interactions, photolysis and radiation. The morphological, thermal, and micro-scale properties of the urban canopy are considered by coupling of a multi-layer of the Urban Canopy Model (ML-UCM) within WRF-Chem. The aspect of the model that relates to the chemical parameterization is briefly explained in the following figure. The simulation approach for the third objective is

presented in Figure 3.18. Box A refers to explanations in Section 3.1.2 and box B shows the accomplishments and endpoints of this objective.
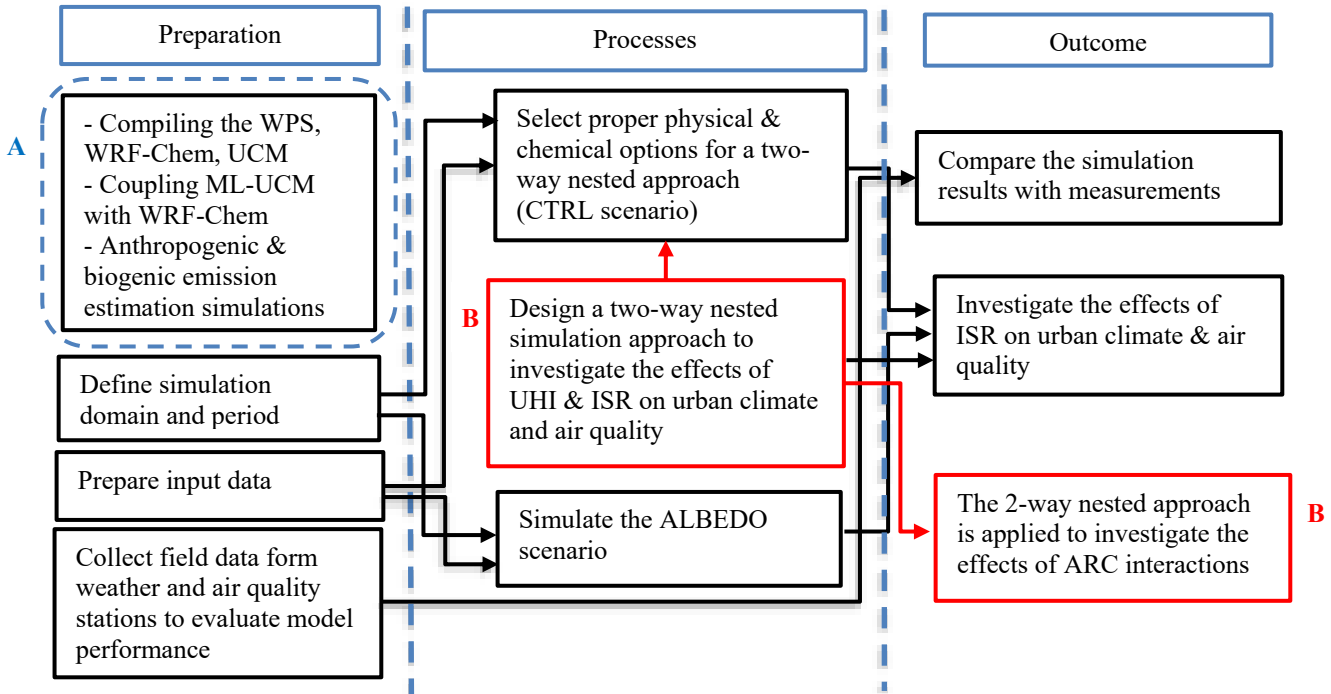
Figure 3.18. Simulation approach to investigate the effects of UHI and ISR on urban climate and air quality with a two-way nested method (ISR=increasing surface reflectivity, CTRL= base case simulation, ALBEDO= increasing urban albedo, ARC=aerosol-radiation-cloud)

3.4.1. Defining Simulation Domain and Period

The first domain covers North America (NA) including Canada, the United States of America, and the Northern part of Mexico with 445 grids in west–east direction and 338 grids in south–north direction. The horizontal resolution is 12km. The second, third, and fourth domains cover the Sacramento area (36 × 31 grids), Houston area (41 × 31 grids), and Chicago area (36 × 31 grids) with the horizontal resolution of 2.4km. The vertical resolution includes 35 vertical layers from the surface to a fixed pressure of ~100 mb (~16 km AGL). Figure 3.19 shows the simulation domains and land use/land cover. The simulation period extended seven consecutive hottest days in 2011, from the 17th to 23rd of July. The first 72h of the simulation is disregarded as a spin-up period. The reason for the 72hrs spin-up is because of the chemistry package and photochemical reactions that

are coupled with the meteorological processes. Hence, the spin up time for WRF-Chem simulations usually took longer than WRF simulations.
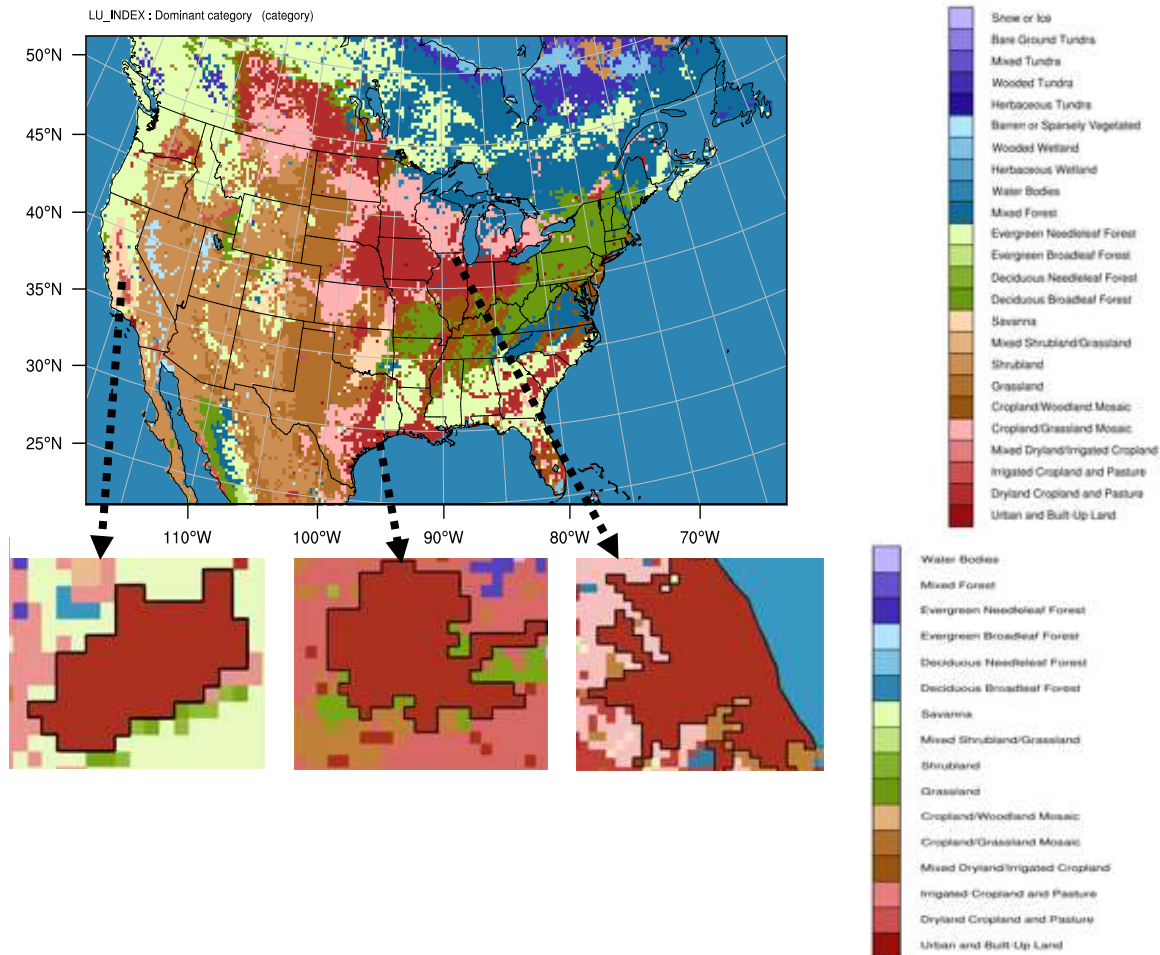
Figure 3.19. Simulation domains and land use/land cover over North America (mother domain, horizontal resolution: 12km) Sacramento, Houston, and Chicago (inner domains, horizontal resolution: 2.4km).

3.4.2. Preparation of Input Data for Physical and Chemical Parameterizations

The simulation is conducted with the initial and boundary conditions obtained from the North American Regional Reanalysis (NARR) (Mesinger et al, 2006). Land use was derived from the USGS 24-category data set. The Lin scheme is used as microphysics model to evaluate six classes of hydrometeors (Lin, Farley, and Orville 1983). Goddard scheme (Janjic Z.I., 1994) and Rapid Radiative Transfer Model (RRTMG; Iacono et al., 2008) are respectively selected for shortwave and longwave radiations. The planetary boundary layer (PBL) is simulated by the Mellor-Yamada-

Janjic scheme using Eta similarity theory (Janjic 2002). The unified NOAH land surface model is applied. For cumulus parameterization, the Grell-Devenyi ensemble scheme (Grell and Devenyi 2002) is used. The positive-define advections of moisture, scalars and turbulent kinetic energy are activated for model stability.

For anthropogenic and biogenic emission estimations, the models of the United States National Emission Inventory for 2011 (US-NEI11) and Model of Emissions of Gases and Aerosols from Nature (MEGAN) are respectively simulated for the inner domains. The results are applied in the solver of WRF-Chem (see section 3.1.2). The Modal Aerosol Dynamics Model for Europe (MADE) (Ackermann et al., 1998) is coupled with the chemistry package to estimate the effects of aerosols on radiation processes and hydrological cycles in the atmosphere. The Regional Atmospheric Chemistry Mechanism (RACM) (Stockwell et al., 1997) is used to estimate the gas-phase reactions. The secondary organic aerosols (SOA) have also been incorporated into MADE by means of the Secondary ORGanic Aerosol Model (SORGAM). Photolysis frequencies are calculated by the Fast_J model scheme (Fast et al, 2006; Grell et al. 2005 and 2014). Wet scavenging, cloud chemistry, sub-grid aqueous chemistry, and aerosols radiation feedback need to be activated in the solver of WRF-Chem for model stability. Table 3.15 presents the physical and chemical parameterizations applied in WRF-Chem.

Table 3.15. Physical and chemical parameterizations applied in WRF_Chem

Category	Option Used
Microphysics	Lin scheme
Shortwave radiation	Goddard
Longwave radiation	RRTMG
Land surface model	NOAH
Planetary boundary layer scheme	Mellor–Yamada–Janjic Scheme
Cumulus parameterization	Grell Devenyi
Chemistry option	RACM
Photolysis scheme	Fast_J
Aerosol option	MADE/SORGAM
Advection scheme	Runge–Kutta third order
LULC data	USGS 24-class
Anthropogenic emissions	US-NEI11
Biogenic emissions	MEGAN
Urban canopy model	ML-UCM

3.4.3. Simulation Scenarios for Urban Climate and Air Quality Assessment

Three cities are selected for detail analyses: Sacramento (California), Houston (Texas), and Chicago (Illinois) based on Akbari et al., (2001, 2003 and 2008) and Rose et al., (2003) findings on the urban fabric of these cities. Using high-resolution orthophotography, they found that roofs

cover 20–25% and pavements cover 30–40% of urban surfaces. Table 3.16 presents the urban fabric of Sacramento, Chicago, and Houston (Rose et al., 2003).

Table 3.16. Urban fabric of three cities in NA (Source: Rose et al., 2003)

Metropolitan Areas	Roofs (%)	Pavements (%)
Sacramento	20	45
Chicago	25	37
Houston	22	30

Two sets of simulations are conducted: CTRL case (UHI effects) and ALBEDO case (increasing surface reflectivity (ISR) effects) during the 2011 heat wave period over the simulation domains. The fraction of urban fabric of these three cities and the changes because of increasing surface reflectivity are applied to calculate the albedo changes over the domains. The changes of surface albedo modification from the CTRL case as 0.2 to full adoption of roofs and pavements can be calculated as: (fraction of roofs in Sacramento) 0.20 × 0.65 (the increase of albedo for roofs) + 0.45 (fraction of pavements in Sacramento) × 0.45 (the increase of albedo for pavements) = 0.33 (as an example for Sacramento; the surface albedo (of roofs and pavements) increased from 0.13 to 0.33 (as a full adaptation of albedo enhancement)). The change to gridded ALBEDO can be calculated as: (Surface albedo enhancement (roofs, walls, and pavements) × Fraction of urban areas per grid cell).

The effects of increasing surface reflectivity are investigated on meteorological (hourly 2-m air temperature (T2, ℃), 10-m wind speed (WS10, m/s), 2-m relative humidity (RH2, %), and dew point temperature (DPT, ℃)) and photochemical parameters (daily particular matters (PM$_{2.5}$, $\mu g/m^3$), ozone (O$_3$, ppb), nitrogen dioxide (NO$_2$, ppb), PM$_{2.5}$ subspecies (particulate sulfate (SO4$_{2.5}$, $\mu g/m^3$), particulate nitrate (NO3$_{2.5}$, $\mu g/m^3$), and organic carbon (OC$_{2.5}$, $\mu g/m^3$)) by comparing the ALBEDO results with the CTRL results.

3.4.4. Collection of Local Meteorological and Air Quality Data to Evaluate Model Performance

The evaluation of the model performance is conducted by comparing the simulation results with measurements obtained from weather and air-quality stations in Sacramento, Houston, and Chicago. The weather and air quality monitoring stations were chosen based on their locations close to the downtown of the selected cities (hereafter referred to as urban) and their surroundings (hereafter referred to as suburb). The hourly 2-m air temperature (T2,℃), 10-m wind speed (WS10, m/s), 2-m relative humidity (RH2, %), and dew point temperature (DPT, ℃) simulation results (as

estimated in Table 3.2) are compared with the measurements obtained from the U.S. Environmental Protection Agency (EPA) Clean Air Status and Trend Network (CASTNET). The daily averaged modelled fine particular matters (PM$_{2.5}$, µg/m^3), ozone (O$_3$, ppb), nitrogen dioxide (NO$_2$, ppb), PM$_{2.5}$ subspecies (particulate sulfate (SO4$_{2.5}$, µg/m^3), particulate nitrate (NO3$_{2.5}$, µg/m^3), and organic carbon (OC$_{2.5}$, µg/m^3)) concentrations are compared with the EPA Air Quality System (AQS) observations using 24-h average data. The time series of simulation results changed to the local time for each specific location: Sacramento: LST= UTC – 7h; Houston and Chicago: LST=UTC – 5h.

3.4.5. Analyses of Meteorological and Photochemical Parameters

The chemical components of WRF-Chem simulation results that are applied to investigate the effects of ISR on urban climate and air quality are: fine particular matters (PM$_{2.5}$, µg/m^3), ozone (O$_3$, ppb), nitrogen dioxide (NO$_2$, ppb), PM$_{2.5}$ subspecies (particulate sulfate (SO4$_{2.5}$, µg/m^3), particulate nitrate (NO3$_{2.5}$, µg/m^3), and organic carbon (OC$_{2.5}$, µg/m^3)). The meteorological components are: 2-m air temperature (T2,^{o}C), 10-m wind speed (WS10, m/s), 2-m relative humidity (RH2, %), and dew point temperature (DPT, ^{o}C). Table 3.17 presents the calculations of wind speed and relative humidity. Other parameters are the output of WRF-Chem.

Table 3.17. WRF-Chem output variables and calculation to obtain other parameters

Parameters to be calculated	Calculations	
10-m wind speed (m/s) (U10, V10)	$\sqrt{(U10)^2 + (V10)^2}$ = WS(m/s)	U10 = horizontal wind speed V10 = vertical wind speed
Mixing ratio (Q2) to estimate the 2-m relative humidity (%)	$SVP = 6.11 \times 10^{\left(\frac{7.5 \times T2}{237.3 + T2}\right)}$ $SMR = 621.97 \dfrac{SVP}{(P_{station} - SVP)}$ $RH = \dfrac{Q2}{SMR} \times 100$	SVP = saturated vapor pressure SMR = saturated mixing ratio P$_{station}$= station pressure (millibar) T2 = 2-m air temperature (^{o}C)

3.5. Effects of Increasing Surface Albedo on Aerosol-Radiation-Cloud Interactions in Urban Atmosphere

To understand the effects of increasing surface reflectivity (ISR) on urban climate, air quality and aerosol-radiation-cloud interactions in the atmosphere, the chemistry package and aerosol scheme are compiled and coupled with the WRF and UCM. Figure 3.21 shows the simulation approaches for the fourth objective. The effects of ISR are separately investigated as aerosol-radiation (AR), aerosol-cloud (AC) and aerosol-radiation-cloud (ARC) interactions. A brief

description is presented for each step. Box A refers to explanations in Section 3.1.2, and box B shows the accomplishments of this objective.
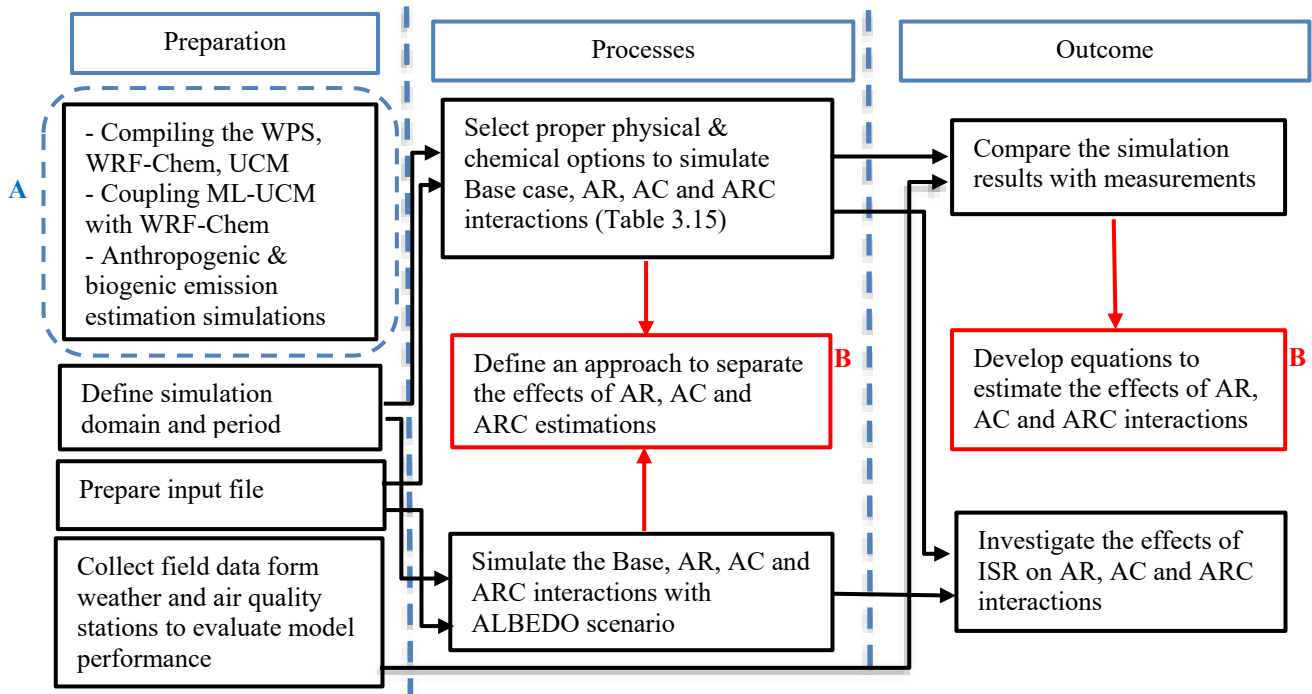
Figure 3.20. Simulation approaches for the 4th objective (AR=aerosol-radiation, AC=aerosol-cloud, ARC=aerosol-radiation-cloud interactions, ISR=increasing surface reflectivity)

3.5.1. Defining Simulation Domain and Period

The horizontal domain of the simulation is composed of three two-way nested domains covering North America (445 × 338 grids), part of Ontario and Quebec provinces (139 × 124 grids), and the Greater Montreal Area (GMA) (101 × 71 grids) with the horizontal resolution of 12km, 4km and 800m, respectively. The vertical resolution includes 35 vertical layers. Figure 3.22 shows the simulation domains and land use/land cover. The simulation period extended over seven consecutive hottest days during the 2011 heat wave period, from the 17th to 23rd of July. The first 48h of the simulation is disregarded as the spin-up period. The reason for the 48h spin-up time is that after this period, the results are stable enough to be extracted and analysed. Here, the simulations are conducted on three paralleled nodes on cluster.
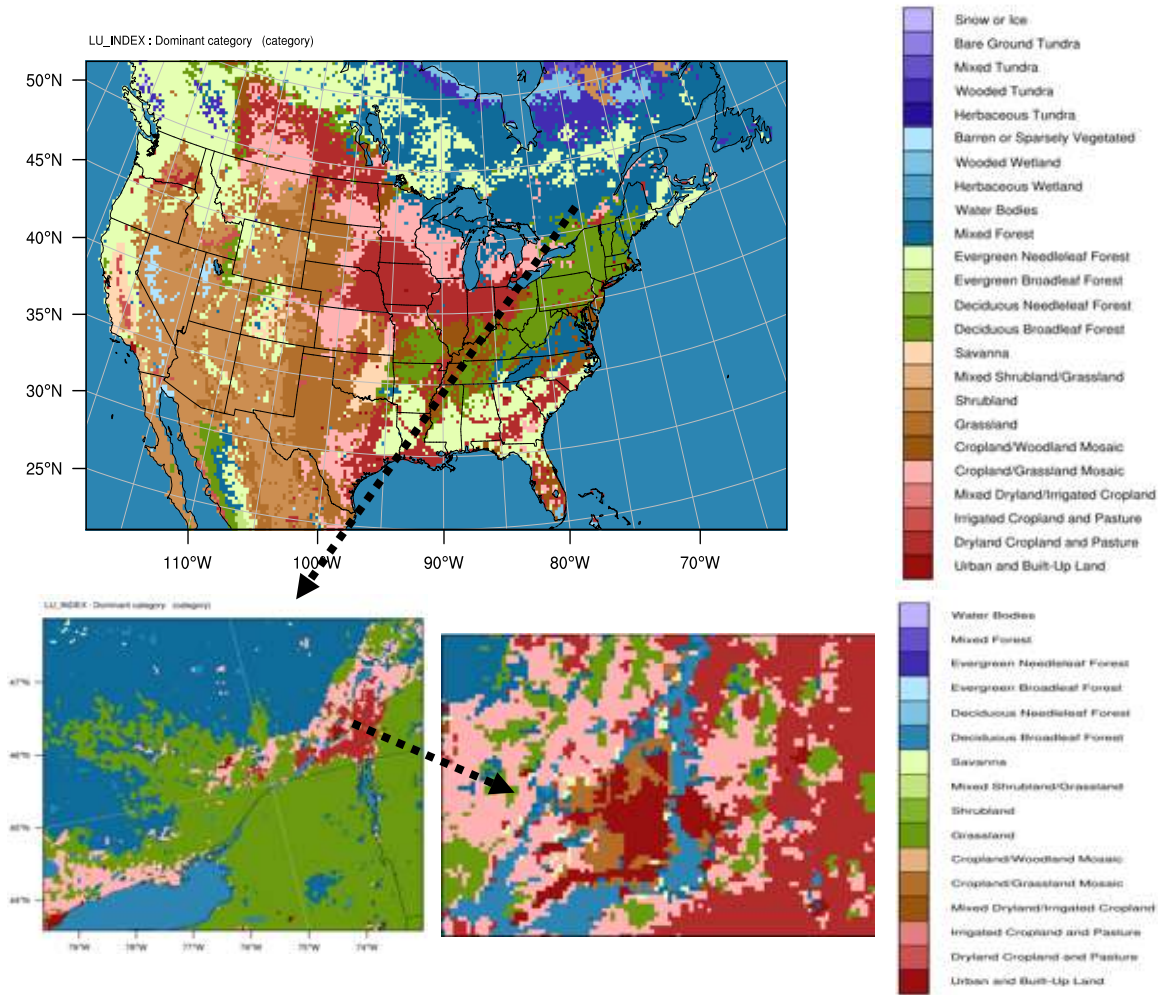
Figure 3.21. The land use/ land cover of the 1st domain over North America (grid size: 12km × 12km), the 2nd domain over Ontario and Quebec provinces (grid size: 4km × 4km) and 3rd domain over Greater Montreal Area (grid size: 800m × 800m)

3.5.2. Preparation of Input Data for Physical and Chemical Parameterizations

The simulation is conducted with the initial and boundary conditions obtained from the North American Regional Reanalysis (NARR). Land use was derived from the USGS 24-category data set. The physical and chemical parameterizations are modified to be coupled with the Model for Simulating Aerosol Interactions with Chemistry (MOSAIC) aerosol scheme (Zaveri et al., 2008) and the Carbon Bond Mechanism (CBM-Z) gas phase chemistry scheme (Zaveri and Peters. 1999). The Morrison double-moment scheme (Morrison et al., 2009) and the Mellor-Yamada-Janjic scheme (Janjic 2002) are selected as microphysics and planetary boundary layer options, respectively. The unified NOAH land surface model is applied as the land surface scheme. The Grell-Devenyi ensemble scheme (Grell and Devenyi 2002) is used for cumulus parameterization. For both shortwave and longwave radiations, the rapid radiative transfer model (RRTMG) is selected (Iacono et al., 2008). The anthropogenic emissions are estimated by the United State

National Emission Inventory (US-NEI11). The Model of Emissions of Gases and Aerosols from Nature (MEGAN, Guenther et al., 2006) is used to calculate the biogenic emissions. The anthropogenic and biogenic emissions are estimated only for the inner domain of the simulation. Then the emission estimations from anthropogenic and biogenic sources are transferred to the solver of WRF-Chem (see Section 3.1.2). The Fast-J is used for the photolysis scheme in WRF-Chem (Fast et al., 2006). For dynamic options, the positive definite advections of chemistry, moisture, scalars and turbulent kinetic energy have been activated. Table 3.18 summarizes the physical and chemical parameterizations in WRF-Chem.

Table 3.18. Selected physical and chemical parameterizations applied in WRF-Chem

Category	Option Used
Microphysics	Morrison double-moment scheme
Radiation Schemes (shortwave & longwave)	RRTMG
Land Surface	NOAH LSM
Planetary Boundary Layer	Mellor-Yamada-Janjic Scheme
Cumulus clouds	Grell3D
Gas-phase Chemistry	CBM-Z
Photolysis	Fast_J
Anthropogenic emissions	US-NEI11
Biogenic emissions	MEGAN
Aerosol scheme	MOSAIC 8-bin
Advection Scheme	Runge–Kutta 3rd order

3.5.3. Simulation Scenarios to Estimate the Effects of Increasing Surface Reflectivity on Aerosol, Radiation and Cloud Interactions

Four scenarios are defined to separate the impacts of aerosol-radiation interactions from aerosol-cloud interactions. The base scenario represents the processes of meteorological and chemical interactions without considering the aerosol interaction with radiation and cloud, wet scavenging and convective parameterizations (hereafter referred to BASE). In the second, third and fourth simulations, model treatments remain the same as the BASE scenario, but the parameters are activated regarding the aerosol-radiation (as direct effect; hereafter referred to AD-DE), aerosol-cloud (as semi-direct effect; hereafter referred to AC-SDE), and aerosol-radiation-cloud interactions (as indirect effect; hereafter referred to ARC-IDE). In addition, the effects of increasing surface reflectivity are investigated on aerosol-radiation-cloud interactions in the atmosphere. Two sets of simulations, each set consisting of the four aforementioned scenarios, are conducted: CTRL case (UHI effects) and ALBEDO case (increasing surface reflectivity (ISR)

effects). Each scenario with albedo enhancement is referred to as ISR. Table 3.19 summarizes these scenarios. The changes are in bold.

Table 3.19. Two sets of simulation: CTRL Cases and ALBEDO Cases. Four sets of scenarios for each case: control simulation with no ARC interactions (BASE), aerosol and radiation interactions as direct effect (AR-DE), aerosol and cloud interactions as semi-direct effect (AC-SDE) and the aerosol-radiation-cloud interactions as indirect effect (ARC-IDE). In ALBEDO cases, each scenario is repeated with regard to Increasing Surface Reflectivity (ISR).

simulations	Scenario	Aerosol-radiative feedback	Aerosol-cloud feedback	Convective parameterization
CTRL Cases	BASE	Off	Off	Off
	AR-DE	**On**	Off	Off
	AC-SDE	Off	**On**	**On**
	ARC-IDE	**On**	**On**	**On**
ALBEDO Cases	ISR-BASE	Off	Off	Off
	ISR-AR-DE	**On**	Off	Off
	ISR-AC-SDE	Off	**On**	**On**
	ISR-ARC-IDE	**On**	**On**	**On**

3.5.4. Collection of Measurements to Evaluate Model Performance

To evaluate the model performance, the ARC-IDE simulation results are compared with measurements obtained from weather and air quality monitoring stations across the Greater Montreal Area. The hourly 2-m air temperature (T2, ºC), 10-m wind speed (WS10, m/s), and 2-m relative humidity (RH2, %) are compared to measurements from four weather stations (McTavish (MT), Pierre Elliott Trudeau Intl (PET), St-Hubert (SH), Ste-Anne-de-Bellevue (SAB)). The hourly modelled fine (diameter less than 2.5 micrometers) particulate matter (PM$_{2.5}$, μg/m^3), ozone (O$_3$, ppb) and nitrogen dioxide (NO$_2$, ppb) are compared with measurements from four air quality monitoring stations (St-Jean-Baptiste (3), Decarie Interchange (28), Montreal Airport (66), and Ste-Anne-de-Bellevue (99)). Figure 3.23 and Table 3.20 present their geographical locations. The time series of simulation results are changed to the local time (LST = UTC – 4h).
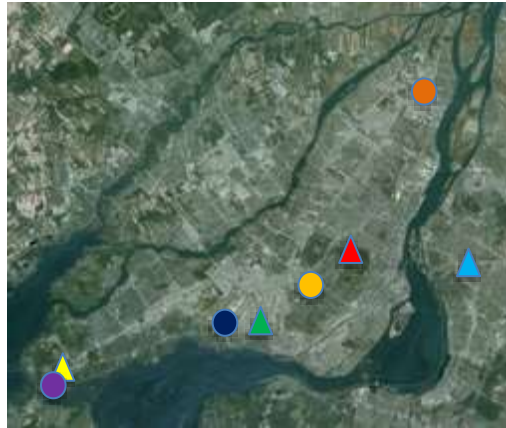
Figure 3.22. The location of weather (shown by triangles) and air quality (shown by circles) monitoring stations in GMA

Table 3.20. Weather and air quality stations in GMA with their locations (Latitude and Longitude)

Stations Type	Station Name	Station Code	Latitude (N)	Longitude (W)
Meteorological stations	McTavish ▲	MT	45.5	-73.57
	Pierre Elliott Trudeau ▲	PET	45.47	-73.75
	St-Hubert ▲	SH	45.52	-73.42
	Ste-Anne-de-Bellevue ▲	SAB	45.42	-73.92
Air-quality stations	St-Jean-Baptiste ●	3	45.63	-73.5
	Decarie Interchange ●	28	45.5	-73.65
	Montreal Airport ●	66	45.47	-73.74
	Ste-Anne-de-Bellevue ●	99	45.42	-73.92

3.5.5. Analyses of Meteorological and Photochemical Parameters

The chemical components of WRF-Chem simulation results that are applied to investigate the effects of ISR on urban climate and air quality are fine particular matter (PM$_{2.5}$, μg/m^3), ozone (O$_3$, ppb), and nitrogen dioxide (NO$_2$, ppb); and the meteorological components are 2-m air temperature (T2,ºC), 10-m wind speed (WS, m/s), 2-m relative humidity (RH, %), down-welling shortwave radiation (SW, W m^{-2}), planetary boundary layer height (PBLH, m), and water mixing ratio (WMR, g/kg), which is a gram of water per kilogram of dry air (g/kg) in the atmosphere.

3.5.6. Estimation of Aerosol-Radiation, Aerosol-Cloud and Aerosol-Radiation-Cloud Interactions

The WRF-Chem has the capability to calculate the radiative fluxes over the domain of interest. The radiative flux occurs because of the shortwave radiation reaching the ground and the outgoing longwave radiation and is a combination of scattering, absorption and emission of shortwave and longwave radiations. These estimations split into the incoming shortwave radiation (SW) and

outgoing longwave radiation (LW) balance. A set of calculations are defined to estimate the radiative budget (RB) over the simulation domain as the difference between the radiation going into the system and the out-going radiation (Eq. 5):

$$RB = SW^{\downarrow} + LW^{\downarrow} - SW^{\uparrow} - LW^{\uparrow} \qquad \text{(Eq. 5)}$$

For the two scenarios (CTRL and ALBEDO), the radiative balance (ΔRB) is defined based on the differences between their simulation results. As the incoming radiation is the same for all scenarios, the ΔRB is estimated to be equal to the differences in outgoing radiation (Eq. 6):

$$\Delta RB = RB_{CTRL} - RB_{ALBEDO} = (SW^{\uparrow} + LW^{\uparrow})|_{CTRL} - (SW^{\uparrow} + LW^{\uparrow})|_{ALBEDO} \qquad \text{(Eq. 6)}$$

The direct, semi-direct and indirect effects of aerosol on the radiation budget is also calculated. The aerosol characteristics are assumed to be the same and the sky is assumed to be clear over the domain during the simulation. The direct SW radiation is calculated based on the differences in upwelling SW radiation in BASE and aerosol-radiation (AR-DE) simulation results (Eq. 7):

$$SW_{Direct} = SW^{\uparrow}_{BASE} - SW^{\uparrow}_{AR\text{-}DE} \qquad \text{(Eq. 7)}$$

The semi-direct effect, with regard to cloud formation, can be calculated based upon the differences between BASE and AC-SDE simulation results (Eq. 8):

$$SW_{Semi\text{-}direct} = SW^{\uparrow}_{BASE} - SW^{\uparrow}_{AC\text{-}SDE} \qquad \text{(Eq. 8)}$$

The indirect effects are estimated with the comparison between BASE results and the aerosol-radiation-cloud interaction (ARC-IDE) simulation results (Eq. 9):

$$SW_{Indirect} = SW^{\uparrow}_{BASE} - SW^{\uparrow}_{ARC\text{-}IDE} \qquad \text{(Eq. 9)}$$

Here, the effects of aerosols on the hydrological cycle, cloud formation and atmospheric stability is minimal, because of the choice of simulation period. It is estimated as the water mixing ratio (Q_{WMR}) (which is a gram of water per kilogram of dry air (g/kg) in the atmosphere). The Q_{WMR} is calculated as a combination of the cloud water mixing ratio ($Q_{C_{WMR}}$), rain water mixing ratio ($Q_{R_{WMR}}$) and water vapor mixing ratio ($Q_{V_{WMR}}$) in the atmosphere (g/kg) (Eq. 10).

$$Q_{WMR} = Q_{C_{WMR}} + Q_{R_{WMR}} + Q_{V_{WMR}} \hspace{4cm} \text{(Eq. 10)}$$

These ARC interactions are nonlinear and thus very complicated to be investigated. It means that the sum of changes because of aerosol-radiation interactions and aerosol-cloud interactions is not necessarily equal to the overall changes in ARC interactions. In a nonlinear system, the total effect of one parameter can be decomposed into the contribution from pure impact and synergistic impact (resulting from the synergy between that parameter and others). Thus, the impact of each individual factor (f)—namely, temperature, ozone, fine particular matters, radiative budget and water mixing ratio—can be derived as the following:

Direct effects: AR-DE = f $_{AR}$ − f $_{BASE}$

Semi-direct effects: AC-SDE = f $_{AC}$ − f $_{BASE}$

Indirect effect: ARC: ARC-IDE= f $_{ARC}$ − f $_{BASE}$

Synergistic impact: SYN= f $_{ARC}$ + f $_{BASE}$ − f $_{AC}$ − f $_{AR}$

The aerosols affect the radiation budget and hydrological cycles in the atmosphere. By increasing surface albedo to mitigate the urban heat island impacts, the aerosol-radiation, aerosol-cloud and aerosol-radiation-cloud interactions will be affected as well. To estimate these nonlinear effects, an approach is developed to calculate the radiation budget and water mixing ratio in the atmosphere. In addition, a set of calculations are developed to investigate the separate effects of AR, AC and ARC simulations on urban climate and air quality. These developed approaches can further be applied to find the full impacts of UHI mitigation strategies on urban climate, air quality and ARC interactions in the atmosphere.

3.6. Summary of Methodology

An appropriate platform is developed to simulate urban climate and heat island mitigation strategy. The Weather Research and Forecasting Model (WRF) is used. WRF is comprised of many physical parameterizations that are applied to predict weather conditions. The model ensemble for urban climate simulation includes parameterizations for microphysics, cumulus, planetary boundary layer (PBL), radiation, land surface, and urban canopy. Characterizing the meteorological parameters (e.g., air temperature, wind speed, relative humidity and precipitation) to a different set of parameterizations (i.e., model ensemble) enables researchers to select the proper

model platform for urban climate simulations. The physical processes can be selected based on a set of sensitivity analyses. Thus, 20 sets of simulations with different physical parameterizations are conducted. The model that has the least error compared to the measurements is proposed as the proper platform for further analysis of heat island mitigation strategy.

Heat wave intensity and duration cause an increase in mortality. The developed platform for urban climate simulations is applied to investigate the effects of increasing surface reflectivity (ISR) on heat-related mortality (HRM). An algorithm is defined to estimate the effects of ISR on HRM. Three indicators are applied to translate the effects of extreme heat events and the potential impact of ISR on HRM rates: air mass type, air temperature and apparent temperature changes for each day during heat wave periods. The air temperature and apparent temperature are calculated based on WRF simulation results. Two air mass categories are considered to estimate HRM: dry tropical (DT) and moist tropical / moist tropical plus (MT/MT+). Figure 3.16 and 3.17 show the applied algorithms to calculate the HRM in MT/MT+ and DT air mass types.

A two-way nested approach is developed. It provides an integrated simulation setup to capture the full impacts of meteorological processes and photochemical reactions. This approach reduces the uncertainties associated with scale separation and grid resolution. The WRF is coupled with the chemistry package (WRF-Chem) and a multi-layer of the Urban Canopy Model (ML-UCM) to predict the morphological, thermal, and micro-scale properties of the urban canopy. The model considers a variety of coupled physical and chemical processes such as transport, deposition, emission, chemical transformation, aerosol interactions, photolysis and radiation. This approach is further used to investigate the effects of heat island mitigation strategy on aerosol interactions in the atmosphere.

Increasing surface reflectivity affects the aerosol-radiation (AR), aerosol-cloud (AC) and aerosol-radiation-cloud (ARC) interactions. To estimate these nonlinear effects, an approach is developed to calculate the radiation budget and water mixing ratio in the atmosphere and at the surface. Four scenarios are defined to separate the impacts of aerosol-radiation interactions from aerosol-cloud interactions. The base scenario represents the processes of meteorological and chemical interactions without considering the aerosol interaction with radiation and cloud, wet scavenging and convective parameterizations. In the second, third and fourth simulations, model treatments remain the same as the base case scenario, but the parameters are activated regarding

the aerosol-radiation (as direct effect), aerosol-cloud (as semi-direct effect), and aerosol-radiation-cloud interactions (as indirect effect). These ARC interactions are nonlinear; that is, the sum of changes because of aerosol-radiation interactions and aerosol-cloud interactions is not necessarily equal to the effects of each one. In a nonlinear system, the total effect of one parameter can be decomposed into the contributions from pure impact and synergistic impact.

The results of these objectives lead to the post-processing analyses of WRF and WRF-Chem simulations. The 2-m air temperature results of these simulations are compared with measurements. The WRF results from the second objective (effects of ISR on HRM in the GMA) are compared with the WRF-Chem results from the fourth objective (effects of ISR on ARC in the GMA). These analyses indicate the separate effects of meteorological processes on predicting air temperature distinguished from the combination effects of meteorological and photochemical reactions on air temperature. Three factors are considered in these comparisons: the initial time and effort to simulate each model, computational resources, and the accuracy of these models in predicting 2-m air temperature by comparing with measurements.

The other post-processing analysis is to assess the correlation between surface albedo enhancement and temperature reduction. The results of the second objective (effects of ISR on HRM in the GMA), third objective (effects of ISR on Sacramento, Houston and Chicago in a two-way nested approach), and fourth objective (effects of ISR on ARC interactions in the GMA) are considered. The size of the inner grid for the second objective is 0.3km × 0.3km; for the third objective it is 2.4km × 2.4km; and for the fourth objective it is 0.8km × 0.8km. The average albedo enhancement in each grid in urban areas is compared with its corresponding temperature reduction.

Chapter 4
Sensitivity Analysis of Physical parameterizations in WRF for Urban Climate and Heat Island Mitigation Strategy

Mesoscale models are comprised of many parameterizations that are used to predict weather conditions. The model ensemble for urban climate simulation includes parameterizations for microphysics, cumulus, planetary boundary layer (PBL), radiation, land surface, and urban canopy. Characterizing the meteorological parameters (e.g., air temperature, wind speed, etc.) in relation to a different set of parameterizations (i.e., model ensemble) enables researchers to select the proper model platform for urban climate simulations and heat island mitigation strategies. The WRF is applied to assess the sensitivity of physical parameterizations on air temperature, wind speed, relative humidity and precipitation over the Greater Montreal Area, Canada for the period of 9–11 August 2009. A multi-layer of urban canopy model is used to consider the turbulence between buildings in urban areas (Chen et al., 2011).

The results of the base case simulations are compared with measurements for the period of 9–11 August 2009, from seven weather stations (McTavish (MT), Pierre Elliott Trudeau Intl (PET), St-Hubert (SH), Ste-Anne-de-Bellevue (SAB), Varennes (VA), Mirabel (MI), and Ste-Clothilde (SC)). A set of metrics calculations are applied to evaluate model performance (mean bias error (MBE), mean absolute error (MAE) and root mean square error (RMSE)). The model ensemble with the least error is presented as an appropriate platform for urban climate simulations to study Urban Heat Island (UHI) mitigation strategies. Increasing surface reflectivity was applied to mitigate the UHI intensity over the domain. The albedo of roofs, walls, and roads increased from 0.2 to 0.65, 0.6, and 0.45, respectively. The physical parameterizations in WRF are explained in detail in Chapter 3, Section 3.2. Here, the results of this study are presented. The research presented in this chapter is summarized in the article by Z. Jandaghian, A. G. Touchaei, and H. Akbari (2017),

4.1. Defining Simulation Domain and Period

The simulation domain is the Greater Montreal Area (GMA) that is centered at the ~45.5ºN and ~73.6ºW. The horizontal domain of the simulations is composed of four two-way nested domains with 37×22, 43×34, 91×61, and 145×91 grid points, and a grid sizes of 9, 3, 1 and 0.333 km × km, respectively. The vertical resolution includes 51 vertical layers from the surface to a fixed pressure of ~100 mb (~16 km AGL). The selected simulation period starts with a clear sky condition (9th of August) and ends with a rainy condition (11th of August). The summer days are selected because results are used to evaluate the effect of urban heat island mitigation strategy (increasing surface reflectivity). Figure 4.1 shows the simulation domains based on USGS land use categories.

Domain 1 (grid size: 9 km × km) Domain 2 (grid size: 3 km × km)

Domain 3 (grid size: 1 km × km) Domain 4 (grid size:0.333 km × km)
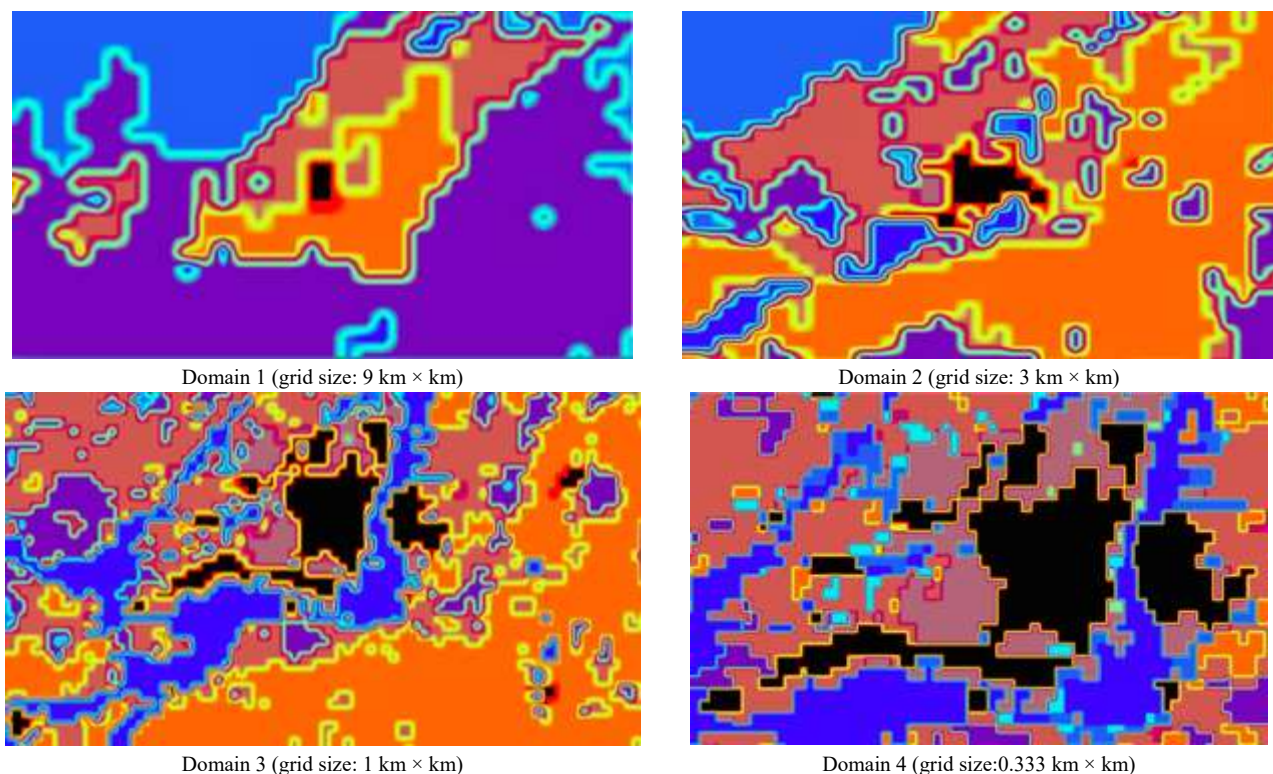
Figure 4.1. Simulation domains (grid sizes of domain 1: 9 km × km, domain 2: 3 km × km, domain 3: 1 km × km, domain 4: 0.333 km × km). Black refers to urban and build-up and cropland/woodland, the blue and purple refer to water bodies

The simulations were conducted with the initial and boundary conditions obtained from the North American Regional Reanalysis (NARR). Land Use/Land Cover (LULC) data was derived from the USGS 24-category data set. Advanced Very High-Resolution Radiometer (AVHRR)

measures the background surface albedo (Csiszar and Gutman 1999). The other physical parameterizations are explained in section 3.2.4. The positive-define advections of moisture, scalars and turbulent kinetic energy is activated to maintain model stability. Each simulation begins at 0000 UTC (LST= UTC - 4h) of the previous day of each period. The first 28h is considered as a spin up period.

4.2. Analysis of Physical Parameterizations in WRF and Effects of Increasing Surface Reflectivity on Urban Climate

The physical parameterizations need to be selected to predict weather conditions. A set of sensitivity analysis are carried. A proper simulation platform provides a better understanding of the effects of UHI and its mitigations strategy on urban climate. The model ensemble for urban climate simulation includes parameterizations for microphysics, cumulus, planetary boundary layer (PBL), radiation, land surface, and urban canopy. Characterizing the meteorological parameters (e.g., air temperature, wind speed, relative humidity and precipitation) to a different set of parameterizations (i.e., model ensemble) enables researchers to select the proper model platform for urban climate simulations. Table 4.1 presents the simulation set-ups with different options on parametrizations. A brief description of these parameterizations has been presented in Chapter 3.

Table 4.1. Simulation set-ups with different options on parameterization of microphysics, cumulus, PBL, and radiation

	Microphysics	Cumulus	PBL	Radiation
S01	WDM (16)[1]	Simplified Arakawa-Schubert (4)[2]	MYJ (2)[3]	RRTMG (4)
S02	WDM (16)	Betts-Miller-Janjic (2)[5]	MYJ (2)	RRTMG (4)
S03	WDM (16)	Grell 3D (5)[6]	BouLac PBL (8)[7]	RRTMG (4)
S04	WDM (16)	Grell 3D (5)	MYJ (2)	Dudhia (1)[8]
S05	Eta (5)[9]	Grell 3D (5)	MYJ (2)	RRTMG (4)
S06	WDM (16)	Grell 3D (5)	MYJ (2)	RRTMG (4)
S07	WDM (16)	Grell-Freitas (3)[10]	MYJ (2)	RRTMG (4)
S08	Goddard (7)[11]	Grell 3D (5)	MYJ (2)	RRTMG (4)
S09	WDM (16)	Kain-Fritsch (1)[12]	MYJ (2)	RRTMG (4)
S10	Lin (2)[13]	Grell 3D (5)	MYJ (2)	RRTMG (4)
S11	Milbrandt-Yau (9)[14]	Grell 3D (5)	MYJ (2)	RRTMG (4)
S12	Morrison (10)[15]	Grell 3D (5)	MYJ (2)	RRTMG (4)
S13	NSSL (17)[16]	Grell 3D (5)	MYJ (2)	RRTMG (4)
S14	NSSL with CCN (18)	Grell 3D (5)	MYJ (2)	RRTMG (4)
S15	WDM (16)	New Simplified Arakawa-Schubert (14)[17]	MYJ (2)	RRTMG (4)
S16	SBU-YLin (13)[18]	Grell 3D (5)	MYJ (2)	RRTMG (4)
S17	Thompson (8)[19]	Grell 3D (5)	MYJ (2)	RRTMG (4)
S18	WDM (16)	Tiedtke (6)[20]	MYJ (2)	RRTMG (4)
S19	WSM (6)[21]	Grell 3D (5)	MYJ (2)	RRTMG (4)
S20	WDM (16)	Zhang-McFarlane (7)22	MYJ (2)	RRTMG (4)

[1] Lim and Hong, (2010), [2] Pan and Wu., (1995), [3] Janjic (1994), [4] Iacono et al. (2008),[5] Janjic (1990), [6] Grell (1993), and Grell and Devenyi (2002), [7] Bougeault and Lacarrere, (1989), [8] Dudhia (1989), and Mlawer et al. (1997), [9] NOAA, (2001), [10] Grell and Freitas (2014), [11] Tao et al. (1989), [12] Kain (2004), [13] Lin (1983), [14] Milbrandt and Yau, (2005a), and Milbrandt and Yau, (2005b), [15] Morrison et al. (2009), [16] Mansellet al. (2010), [17] Han and Pan (2011), [18] Lin and Colle (2011), [19] Thompson et al. (2008), [20] Tiedtke (1989), and Zhang et al. (2011), [21] Hong and Lim, (2006), [22] Zhang and McFarlane, (1995)

4.2.1. Air Temperature

The 2-m air temperature of simulations' results are compared with measurements. Figure 4.2 shows the hourly 2-m air temperature of the simulated results of the S06 model ensemble (solid line) vs. measurements (dashed line) from seven weather stations for a period of 09-11 Aug-2009 across GMA (McTavish (MT), Pierre Elliott Trudeau Intl (PET), St-Hubert (SH), Ste-Anne-de-Bellevue (SAB), VArennes (VA), MIrabel (MI), Ste-Clothide (SC)). Table 4.2, 4.3 and 4.4 present the MBE, MAE and RMSA, respectively. For these simulations, the average MBEs (-1.5 ºC) indicates that the model on average underestimates the 2-m air temperature. The main reason for this underestimation is the exclusion of anthropogenic heat emission in WRF solver. The anthropogenic heat emission as traffic and human activities can significantly contribute to an increase in the air temperature of urban areas by up to 2°C (Salamanca et al., 2014). The MAE is the highest in S04 that the Dudhia model is used for the radiation estimation. Skin temperature is sensitive to shortwave radiation; consequently, the 2-m air temperature is sensitive to the selected options for radiation parameterization. The RRTMG parameterization is more accurate than the combination of the Dudhia scheme for shortwave and RRTM scheme for longwave radiation. The least MAE (1.6 °C) is in WDM (WRF Double-Moment 6-class Scheme) coupled with Grell 3D (S06) and with New Simplified Arakawa-Schubert (S01) as microphysics and cumulus scheme, respectively (Table 4.3). In the urban weather station, the MAE is minimized (1.4 °C). by using the WDM as microphysics scheme coupled with the choice of MYJ as PBL and RRTMG as the radiation scheme. The choices of PBL (MYJ and BouLac; coupled to ML-UCM) show a good agreement in predicting the 2-m air temperature in the urban area. In rural areas, the MAE of the model ensemble using the MYJ scheme was 0.2 °C less than the MAE of S03 using the BouLac scheme. Table 4.4 and Figure 4.3 present the RMSE of the simulations and accuracy of models. S06, S01, S16 and S07 have the least RMSE of about 2 °C. Figure 4.4 indicates that the least RMSE belongs to the urban area (McTavish weather station). Thus, the RMSE is higher in rural areas than urban ones. The combination of WDM6 (Lim and Hong, 2010) for microphysics, MYJ (Janjic, 1994) for planetary boundary layer, and RRTMG (Iacono et al., 2008) for radiation schemes provided better results compared with measurements.

The temperature differences between CTRL and ALBEDO scenario presents in Table 4.5. The results of S10, S12, S07 and S01 simulations indicate a higher temperature reduction (Figure 4.5).

However, the average calculated temperature differences of these simulations are 0.2°C. Figure 4.6 indicates that the urban areas` temperature is decreased more compared to their surroundings by increasing surface albedo.

SC
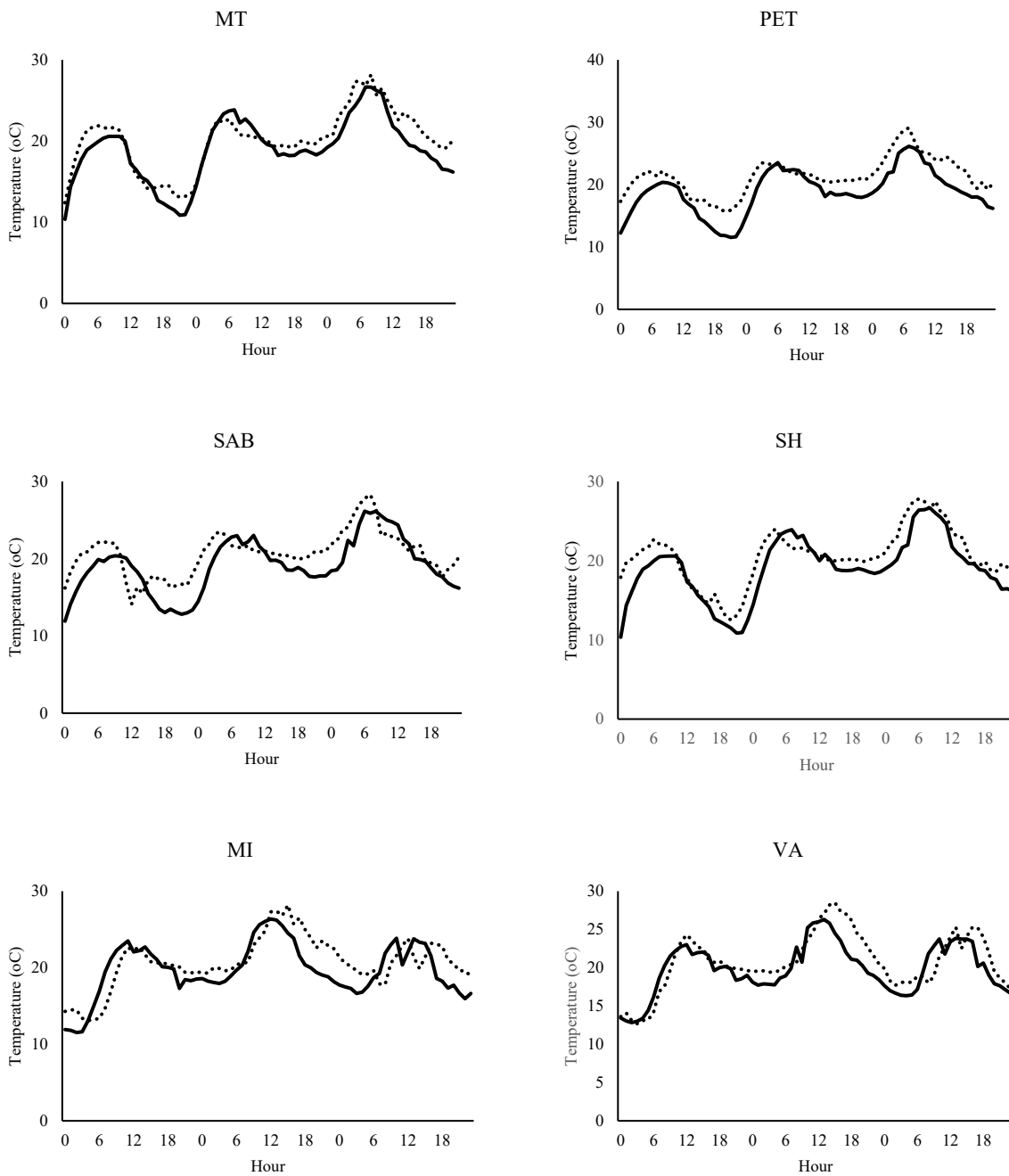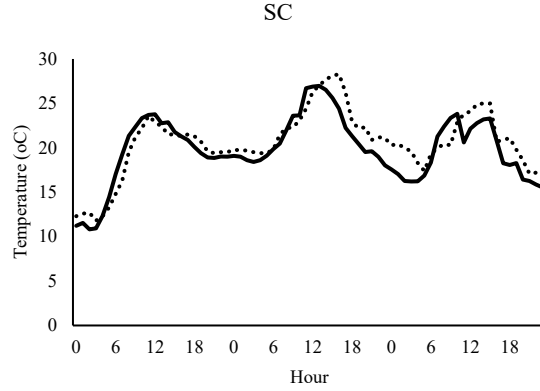
Figure 4.2. The hourly 2-m air temperature of the simulated of the S06 model ensemble (solid line) vs. measurements (dashed line) from seven weather stations for a period of 09-11 Aug-2009 across GMA (McTavish (MT), Pierre Elliott Trudeau Intl (PET), St-Hubert (SH), Ste-Anne-de-Bellevue (SAB), VArennes (VA), MIrabel (MI), Ste-Clothide (SC))

Table 4.2. Mean Bias Error (MBE) in predicted 2-m air temperature (°C) with different WRF settings (McTavish (MT), Pierre Elliott Trudeau Intl (PET), St-Hubert (SH), Ste-Anne-de-Bellevue (SAB), VArennes (VA), MIrabel (MI), Ste-Clothide (SC))

MBE	MT	PET	SAB	SH	VA	MI	SC	Average
S01	-0.7	-2.2	-1.2	-1.3	-0.7	-0.7	-0.7	-1.1
S02	-0.3	-2.3	-1.4	-1.5	-2.0	-2.1	-2.0	-1.6
S03	0.4	-1.9	-0.9	-1.2	-2.0	-2.5	-2.4	-1.5
S04	-0.9	-2.8	-1.8	-1.9	-2.2	-2.3	-2.2	-2.0
S05	-0.8	-2.5	-1.6	-1.6	-1.7	-0.8	-0.8	-1.4
S06	-1.1	-1.5	-1.5	-1.5	-0.9	0.0	-0.8	-1.2
S07	-0.7	-2.4	-1.5	-1.3	-1.0	-0.8	-1.6	-1.3
S08	-0.7	-2.5	-1.6	-1.6	-1.6	-1.7	-1.6	-1.6
S09	-0.6	-2.5	-1.5	-1.6	-1.6	-1.7	-0.7	-1.5
S10	-0.7	-2.4	-1.6	-1.4	-2.0	-1.9	-1.5	-1.6
S11	-0.7	-2.2	-1.2	-1.3	-1.7	-1.8	-1.6	-1.5
S12	-0.7	-2.1	-1.7	-1.6	-1.8	-1.3	-1.5	-1.5
S13	-0.5	-2.4	-1.6	-1.6	-2.1	-2.1	-2.0	-1.7
S14	-0.5	-2.5	-1.6	-1.6	-2.1	-2.2	-2.0	-1.8
S15	-0.6	-2.5	-1.6	-1.6	-2.0	-2.1	-1.9	-1.8
S16	-0.9	-2.3	-1.6	-1.3	-2.2	-0.6	-0.7	-1.4
S17	-0.6	-2.4	-1.6	-1.6	-2.0	-1.9	-1.9	-1.7
S18	-0.5	-2.4	-1.6	-1.6	-2.0	-1.9	-1.9	-1.7
S19	-0.6	-2.4	-1.6	-1.4	-1.6	-0.6	-1.4	-1.4
S20	-0.6	-2.1	-1.6	-1.2	-0.7	-0.6	-1.2	-1.1
Avg	-0.6	-2.4	-1.5	-1.5	-1.7	-1.5	-1.5	-1.5

Note: The definitions of statistical measurements are as follows Zhang et al. (2006) [51]: MBE = $\frac{1}{N}\sum_1^N(C_M - C_O)$, C_M and C_O are modeled and observed concentrations, respectively and N is the total number of model and observation pairs.

Table 4.3. Mean Absolute Error (MAE) in predicted 2-m air temperature (°C) with different WRF settings (McTavish (MT), Pierre Elliott Trudeau Intl (PET), St-Hubert (SH), Ste-Anne-de-Bellevue (SAB), VArennes (VA), MIrabel (MI), Ste-Clothide (SC))

MAE	MT	PET	SAB	SH	VA	MI	SC	Average
S01	1.3	2.3	1.9	1.6	1.6	2.1	1.4	1.7
S02	1.4	2.4	2.2	1.9	2.8	3.1	2.7	2.4
S03	1.3	1.9	2.1	1.7	3.8	3.6	4.2	2.7
S04	1.6	2.8	2.3	2.2	3.3	3.6	3.3	2.7
S05	1.5	2.6	2.3	1.9	4.3	3.4	1.6	2.5
S06	1.5	2.6	2.3	1.9	1.7	0.0	1.5	1.6
S07	1.5	2.5	2.3	1.7	1.9	2.2	3.2	2.2
S08	1.5	2.5	2.2	1.8	5.0	4.6	4.9	3.2
S09	1.5	2.5	2.3	1.8	4.3	4.2	1.4	2.6
S10	1.4	2.4	2.2	1.7	3.2	3.2	2.7	2.4
S11	1.3	2.3	1.9	1.6	3.0	4.2	3.2	2.5
S12	1.5	2.3	2.3	1.9	4.3	3.9	2.7	2.7
S13	1.4	2.5	2.3	1.9	3.0	3.4	3.0	2.5
S14	1.3	2.6	2.3	1.9	3.0	3.4	3.1	2.5
S15	1.4	2.6	2.3	1.8	3.3	3.7	3.2	2.6
S16	1.4	2.4	2.2	1.6	3.5	1.9	1.4	2.1
S17	1.4	2.5	2.3	1.8	3.3	3.8	3.3	2.6
S18	1.3	2.5	2.3	1.8	3.9	3.9	3.4	2.7
S19	1.4	2.5	2.2	1.7	5.1	1.9	5.0	2.8
S20	1.4	2.3	2.2	1.5	1.6	1.9	5.1	2.3
Avg	1.4	2.4	2.2	1.8	3.3	3.1	3.0	2.5

Note: The definitions of statistical measurements are as follows Zhang et al. (2006) [51]: $MAE = \frac{1}{N}\sum_1^N |C_M - C_O|$ C_M and C_O are modeled and observed concentrations, respectively and N is the total number of model and observation pairs.

Table 4.4. Root Mean Square Error (RMSE) in predicted 2-m air temperature (°C) with different WRF settings (McTavish (MT), Pierre Elliott Trudeau Intl (PET), St-Hubert (SH), Ste-Anne-de-Bellevue (SAB), VArennes (VA), MIrabel (MI), Ste-Clothide (SC))

RMSE	MT	PET	SAB	SH	VA	MI	SC	Average
S01	1.6	2.7	2.3	1.9	2.1	2.5	1.7	2.1
S02	1.7	2.8	2.6	2.4	3.5	3.8	3.5	2.9
S03	1.6	2.4	2.5	2.2	5.0	4.8	5.5	3.4
S04	1.9	2.8	2.8	2.9	4.1	4.3	4.1	3.3
S05	1.8	2.9	2.6	2.3	5.0	4.0	1.9	2.9
S06	1.8	2.9	2.7	2.3	2.1	0.0	1.8	1.9
S07	1.8	2.8	2.6	2.0	2.4	2.6	4.0	2.6
S08	1.8	2.9	2.6	2.1	5.7	5.3	5.8	3.7
S09	1.7	2.9	2.6	2.3	4.9	4.9	1.7	3.0
S10	1.7	2.7	2.6	2.0	3.9	3.8	3.4	2.9
S11	1.6	2.7	2.3	1.9	3.7	4.9	4.0	3.0
S12	1.8	2.7	2.7	2.3	5.0	4.5	3.4	3.2
S13	1.6	2.8	2.7	2.3	3.7	4.1	3.8	3.0
S14	1.6	2.9	2.7	2.3	3.7	4.1	3.9	3.0
S15	1.7	2.9	2.7	2.3	4.0	4.3	4.0	3.1
S16	1.7	2.7	2.6	1.9	4.3	2.3	1.7	2.5
S17	1.6	2.9	2.7	2.3	4.0	4.4	4.1	3.1
S18	1.6	3.0	2.7	2.4	4.6	4.6	4.2	3.3
S19	1.7	2.8	2.6	2.0	5.8	2.3	5.8	3.3
S20	1.7	2.7	2.6	1.9	2.1	2.3	5.8	2.7
Avg	1.7	2.8	2.6	2.2	4.0	3.7	3.7	3.0

$RMSE = \left[\frac{1}{N}\Sigma_1^N(C_M - C_O)^2\right]^{1/2}$ C_M and C_O are modeled and observed concentrations, respectively and N is the total number of model and observation pairs.

Figure 4.3. Root mean square error in predicted 2-m air temperature (°C) with different WRF settings
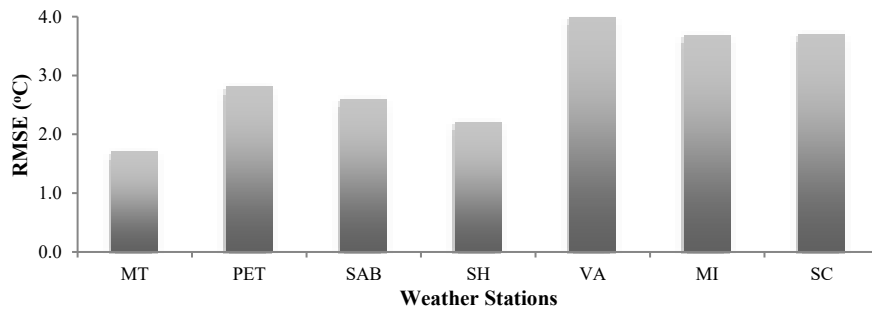
Figure 4.4. Root mean square error in predicted 2-m air temperature (°C) in weather station over the domain (McTavish (MT), Pierre Elliott Trudeau Intl (PET), St-Hubert (SH), Ste-Anne-de-Bellevue (SAB), VArennes (VA), MIrabel (MI), Ste-Clothide (SC))

Table 4.5. 2-m air temperature (°C) differences between CTRL & ALBEDO scenarios (McTavish (MT), Pierre Elliott Trudeau Intl (PET), St-Hubert (SH), Ste-Anne-de-Bellevue (SAB), VArennes (VA), MIrabel (MI), Ste-Clothide (SC))

ΔT	MT	PET	SAB	SH	VA	MI	SC	Average
S01	0.2	0.1	0.1	0.1	0.3	0.3	0.1	0.2
S02	0.2	0.1	0.1	0.1	0.1	0.1	0.1	0.1
S03	0.2	0.1	0.2	0.1	0.2	0.1	0.1	0.1
S04	0.2	0.1	0.2	0.1	0.2	0.1	0.1	0.1
S05	0.3	0.1	0.2	0.1	0.2	0.2	0.0	0.1
S06	0.2	0.1	0.2	0.2	0.1	0.0	0.1	0.1
S07	0.2	0.1	0.2	0.2	0.7	0.1	0.0	0.2
S08	0.2	0.1	0.1	0.1	0.1	0.1	0.1	0.1
S09	0.2	0.2	0.2	0.1	0.2	0.2	0.1	0.2
S10	0.2	0.2	0.1	0.1	0.0	0.4	0.7	0.2
S11	0.2	0.1	0.2	0.1	0.2	0.5	0.2	0.2
S12	0.2	0.5	0.1	0.1	0.1	0.5	0.2	0.2
S13	0.2	0.1	0.0	0.0	0.0	0.1	0.3	0.1
S14	0.2	0.1	0.1	0.0	0.1	0.1	0.2	0.1
S15	0.2	0.2	0.1	0.1	0.1	0.2	0.1	0.1
S16	0.1	0.1	0.1	0.1	-0.5	0.2	0.6	0.1
S17	0.2	0.2	0.1	0.1	0.1	0.2	0.1	0.1
S18	0.2	0.2	0.1	0.1	0.0	0.2	0.1	0.1
S19	0.4	0.1	0.1	0.1	0.1	0.2	0.1	0.2
S20	0.3	0.4	0.1	-0.5	0.4	0.2	0.3	0.2
Avg	0.2	0.2	0.1	0.1	0.1	0.2	0.2	0.2
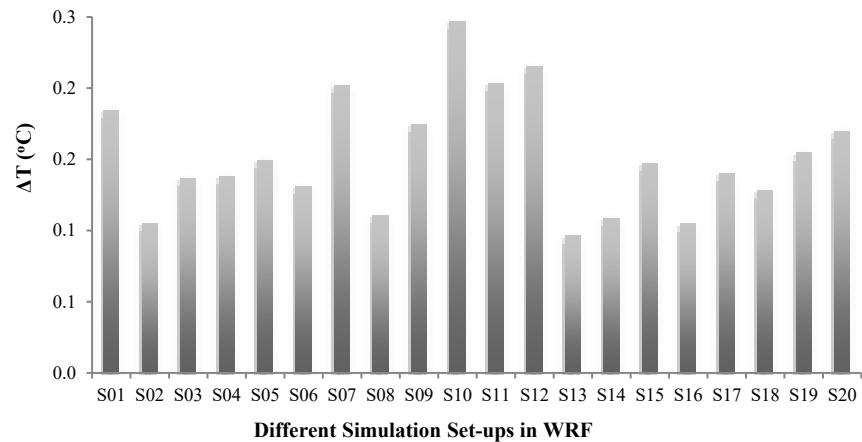
Figure 4.5. 2-m air temperature (°C) differences (CTRL- ALBEDO) in different physical parameterization
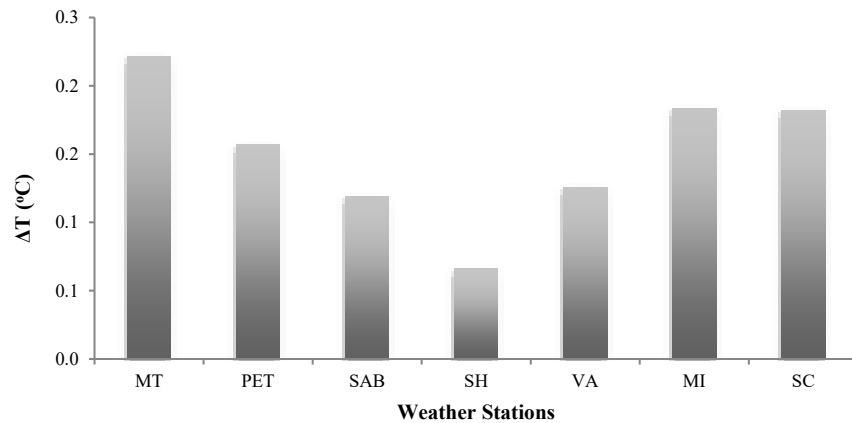
Figure 4.6. 2-m air temperature (°C) differences (CTRL- ALBEDO) in weather station over the domain (McTavish (MT), Pierre Elliott Trudeau Intl (PET), St-Hubert (SH), Ste-Anne-de-Bellevue (SAB), VArennes (VA), MIrabel (MI), Ste-Clothide (SC))

4.2.2. Wind Speed

Wind speed plays an important role in calculating air temperature from skin temperature in land surface model. The transient effect of wind speed on air temperature is complicated. An increase in wind speed increases the convection heat transfer that reduces the skin temperature, which simultaneously causes a decrease in convection heat transfer. The wind speed is typically measured at a 10-m height from the ground; so, the 10-m wind speed is compared for current analysis. All model ensembles underestimate the wind speed in rural and urban areas. The underestimation of 2-m air temperature is probably because of the underestimation in 10-m wind speed. The main justification for underestimation of 2-m air temperature is inaccuracy of predicting

wind speed by PBL options. PBL options with the coupling capability to UCMs are not well designed for very fine-resolution grids.

Figure 4.7 shows the hourly 10-m wind speed of the simulated results of the S06 model ensemble (solid line) vs. measurements (dashed line) from seven weather stations for a period of 09-11 Aug-2009 across GMA (McTavish (MT), Pierre Elliott Trudeau Intl (PET), St-Hubert (SH), Ste-Anne-de-Bellevue (SAB), VArennes (VA), MIrabel (MI), Ste-Clothide (SC)). The MBE and MAE for wind speed calculations is fairly large (Table 4.6 and Table 4.7). Microphysics and cumulus parameterizations that introduce higher inaccuracies in predicting 2-m air temperature have high MBE, which shows the high dependency of the calculated air temperature on wind speed. The predicted wind speed in the urban area has a MAE of about 1 m/s. The average performance of model ensembles through the simulation domain based on MAE is almost the same (about 1 to 2 m/s). Table 4.8, Figure 4.8 and 4.9 provide the resulting RMSE for the weather stations and the selected model ensembles. The highest RMSE belong to S03 and S16. The combination of WDM6 (Lim and Hong, 2010) for microphysics, MYJ (Janjic, 1994) for planetary boundary layer, and RRTMG (Iacono et al., 2008) for radiation schemes provided better results compared with measurements.

Table 4.9 and Figure 4.10 present the wind speed differences between CTRL and ALBEDO scenario. The results show a slight increase in wind speed (an average of 0.1 m/s) when the surface albedo increases. The highest increase in wind speed is for S02 and S17, while the lowest belongs to S03, S13 and S14. Figure 4.11 indicates the results in weather stations over the domain. The wind speed increases in urban areas (McTavish) more than rural parts. The result demonstrates that an increase in surface albedo will slightly increase the wind speed, which will assist the decrease in air temperature eventually.
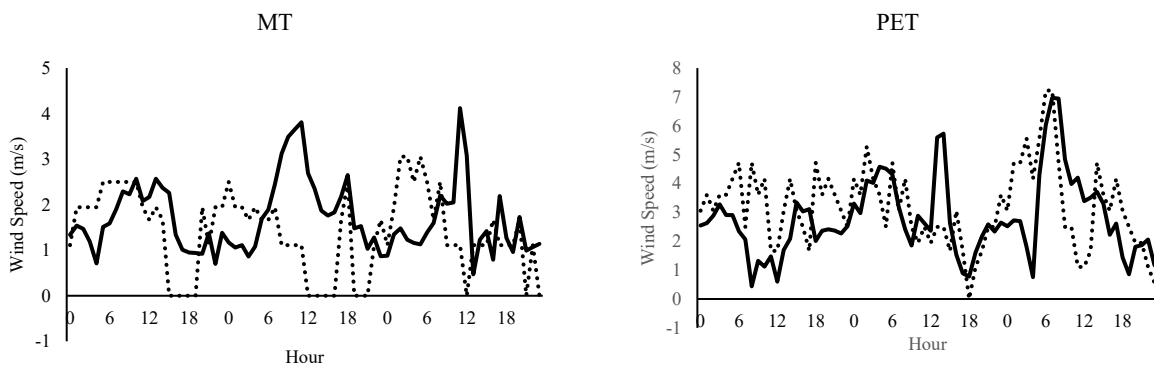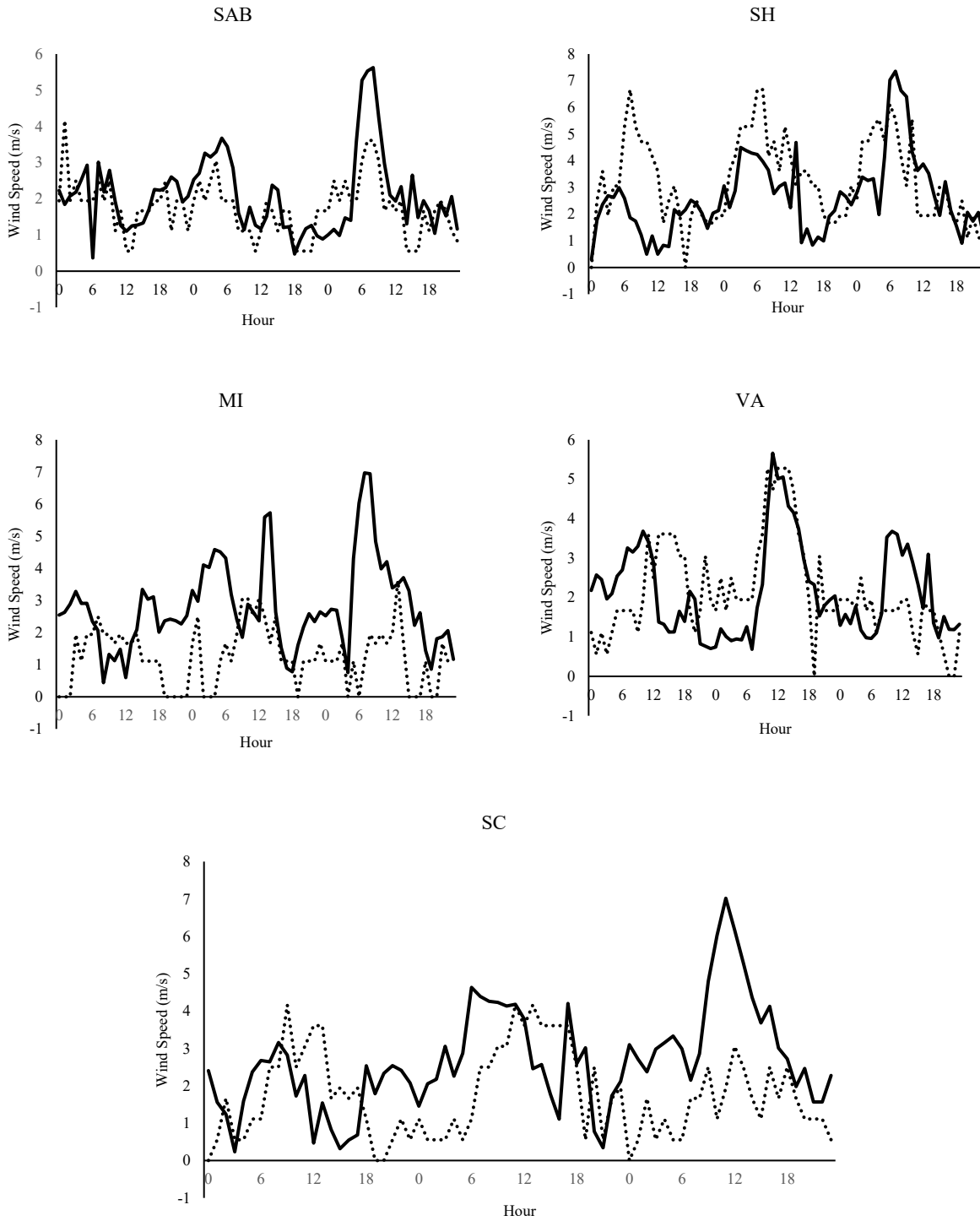
Figure 4.7. The hourly 10-m wind speed of the simulated (solid line) vs. measurements (dashed line) from seven weather stations for a period of 09-11 Aug-2009 across GMA (McTavish (MT), Pierre Elliott Trudeau Intl (PET), St-Hubert (SH), Ste-Anne-de-Bellevue (SAB), VArennes (VA), MIrabel (MI), Ste-Clothide (SC))

Table 4.6. Mean Bias Error (MBE) in predicted wind speed (m/s) with different WRF settings (McTavish (MT), Pierre Elliott Trudeau Intl (PET), St-Hubert (SH), Ste-Anne-de-Bellevue (SAB), VArennes (VA), MIrabel (MI), Ste-Clothide (SC))

MBE	MT	PET	SAB	SH	VA	MI	SC	Average
S01	0.6	0.2	0.5	0.0	0.0	1.8	1.1	0.6
S02	0.3	-0.5	0.3	-0.7	-0.2	1.4	-0.7	0.0
S03	0.9	-0.1	0.8	-0.4	-0.1	1.9	1.1	0.6
S04	0.3	-0.4	0.2	-0.7	-0.2	1.5	0.7	0.2
S05	0.3	-0.4	0.3	-0.7	-0.1	1.5	0.9	0.3
S06	0.3	-0.4	0.3	-0.6	0.0	1.5	0.9	0.3
S07	0.3	-0.5	0.3	-0.7	-0.1	1.5	0.9	0.2
S08	0.3	-0.4	0.2	-0.7	-0.1	1.6	0.9	0.2
S09	0.4	-0.4	0.4	-0.5	0.0	1.6	1.0	0.4
S10	0.3	-0.4	0.3	-0.7	-0.1	1.5	0.9	0.2
S11	0.4	-0.2	0.5	-0.5	0.0	1.7	1.0	0.4
S12	0.4	-1.5	0.3	-0.7	-0.1	0.5	0.9	0.0
S13	0.4	-0.2	0.4	-0.4	0.0	1.7	1.0	0.4
S14	0.4	-0.2	0.5	-0.5	0.0	1.7	1.0	0.4
S15	0.3	-0.3	0.3	-0.7	-0.1	1.6	0.8	0.3
S16	1.2	-0.4	0.5	-0.8	0.0	1.5	0.8	0.4
S17	0.4	0.0	0.0	-0.6	0.5	1.4	0.9	0.4
S18	0.3	-0.5	0.9	-0.5	0.5	1.4	0.9	0.4
S19	0.3	-0.5	0.3	-0.8	-0.1	1.5	0.8	0.2
S20	0.3	-0.6	0.3	-0.7	-0.1	1.4	0.9	0.2
Avg	0.4	-0.4	0.4	-0.6	0.0	1.5	0.8	0.3

Note: The definitions of statistical measurements are as follows Zhang et al. (2006) [51]: MBE $= \frac{1}{N}\sum_1^N(C_M - C_O)$, C_M and C_O are modeled and observed concentrations, respectively and N is the total number of model and observation pairs.

Table 4.7. Mean Absolute Error (MAE) in predicted wind speed (m/s) with different WRF settings (McTavish (MT), Pierre Elliott Trudeau Intl (PET), St-Hubert (SH), Ste-Anne-de-Bellevue (SAB), VArennes (VA), MIrabel (MI), Ste-Clothide (SC))

MAE	MT	PET	SAB	SH	VA	MI	SC	Average
S01	1.0	1.2	0.9	1.3	1.1	1.8	1.2	1.2
S02	0.8	1.4	0.7	1.4	1.1	1.5	1.4	1.2
S03	1.3	1.5	1.0	1.4	1.4	2.0	1.6	1.5
S04	0.9	1.2	0.7	1.5	1.2	1.6	1.3	1.2
S05	0.9	1.2	0.7	1.4	1.4	1.8	1.8	1.3
S06	1.0	1.3	0.7	1.4	1.1	1.7	1.6	1.2
S07	0.9	1.3	0.7	1.4	1.4	1.8	1.8	1.3
S08	0.9	1.3	0.6	1.3	1.4	1.9	1.7	1.3
S09	0.9	1.3	0.8	1.4	1.5	1.8	1.9	1.4
S10	0.8	1.3	0.7	1.4	1.2	1.8	1.8	1.3
S11	0.8	1.3	0.8	1.4	1.3	1.8	1.5	1.3
S12	0.9	1.6	0.7	1.4	1.4	1.0	1.7	1.2
S13	0.8	1.3	0.8	1.3	1.3	1.8	1.5	1.3
S14	0.8	1.3	0.8	1.4	1.3	1.8	1.5	1.3
S15	0.8	1.2	0.7	1.4	1.3	1.7	1.5	1.2
S16	1.6	1.3	0.8	1.4	1.3	1.9	1.9	1.4
S17	0.9	0.0	0.0	1.4	1.5	1.6	1.8	1.0
S18	0.8	1.3	1.1	1.4	1.3	1.6	1.4	1.3
S19	0.9	1.3	0.8	1.4	1.3	1.9	1.8	1.3
S20	0.9	1.3	0.8	1.3	1.4	1.8	1.7	1.3
Avg	0.9	1.2	0.7	1.4	1.3	1.7	1.6	1.3

Note: The definitions of statistical measurements are as follows Zhang et al. (2006) [51]: $MAE = \frac{1}{N}\sum_1^N|C_M - C_O|$ C_M and C_O are modeled and observed concentrations, respectively and N is the total number of model and observation pairs.

Table 4.8. Root Mean Square Error (RMSE) in predicted wind speed (m/s) with different WRF settings (McTavish (MT), Pierre Elliott Trudeau Intl (PET), St-Hubert (SH), Ste-Anne-de-Bellevue (SAB), VArennes (VA), MIrabel (MI), Ste-Clothide (SC))

RMSE	MT	PET	SAB	SH	VA	MI	SC	Average
S01	1.3	1.5	1.1	1.6	1.3	2.1	1.4	1.5
S02	1.0	1.8	0.9	1.7	1.5	1.9	1.7	1.5
S03	1.7	1.9	1.4	1.8	1.8	2.6	2.1	1.9
S04	1.1	1.6	0.8	1.8	1.6	2.1	1.6	1.5
S05	1.1	1.6	0.9	1.8	1.8	2.2	2.2	1.6
S06	1.3	1.6	0.9	1.8	1.3	2.2	1.9	1.6
S07	1.1	1.6	0.9	1.8	1.7	2.3	2.3	1.7
S08	1.1	1.6	0.8	1.7	1.8	2.3	2.2	1.6
S09	1.1	1.6	1.0	1.8	1.9	2.2	2.2	1.7
S10	1.0	1.6	0.9	1.8	1.7	2.3	2.3	1.7
S11	1.0	1.6	1.0	1.8	1.7	2.2	1.9	1.6
S12	1.1	1.9	0.9	1.8	1.8	1.4	2.1	1.6
S13	1.0	1.5	1.0	1.7	1.7	2.2	1.8	1.6
S14	1.0	1.6	1.0	1.8	1.7	2.2	1.9	1.6
S15	1.0	1.5	0.9	1.8	1.7	2.1	1.8	1.5
S16	2.0	1.6	1.0	1.8	1.7	2.4	2.4	1.8
S17	1.1	0.4	0.4	1.8	1.9	2.0	2.2	1.4
S18	1.0	1.5	1.4	1.6	1.7	1.9	1.8	1.6
S19	1.1	1.7	0.9	1.8	1.7	2.3	2.2	1.7
S20	1.0	1.5	1.0	1.7	1.8	2.2	2.2	1.6
Avg	1.1	1.6	1.0	1.8	1.7	2.2	2.0	1.6

Note: The definitions of statistical measurements are as follows Zhang et al. (2006) [51]: $RMSE = \left[\frac{1}{N}\sum_1^N(C_M - C_O)^2\right]^{1/2}$ C_M and C_O are modeled and observed concentrations, respectively and N is the total number of model and observation pairs.

Figure 4.8. Root mean square error in predicted wind speed (m/s) with different WRF settings

Figure 4.9. Root mean square error in predicted wind speed (m/s) in weather station over the domain (McTavish (MT), Pierre Elliott Trudeau Intl (PET), St-Hubert (SH), Ste-Anne-de-Bellevue (SAB), VArennes (VA), MIrabel (MI), Ste-Clothide (SC))

Table 4.9. 10-m wind speed (m/s) differences between CTRL & ALBEDO scenarios (McTavish (MT), Pierre Elliott Trudeau Intl (PET), St-Hubert (SH), Ste-Anne-de-Bellevue (SAB), VArennes (VA), MIrabel (MI), Ste-Clothide (SC))

ΔWS	MT	PET	SAB	SH	VA	MI	SC	Average
S01	0.2	0.2	0.2	0.1	0.2	0.2	0.1	0.1
S02	0.2	0.2	0.1	-0.1	0.1	0.2	0.8	0.2
S03	0.1	-0.2	0.1	0.0	-0.1	0.1	0.0	0.0
S04	0.2	0.1	0.1	0.1	0.1	0.1	0.1	0.1
S05	0.1	0.1	0.1	0.0	0.1	0.1	0.0	0.1
S06	0.1	0.0	0.2	0.0	0.3	0.0	0.0	0.1
S07	0.1	0.0	0.1	0.0	0.1	0.0	0.0	0.0
S08	0.2	0.1	0.0	0.0	0.1	0.1	0.0	0.0
S09	0.2	0.1	0.1	0.0	0.1	0.1	0.0	0.1
S10	0.1	0.1	0.1	0.0	0.1	0.1	0.0	0.1
S11	0.2	0.1	0.0	0.1	0.0	0.1	0.1	0.1
S12	0.1	-0.2	0.1	0.6	0.1	-0.2	-0.1	0.1
S13	0.1	-0.1	0.1	0.0	0.1	-0.1	0.0	0.0
S14	0.0	0.1	0.1	0.0	0.1	0.1	0.0	0.0
S15	0.1	0.1	0.1	0.0	0.1	0.1	0.0	0.1
S16	1.0	0.0	0.1	-0.1	0.1	0.0	-0.1	0.2
S17	0.1	0.4	0.7	0.0	0.2	0.3	0.0	0.2
S18	0.1	0.0	0.7	0.0	0.7	0.0	0.0	0.2
S19	0.1	0.0	0.1	0.0	0.1	0.0	0.0	0.0
S20	0.1	0.0	0.1	0.0	0.1	0.0	0.0	0.0
Avg	0.2	0.0	0.2	0.0	0.1	0.1	0.0	0.1

Figure 4.10. 10-m Wind speed (m/s) differences (CTRL- ALBEDO) in different physical parameterizations
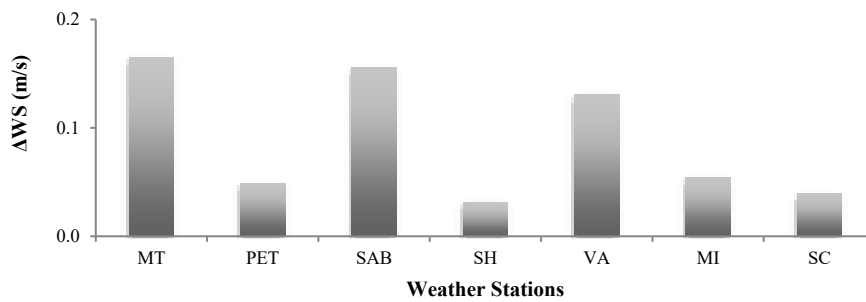
Figure 4.11. 10-m Wind speed (m/s) differences (CTRL- ALBEDO) in weather station over the domain (McTavish (MT), Pierre Elliott Trudeau Intl (PET), St-Hubert (SH), Ste-Anne-de-Bellevue (SAB), VArennes (VA), MIrabel (MI), Ste-Clothide (SC))

4.2.3. Relative Humidity

Relative humidity is a function of moisture content, air temperature, and surface pressure. Therefore, it carries part of the error from the inaccuracy in predicting the air temperature. The RH calculations are explained in Chapter 3. The relative humidity at 2-m height is underestimated by all model ensembles and the average MBE is -2.8% (Table 4.10). The least MAE (Table 4.11) is observed in the urban areas. The average MAE is 14.4% (varied from 13% to 17%). The model ensembles have the same performance by means of their RMSE (Table 4.12) with the average of 17.7%. However, the predicted relative humidity in the urban areas is more accurate compared to rural areas because of the lack of moisture in urban regions. In urban areas, both moisture content of the air and moisture flux from the ground are low. Figure 4.12 and 4.13 present the RMSE

relative humidity (%) at 2-m height with different WRF settings and within various weather stations, respectively. The combination of WDM6 (Lim and Hong, 2010) for microphysics, MYJ (Janjic, 1994) for planetary boundary layer, and RRTMG (Iacono et al., 2008) for radiation schemes provided better results compared with measurements.

The relative humidity differences between CTRL and ALBEDO scenario are presented in Table 4.13 and Figures 4.14. The results show a decrease in relative humidity as an average of 3.2% as the surface reflectivity of roofs, walls and grounds increases. The highest decrease in RH is in S03, S04, S05 and S18 simulations. The two WRF setting that the differences are positive and indicate a slight increase in RH are S06 and S07, where the Grell-Freitas and Grell-3D used as the cumulus model. Figure 4.15 indicates the results in various weather stations over the domain. The relative humidity decreases less in rural areas compared to the urban areas because of the more greening spaces that exist in rural parts.

Table 4.10. Mean Bias Error (MBE) in predicted relative humidity (%) at 2-m height with different WRF settings (McTavish (MT), Pierre Elliott Trudeau Intl (PET), St-Hubert (SH), Ste-Anne-de-Bellevue (SAB), VArennes (VA), MIrabel (MI), Ste-Clothide (SC))

MBE	MT	PET	SAB	SH	VA	MI	SC	Average
S01	-0.4	9.7	-0.3	0.5	-1.4	4.2	-5.7	1.0
S02	-9.2	2.0	-7.7	-7.2	-7.6	-2.6	-6.7	-5.6
S03	-11.1	0.9	-10.6	-7.0	-10.5	-3.6	-6.5	-6.9
S04	-5.5	4.4	-5.4	-3.7	-5.3	-0.2	-3.2	-2.7
S05	-6.1	4.2	-5.8	-3.8	-5.7	-3.9	-4.8	-3.7
S06	-0.8	4.3	-5.9	-4.4	-0.2	7.8	-1.0	0.0
S07	-5.7	4.7	-5.2	-4.1	-6.3	-1.3	-0.9	-2.7
S08	-6.1	4.8	-5.3	-3.9	-5.2	0.3	-3.4	-2.7
S09	-7.1	3.5	-6.1	-5.0	-6.0	-1.1	-6.7	-4.1
S10	-5.3	5.3	-4.1	-3.0	-1.3	4.6	0.4	-0.5
S11	-7.6	3.2	-7.7	-5.0	-4.1	1.2	-1.4	-3.0
S12	-6.2	-1.0	-1.1	0.3	-1.0	-5.5	1.2	-1.9
S13	-7.1	2.8	-2.6	-1.6	-2.6	-1.7	-1.1	-2.0
S14	-7.0	3.3	-6.9	-4.6	-6.8	-1.3	-4.1	-3.9
S15	-7.1	3.0	-6.4	-5.6	-6.4	-1.5	-5.1	-4.2
S16	-1.2	4.9	-3.7	-4.1	0.1	-1.4	-3.6	-1.3
S17	-6.3	3.8	-2.8	-4.4	-2.8	-0.7	-4.0	-2.5
S18	-7.4	2.6	-4.2	-5.7	-4.0	-2.0	-5.2	-3.7
S19	-6.1	5.1	-4.6	-3.6	-4.5	-1.8	-3.2	-2.7
S20	-6.2	3.8	-4.2	-4.4	-7.2	-1.2	-3.9	-3.3
Avg	-6.0	3.8	-5.0	-4.0	-4.4	-0.6	-3.4	-2.8

Note: The definitions of statistical measurements are as follows Zhang et al. (2006) [51]: MBE $= \frac{1}{N}\sum_1^N(C_M - C_O)$, C_M and C_O are modeled and observed concentrations, respectively and N is the total number of model and observation pairs.

Table 4.11. Mean Absolute Error (MAE) in predicted relative humidity (%) at 2-m height with different WRF settings (McTavish (MT), Pierre Elliott Trudeau Intl (PET), St-Hubert (SH), Ste-Anne-de-Bellevue (SAB), VArennes (VA), MIrabel (MI), Ste-Clothide (SC))

MAE	MT	PET	SAB	SH	VA	MI	SC	Average
S01	6.5	10.4	8.1	4.2	7.1	7.9	15.5	8.5
S02	14.5	12.5	12.9	11.9	13.0	12.9	10.1	12.5
S03	18.8	15.9	20.2	16.1	15.6	13.0	15.0	16.4
S04	15.3	13.4	11.0	11.4	15.1	14.3	10.8	13.0
S05	16.8	14.2	12.5	13.8	17.9	18.8	16.1	15.7
S06	14.2	14.6	12.7	13.7	7.7	13.9	5.7	11.8
S07	18.3	15.5	13.7	15.5	18.4	18.6	13.8	16.3
S08	17.7	15.7	13.7	15.9	19.6	15.9	16.0	16.4
S09	16.5	14.1	12.5	13.8	17.9	15.1	15.9	15.1
S10	19.0	16.2	15.5	16.6	14.6	18.2	14.3	16.3
S11	18.0	15.9	16.9	16.2	14.0	15.8	14.5	15.9
S12	17.0	16.3	15.0	15.1	19.9	18.4	14.3	16.6
S13	14.2	12.4	13.1	12.5	15.3	13.5	11.4	13.2
S14	14.4	12.6	12.0	11.4	13.8	13.3	10.6	12.6
S15	15.1	12.7	11.4	11.3	15.4	14.3	11.4	13.1
S16	15.7	16.1	15.1	16.6	14.5	18.0	15.6	15.9
S17	15.1	13.2	11.8	11.8	14.3	14.0	11.3	13.1
S18	14.2	10.8	10.4	9.8	11.8	12.3	10.1	11.3
S19	18.7	15.9	14.7	16.6	19.7	17.6	16.6	17.1
S20	18.9	15.2	14.8	15.7	17.4	18.1	15.7	16.6
Avg	15.9	14.2	13.4	13.5	15.1	15.2	13.2	14.4

Note: The definitions of statistical measurements are as follows Zhang et al. (2006) [51]: MAE $= \frac{1}{N}\sum_1^N |C_M - C_O|$ C_M and C_O are modeled and observed concentrations, respectively and N is the total number of model and observation pairs.

Table 4.12. Root Mean Square Error (RMSE) in predicted relative humidity (%) at 2-m height with different WRF settings (McTavish (MT), Pierre Elliott Trudeau Intl (PET), St-Hubert (SH), Ste-Anne-de-Bellevue (SAB), VArennes (VA), MIrabel (MI), Ste-Clothide (SC))

RMSE	MT	PET	SAB	SH	VA	MI	SC	Average
S01	8.7	12.8	10.1	5.4	10.3	10.1	20.2	11.1
S02	19.6	15.4	17.4	16.1	16.7	15.3	14.1	16.4
S03	23.9	19.1	24.4	20.2	20.8	17.3	19.0	20.7
S04	18.2	15.6	15.3	14.8	17.9	16.2	14.0	16.0
S05	19.7	17.0	15.9	16.7	20.6	22.2	20.2	18.9
S06	16.5	17.2	15.9	16.5	10.4	27.8	8.1	16.1
S07	21.2	18.5	16.8	18.4	21.5	23.1	17.7	19.6
S08	21.3	18.6	16.9	19.1	22.8	18.9	19.9	19.6
S09	19.7	17.0	15.9	16.5	20.7	17.8	20.3	18.3
S10	22.2	19.2	18.3	19.7	17.2	22.2	18.5	19.6
S11	22.6	21.7	21.3	21.8	18.7	18.6	18.5	20.5
S12	19.8	18.6	17.5	17.8	22.8	21.4	18.5	19.5
S13	18.1	15.0	16.7	15.4	18.6	15.6	14.1	16.2
S14	18.4	15.2	16.5	14.9	17.2	15.5	13.6	15.9
S15	18.4	15.3	15.9	14.9	18.4	16.4	14.1	16.2
S16	18.4	19.1	17.8	19.3	17.3	24.1	20.4	19.5
S17	18.2	15.5	15.1	15.1	16.2	16.1	14.3	15.8
S18	17.3	13.4	13.6	12.9	14.4	14.4	12.4	14.0
S19	21.8	19.0	17.5	19.5	23.1	23.5	20.3	20.7
S20	22.0	17.9	17.5	18.7	21.0	23.5	19.5	20.0
Avg	19.3	17.1	16.8	16.7	18.3	19.0	16.9	17.7

Note: The definitions of statistical measurements are as follows Zhang et al. (2006) [51]: RMSE $= \left[\frac{1}{N}\sum_{1}^{N}(C_M - C_O)^2\right]^{1/2}$ C_M and C_O are modeled and observed concentrations, respectively and N is the total number of model and observation pairs.
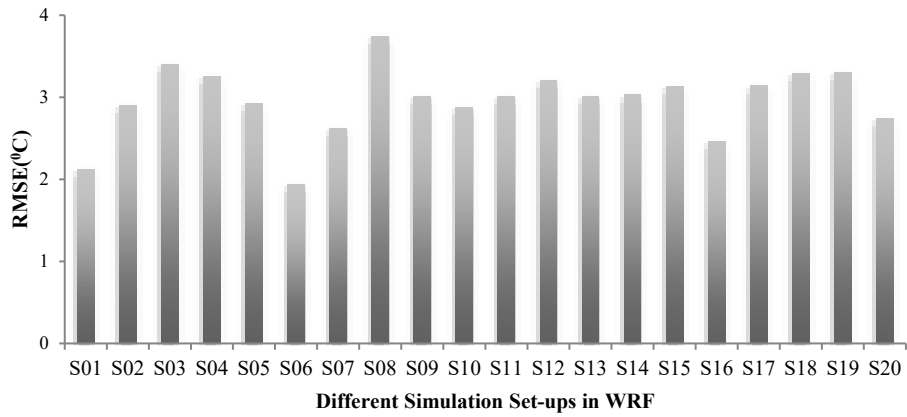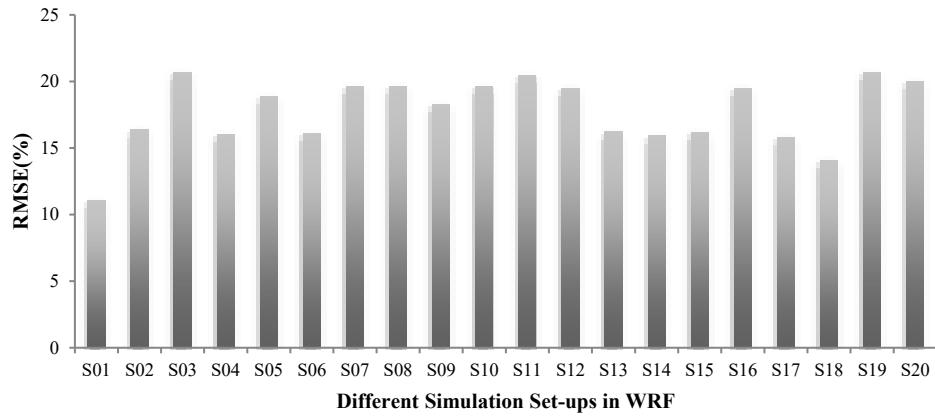
Figure 4.12. Root mean square error in predicted relative humidity (%) at 2-m height with different WRF settings
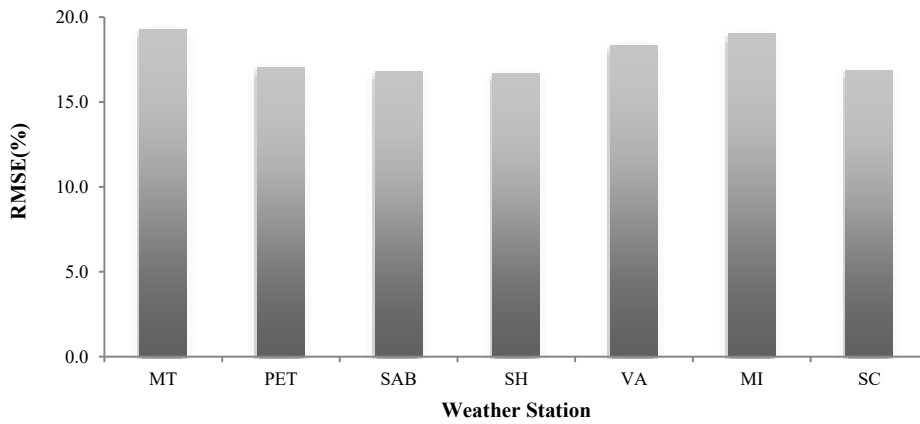
Figure 4.13. Root mean square error in predicted relative humidity (%) at 2-m height in weather station over domain (McTavish (MT), Pierre Elliott Trudeau Intl (PET), St-Hubert (SH), Ste-Anne-de-Bellevue (SAB), VArennes (VA), MIrabel (MI), Ste-Clothide (SC))

Table 4.13. Relative humidity (%) at 2-m height differences between CTRL & ALBEDO scenario (McTavish (MT), Pierre Elliott Trudeau Intl (PET), St-Hubert (SH), Ste-Anne-de-Bellevue (SAB), VArennes (VA), MIrabel (MI), Ste-Clothide (SC))

ΔRH	MT	PET	SAB	SH	VA	MI	SC	Average
S01	-0.8	-0.5	-0.8	-0.5	-1.9	-1.5	-7.2	-1.9
S02	-3.6	-5.1	-3.6	12.7	-3.6	-5.1	-6.0	-2.0
S03	-7.2	-9.2	-7.2	-9.5	-7.2	-9.2	-9.5	-8.4
S04	-7.2	-9.6	-7.9	-9.3	-7.9	-9.6	-9.3	-8.7
S05	-7.7	-8.1	-7.1	-8.9	-7.1	-6.0	-5.1	-7.2
S06	1.6	-2.0	-1.7	-1.3	5.7	6.5	3.0	1.7
S07	0.1	0.6	0.8	1.1	-0.4	1.9	3.9	1.1
S08	-1.4	-1.0	-1.1	-0.9	-1.1	-1.0	-0.9	-1.0
S09	-1.8	-2.8	-2.2	-1.9	-2.7	-2.8	-2.0	-2.3
S10	-2.8	-3.4	-2.1	-2.6	-1.6	-5.0	-6.3	-3.4
S11	0.7	-0.8	-3.1	-4.0	-2.8	-8.1	-5.7	-3.4
S12	-1.9	-6.7	-1.4	-1.4	-1.4	-6.7	-1.0	-2.9
S13	-1.5	-1.3	-0.6	-1.1	-0.6	-1.3	-2.3	-1.2
S14	-0.7	-0.5	-0.3	1.2	-0.3	-0.5	0.4	-0.1
S15	-2.4	-4.1	-2.1	-3.3	-2.1	-4.1	-3.3	-3.1
S16	-1.8	-6.8	-4.9	-6.7	-1.1	-3.9	-6.7	-4.6
S17	-3.8	-5.4	-1.0	-4.8	-1.0	-5.4	-4.8	-3.7
S18	-6.0	-8.4	-3.9	-7.9	-3.7	-8.4	-7.9	-6.6
S19	-5.0	-4.5	-3.9	-5.3	-3.9	-3.1	-5.3	-4.4
S20	-3.0	-3.1	-1.7	-1.0	-2.7	-1.6	-2.6	-2.2
Avg	-2.8	-4.1	-2.8	-2.8	-2.4	-3.7	-3.9	-3.2
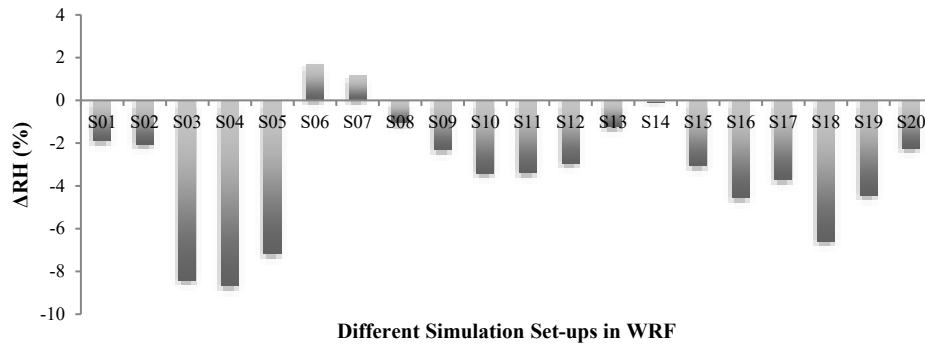
**Figure 4.14.** 2-m Relative humidity (%) differences (CTRL- ALBEDO) in different physical parameterizations
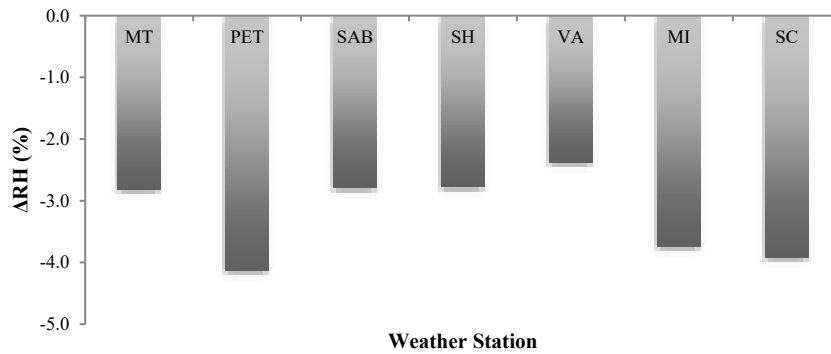
Figure 4.15. 2-m Relative humidity (%) (CTRL- ALBEDO) in weather station over the domain (McTavish (MT), Pierre Elliott Trudeau Intl (PET), St-Hubert (SH), Ste-Anne-de-Bellevue (SAB), VArennes (VA), MIrabel (MI), Ste-Clothide (SC))

4.2.4. Precipitation

The numerical weather prediction models cannot fully capture the hydrological cycles and the effects of clouds and water processes in the atmosphere. The assessment of the precipitation by WRF is in a cumulative form meaning that even when the hourly precipitation for 5-h event is 1.0, 0.0, 0.3, 0.0, 3.0, the model still gets this magnitude correct for the total daily and or total episode. The comparisons of precipitation can provide a qualitative assessment of the prediction of water cycle by these models' ensembles. The average MBA (Table 4.14) of all model ensembles are almost the same except the S02 with Betts-Miller-Janjic cumulus scheme which is 0 mm. It indicates that this cumulus model performs well in predicting precipitation using fine resolution grid size. In the urban area, MAE (Table 4.15) of the predicted precipitation by other model ensembles was almost the same. The MAE of all models is less than 3 mm. Table 4.16 and Figures

4.16 and 4.17 provide the calculated RMSE of the model ensemble in predicting the rainfall episode during the simulation period with different WRF settings.

Table 4.14. Mean Bias Error (MBE) in predicted precipitation (mm) with different WRF settings (McTavish (MT), Pierre Elliott Trudeau Intl (PET), St-Hubert (SH), Ste-Anne-de-Bellevue (SAB), VArennes (VA), MIrabel (MI), Ste-Clothide (SC))

MBA	MT	PET	SAB	SH	VA	MI	SC	Average
S01	-0.2	-0.3	-0.3	-0.3	-0.3	-0.3	-0.3	-0.3
S02	-0.3	-0.2	-0.2	1.5	-0.2	-0.2	-0.2	0.0
S03	-0.3	-0.3	-0.3	-0.3	-0.3	-0.3	-0.3	-0.3
S04	-0.3	-0.3	-0.3	-0.3	-0.3	-0.3	-0.3	-0.3
S05	-0.2	-0.3	-0.3	-0.2	-0.3	-0.3	-0.3	-0.3
S06	-0.2	-0.3	-0.3	-0.3	-0.3	-0.3	-0.3	-0.3
S07	-0.3	-0.3	-0.3	-0.3	-0.3	-0.3	-0.3	-0.3
S08	-0.2	-0.2	-0.2	-0.1	-0.2	-0.2	-0.1	-0.2
S09	-0.3	-0.3	-0.3	-0.3	-0.3	-0.3	-0.3	-0.3
S10	-0.2	-0.2	-0.3	-0.1	-0.2	-0.2	-0.1	-0.2
S11	-0.2	-0.2	-0.2	-0.1	-0.2	-0.2	-0.1	-0.2
S12	-0.2	-0.2	-0.2	-0.1	-0.2	-0.2	-0.1	-0.2
S13	-0.1	-0.3	-0.2	0.2	-0.2	-0.3	0.2	-0.1
S14	-0.2	-0.3	-0.2	0.1	0.0	-0.1	0.3	0.0
S15	-0.2	-0.3	-0.3	-0.3	-0.3	-0.3	-0.3	-0.3
S16	-0.2	-0.1	-0.1	-0.2	-0.1	-0.1	-0.2	-0.1
S17	-0.2	-0.2	-0.1	-0.1	-0.1	-0.2	-0.2	-0.2
S18	-0.2	-0.3	-0.3	-0.3	-0.2	-0.3	-0.2	-0.3
S19	-0.2	-0.2	-0.3	-0.2	-0.2	-0.2	-0.2	-0.2
S20	-0.2	-0.3	-0.3	-0.3	-0.3	-0.3	-0.3	-0.3
Avg	-0.2	-0.3	-0.2	-0.1	-0.2	-0.3	-0.2	-0.2

Note: The definitions of statistical measurements are as follows Zhang et al. (2006) [51]: $MBE = \frac{1}{N}\sum_{1}^{N}(C_M - C_O)$, C_M and C_O are modeled and observed concentrations, respectively and N is the total number of model and observation pairs.

Table 4.15. Mean Absolute Error (MAE) in predicted precipitation (mm) with different WRF settings (McTavish (MT), Pierre Elliott Trudeau Intl (PET), St-Hubert (SH), Ste-Anne-de-Bellevue (SAB), VArennes (VA), MIrabel (MI), Ste-Clothide (SC))

MAE	MT	PET	SAB	SH	VA	MI	SC	Average
S01	0.2	0.3	0.3	0.3	0.3	0.3	0.3	0.3
S02	0.3	0.2	0.2	0.0	0.2	0.2	0.2	0.2
S03	0.3	0.3	0.3	0.3	0.3	0.3	0.3	0.3
S04	0.3	0.3	0.3	0.3	0.3	0.3	0.3	0.3
S05	0.2	0.3	0.3	0.2	0.3	0.3	0.3	0.3
S06	0.2	0.3	0.3	0.3	0.3	0.3	0.3	0.3
S07	0.3	0.3	0.3	0.3	0.3	0.3	0.3	0.3
S08	0.2	0.2	0.2	0.1	0.2	0.2	0.1	0.2
S09	0.3	0.3	0.3	0.3	0.3	0.3	0.3	0.3
S10	0.2	0.2	0.3	0.1	0.2	0.2	0.1	0.2
S11	0.2	0.2	0.2	0.1	0.2	0.2	0.1	0.2
S12	0.2	0.2	0.2	0.1	0.2	0.2	0.1	0.2
S13	0.1	0.3	0.2	0.2	0.2	0.3	0.2	0.2
S14	0.2	0.3	0.2	0.1	0.2	0.1	0.3	0.2
S15	0.2	0.3	0.3	0.3	0.3	0.3	0.3	0.3
S16	0.2	0.1	0.1	0.2	0.1	0.1	0.2	0.2
S17	0.2	0.2	0.1	0.1	0.1	0.2	0.2	0.2
S18	0.2	0.3	0.3	0.3	0.2	0.3	0.2	0.3
S19	0.2	0.2	0.3	0.2	0.2	0.2	0.2	0.2
S20	0.2	0.3	0.3	0.3	0.3	0.3	0.3	0.3
Avg	0.2	0.3	0.2	0.2	0.2	0.3	0.2	0.2

Note: The definitions of statistical measurements are as follows Zhang et al. (2006) [51]: $MAE = \frac{1}{N}\sum_1^N |C_M - C_O|$ C_M and C_O are modeled and observed concentrations, respectively and N is the total number of model and observation pairs.

Table 4.16. Root Mean Square Error (RMSE) in predicted precipitation (mm) with different WRF settings (McTavish (MT), Pierre Elliott Trudeau Intl (PET), St-Hubert (SH), Ste-Anne-de-Bellevue (SAB), VArennes (VA), MIrabel (MI), Ste-Clothide (SC))

RMSE	MT	PET	SAB	SH	VA	MI	SC	Average
S01	1.4	2.0	1.8	1.7	1.7	2.0	1.8	1.8
S02	1.6	1.5	1.4	0.0	1.4	1.5	1.2	1.2
S03	1.7	2.0	1.8	1.8	1.9	2.0	1.9	1.9
S04	1.7	2.0	1.8	1.8	1.9	2.0	1.9	1.9
S05	1.5	1.8	1.6	1.1	1.9	1.7	1.9	1.6
S06	1.2	0.0	1.8	1.8	1.7	2.0	1.9	1.5
S07	2.0	1.8	1.8	2.0	1.7	2.0	1.9	1.9
S08	1.3	1.3	1.1	0.5	1.0	1.0	0.7	1.0
S09	1.7	2.0	1.8	1.8	1.7	1.7	1.9	1.8
S10	1.2	1.3	1.5	0.7	1.5	1.3	0.8	1.2
S11	1.3	1.3	1.1	0.5	1.0	1.3	0.7	1.0
S12	1.2	1.3	1.3	0.6	1.2	1.3	0.7	1.1
S13	0.8	1.9	1.3	1.0	1.2	2.0	1.0	1.3
S14	1.4	1.6	1.1	0.6	1.1	0.8	2.1	1.2
S15	1.4	2.0	1.8	1.8	1.7	2.0	1.9	1.8
S16	1.4	0.9	0.9	1.2	0.7	0.9	1.3	1.1
S17	1.4	1.1	0.9	0.9	0.9	1.1	1.1	1.0
S18	1.4	2.0	1.8	1.8	1.4	2.0	1.4	1.7
S19	1.4	1.3	1.5	1.1	1.5	1.4	1.2	1.4
S20	1.4	2.0	1.8	1.8	1.7	2.0	1.9	1.8
Avg	1.4	1.5	1.5	1.2	1.5	1.6	1.5	1.5

Note: The definitions of statistical measurements are as follows Zhang et al. (2006) [51]: RMSE $= \left[\frac{1}{N}\sum_1^N(C_M - C_O)^2\right]^{1/2}$ C_M and C_O are modeled and observed concentrations, respectively and N is the total number of model and observation pairs.
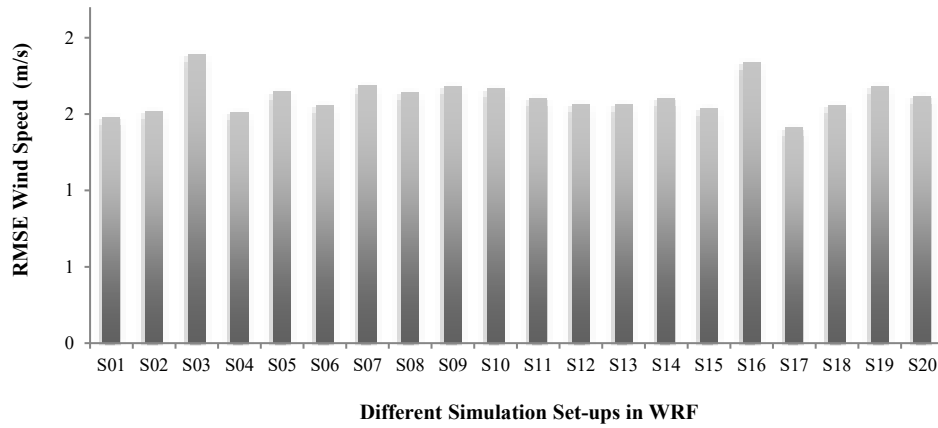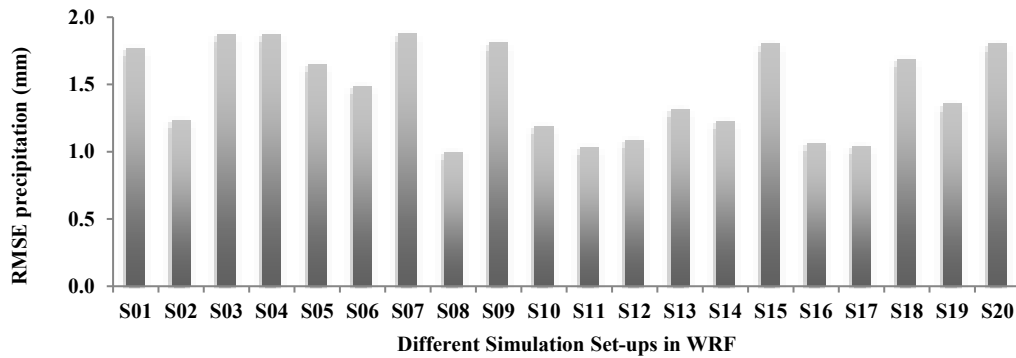
Figure 4.16. Root mean square error in predicted precipitation (mm) with different WRF setting
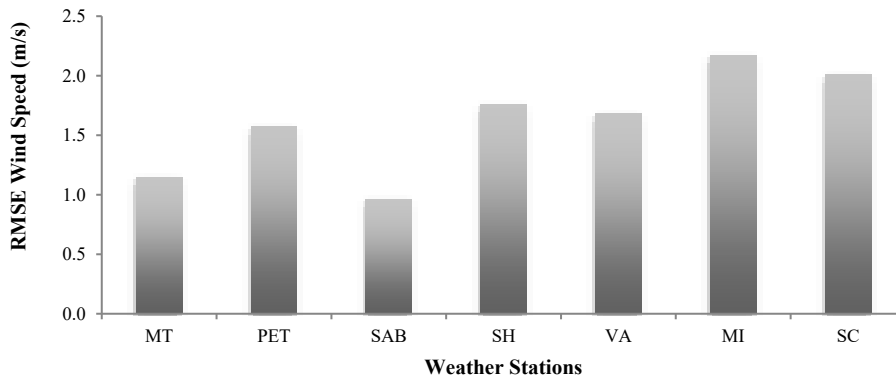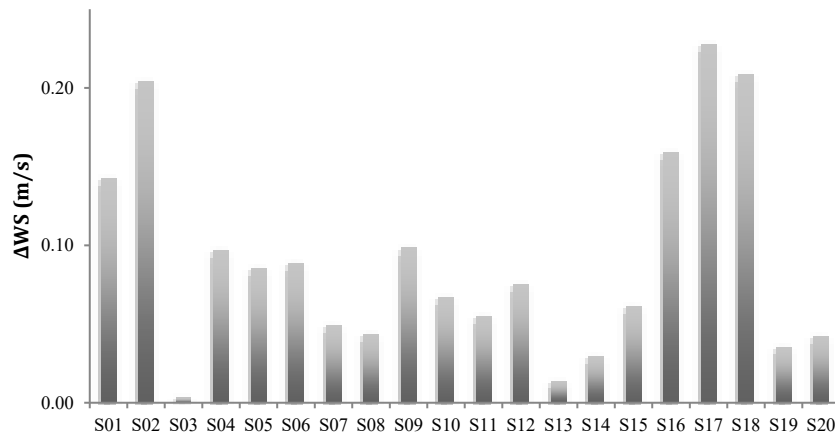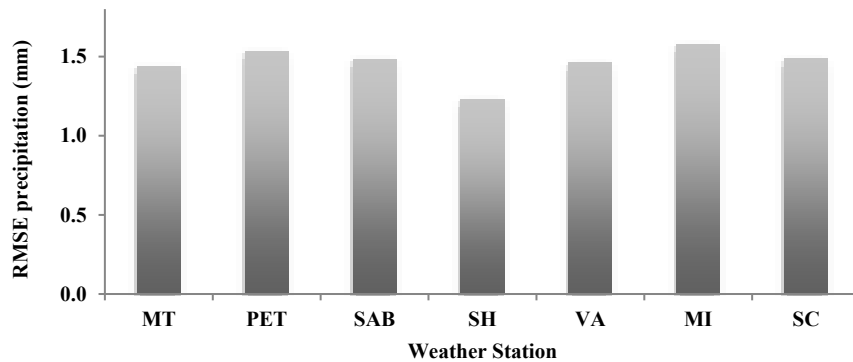

Figure 4.17. Root mean square error in predicted precipitation (mm) in weather station over the domain (McTavish (MT), Pierre Elliott Trudeau Intl (PET), St-Hubert (SH), Ste-Anne-de-Bellevue (SAB), VArennes (VA), MIrabel (MI), Ste-Clothide (SC))

The precipitation differences between CTRL and ALBEDO scenario are presented in Table 4.17 and Figure 4.18. In general, an increase of albedo reduces the absorption of solar radiation and the transfer of sensible and latent heat into the atmosphere. The convective clouds reduce the downward flux of long wave radiation and thus the net absorption of radiation is decreased. Therefore, an increase in albedo leads to a net decrease of radiative flux into the ground and a net decrease of convective cloud and precipitation. But, in these simulations, the results show a slight increase in precipitation in S02, S06, and S08 and not a significant change in S11, S12, S13 and S14, and a decrease in other model ensembles. In general precipitation decreases as 0.2 mm if the surface reflectivity of roofs, walls and grounds increases. Figure 4.19 shows the precipitation differences between CTRL and ALBEDO for different weather stations over the domain.

Table 4.17. Precipitation (mm) differences between CTRL & ALBEDO scenarios (McTavish (MT), Pierre Elliott Trudeau Intl (PET), St-Hubert (SH), Ste-Anne-de-Bellevue (SAB), VArennes (VA), MIrabel (MI), Ste-Clothide (SC))

ΔRain	MT	PET	SAB	SH	VA	MI	SC	Average
S01	0.5	-0.1	0.0	-2.0	-0.3	-0.1	-1.0	-0.5
S02	-0.4	-0.1	0.3	0.0	0.3	-0.1	0.5	0.1
S03	-0.5	-0.5	-0.6	-0.6	-0.3	-0.5	-0.5	-0.5
S04	-0.4	-0.6	-0.4	-1.3	-0.3	-0.4	-0.4	-0.5
S05	-1.1	0.1	-0.2	-0.5	0.1	0.1	-0.6	-0.3
S06	2.2	0.5	-0.5	-0.4	-0.2	-0.1	-0.2	0.2
S07	-0.8	-0.8	-0.8	-0.9	-1.1	-0.7	-0.7	-0.8
S08	-0.4	1.3	1.8	1.7	0.1	0.5	-0.5	0.6
S09	-0.5	-0.9	-0.9	-0.5	-0.4	-0.6	-1.2	-0.7
S10	-0.2	-1.7	-1.5	0.6	-1.8	0.4	-0.3	-0.7
S11	0.1	0.1	2.5	-3.0	-0.1	0.1	0.4	0.0
S12	-0.7	0.5	-0.6	-0.8	0.3	1.5	0.0	0.0
S13	0.0	-0.1	0.1	-0.9	1.0	-0.2	0.0	0.0
S14	-0.2	-2.2	0.4	1.8	1.4	-0.2	-0.7	0.0
S15	0.2	-0.4	-0.3	-0.3	-0.2	-0.4	-0.3	-0.2
S16	-0.2	-1.1	-0.9	-0.2	-0.9	-1.1	-0.7	-0.7
S17	-0.9	-0.1	2.3	-1.4	1.9	-0.1	0.1	0.3
S18	-0.2	-0.4	-0.6	-0.3	-0.2	-0.2	-0.2	-0.3
S19	0.1	0.1	-1.4	-0.7	-1.0	0.1	-0.1	-0.4
S20	-0.2	-0.2	-0.2	-0.4	-0.6	-0.2	-0.6	-0.4
Avg	-0.2	-0.3	-0.1	-0.5	-0.1	-0.1	-0.3	-0.2
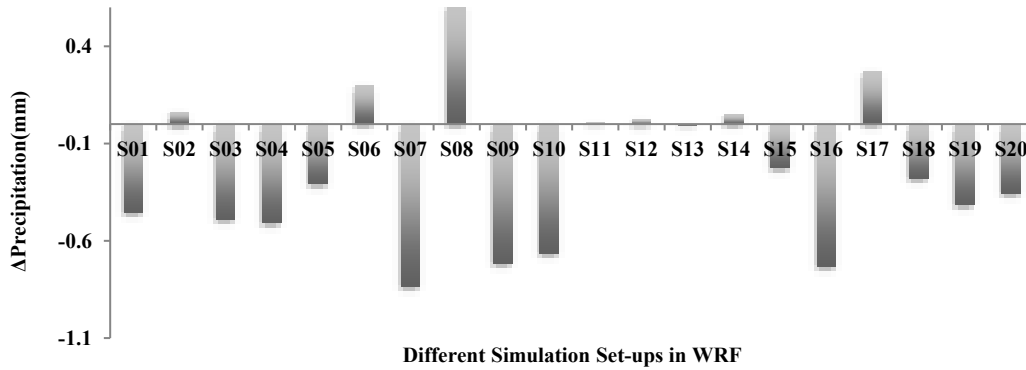
Figure 4.18. Precipitation (mm) differences (CTRL- ALBEDO) with different physical parameterizations
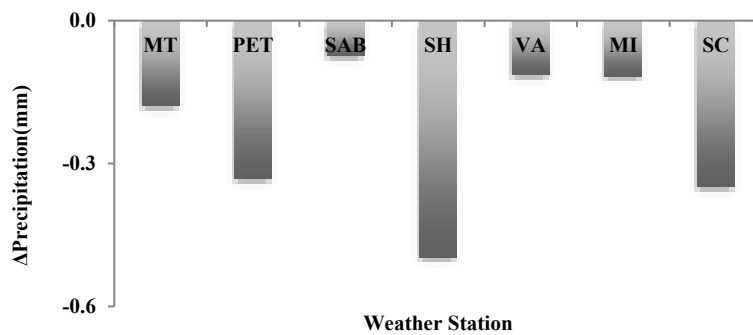
Figure 4.19. Precipitation (mm) differences (CTRL- ALBEDO) in weather stations over the domain (McTavish (MT), Pierre Elliott Trudeau Intl (PET), St-Hubert (SH), Ste-Anne-de-Bellevue (SAB), VArennes (VA), MIrabel (MI), Ste-Clothide (SC))

4.3. Discussion and Conclusion of Physical Parameterizations in WRF and Effects of Increasing Surface Reflectivity

A sensitivity analysis of physical parametrizations in WRF are conducted (for a total of 20 model ensembles) to evaluate their performance on predicting urban climate (2-m air temperature, 10-m wind speed, 2-m relative humidity, and precipitation). A period of three days in August (09-Aug-2009 to 11-Aug-2009) is selected. The simulation starts from a sunny day and ends with a rainy condition. Four domains are telescopically nested to cover the Greater Montreal Area with the resolution of 333 m. The hourly data of the aforementioned parameters are estimated. This specific time frame shows the close combination of sunny and rainy conditions over the interested domain. To see the results of choice of parameterizations change under different weather patterns, more simulations need to be carried out during sunny, rainy and very warm episodes to indicate the choice of parameterizations. However, the results from these simulations are episode-specific

and might not be transferrable to other locations and conditions. The anthropogenic heat emission estimation needs to be available to achieve more accurate and reliable results in the future.

The S06 simulation setup (Table 4.1) shows the reasonable results compared with measurements. The combination of WDM6 (Lim and Hong, 2010), Grell 3D (Grell, 1993; Grell and Devenyi, 2002), MYJ (Janjic, 1994), and RRTMG (Iacono et al., 2008) as microphysics, cumulus, planetary boundary layer, and radiation schemes, respectively, resulted in the least error in 2-m air temperature (RMSE = 1.9 $^{\circ}$C) compared to the measurements (Table 4.4 and Figure 4.2). The combination of S01 and S20 that used the same microphysics, planetary boundary layer height and radiation provides the least error comparing to other model ensembles, as well. The comparisons of wind speed indicated that S06 results are close to S02, S04 and S17. But these models could not predict the 2-m air temperature as accurately as S06. The relative humidity results indicated that S06 has the least error compared to measurements except in the S01 simulation. The reason is that the S01 uses the Simplified Arakawa-Schubert scheme for cumulus modelling and thus predicts the rainy condition better. But this scheme cannot accurately predict the T2 on a sunny day (Table 4.12 and Figure 4.11). The precipitation results are better in S08, S11, S16 and S17 compared to S06, but again, these simulation setups cannot predict the T2 and WS accurately (Table 4.16 and Figure 4.15). Since the prediction of T2 is more important in terms of heat island mitigation strategy, the S06 model ensemble is selected. The other reason for S06 selection is its computational time, which is 10% less compared to other simulation setups. The result of model performance in terms of T2 (S06) is compared with other studies with different physical parametrizations (Table 4.18). The results of T2 in estimates of S06 simulation setup are in good agreement with other studies, considering different episodes and periods of simulations (rainy conditions for this study).

Table 4.18. Comparisons of 2-m air temperature results of S06 with other studies with different physical parameterizations

Study	Microphysics	Cumulus	PBL	Radiation	T2 evaluation results
S06 (the present study), rainy episode in GMA, 2009	WDM6	Grell 3D	MYI	RRTMG	RMSE= 1.9
Fallmann et al., 2014 Stuttgart, heat wave 2003	WSM06	Kain-Fritch	MYJ	Shortwave: Goddard Longwave: RRTM	R2 = 0.71
Salamanca et al., 2012, Madrid, two separate hottest day in summer 2008	WSM03	_	MYJ	Shortwave: Dudhia Longwave: RRTM	RMSE = 1.5
Vahmani & Ban-Weiss. 2016, LA, 6-11 July 2012	Lin	Kain-Fritch	YSU	Shortwave: Dudhia Longwave: RRTM	RMSE = 3.8

| Chen et al., 2013, Hangzhou, China, July 2009 | WSM06 | Betts–Miller–Janjic | YSU | Shortwave: Dudhia Longwave: RRTM | RMSE = 1.61 |

YSU: Yonsei University scheme; WDM06: WRF Double-Moment 6-class; WSM06: WRF Single-Moment 6-class; MYJ: Mellor-Yamada-Janjic; RMSE: Root Mean Square Error; RRTMG: Rapid Radiative Transfer Model

All models on average slightly underestimate the meteorological parameters. One of the main reasons is that the WRF cannot estimate the anthropogenic heat emissions. Human activities are the main source of heat emission in urban areas—for example, the use of transportation and air conditioning in summer time. Another important issue is the possible impact of other micro-scale effects that are not captured by the model resolution. The exact characteristics, height and direction of buildings cannot be simulated in the model, while these parameters affect the results of measurements in weather stations.

As the surface reflectivity of roofs, walls and roads increased, the results indicated that the averaged 2-m air temperature decreased by 0.2 °C, the 10-m wind speed slightly increased, the relative humidity decreased by an average of 3.2%, and the precipitation decreased by 0.2 mm. However, the results from these simulations are episode-specific and might not be transmissible to other locations and conditions. The anthropogenic heat emission estimation needs to be available to achieve more accurate and reliable results in the future.

4.4. Applications of the Developed Platform for Urban Climate Simulation and Heat Island Mitigation Strategy

The developed model is an appropriate platform for urban climate simulations. This meteorological platform (with proper physical options for microphysics, cumulus, PBL and radiation models) enable environmental policymakers to have a better understanding of the effects of heat island and mitigations strategies on urban areas in cold climates. This platform is verified by comparing the simulation results with measurements and thus further is applied to perform other objectives. The same physical parameterizations and simulation approach is used to assess the effects of heat island and increasing surface reflectivity on heat-related mortality in the Greater Montreal Area during the 2005 and 2011 heat wave periods. The results of this study are presented in Chapter 5. In addition, the developed platform provides a good understanding of each physical parametrization in WRF and their impacts on meteorological parameters in a cold climate.

Chapter 5
Effects of Increasing Surface Reflectivity on Heat-Related Mortality

Heat-related mortality is increasing as a result of climate change and extreme heat events. Climate change can exacerbate extreme heat events and the duration of high temperatures (IPCC, 2014). High temperature intensity and duration cause an increase in morbidity and mortality. According to the Canadian Environmental Health Atlas (CEHA 2018), 121 people die every year in Montreal because of heat-related issues. In another study, the number of heat-related deaths was estimated to be 209 people during the July 2010 heat wave period in Montreal (Bustinza et al., 2013). Increasing surface reflectivity is applied to mitigate the effects of heat island and high temperature in urban areas. ISR decreases heat-related mortality by 3 to 16% in different locations (Kalkstein and Sheridan, 2003; Kalkstein et al., 2011 and 2013). In addition, increasing surface albedo can shift days to less oppressive air mass conditions by 50% (Kalkstein et al., 2011 and 2013), and thus provide a more pleasant environment for urban dwellers.

The Weather Research and Forecasting model (WRF) is coupled with a multi-layer of the Urban Canopy Model (ML-UCM) to investigate the effects of urban heat island intensity during the 2005 and 2011 heat wave periods in the Greater Montreal Area (GMA), Canada. Each day of simulation is categorized into an air mass type using the Spatial Synoptic Classification (SSC). The non-accidental mortality data during the summer period is employed and the number of deaths above the expected mean anomalous daily mortality is calculated for each air mass classification. Results indicate that moist tropical plus (hotter and more humid conditions than the moist tropical) and dry tropical (the hottest and driest conditions) weather have the highest rank in heat-related deaths. The effects of increasing surface reflectivity (ISR) is assessed using four meteorological parameters: 2-m air temperature (T2), 10-m wind speed (WS10), 2-m relative humidity (RH2), and dew point temperature (DPT), and four heat stress indices: National Weather Service – Heat Index (NWS-HI), Apparent Temperature (AT), Canadian Humid Index (CHI), and Discomfort Index (DI).

The meteorological parameters of the CTRL scenario (where the albedo of roofs, walls, and roads are assumed to be 0.2) are compared with the measurements obtained from urban (McTavish (MT) and Pierre Elliott Trudeau Intl (PET)) and rural (Montreal/St-Hubert (SH) and Ste-Anne-de-Bellevue (SAB)) weather stations across the domain. A set of metrics calculations are applied to evaluate model performance (mean bias error (MBE), mean absolute error (MAE) and root mean square error (RMSE)). In the ALBEDO scenario, the albedo of roofs, walls, and roads are increased from 0.2 to 0.65, 0.60, and 0.45, respectively. The effects of ISR are investigated on urban climate, heat stress indices and heat-related mortality by comparing the CTRL and ALBEDO results.

Air mass type, air temperature and apparent temperature changes for each day are applied to translate the effects of extreme heat events and the potential of increasing surface reflectivity on heat-related mortality during the 2005 and 2011 heat wave periods. The daily heat-related mortality (HRM) is estimated for two air mass classifications in the GMA: DT (dry tropical) and MT/MT+ (moist tropical and moist tropical plus). The algorithms to estimate heat-related mortality are explained in detail in Chapter 3, Section 3.3. Here, the results of this study are presented. The research addressed in this chapter is summarized in the article by Z. Jandaghian and H. Akbari (2018), *"The effects of increasing surface reflectivity on heat-related mortality in the Greater Montreal Area, Canada"* (https://doi.org/10.1016/j.uclim.2018.06.002).

5.1. Defining Simulation Domain and Period

The simulation domain is Greater Montreal Area. Figure 5.1 shows the simulation domain and land use, land cover. The simulations are conducted during the 2005 (10th -12th July) and the 2011 (20th – 23rd July) heat wave events.
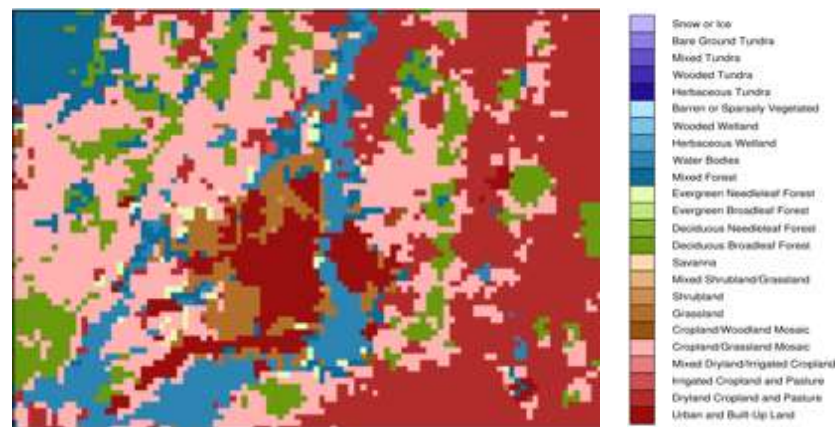
Figure 5.1. Simulation domain and Land Use Land Cover (LULC) of GMA

The simulations were conducted with the initial and boundary conditions obtained from the North American Regional Reanalysis (NARR). A vertical resolution of 51eta level is defined to take full advantages of the urban parameterizations. The proper physical parameterizations of the previous task (1st objective) is used to simulate the CTRL and ALBEDO cases of the 2005 and 2011 heat wave period over Greater Montreal Area.

5.2. Evaluation of Meteorological Model Performance

To evaluate the simulations performances, the meteorological parameters namely: 2-m air temperature (T2), 10-m wind speed (WS10), relative humidity (RH), and dew point temperature (DPT) are collected from four weather stations (McTavish (MT), Pierre Elliott Trudeau Intl (PET), St-Hubert (SH), Ste-Anne-de-Bellevue (SAB)) across the Greater Montreal Area for two heat wave period in 2005 and 2011. Table 3.3 presents their geographical locations.

The parameters that are directly extracted from the simulation results are the 2-m air temperature (T2, K), dew point temperature (DPT, K), horizontal and vertical wind speed (U10, V10, m/s), and water mixing ratio (Q2, %). Other parameters are calculated as presented in Table 3.10 namely 10-m wind speed (WS10), 2-m relative humidity (RH2), and 3 heat stress indices: apparent temperature (AT), Canadian Humid Index (CHI), and Discomfort Index (DI). The parameters that are analysed for the two heat wave periods are T2, WS10, RH2, DPT, AP, CHI, DI, and the National Weather Service – Heat Index (NWS-HI). The NWS-HI is a measurement to show how hot it feels when RH2 is factored in with the actual T2.

Table 5.1 presents the maximum air temperature measured in weather stations for the 2005 and 2011 heat wave periods during three consecutive days in July. The hourly data obtained from weather stations are compared with the hourly simulated values for CTRL case simulations. Table 5.2 presents the MBE, MAE and RSME of aforementioned parameters. Figure 5.2, Figure 5.3, Figure 5.4, Figure 5.6 respectively show comparisons between simulated averaged 3-day cycle and observed 2-m air temperature, 10-m wind speed, and dew point temperature in four weather stations and 2-m relative humidity for urban and rural areas.

The model, on average, slightly overestimates the air temperature, wind speed and dew point temperature in the 2005 simulation. The model slightly underestimates the air temperature and wind speed in the 2011 simulation. One of the reasons is that the effects of micro scale parameters

cannot be captured in mesoscale models precisely. The heat emission from buildings and the transportation sectors cannot be estimated in the model solver. The relative humidity at the 2-m height is estimated based on a calculation from National Oceanic and Atmospheric Administration (NOAA) weather services and is addressed in Chapter 3. The measurements of heat stress indices are also presented in Chapter 3. In other studies, the comparison of thermal components of WRF and the Fifth-Generation NCAR/Penn State Mesoscale Model (MM5) indicated that both models have the MBE of T2 as almost -3.8°C to 0.2°C during a year (Gilliam et al., 2006; Wu et al., 2008; Wang et al., 2009; Liu et al., 2010). Thus, the performance of WRF is generally consistent with the measurements and the results are well reliable for further investigations.

Table 5.1. Max air temperature measured in four weather stations over GMA in 2005 and 2011 heat wave periods (McTavish (MT), Pierre Elliott Trudeau Intl (PET), St-Hubert (SH), Ste-Anne-de-Bellevue (SAB))

Heat wave periods	July 2005	Max Temperature (°C)			
		MT	PET	SH	SAB
July 2005	10th	31.6	31.5	311	30.8
	11th	32.3	32.8	31.5	32.2
	12th	30.6	30.6	30.7	30.3
	July Average T (°C)	**26.9**	**27.3**	**27.0**	**27.1**
July 2011	21th	34.9	35.6	36.0	34.7
	22nd	31.3	31.9	32.6	32.2
	23rd	31.6	32.6	32.6	31.9
	July Average T (°C)	**28.3**	**28.5**	**29.0**	**28.5**

Table 5.2. MBE (Mean Bia Error), MAE (Mean Absolute Error), and RSME (Root Mean Square Error) of 2-m air temperature (ºC), 10-m wind speed (km/h) and dew point temperature (ºC) simulation results in CTRL case vs. measurements obtained from weather stations over the domain in 2005 and 2011
(McTavish (MT), Pierre Elliott Trudeau Intl (PET), St-Hubert (SH), Ste-Anne-de-Bellevue (SAB))

Station Code	2-m air temperature (ºC) in 2005			2-m air temperature (ºC) in 2011		
	MBE	MAE	RMSE	MBE	MAE	RMSE
MT	0.08	1.50	1.76	0.07	1.51	1.91
PET	-0.62	1.20	1.44	-0.88	1.37	1.83
SH	0.02	1.19	1.50	-0.94	1.30	1.70
SAB	1.07	1.28	1.65	0.03	1.10	1.47
Average	0.12	1.25	1.53	-0.43	1.32	1.73
Station Code	10-m wind speed (m/s) in 2005			10-m wind speed (m/s) in 2011		
	MBE	MAE	RMSE	MBE	MAE	RMSE
MT	1.66	1.82	2.30	-0.61	0.85	0.91
PET	-0.63	1.88	2.11	-2.17	2.25	2.40
SH	-0.13	2.38	2.21	-2.83	3.11	2.11
SAB	0.54	1.88	2.11	-0.33	1.25	2.81
Average	0.36	1.99	2.18	-0.93	1.86	2.05
Station Code	dew point temperature (ºC) in 2005			dew point temperature (ºC) in 2011		
	MBE	MAE	RMSE	MBE	MAE	RMSE
MT	0.82	0.83	0.90	0.52	0.58	0.71
PET	0.33	0.55	0.61	0.71	0.74	0.91
SH	-0.19	0.51	0.61	0.47	0.48	0.61
SAB	-0.16	0.38	0.52	0.93	0.93	1.01
Average	0.21	0.56	0.44	0.65	0.68	0.81

Note: The definitions of statistical measurements are as follows Zhang et al. (2006) [51]: $MBE = \frac{1}{N}\sum_1^N(C_M - C_O)$, $MAE = \frac{1}{N}\sum_1^N|C_M - C_O|$, $RMSE = \left[\frac{1}{N}\sum_1^N(C_M - C_O)^2\right]^{1/2}$, C_M and C_O are modeled and observed concentrations, respectively and N is the total number of model and observation pairs.
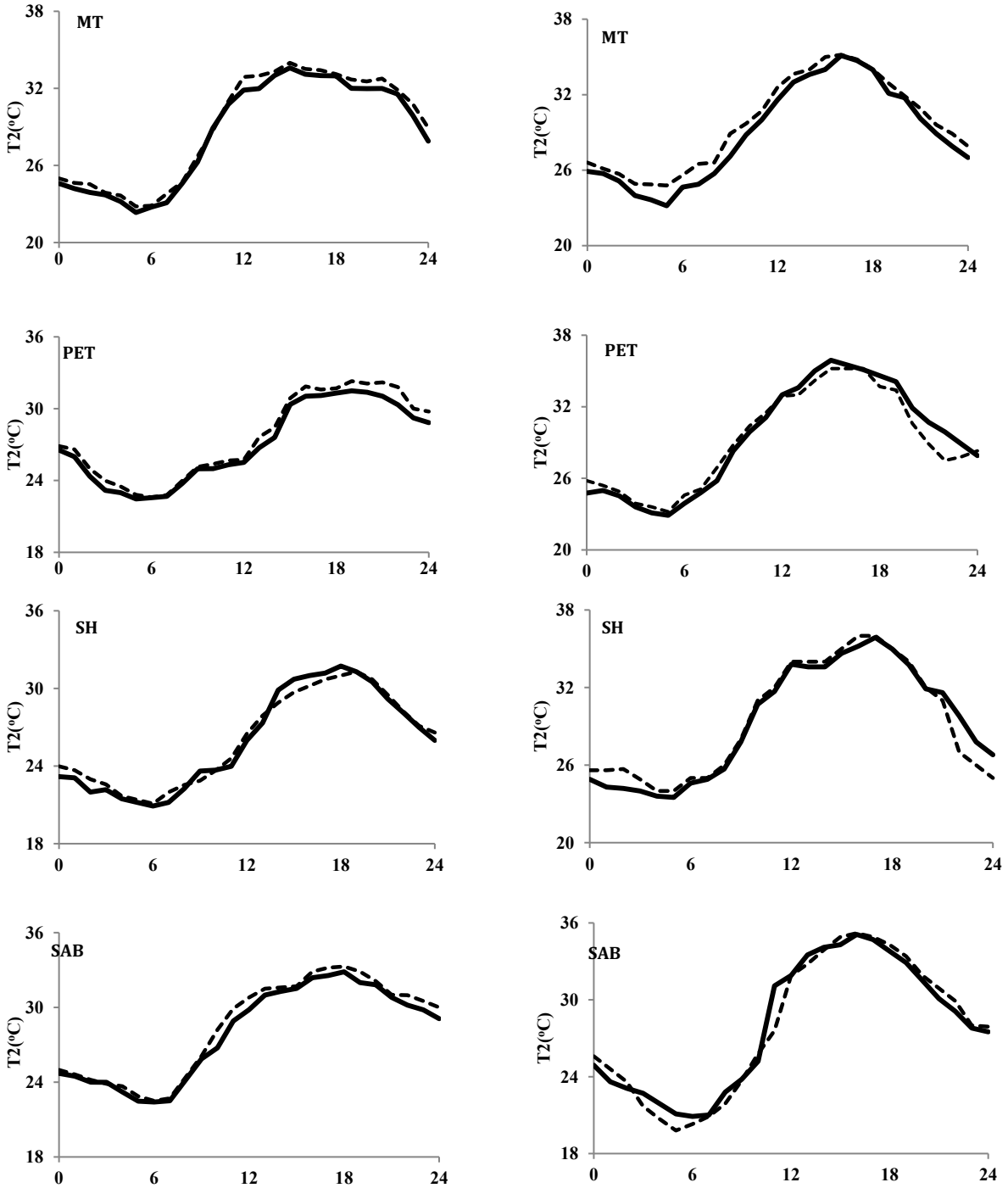
Figure 5.2. Simulated averaged 3-day cycle of 2-m air temperature (ºC) in CTRL [solid line] vs. measurements [dashed line] from four weather stations over GAM during 2005 [left] and 2011 [right] heat wave periods (McTavish (MT), Pierre Elliott Trudeau Intl (PET), St-Hubert (SH), Ste-Anne-de-Bellevue (SAB))
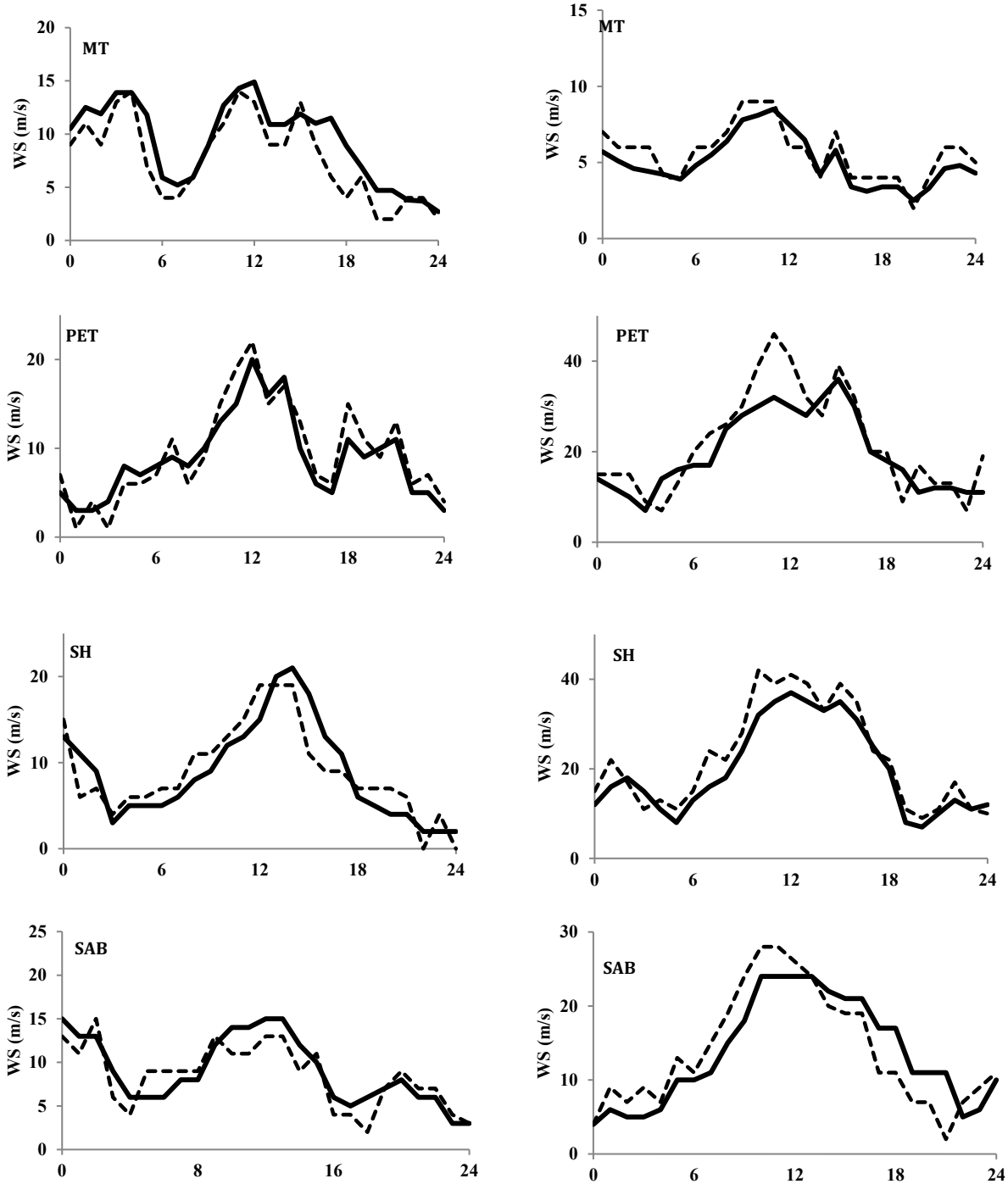
Figure 5.3. Simulated averaged 3-day cycle of 10-m wind speed (m/s) in CTRL [solid line] vs. measurements [dashed line] from four weather stations over GAM during 2005 [left] and 2011 [right] heat wave periods (McTavish (MT), Pierre Elliott Trudeau Intl (PET), St-Hubert (SH), Ste-Anne-de-Bellevue (SAB))

103
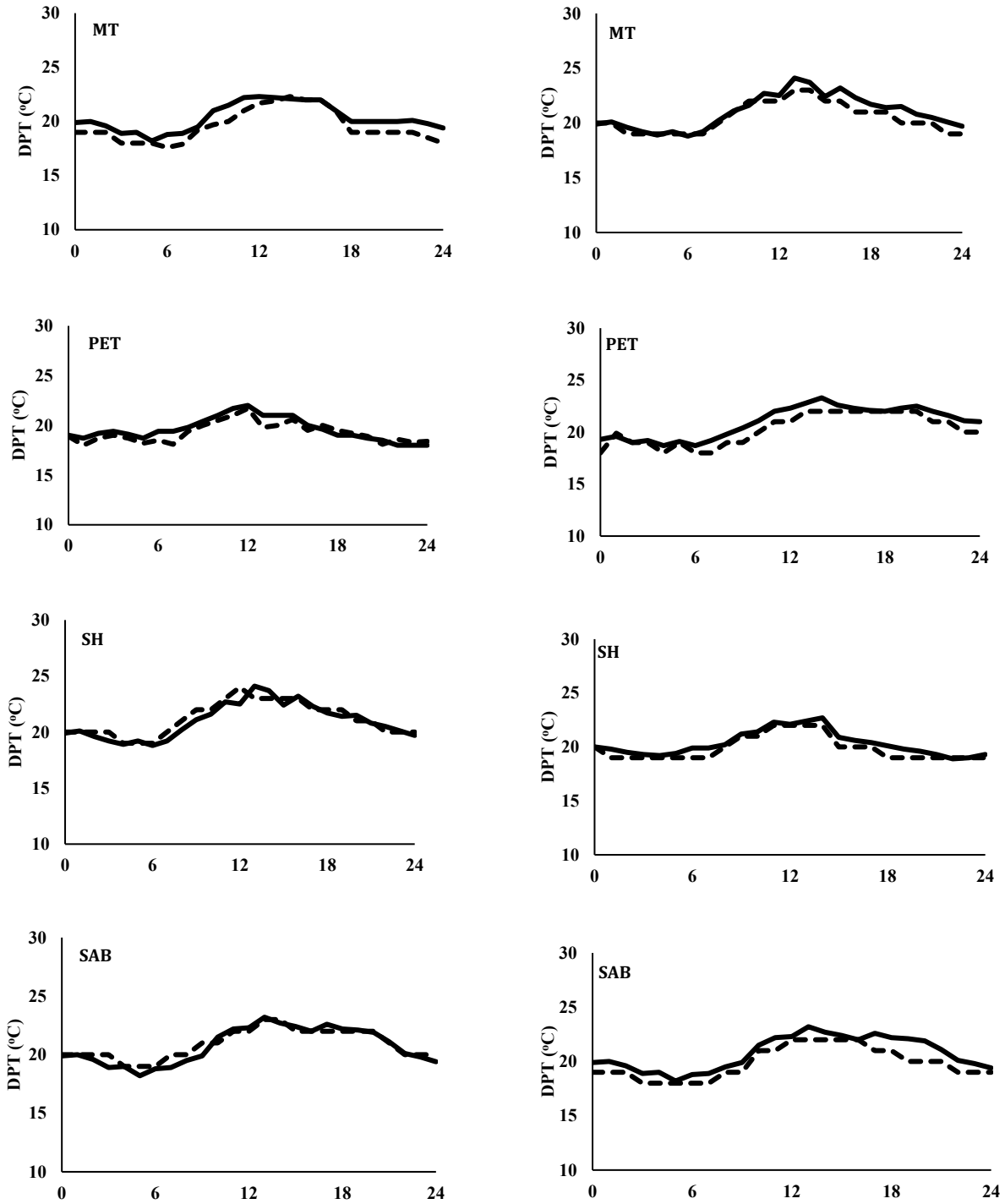
Figure 5.4. Simulated averaged 3-day cycle of dew point temperature (ºC) in CTRL [solid line] vs. measurements [dashed line] from four weather stations over GAM during 2005 [left] and 2011 [right] heat wave periods (McTavish (MT), Pierre Elliott Trudeau Intl (PET), St-Hubert (SH), Ste-Anne-de-Bellevue (SAB))
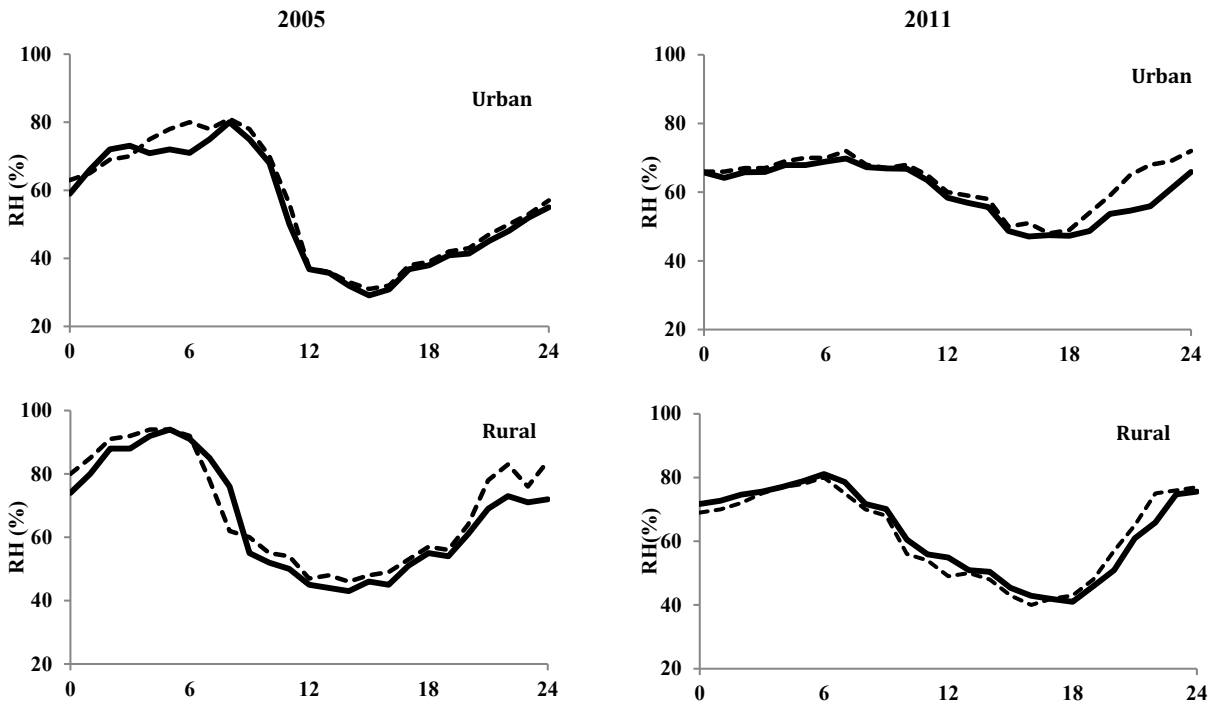
Figure 5.5. Simulated averaged 3-day cycle of 2-m relative humidity (%) in CTRL [solid line] vs. measurements [dashed line] in urban and rural areas over GAM during 2005 [left] and 2011 [right] heat wave periods

5.3. Effects of Increasing Surface Reflectivity on Meteorological Parameters and Heat Stress Indices

Table 5.3 presents the daily averaged 2-m air temperature, 10-m wind speed, 2-m relative humidity and dew point temperature differences between CTRL and ALBEDO scenarios. By increasing surface reflectivity, the daily averaged 2-m air temperature decreased by 0.8°C in urban areas (MT and PET) and by 0.4°C in rural areas (SH and SAB). The simulation results indicate that the T2 reduces less at 12 p.m. compared to 6 p.m. because of the thermal inertia that is absorbed by the ground surface during sunlight and then released at sunset and thus added up to the air temperature in the evening. The averaged 10-m wind speed differences between CTRL and ALBEDO scenarios indicate that an increase in surface albedo causes a slight increase in wind speed in some parts of the domain and a decrease in others. The increase in wind assists the decrease in air temperature in those areas. The averaged 2-m relative humidity differences between these scenarios show a slight increase in relative humidity. The relative humidity increases less in rural areas compared to the urban areas because of more vegetation in rural parts. Figure 5.6 shows the daily (3-day) averaged 2-m air temperature, 10-m wind speed, 2-m relative humidity and dew point

105

temperature differences between CTRL and ALBEDO scenarios during these two heat wave periods. Spatially averaged values for urban and rural areas are shown with solid and dashed lines, respectively.

Figure 5.7 shows the daily averaged discomfort index (DI) and apparent temperature (AT) for CTRL and ALBEDO scenarios. The results indicate that an increase in surface albedo causes a decrease in apparent temperature and discomfort indices that makes the environment more preferable and suitable for human beings during summer time. Thus, it reduces the risk of heat-related morbidity and mortality. Two indicators are applied (2-m air temperature and 2-m relative humidity) that are also extracted from ALBEDO simulation results in these estimations. Because of albedo enhancement, the DI improved by nearly 3% and 1.7% in urban and rural areas. The AT decreased by nearly 2.6°C and 1.8°C in urban and rural areas, respectively (Figure 5.8). In general, the urban diurnal range of heat indices (HI) is higher than the rural ones; thus, the consequences of increasing surface reflectivity in urban areas are more measurable.
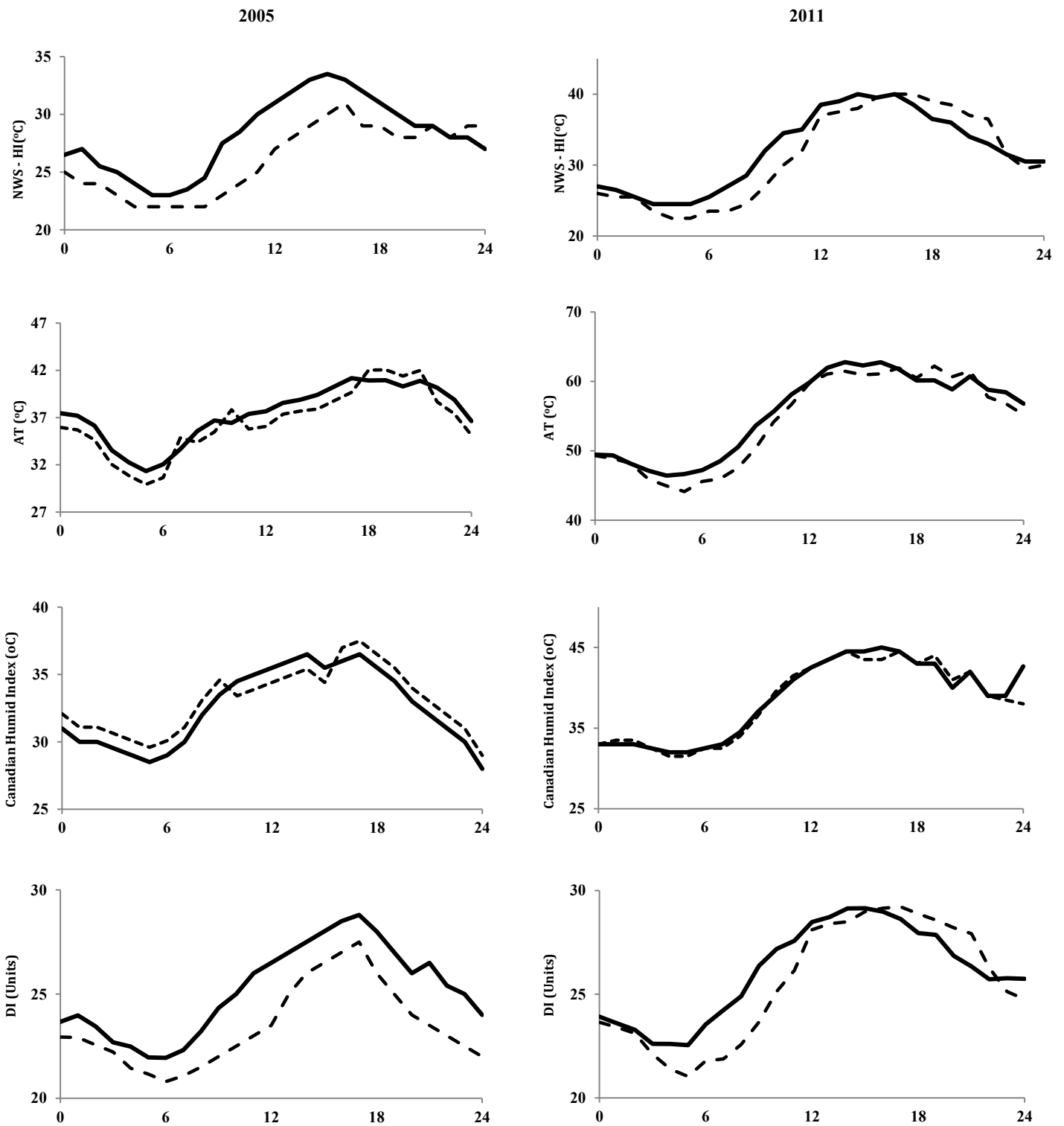
Figure 5.6. Simulated averaged diurnal (3-day) cycle of National Weather Service – Heat Index (°C), Apparent Temperature (°C), Canadian Humid Index (°C), Discomfort Index (Units) in CTRL scenarios in 2011 [left] and 2005 [right] shown in urban areas [solid line] and rural areas [dashed line]

Table 5.3. Averaged 3-day differences of 2-m air temperature (ºC), 10-m wind speed (m/s), dew point temperature (ºC), and 2-m relative humidity (%) between CTRL and ALBEDO scenarios in GAM during 2005 and 2011 heat wave periods

CTRL-ALBEDO	Heat-wave	MT	PET	SH	SAB
ΔT2 (ºC)	2005	0.7	0. 5	0.2	0.7
	2011	0.8	0.7	0.2	0.6
ΔWS$_{10}$ (m/s)	2005	0.2	-0.05	-0.01	0.01
	2011	0.3	-0.09	-0.02	0.01
ΔDPT (ºC)	2005	-0.19	-0.27	-0.18	-0.25
	2011	-0.28	-0.38	-0.13	-0.29
ΔRH$_2$ (%)	2005	-0.4	-0.2	-0.09	-0.13
	2011	-0.3	-0.4	-0.17	-0.11
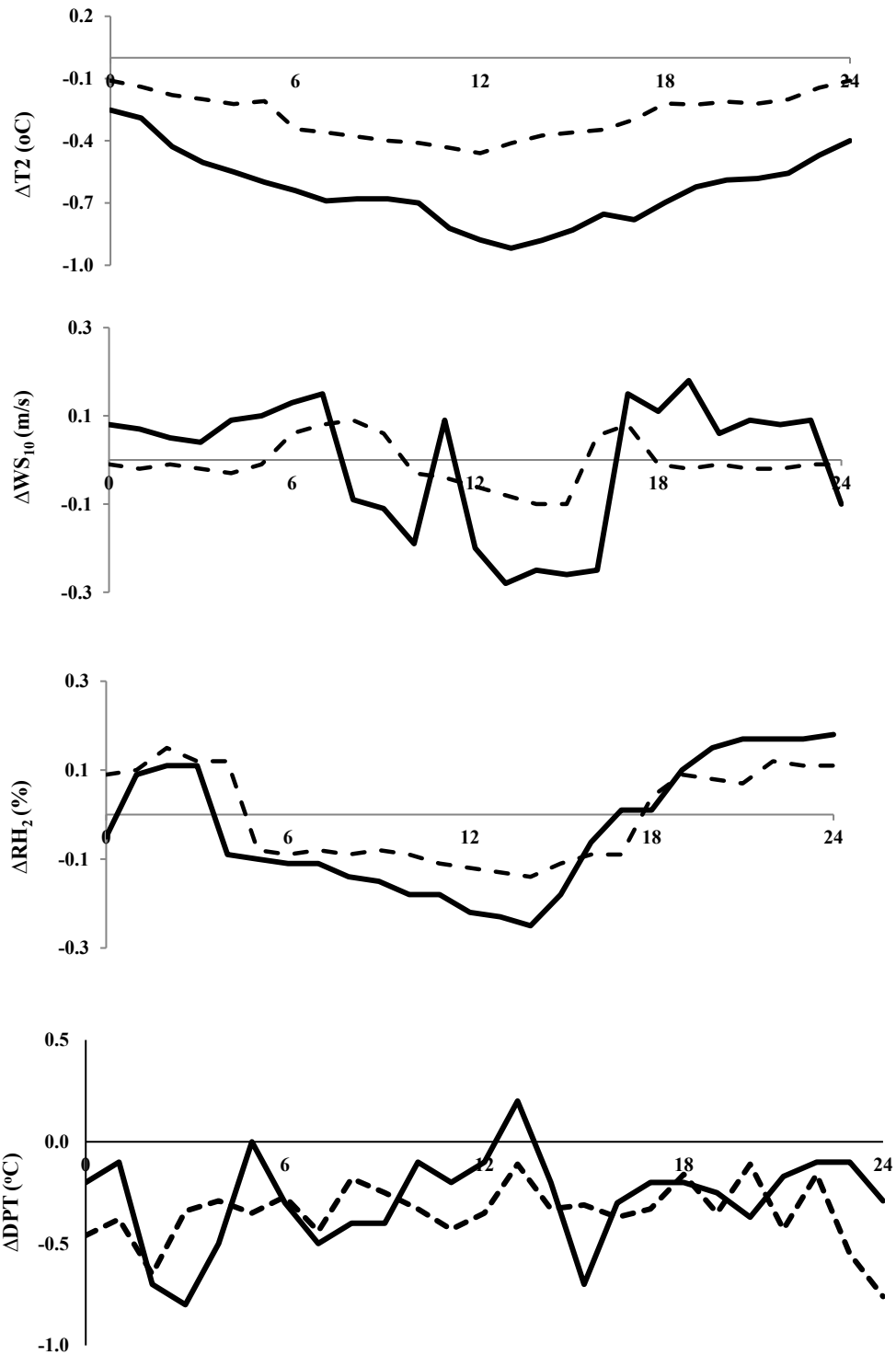
Figure 5.7. Daily averaged 2-m air temperature (°C), 10-m wind speed (km/s), dew point temperature (°C), and 2-m relative humidity (%) and differences between CTRL and ALBEDO in GAM during 2005 & 2011 heat wave period. Spatially averaged values for urban (solid line) and rural (dashed line) areas are shown with solid and dashed line, respectively.

109
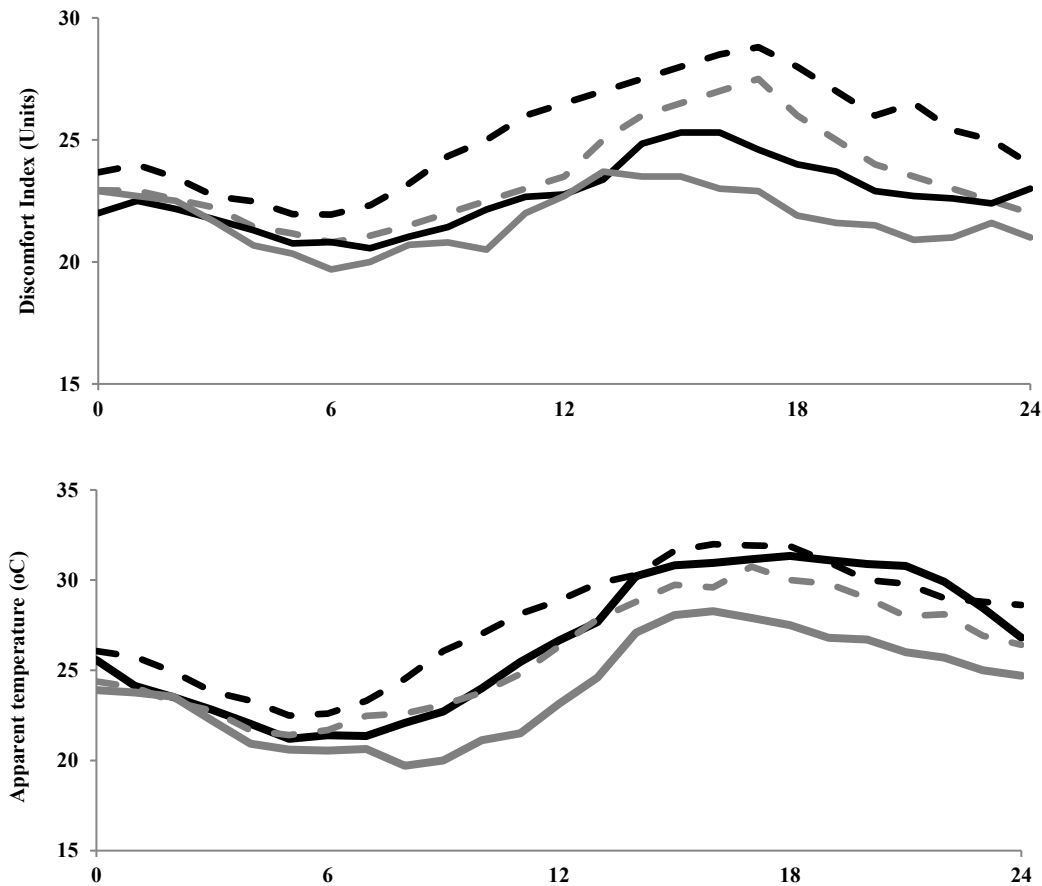
Figure 5.8. Daily averaged discomfort index (Units) and apparent temperature (ºC) shown in CTRL [dashed line] and ALBEDO [solid line] scenarios during 2005 & 2011 heat wave period

5.4. Reduction in Heat-Related Mortality (HRM) by Increasing Urban Albedo

The algorithms to estimate the heat-related mortality is explained in Chapter 3. Here, the results address the effects of UHI mitigation strategy on modifying air mass classifications and decreasing heat-related death. Increasing surface reflectivity leads to a decrease in air temperature, an increase in relative humidity and dew point temperature, and a slight increase in wind speed. Table 5.4 presents the 2-m air temperature (T2, (ºC)), dew point temperature (DPT, (ºC)) and apparent temperature (AT, (ºC)) at 1600h (because this hour is a good representer of the changes in temperature, apparent temperature and relative humidity), in CTRL and ALBEDO scenarios. These changes can lead to a significant improvement in human health and comfort and thus reduces heat-related mortality during heat wave events.

Table 5.4. 2-m air temperature (T2, (ºC)), dew point temperature (DPT, (ºC)), and apparent temperature (AT, (ºC)) at 1600h, in CTRL and ALBEDO scenarios during 2005 & 2011 heat wave events in GAM

	CTRL Scenario			ALBEDO Scenario		
Averaged variables	T2 (ºC)	DPT (ºC)	AT (ºC)	T2 (ºC)	DPT (ºC)	AT (ºC)
10-Jul-2005	29.4	22.5	32.2	28.5	22.7	31.9
11-Jul-2005	32.4	20.9	35.3	31.4	21.3	34.2
12-Jul-2005	31.7	21.8	34.8	30.8	22.1	34.1
Event Average	**31.6**	**21.7**	**34.1**	**30.2**	**22.1**	**33.3**
21-Jul-2011	32.9	22.3	35.4	32.2	22.5	35.2
22-Jul-2011	31.7	23.2	34.8	30.9	23.6	34.2
23-Jul-2011	31.2	20.6	35.2	29.4	20.9	32.2
Event Average	**31.9**	**22.0**	**35.1**	**30.8**	**22.4**	**33.8**

Each day is categorized into an air mass classification. These air mass classifications are based on meteorological changes such as air temperature, relative humidity, and wind speed. Table 5.5 presents the air mass type for each day during the 2005 and 2011 heat wave periods for CTRL and ALBEDO scenarios. The moist tropical plus air mass type is improved to moist tropical because of the mitigation strategy and surface modification that leads to a decrease in air temperature and a relative humidity. The dry tropical classification has also transformed to dry moderate, which is a more benign condition. These changes cause a decrease in heat-related mortality during these two heat wave events.

Table 5.5. Air mass classifications on each day during 2005 & 2011 heat wave periods in GAM, the bold entries show changes in air mass type resulted in increasing surface albedo

Scenario	CTRL	ALBEDO
10-Jul-2005	DT	DT
11-Jul-2005	**MT+**	**MT**
12-Jul-2005	DT	DT
21-Jul-2011	**MT+**	**MT**
22-Jul-2011	MT	MT
23-Jul-2011	**DT**	**DM**

Dry Tropical (DT): the hottest and driest conditions; Moist Tropical (MT): warm and very humid; Moist Tropical Plus (MT+): hotter and more humid subset of MT (Source: Sheridan, 2002)

Two categories are considered regarding the air mass classifications for heat-related mortality estimation: dry tropical (DT) and moist tropical/ moist tropical plus (MT/MT+). The approach to define the HRM correlation is explained in Chapter 3. The daily heat-related mortality calculation for Dry Tropical (DT) that represent hottest and driest condition is (Eq.1):

$$HRM_D = -4.32 + 1.07DIS - 0.066TOS + 0.339\,AT \qquad \text{(Eq. 5.1)}$$

and for Moist Tropical (MT) and Moist Tropical Plus (MT+) that represent very warm and humid condition is (Eq. 2):

$$HRM_D = 2.70 - 0.016TOS + 0.339AT \qquad \text{(Eq. 5.2)}$$

Table 5.6 represents the results of heat-related mortality estimation in CTRL and ALBEDO scenarios. The consequences of surface modifications in urban areas indicate that in the 2005 and 2011 heat wave, there would be 2.7% and 3.7% reduction in heat-related mortality. As the air mass classification shifted from oppressive condition (e.g., DT) to a benign situation (e.g., DM), a reduction in HRM is more noticeable.

Table 5.6. Daily heat-related mortality estimation per 100,000 population based on above calculations for DT, MT and MT+ during 2005 & 2011 heat wave periods. For human lives, the numbers are shown with 1 decimal

Mortality Estimations		
Scenario	**CTRL**	**ALBEDO**
10-Jul-2005	4.9	4.8
11-Jul-2005	13.9	13.6
12-Jul-2005	7.8	7.6
Total HRM	~ 27	~ 26
Average Mortality	8.9	8.7
Averaged Reduction (%)		**2.7%**
21-Jul-2011	13.9	13.8
22-Jul-2011	13.6	13.4
23-Jul-2011	7.3	6.2
Total HRM	~ 35	~ 33
Average Mortality	11.6	11.2
Averaged Reduction (%)		**3.7%**

5.5. Discussion and Limitation of Heat-Related Mortality Estimation

The simulations show that increasing surface reflectivity decreases urban ambient temperature. The positive impacts of lower temperatures are: (1) improving human health and comfort and (2) decreasing heat-related mortality during heat-wave periods. Decreasing air temperature also has the following positive effects on air quality: (1) a decrease in temperature-dependent rates of certain

photochemical reactions (O$_3$ formation), (2) a decrease in evaporation losses of organic compounds from mobile and stationary sources, and (3) a decrease in cooling energy demands during summer. Human thermal comfort depends on many factors such as air temperature, humidity, wind speed, radiant temperature, metabolic rates, clothing levels and each individual physiology and states. Here, the focus of the study is on the temperature, humidity, and wind speed. The other factors are disregarded because they are mostly concerning the human thermal comfort.

Here, the effects of a decrease in ambient temperature on HRM is evaluated, whereas the rate of mortality is not necessarily related to outside temperature. Other factors such as age, gender, economic and educational level of the society have not been accounted for. Current and previous health issues that would be more affected during heatwave periods and lead to death, have not been estimated. The consequences of heatwave on air quality and ozone production have not been considered.

The simulations and analyses presented here are based on the assumptions that; (1) the population density and urban structure over the domain is homogenous, (2) other parameters apart than temperature, humidity and wind speed have minimal effects on UHI phenomenon, heatwave events and heat-related mortality, (3) changes on air mass classification during summer is based on previous studies during 20 years in GMA, (4) the results are based on three consecutive days during heatwave events (but the simulation of the entire summer or even a year is required to achieve a more definite conclusion), (5) the effects of air quality on HRM is negligible.

Three of the six heat wave days presented air mass changes from more to less oppressive conditions. The results are somewhat similar to other studies. Kalkstein et al. (2013) showed that the UHI mitigation strategies in the District of Columbia (DC) led to the air mass type changes on two of the four heatwave events. These changes contribute to a 7% reduction in the total number of heat-related mortality. They conducted additional research in the District of Columbia in 2011, during a 10-year period and demonstrated that 11% of summer days in DC area experience the oppressive air mass type that will be modified to more benign ones by increasing surface albedo (Kalkstein et al., 2013). The study is limited to the effects of increasing surface reflectivity on heat-related mortality. However, there is no one strategy that can fit all the needs of a city. Mitigation strategies need to be region specific and the installation and implementation of cool surfaces need to be evaluated based on urban morphology, building layout patterns, trees arrangements, and wind speed and distribution.

Kalkstein et al. (2013) also investigated the effects of UHI mitigation strategies on health-debilitation air masses in four cities across the US. The results of increasing albedo and vegetation indicated that the air mass type changed by an average of 7%, 16%, 3% and 4% in Detroit, Los Angeles, New Orleans and Philadelphia, respectively. The heat-related death decreased by an average of 5 to 10% in these cities. The results of another study by Kalkstein (1999) showed that a 1-2 °C reduction in outdoor temperature, along with some other meteorological changes, could reduce mortality by 10–20%. Here, the ratio of 50% positive modification in air mass classifications is similar to EPA study (Kalkstein and Sheridan, 2003). Results indicate an average of 3.2% reduction in heat- related mortality during the 2005 and 2011 heat wave period in GMA (a 2.7% reduction in HRM in the 2005 heat wave period and a 3.7% reduction in the 2011 heat wave period), corroborate with EPA-sponsored studies on cool cities (Kalkstein and Sheridan, 2003; Vanos et al., 2013, 2014; Sheridan and Kalkstein, 2004; Sheridan et al., 2009). According to Canadian Environmental Health Atlas (CEHA 2018), 121 people die every year in Montreal because of heat related issues; a 3.2% reduction because of albedo increase in GMA, could save 4 lives per year. In another study carried out by Bustinza et al. (2013), the number of heat- related death in GMA (including Montreal, Laval, Monteregie, and Lanaudiere with the total population of 4,221,002) was estimated to be 209 people during July 2010 heat wave period alone. A 3.2% reduction in HRM would results in savings life of 6 people during that period.

5.6. Summary of the Effects of Increasing Surface Reflectivity on Heat-Related Mortality

The main objective of this study was to investigate the effects of increasing surface reflectivity on heat-related mortality in the Greater Montreal Area during the 2005 and 2011 heat wave periods. Numerical simulations were conducted using the online Weather Research and Forecasting model (WRFV3.6.1) coupled with a multi-layer of the Urban Canopy Model (ML-UCM). The simulation results were analysed in terms of four meteorological parameters: 2-m air temperature, 10-m wind speed, 2-m relative humidity, dew point temperature and four heat stress indices: National Weather Service – Heat Index, apparent temperature, Canadian Humid Index, and Discomfort Index. A series of metrics calculations were employed to evaluate model performance and to compare the simulation results with the measurements obtained from four weather stations over the domain.

The comparisons of the base case simulations indicated that the model on average slightly overestimates the meteorological variables.

The albedo of roofs, walls and grounds were increased from 0.2 in CTRL scenarios to 0.65, 0.60, and 0.45 in ALBEDO scenarios, respectively. The results showed that the differences between the meteorological parameters (T2, WS10, RH2, DPT) in CTRL and ALBEDO scenarios are more significant in urban areas than in surrounding areas. The average daily 2-m air temperature reduced by 0.8 °C in the urban area during both heat wave events, whereas this amount in rural areas was around 0.4 °C. The albedo enhancement caused a slight increase in wind speed in urban areas that increased the convection heat transfer and thus decreased the skin temperature. A higher wind speed reduces the effects of heat and ambient temperature and produces a more pleasant condition for urban dwellers. The results show an increase in relative humidity and dew point temperature by nearly 2%. The relative humidity changes are less obvious in rural areas compared to the urban area because of the existence of more vegetation spaces, and thus moisture in the region. In addition, albedo enhancement causes a decrease in boundary-layer height that reduces the chance of advection and diffusion of pollutants and hence increases the pollutants concentrations. The effects of increasing albedo have also been investigated by means of four indices of heat stress. The results showed that since surface albedo modifications reduced temperature and increased relative humidity, these indices were also modified and improved to some extent. Increasing surface albedo is a verifiable strategy to mitigate the UHI effects. It should be noted that this strategy is region-specific and needs to be evaluated for any area of interest because it depends on the particular urban characteristics and morphology.

Here, three indicators are applied to translate the effects of extreme heat events and the potential of increasing surface reflectivity on heat-related mortality rates: air mass type, air temperature, and apparent temperature changes for each day during heat wave periods. As a consequence of ISR, the moist tropical plus and dry tropical air mass types are shifted to moist tropical and dry moderate, respectively. These changes cause a decrease in heat-related mortality during these two heat wave events. Three of the six heat wave days showed air mass changes from more to less oppressive conditions. The beneficial outcome is a reduction in heat- related deaths by approximately 3.2% during heat wave periods, meaning that 4–6 lives per year could be saved. It should be noted that by reducing ambient temperature, the pollutant emission from biogenic and anthropogenic sources and thus photochemical reaction rates will reduce. So, the deaths related to air quality will also be

reduced. In addition, increasing surface reflectivity shifts days into less oppressive air masses by 50% (3 of 6 days during heat wave periods).

The heat-related mortality estimation is based upon some assumptions and limitations. One limitation is that the HRM algorithms are rather simplistic. Epidemiologists tend to focus on ambient conditions even though most individuals spend 85% of their time indoors and indoor exposure is implicated in a large fraction of heat-related deaths. But, here the focus of this study is on the effects of albedo enhancement only on ambient temperature and then its effects on heat-related mortality. The details of how people losing their lives and how their bodies react to extreme heat events are still not known. However, here the effort is made by using other correlations and modifying them for Greater Montreal Area based on its specific air mass condition. The effects of ozone concentrations because of elevated heat is neglected. The impacts of wind speed and radiation budget changes since meteorological parameters and human physical characteristics, such as age, gender, economic and educational status, have not been considered. Hence, the cumulative effects of these factors need to be considered in future studies. While it appears unlikely that increasing surface reflectivity contributes to large reductions in ambient temperature in urban areas (as 2 °C or greater), the study shows that cooling temperature even by less than a degree can lead to air mass category changes and reduce the adverse effects of elevated temperature in urban areas, thus improving human comfort and decreasing heat-related mortality to a noticeable extent.

5.7. Applications of Heat-Related Mortality Estimation

The developed correlations to estimate the effects of high temperature on mortality can be used to investigate the effects of other heat island mitigation strategies (e.g., increasing surface vegetation and controlling anthropogenic heat) on the rate of heat deaths in the Greater Montreal Area. Results could be used by decision-makers to make policies to improve lives of urban dwellers in the GMA. In addition, these analyses indicated that increasing surface reflectivity can facilitate a positive change in air mass classifications. Albedo enhancement shifts days into less oppressive air masses, which in turn improves human health and comfort.

With the heat-related mortality correlations and region-specific algorithm provided, the approach used here illuminates the essential steps for developing HRM equations for other locations and episodes. It should be noted that the HRM is a result of air quality degradation as well. The reason is because of an increase in temperature-dependent photochemical reactions rates

and an increase in emissions from pollutant sources in urban areas. Thus, further analysis of the effects of high temperature on air quality needs to be carried out. The indirect effects of high temperature on HRM are required be estimated by photochemical models such as WRF-Chem. Hence, the WRF-Chem is applied to investigate the effects of heat island mitigation strategy on urban climate as well as air quality for other objectives in the following chapters.

Chapter 6
Effects of Increasing Surface Albedo on Urban Climate and Air Quality over a Large Geographical Area within Nested Domains as Urban Areas

Most previous studies have used a one-way simulation (climate simulations first, followed by air quality simulations). This approach does not provide feedback on the effect of atmospheric pollutants on the climate. Previous simulations are used to estimate the effects of surface modifications and changes in surface albedo on urban climate and air quality through a one-way simulation approach at local, regional and global scales (Arnfield, 2003; Ban-Weiss et al., 2015; Taha 2008 and 2009; Salamanca et al., 2012; Li and Bou-Zeid 2014; Bhati and Mohan 2016). Thus, the interaction between regional atmosphere and local climate is disregarded. The one-way approach does not simulate the complete interactions between urban climate and air quality. The meteorological processes and photochemical reactions in the urban atmosphere magnify the UHI effects. These interactions in the urban environment cause changes in regional climate. The changes in regional atmosphere affect local pollution. Thus, a two-way nested simulation approach is required to capture the full impacts of these processes from the regional to the local scale. A two-way nested approach provides an integrated simulation setup to simulate the full impacts of meteorological and photochemical interactions. This approach decreases the uncertainties associated with scale separation and grid resolution. In addition, this method reveals more details of the effects of surface modifications on urban climate and regional air quality.

The Weather Research and Forecasting Model (WRF) is coupled with the chemistry package (WRF-Chem) and a multi-layer of the urban canopy model (ML-UCM). The model investigates the effects of increasing surface reflectivity on urban climate and air quality over North America focusing on three populated cities: Sacramento (in California), Houston (in Texas), and Chicago (in Illinois) during the 2011 heat wave period. The methodology and simulation approaches are

explained in Chapter 3. Here, the results of these simulations are presented. This research is summarized in the article by Z. Jandaghian and H. Akbari (2018), *"The Effects of Increasing Surface Albedo on Urban Climate and Air Quality: A Detailed Study for Sacramento, Houston, and Chicago"* (*Climate 2018*, 6, 19; doi:10.3390/cli6020019).

6.1. Defining Simulation Domain and Period

The first domain covers North America (NA) including Canada, the United States of America, and the Northern part of Mexico with 445 grids in west–east direction and 338 grids in south–north direction. The horizontal resolution is 12km. The second, third, and fourth domains cover the Sacramento area (36 × 31 grids), Houston area (41 × 31 grids), and Chicago area (36 × 31 grids) with the horizontal resolution of 2.4km. The vertical resolution includes 35 vertical layers from the surface to a fixed pressure of ~100 mb (~16 km AGL). Figure 6.1 shows the simulation domains and land use/land cover. The simulation period extended seven consecutive hottest days in 2011, from the 17th to 23rd of July. The first 72h of the simulation is disregarded as a spin-up period.
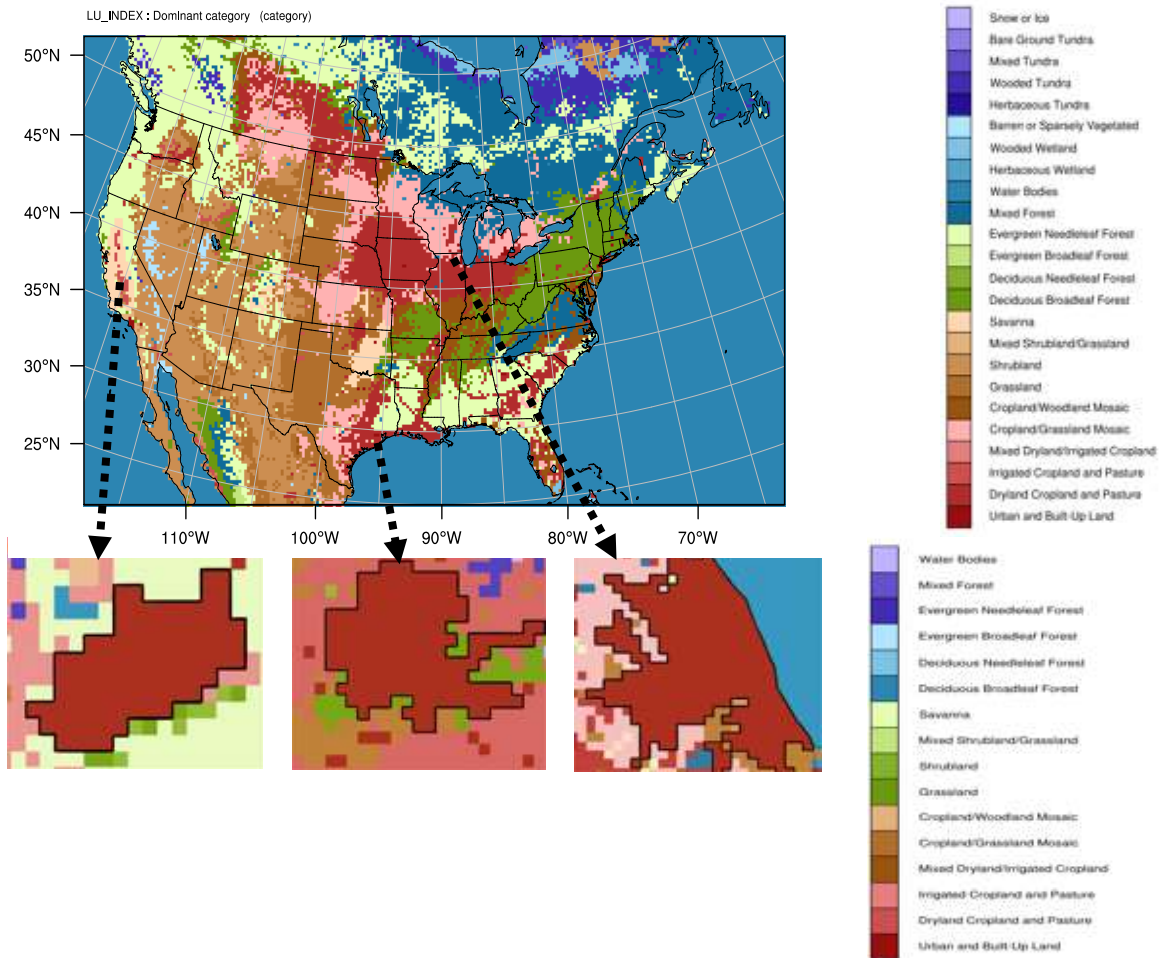
Figure 6.1. Simulation domains and land use/land cover over North America (mother domain, horizontal resolution: 12km) Sacramento, Houston, and Chicago (inner domains, horizontal resolution: 2.4km).

Table 6.1 presents the physical and chemical parameterizations applied in WRF-Chem.

Table 6.1. Physical and chemical parameterizations applied in WRF_Chem

Category	Option Used
Microphysics	Lin scheme
Shortwave radiation	Goddard
Longwave radiation	RRTMG
Land surface model	NOAH
Planetary boundary layer scheme	Mellor–Yamada–Janjic Scheme
Cumulus parameterization	Grell Devenyi
Chemistry option	RACM
Photolysis scheme	Fast_J
Aerosol option	MADE/SORGAM
Advection scheme	Runge–Kutta third order
LULC data	USGS 24-class
Anthropogenic emissions	US-NEI11
Biogenic emissions	MEGAN
Urban canopy model	ML-UCM

6.2. Simulation Scenarios for Urban Climate and Air Quality Assessment

Three cities are selected for detail analyses: Sacramento (California), Houston (Texas), and Chicago (Illinois) based on Akbari et al., (2001, 2003 and 2008) and Rose et al., (2003) findings on the urban fabric of these cities. Using high-resolution orthophotography, they found that roofs cover 20–25% and pavements cover 30–40% of urban surfaces. Table 6.2 presents the urban fabric of Sacramento, Chicago, and Houston (Rose et al., 2003).

Table 6.2. Urban fabric of three cities in NA (Source: Rose et al., 2003)

Metropolitan Areas	Roofs (%)	Pavements (%)
Sacramento	20	45
Chicago	25	37
Houston	22	30

Two sets of simulations are conducted: CTRL case (UHI effects) and ALBEDO case (increasing surface reflectivity (ISR) effects) during the 2011 heat wave period over the simulation domains. The fraction of urban fabric of these three cities and the changes because of increasing surface reflectivity are applied to calculate the albedo changes over the domains. The changes of surface albedo modification from the CTRL case as 0.2 to full adoption of roofs and pavements can be calculated as: (fraction of roofs in Sacramento) 0.20×0.65 (the increase of albedo for roofs) + 0.45 (fraction of pavements in Sacramento) $\times 0.45$ (the increase of albedo for pavements) = 0.33 (as an example for Sacramento; the surface albedo (of roofs and pavements) increased from 0.13 to 0.33 (as a full adaptation of albedo enhancement)). The change to gridded ALBEDO can be calculated as: (Surface albedo enhancement (roofs, walls, and pavements) $\times$ Fraction of urban areas per grid cell).

6.3. Evaluation of Meteorological and Photochemical Model Performance

The model performance of WRF-Chem is evaluated by comparing the simulation results with observations obtained from weather and air-quality stations in Sacramento, Houston, and Chicago. The weather and air quality monitoring stations were chosen based on their locations close to the downtown of the selected cities (hereafter referred to as urban) and their surroundings (hereafter referred to as suburb). The hourly 2-m air temperature (T2), 10-m wind speed (WS10), 2-m relative humidity (RH2), and dew point temperature (TD) simulation results are compared with the measurements obtained from the U.S. Environmental Protection Agency (EPA) Clean Air Status

and Trend Network (CASTNET). Since the measurements from air quality stations were averaged 24-h, the daily averaged modelled chemical components are extracted and evaluated to have the same temporal basis. Thus, the daily averaged modelled fine particular matters ($PM_{2.5}$), ozone (O_3), nitrogen dioxide (NO_2), $PM_{2.5}$ subspecies (particulate sulfate ($SO4_{2.5}$), particulate nitrate ($NO3_{2.5}$), and organic carbon ($OC_{2.5}$)) concentrations are compared with the EPA Air Quality System (AQS) observations using 24-h average data.

Here, the time series of simulation results changed to the local time for each specific location: Sacramento: LST = UTC – 7 h; Houston and Chicago: LST = UTC – 5 h. The performance and accuracy of the simulation results are quantitatively based on a series of metrics estimations (Boylan and Russell, 2006). The Zhang et al. (2006) approach is followed and the mean bias error (MBE), mean absolute error (MAE), and the root mean square error (RMSE) are calculated for meteorological and chemical parameters.

In terms of meteorological components of the model, the WRF-Chem effectively captures the diurnal variations of 2-m air temperature, overpredicts 10-m wind speed, overpredicts dew point temperature, and under-predicts 2-m relative humidity. The MBA of T2 (-0.07 °C) shows that the model is capable in predicting air temperature. A small underprediction can be seen in urban areas (~-0.3 °C) that indicates the model deficiency in calculating the heat emission from anthropogenic sources in urban areas accurately. The MAE and RMSE of T2 are approximately 1 °C.

Wind speed plays an important role in calculation of air temperature from skin temperature in the land surface model. The 10-m wind speed comparisons show small to large overpredictions (0.3 to 3.15 m/s). The MBA is 1.65 m/s, that shows the model is unable to capture the effects of micro scales and wind patterns. The MAE and RMSE of WS10 are almost 2 m/s.

Relative humidity is a function of moisture content, air temperature, and surface pressure. The spatial distribution of RH2 represents an underestimation with the MBE of -1.42%. This underestimation shows that the microphysics scheme does not accurately account for the processes of transforming water (rain, vapor, cloud, etc.) and moisture fluxes. It also shows the model limitation in capturing the sea surface temperature, wind speed, and their impacts on water mixing ratio and water content of the air properly. The MAE and RMSE of RH2 are nearly 10% and 13%, respectively. Figure 6.2 shows the time series (hourly) of the observed vs. simulated T2 (°C), WS10 (m/s), and RH2 (%) in the urban areas of Sacramento, Houston, and Chicago. The dew point temperature is also calculated. The MBA, MAE, and RMSE of dew point temperature (0.39, 0.53,

and 0.65 °C, respectively) show that the model overpredicts the moisture content in the atmosphere especially in urban areas (~0.5 °C).

In terms of the chemical component of the model, the WRF_ChemV3.6.1, as configured here, tends to under-predict 24-h fine particular matters ($PM_{2.5}$) and over-predict the 24-h O_3 concentrations during the 2011 heat wave period. The MBE of the 24-h avg. $PM_{2.5}$ is −1.42 μg/m^3. The MAE and RMSE of $PM_{2.5}$ are approximately 4 μg/m^3. This is because the accuracy in fine particular matters concentrations is to some extent a function of its subspecies estimations as particulate sulfate, particulate nitrate, and organic carbons. Thus, the simulation results of $SO4_{2.5}$ (μg/m^3), $NO3_{2.5}$ (μg/m^3), and $OC_{2.5}$ (μg/m^3) are compared with observations at urban areas of aforementioned cities.

The performance of $PM_{2.5}$ subspecies is a combination of overprediction of particulate sulfate (MBE ~ 5 μg/m^3) and underprediction of particulate nitrate (MBE ~ −4 μg/m^3) and organic carbon (MBE ~ −3 μg/m^3). The MAE and RMSE of $SO4_{2.5}$, $NO3_{2.5}$, and $OC_{2.5}$ are approximately 5, 4, and 3 μg/m^3, respectively. The comparison between simulated ozone and measurements indicated an overestimation of O_3 across the domains (MBE ~ 5 ppb). The O_3 concentrations is overestimated due to the NO_x and VOCs overestimation in emission inventories and their calculations in chemistry packages (US-NEI11 and MEGAN). The average MAE and RMSE of O_3 are around 7 ppb and 8 ppb, respectively. In addition, the NO_2 concentrations is calculated as one of the precursors in ozone formation. The MBE of NO_2 in urban areas (~2.5 ppb) show that the model tends to overpredict the nitrogen dioxide. The MAE and RMSE of NO_2 is around 4 ppb.

Figure 6.3 shows the observed vs. simulated $PM_{2.5}$ (μg/m^3) and O_3 (ppb) concentrations in the urban areas of Sacramento, Houston, and Chicago. Tables 6.3, 6.4, and 6.5 respectively represent the mean bias error (MBE), mean absolute error (MAE), and the root mean square error (RMSE) of T2 (°C), WS10 (m/s), RH2 (%), $PM_{2.5}$ (μg/m^3), and O_3 (ppb) for the three cities. There are several limitations and assumptions in these comparisons. The simulation results are extracted hourly for all variables, whereas the observation in terms of $PM_{2.5}$ and O_3 are reported as a 24-h average. Figure 6.4 shows the overall comparison between observed vs. simulated aforementioned parameters in terms of MBA, MAE, and RMSE. Despite the model biases in simulating meteorological and chemical variables, the performance of WRF-Chem is generally consistent with most air quality models (Gilliam et al., 2006; Wu et al., 2008; Wang et al., 2009; Liu et al., 2010; Appel et al., 2012). Thus, the WRF-Chem is mostly suited for application of simulating and

investigating the effects of urban heat island and its mitigation strategies on urban climate and air quality in a two-way nested simulation approach.

Table 6.3. Mean bias error (MBE) of T2 (°C), WS10 (m/s), Td (°C), RH2 (%), O_3 (ppb), $PM_{2.5}$ ($\mu g/m^3$), $SO4_{2.5}$ ($\mu g/m^3$), $NO3_{2.5}$ ($\mu g/m^3$), $OC_{2.5}$ ($\mu g/m^3$), and NO_2 (ppb) at selected monitoring stations across Sacramento, Houston, and Chicago.

| Variables | Mean Bias Error (MBE) | | | | | | Average |
| | Sacramento | | Houston | | Chicago | | |
	Suburb	Urban	Suburb	Urban	Suburb	Urban	
T2 (°C)	0.15	−0.34	0.22	−0.34	−0.30	0.19	−0.07
WS10 (m/s)	1.90	3.15	0.87	0.34	1.28	1.05	1.43
Td (°C)	0.21	0.61	0.24	0.47	0.33	0.47	0.39
RH2 (%)	−5.43	−5.63	−1.03	8.16	1.88	−6.45	−1.42
24-h avg. O_3 (ppb)	9.72	4.68	3.17	3.85	2.31	4.38	4.68
24-h avg. $PM_{2.5}$ ($\mu g/m^3$)	−5.94	2.30	−3.26	2.07	−3.86	−2.33	−1.84
24-h avg. $SO4_{2.5}$ ($\mu g/m^3$)	-	4.20	-	5.30	-	3.89	4.46
24-h avg. $NO3_{2.5}$ ($\mu g/m^3$)	-	−3.75	-	−4.40	-	−3.52	−3.91
24-h avg. $OC_{2.5}$ ($\mu g/m^3$)	-	−1.80	-	−2.33	-	−3.68	−2.60
24-h avg. NO_2 (ppb)	-	2.61	-	3.40	-	1.25	2.42

Note: The definitions of statistical measurements are as follows Zhang et al. (2006) [51]: $MBE = \frac{1}{N}\sum_1^N(C_M - C_O)$, C_M and C_O are modeled and observed concentrations, respectively and N is the total number of model and observation pairs.

Table 6.4. Mean absolute error (MAE) of T2 (°C), WS10 (m/s), Td (°C), RH2 (%), O_3 (ppb), $PM_{2.5}$ ($\mu g/m^3$), $SO4_{2.5}$ ($\mu g/m^3$), $NO3_{2.5}$ ($\mu g/m^3$), $OC_{2.5}$ ($\mu g/m^3$), and NO_2 (ppb) at selected monitoring stations across Sacramento, Houston, and Chicago.

| Variables | Mean Absolute Error (MAE) | | | | | | Average |
| | Sacramento | | Houston | | Chicago | | |
	Suburb	Urban	Suburb	Urban	Suburb	Urban	
T2 (°C)	1.05	0.88	1.20	0.88	0.77	1.12	0.99
WS10 (m/s)	1.96	3.33	1.26	1.20	2.31	1.79	1.97
Td (°C)	0.56	0.30	0.49	0.63	0.56	0.66	0.53
RH2 (%)	15.32	9.45	5.38	9.54	8.98	10.11	9.80
24-h avg. O_3 (ppb)	9.72	9.90	6.92	6.01	2.56	5.88	6.83
24-h avg. $PM_{2.5}$ ($\mu g/m^3$)	6.24	3.05	3.26	3.70	3.86	2.33	3.74
24-h avg. $SO4_{2.5}$ ($\mu g/m^3$)	-	4.20	-	5.30	-	3.89	4.46
24-h avg. $NO3_{2.5}$ ($\mu g/m^3$)	-	3.75	-	4.45	-	3.52	3.91
24-h avg. $OC_{2.5}$ ($\mu g/m^3$)	-	1.80	-	2.33	-	3.68	2.60
24-h avg. NO_2 (ppb)	-	4.71	-	3.40	-	2.54	3.55

Note: The definitions of statistical measurements are as follows Zhang et al. (2006) [51]: $MAE = \frac{1}{N}\sum_1^N|C_M - C_O|$ C_M and C_O are modeled and observed concentrations, respectively and N is the total number of model and observation pairs.

Table 6.5. Root mean square error (RMSE) of T2 (°C), WS10 (m/s), Td (°C), RH2 (%), O_3 (ppb), $PM_{2.5}$ ($\mu g/m^3$), $SO4_{2.5}$ ($\mu g/m^3$), $NO3_{2.5}$ ($\mu g/m^3$), $OC_{2.5}$ ($\mu g/m^3$), and NO_2 (ppb) at selected monitoring stations across Sacramento, Houston, and Chicago.

| Variables | Root Mean Square Error (RMSE) | | | | | | Average |
| | Sacramento | | Houston | | Chicago | | |
	Suburb	Urban	Suburb	Urban	Suburb	Urban	
T2 (°C)	1.35	1.13	1.44	1.13	1.01	1.32	1.23
WS10 (m/s)	2.29	3.68	1.58	1.47	2.86	2.22	2.35
Td (°C)	0.68	0.37	0.58	0.77	0.67	0.80	0.65
RH2 (%)	18.94	12.32	7.52	12.26	11.36	13.48	12.65
24-h avg. O_3 (ppb)	10.51	14.21	7.89	6.71	3.09	8.21	8.44
24-h avg. $PM_{2.5}$ ($\mu g/m^3$)	7.74	3.25	4.04	4.30	4.82	2.81	4.49
24-h avg. $SO4_{2.5}$ ($\mu g/m^3$)	-	4.44	-	6.24	-	3.93	4.87
24-h avg. $NO3_{2.5}$ ($\mu g/m^3$)	-	3.96	-	4.87	-	4.28	4.37
24-h avg. $OC_{2.5}$ ($\mu g/m^3$)	-	1.93	-	2.39	-	3.76	2.69
24-h avg. NO_2 (ppb)	-	5.74	-	4.10	-	2.89	4.24

Note: The definitions of statistical measurements are as follows Zhang et al. (2006) [51]: $RMSE = \left[\frac{1}{N}\Sigma_1^N (C_M - C_O)^2\right]^{1/2}$ C_M and C_O are modeled and observed concentrations, respectively and N is the total number of model and observation pairs.
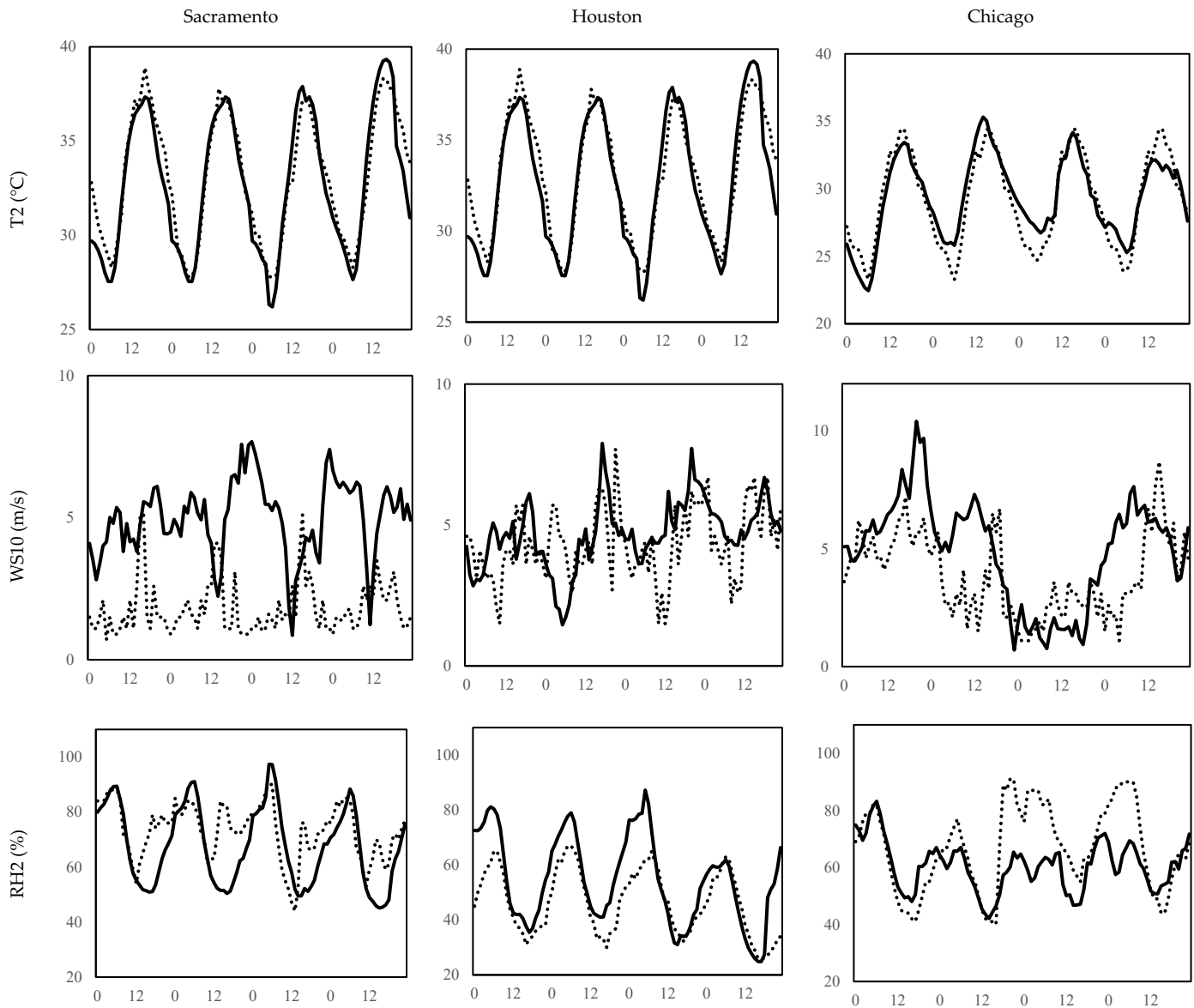
Figure 6.2. The time series (hourly) of the simulated (solid line) vs. measurements (dashed line) T2 (°C), WS10 (m/s), and RH2 (%) at urban monitoring stations across Sacramento, Houston, and Chicago.
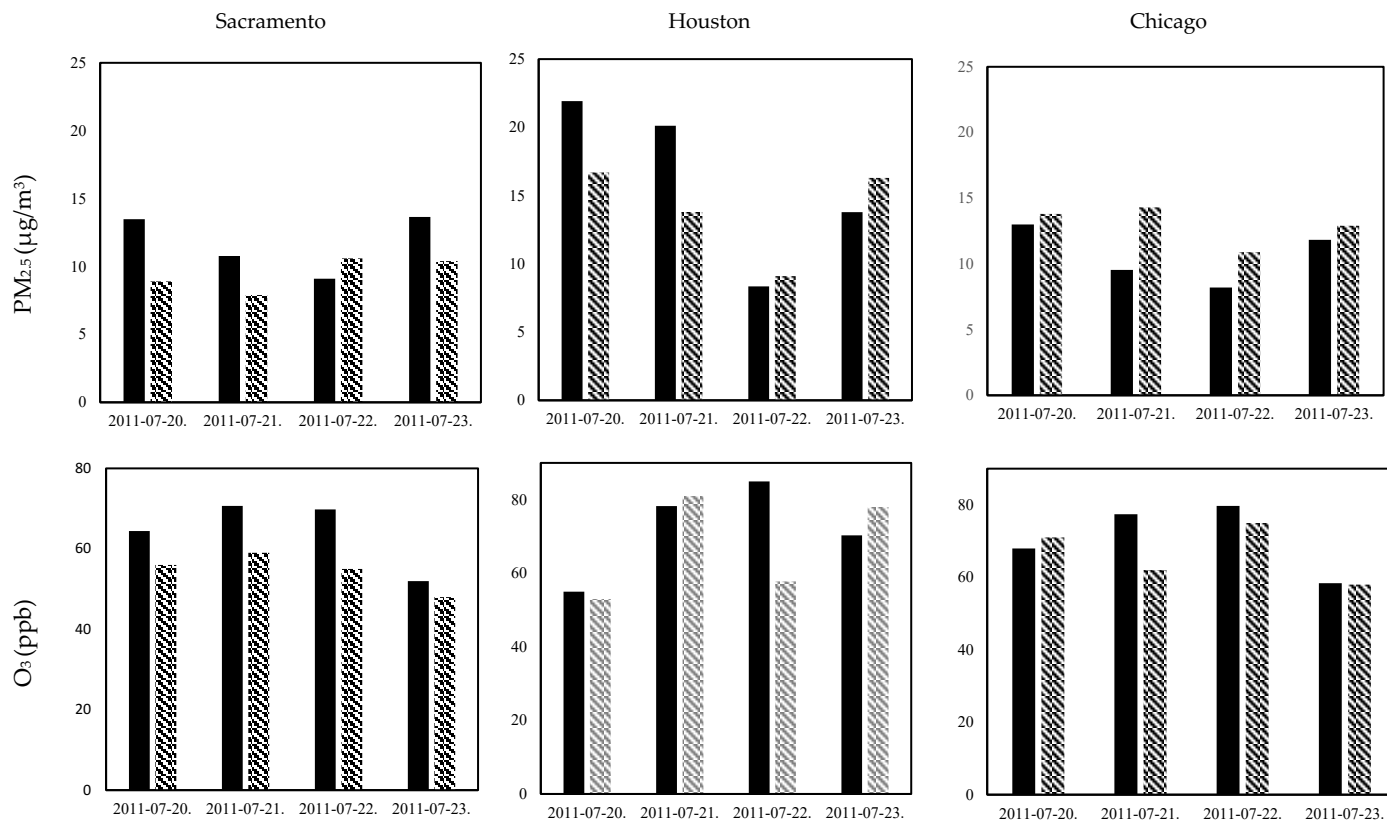
Figure 6.3. The time series (averaged 24-h) of simulated (black bar chart) vs. measurements (patterned downward diagonal bar chart) of PM$_{2.5}$ (µg/m^3) and O$_3$ (ppb) concentrations at urban monitoring stations across Sacramento, Houston, and Chicago.

Mean Bias Error (MBE) of parameters
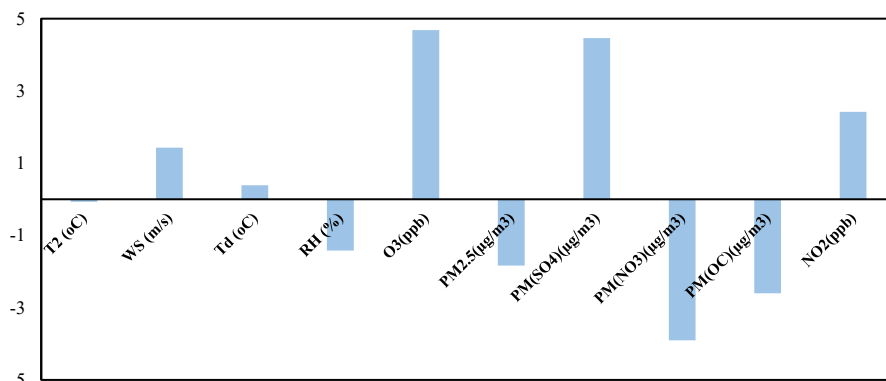
Mean Absolute Error (MAE) of parameters

Root Mean Square Error (RMSA) of parameters
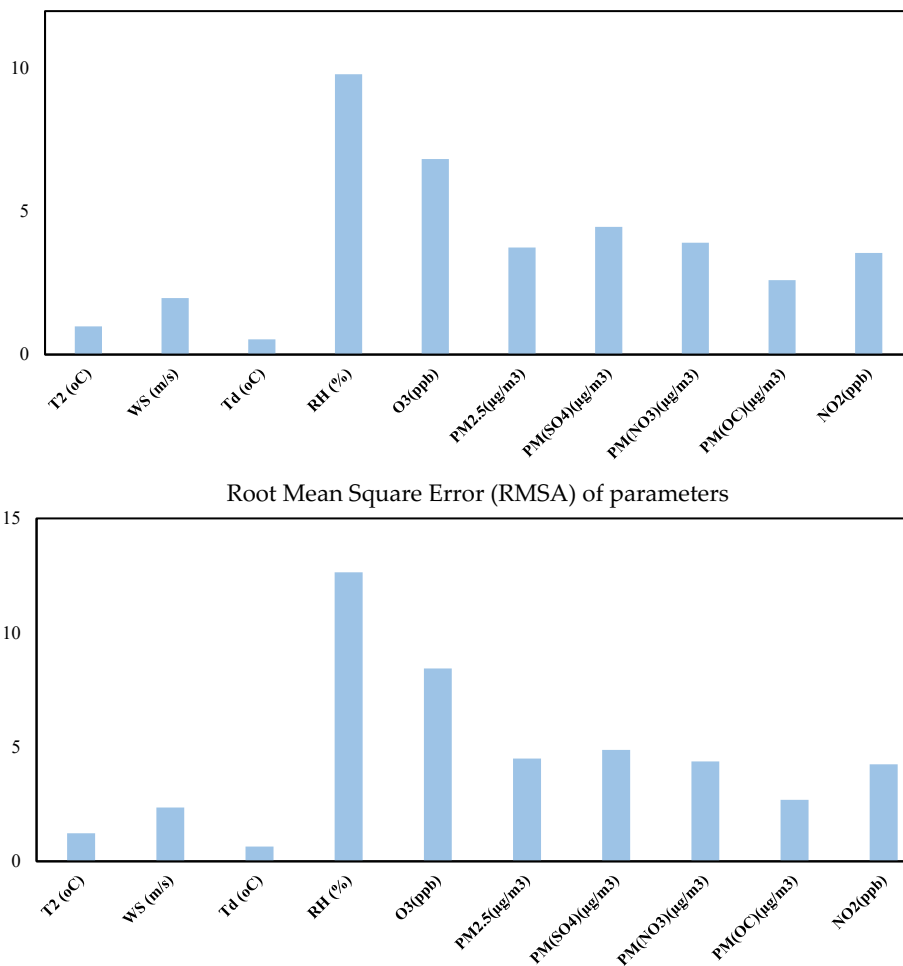
Figure 6.4. The overall mean bias error (MBE), mean absolute error (MAE), and root mean square error (RMSA) of T2 (°C), WS10 (m/s), Td (°C), RH2 (%), O_3 (ppb), $PM_{2.5}$ ($\mu g/m^3$), $SO4_{2.5}$ ($\mu g/m^3$), $NO3_{2.5}$ ($\mu g/m^3$), $OC_{2.5}$ ($\mu g/m^3$), and NO_2 (ppb) during the 2011 heat wave period.

6.4. Effects of Increasing Surface Reflectivity on Urban Climate and Air Quality

Results discussed here are based on the comparison between the ALBEDO and CTRL scenarios for each city. Table 6.6 and Figure 6.5 represent the average differences in T2 (°C), WS10 (m/s), Td (°C), RH2 (%), $PM_{2.5}$ ($\mu g/m^3$), O_3 (ppb), $SO4_{2.5}$ ($\mu g/m^3$), $NO3_{2.5}$ ($\mu g/m^3$), $OC_{2.5}$ ($\mu g/m^3$), and NO_2 (ppb) during the 2011 heat wave period across the second, third, and fourth domains: Sacramento (CA), Houston (TX), and Chicago (IL). Figure 6.6 shows the averaged differences of T2 (°C) and O_3 (ppb) concentrations in suburb and urban areas of the aforementioned cities.

Sacramento, California is located in the central valley near the Sierra foothills. It is at the confluence of the Sacramento River and the American River and is known as the Sacramento Valley. The city has a population of approximately 500,000 people and covers over 253 km^2 (United States Census Bureau, 2011). Its climate is characterized by mild year-round temperature. It has a hot-dry-

summer Mediterranean climate with little humidity and an abundance of sunshine. Based on the National Oceanic and Atmospheric Administration (NOAA) Online Weather Data (2017), Sacramento has the summer temperature exceeding 32 °C on 73 days and 38 °C on 15 days. The State of the Air 2017 report, by American Lung Association (2017), ranks the USA metropolitan areas based on ozone and some particular pollutions during 2013, 2014, and 2015 period. They used the official data from the U.S. Environmental Protection Agency (EPA). Sacramento ranks fifth because of its high ozone concentration.

In a study performed at the Lawrence Berkeley National Laboratory (LBNL), Taha et al. (2000) applied the Colorado State Urban Meteorological Model (CSUMM) and the Urban Airshed Model (UAM-IV) to estimate the impacts of heat island mitigation strategies in Sacramento on the area's local meteorology and ozone air quality in 2000. The albedo level and vegetative cover increased by approximately 0.11 and 0.14, respectively. Using 11–13 July 1990 as the modeling period, the average daily ozone and temperature decreased by up to 10 ppb and 1.6 °C, respectively. In a more recent study, Taha et al. (2015) applied WRF with CMAQ in Sacramento Valley with the inner domain of 1 km resolution. The albedo of roofs, walls, and pavements increased by 0.4, 0.1, and 0.2, respectively. The surface temperature and air temperature were reduced by up to 7 °C and 2–3 °C, respectively. The ozone concentrations also decreased by up to 5–11 ppb during the daytime.

The simulation results for Sacramento show that albedo enhancement leads to a net decrease in 2-m air temperature by up to 2.5 °C and 0.7 °C in urban and suburban areas, respectively. Most of the decreases occur between 1200 and 1600 LST as shown in Figure 6.7. Figure 6.8-Sa (CTRL) shows the maximum air temperature across the simulation domain in the heat wave period. By increasing surface reflectivity, the maximum temperature reduction is around 3 °C almost in all parts of the city (Figure 6.8-Sb-ALBEDO) and this reduction is more obvious in the western part of the domain. The wind speed slightly decreased over the entire domain. The relative humidity increased by 7% and 3% in urban and suburban areas, respectively. Increasing surface reflectivity affords a decrease of nearly 2.4 $\mu g/m^3$ in $PM_{2.5}$ concentrations in urban area (Figure 6.7) and 1 $\mu g/m^3$ in suburb. Figure 6.7-Sc shows the maximum $PM_{2.5}$ concentrations across the domain. The maximum is around 12 $\mu g/m^3$ in urban area that decreases by 2–3 $\mu g/m^3$ as the results of albedo enhancement (Figure 6.8-Sd). The heat island mitigation strategy causes a decline in O_3 by almost 8 ppb in urban (Figure 6.7) and 3 ppb in suburb of the Sacramento area. Figure 6.8-Se shows the maximum O_3 concentrations as nearly 80 ppb across the simulation domain that decreases to nearly

70 ppb by UHI mitigation strategy (Figure 6.8-Sf). The results resemble those of previous studies (Taha et al., 2008, 2013 and 2015). In addition, the particulate sulfate, particulate nitrate, organic carbon, and nitrogen dioxide are compared in CTRL and ALBEDO simulations results. Albedo enhancement causes no changes to minimal changes to particular matters subspecies but decreases the NO_2 concentration by ~1 ppb.

Houston is the fourth most populous city in the U.S. with a population of 2.3 million within a land area of 1700 km^2 (United States Census Bureau, 2017). It is located in the Southeast Texas near the Gulf of Mexico. Houston's climate is classified as humid subtropical. During the summer, the temperature commonly reaches 34 °C, and some days it reaches to even 40 °C. The wind comes from the south and southeast and brings heat and moisture from the Gulf of Mexico. The highest temperature recorded in Houston is 43 °C, which occurred during the 2011 heat wave period (NOAA Online Weather Data). Houston also suffers from excessive ozone levels and the American Lung Association (2017) named the city as the 12th most polluted city in the U.S., based on EPA 2013, 2014, and 2015 data base.

Taha (2008) used MM5 to evaluate the model's episode performance and its response to increasing surface albedo and vegetation in Houston during several days in August 2000. In ALBEDO scenario, the roof albedo was increased from an average of 0.1 to an average of 0.3; wall albedo was increased from an average of 0.25 to an average of 0.3; pavement albedo was increased from an average of 0.08 to 0.2. The results indicated a reduction in temperature by up to 3.5 °C, and also caused warming in some areas by up to 1.5 °C. Results indicated that cooling usually occurs during daytime, while heating occurs at night. The other simulations show the same results (Taha 2003 and 2005).

The simulation results for Houston show that albedo enhancement leads to a net decrease in 2-m air temperature by up to 3 °C and 0.8 °C in urban (Figure 6.7) and suburban areas, respectively. Unlike previous studies, no heating effect is witnessed in these simulations. The reason is because of the sea breeze consideration in the solver of WRF-Chem. Figure 6.8-Ha illustrates the maximum air temperature across the Houston in the heat wave period. The maximum temperature reduction is above 3 °C almost in all parts of the city (Figure 6.8-Hb). The model tends to perform relatively better in urban rather than in suburb areas. With albedo enhancement, the wind speed slightly decreased, and the relative humidity increased by up to 7% in urban and 3% in suburb. Increasing surface reflectivity affords a decrease of $PM_{2.5}$ concentrations by up to 3.5 $\mu g/m^3$ and 2.6 $\mu g/m^3$ in

urban and suburban areas, respectively. Figure 6.8-Hc shows the maximum $PM_{2.5}$ concentrations across Houston. The maximum is above 20 $\mu g/m^3$ in urban area that decreases to 16 $\mu g/m^3$ as the results of albedo enhancement (Figure 6.8-Hd). The O_3 concentrations also decrease by up to 7.2 ppb and 3 ppb in urban and suburban areas, respectively. Figure 6.8-He shows the maximum O_3 concentrations as above 80 ppb across the simulation domain that decreases to nearly 70 ppb all over the domain (Figure 6.8-Hf). Here, the results resemble to previous studies (Taha 2003, 2005 and 2008). Increasing surface albedo in the urban area of Houston causes no changes in particular matters subspecies and a decrease of 1.2 ppb in NO_2 concentration.

Chicago is the third most populous city in the U.S. with over 2.7 million residents. The city area is 606 km^2 (United State Census Bureau). The city lies on the southwestern shores of Lake Michigan and has two rivers: the Chicago River and the Calumet River. Chicago has a humid continental climate. Summer temperatures can reach up to 32 °C. Taha et al., (1998) used a three-dimensional, Eulerian, mesoscale meteorological model (CSUMM) to simulate the effects of large scale surface modifications on meteorological conditions in 10 cities across the U.S. Surface modifications included increasing albedo by 0.03 ± 0.05 and increasing vegetative fraction by 0.03 ± 0.04. The results indicated that the air temperature was reduced by up to 1 °C in the Chicago area.

The simulation results for Chicago show that albedo enhancement leads to a net decrease in 2-m air temperature by up to nearly 2 °C and 0.8 °C in urban (Figure 6.7) and suburban areas, respectively. Figure 6.8-Ca shows the maximum air temperature across the simulation domain. With albedo enhancement, the air temperature reduced over the domain (Figure 6.8-Cb). The wind speed slightly reduces in suburbs, with no changes in urban areas. The results show a slight decrease in relative humidity by up to 0.2% in Chicago's urban areas. The reason is because of the wind speed direction that is north to west (passing the bodies of water) and the city's location that is along one of the Great Lakes, Lake Michigan, and has the Mississippi River Watershed and the Chicago River. The other reason is due to the increasing surface reflectivity that reduces the skin temperature and thus air temperature that might also decrease the chance of evaporation and thus decreases moisture content above the ground. This strategy also affords a decrease of $PM_{2.5}$ concentrations by up to 2.5 $\mu g/m^3$ and 0.6 $\mu g/m^3$ in urban and suburban areas, respectively. The maximum $PM_{2.5}$ concentrations across Chicago is nearly 12 $\mu g/m^3$, that decreases to nearly 9 $\mu g/m^3$ as the results of albedo enhancement (Figure 6.8-Cc and 4.27-Cd). The O_3 concentrations decrease by up to 4.2 ppb in urban area and 1.7

ppb in suburb. Figure 6.7-Ce shows the maximum O_3 concentrations as nearly 70 ppb across the simulation domain that decreases to almost 65 ppb all over the domain (Figure 6.8-Cf). Increasing urban albedo in Chicago leads to an increase of particulate nitrate by 3 ppb and a decrease of NO_2 concentration by ~ 1ppb.

Overall, the results indicate that with albedo enhancement, the air temperature drops (~1.5 °C) and thus causes a decrease in ozone concentrations (~5 ppb) and nitrogen dioxide (~1 ppb). Increasing surface solar reflectance lead to a minimal decrease in particular matters (~2 $\mu g/m^3$) and no significant changes in its subspecies. The $SO4_{2.5}$ and $NO3_{2.5}$ concentrations reduced slightly in urban areas (~0.1 $\mu g/m^3$) because of the decrease in air temperature and thus photochemical reaction rates, but there is no change in $OC_{2.5}$ ($\mu g/m^3$). The UHI mitigation strategy increased the relative humidity and dew point temperature. The results show that there are no significant changes in the wind speed over the domain and the differences between two scenarios is 0.05 m/s. This minimal change is because of the WRF-Chem configurations and it does not reflect any changes in momentum transport from the shallow boundary layer.

Table 6.6. The differences between CTRL and ALBEDO scenarios of T2 (°C), WS10 (m/s), RH2 (%), O3 (ppb), PM2.5 (µg/m3), SO42.5 (µg/m3), NO32.5 (µg/m3), OC2.5 (µg/m3), and NO2 (ppb) during the 2011 heat wave period across Sacramento, Houston, and Chicago.

Δ ALBEDO							
CTRL-ALBEDO	**Sacramento**		**Houston**		**Chicago**		**Average**
	Suburb	**Urban**	**Suburb**	**Urban**	**Suburb**	**Urban**	
Δ T2 (°C)	0.72	2.37	0.81	2.68	0.75	1.76	1.52
Δ WS10 (m/s)	0.03	0.02	0.33	0.02	−0.08	0.00	0.05
Δ Td (°C)	−0.26	−0.39	−0.27	−0.46	−0.21	−0.34	−0.32
Δ RH2 (%)	−2.99	−6.88	−2.44	−6.89	−0.81	0.21	−3.30
24-h avg. O_3 (ppb)	2.98	7.52	2.85	7.23	1.77	4.23	4.43
24-h avg. $PM_{2.5}$ ($\mu g/m^3$)	0.98	2.36	2.59	3.49	0.61	2.48	2.08
24-h avg. $SO4_{2.5}$ ($\mu g/m^3$)	-	0.02	-	0.01	-	0.06	0.03
24-h avg. $NO3_{2.5}$ ($\mu g/m^3$)	-	0.01	-	0.05	-	0.23	0.09
24-h avg. $OC_{2.5}$ ($\mu g/m^3$)	-	0.00	-	0.00	-	0.00	0.00
24-h avg. NO_2 (ppb)	-	0.82	-	1.21	-	0.91	0.98
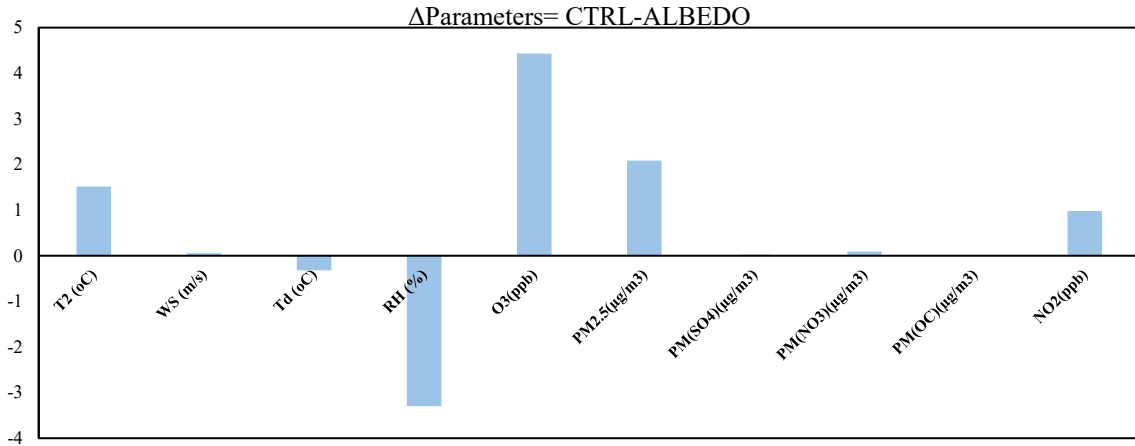
Figure 6.5. The average differences between CTRL and ALBEDO scenarios in T2 (°C), WS10 (m/s), RH2 (%), O₃ (ppb), PM₂.₅ (µg/m³), SO4₂.₅ (µg/m³), NO3₂.₅ (µg/m³), OC₂.₅ (µg/m³), and NO₂ (ppb) during the 2011 heat wave period.
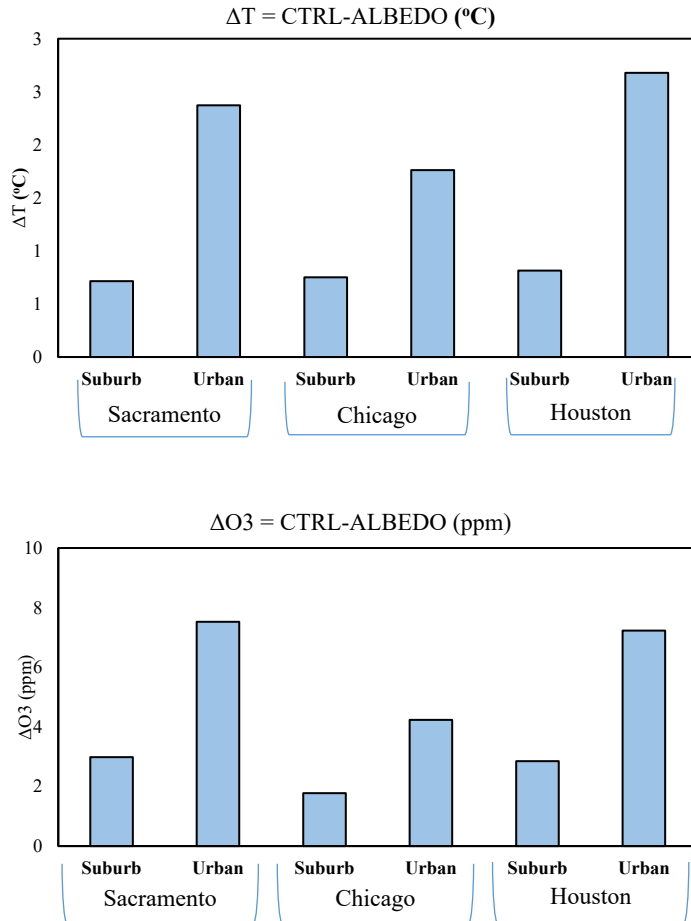
Figure 6.6. The average differences between CTRL and ALBEDO scenarios of T2 (°C) and O₃ (ppb) during the 2011 heat wave period in suburb and urban areas of Sacramento, Chicago, and Houston.

132
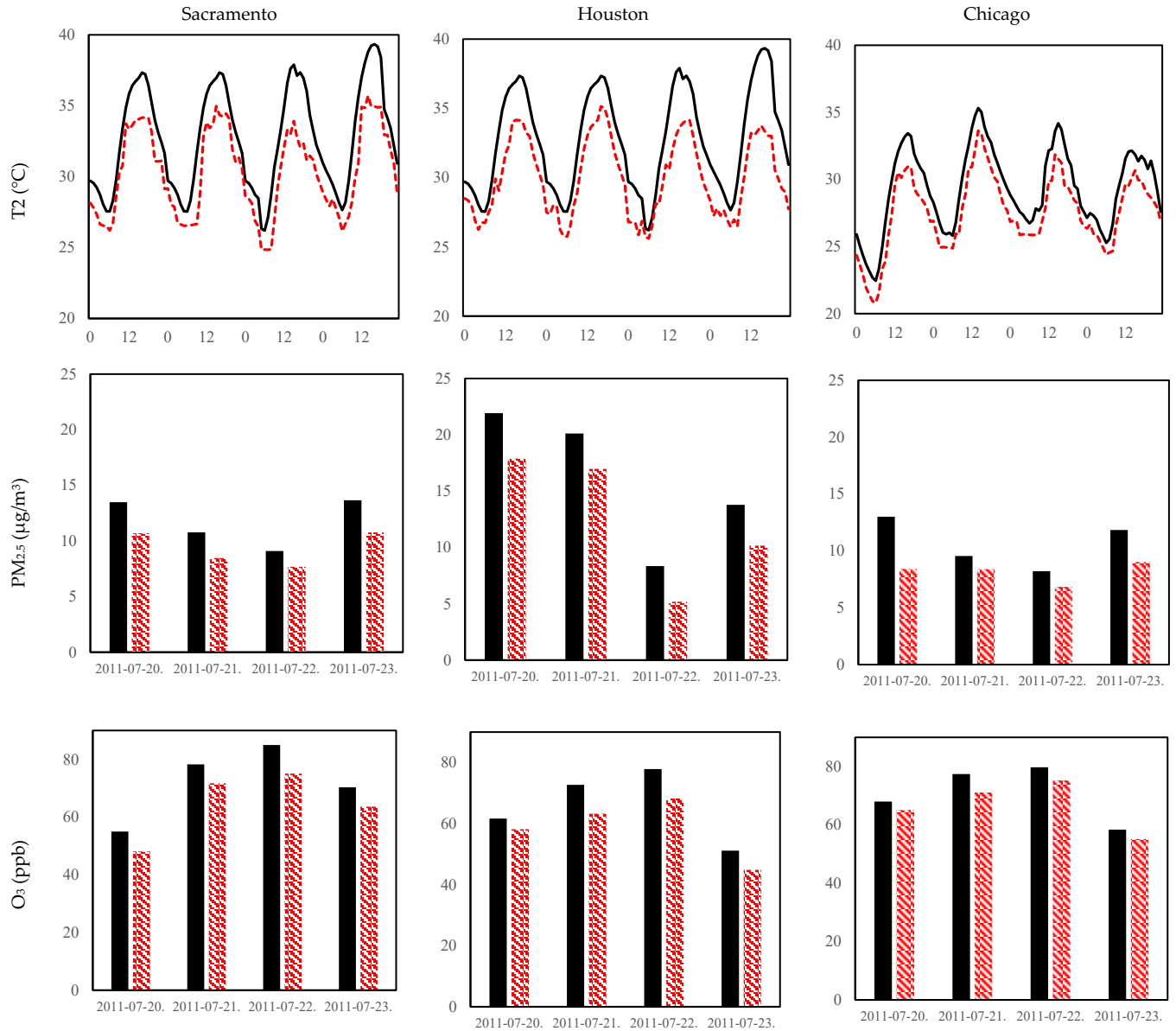
Figure 6.7. The differences between CTRL (solid line and black bar chart) and ALBEDO (red dashed line and patterned downward diagonal bar chart) scenarios in hourly T2 (°C) and 24-h avg. PM$_{2.5}$ (µg/m^3) and O$_3$ (ppb) concentrations during the 2011 heat wave period across the urban areas of Sacramento, Houston, and Chicago
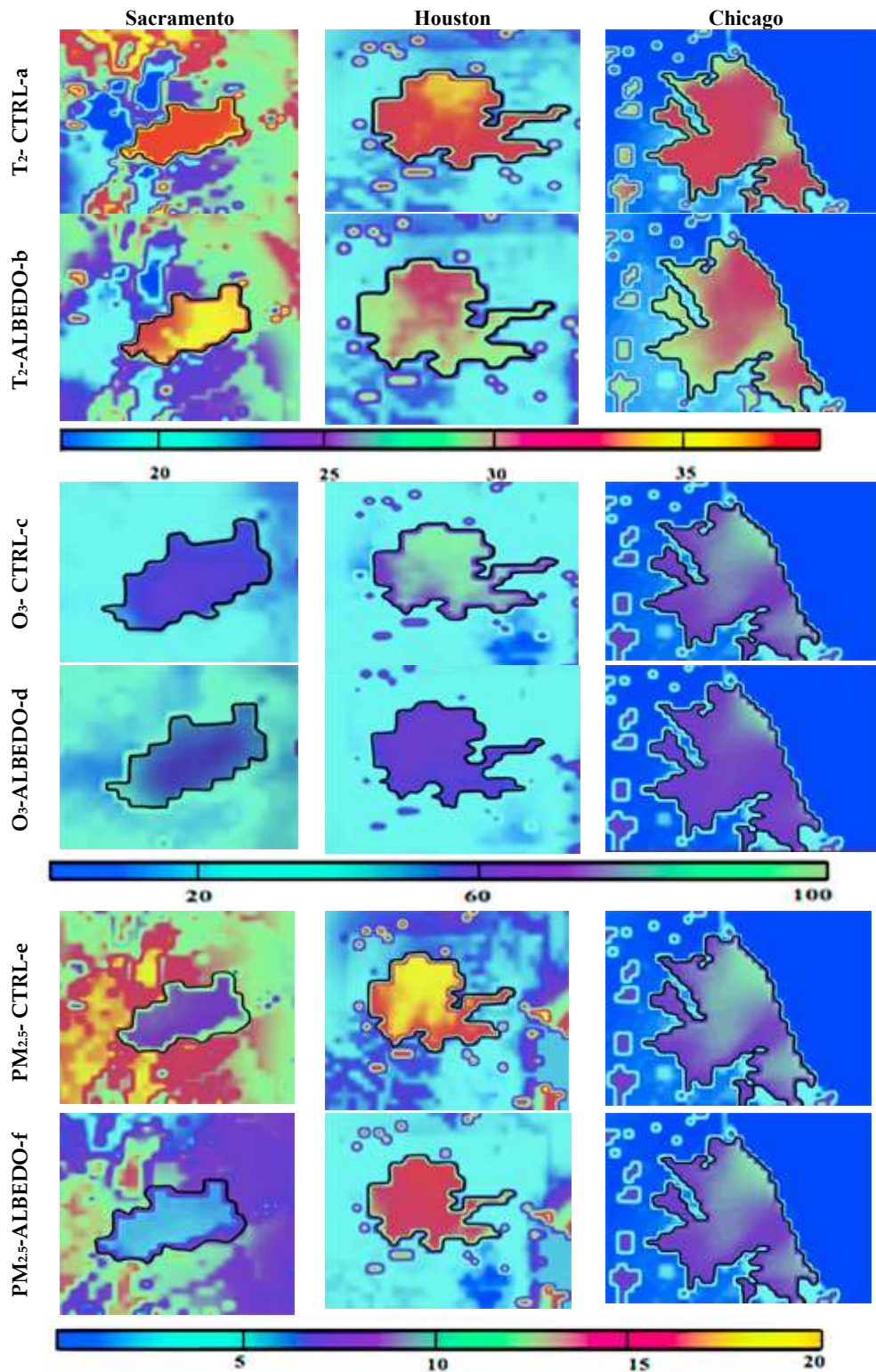
Figure 6.8. The maximum 2-m air temperature (°C), PM$_{2.5}$ (µg/m^3) and O$_3$ (ppb) concentrations in CTRL and ALBEDO scenarios across Sacramento, Houston, and Chicago during the 2011 heat wave period.

6.5. Discussion and Limitations of Urban Climate and Air Quality Studies

Comparing the simulation results with measurements indicates that the WRF-Chem generally reproduces well the hourly variations of meteorological variables, but overpredicts or underpredicts the air pollutant concentrations during the 2011 heat wave period. One of the reasons is that the simulation results are extracted at the start of each hour, whereas the measurements are reported as hourly or daily averages. This means that the comparisons are not made exactly at the same time. Another reason concerns the anthropogenic and biogenic estimations by US-NEI11 (spatial resolution of 1 km) and MEGAN (spatial resolution of 4 km): the spatial resolution of these models cannot accurately account for the actual emissions of anthropogenic and biogenic pollutions into the atmosphere.

The 2011 heat wave period is selected for these simulations to investigate the effects of increasing albedo during the heat wave period in each city. However, in order to specify the effects of increasing albedo, another simulation should be carried out in normal conditions during summer. Then the results need to be compared with the heat wave period to see the typical effects of albedo enhancement in each location. A study to assess the effects of increasing surface albedo for a whole year is also suggested to see its effects during the winter season and during a year as well. Simulation of the entire year can reveal more information on the annual effects of the mitigation strategy. In addition, it is recommended to assesses the effects of other UHI mitigation strategies (such as increasing the fraction of vegetative cover) on urban climate and air quality within a two-way nested approach.

To gain better results of the effectiveness of high-albedo strategy in improving the regional ozone air quality, other episodes and locations with more reliable emission inventories should be further investigated, modeled, and analysed in a more detailed modeling approach. The information on an area's local climate can help to focus on heat island mitigation strategies that best suit their region. For example, cities with dry climates may achieve greater benefits from increasing the vegetative fraction of urban areas (yielding more evapotranspiration) than would cities in humid climates. However, dry-climate cities also need to consider the availability of water to maintain vegetation. A more detailed analysis of simulation results is suggested to investigate the effects of surface modifications on decreasing the temperature-dependent photochemical reaction rates, as

well as decreasing evaporation losses of organic compounds from industrial sectors, and mobile and stationary sources.

6.6. Summary of the Effects of Increasing Surface Albedo on Urban Climate and Air Quality within a Two-Way Nested Simulation Approach

A two-way nested simulation approach is applied to evaluate the surface modification consequences on meteorological processes (air temperature, wind speed, relative humidity, dew point temperature) and chemical reactions (ozone, nitrogen dioxide, fine particulate matters, $PM_{2.5}$ subspecies (particulate sulfate ($SO4_{2.5}$), particulate nitrate ($NO3_{2.5}$) and organic carbon ($OC_{2.5}$)) in a unified continental scale through regional scales. The simulations are conducted over North America through Sacramento, Houston, and Chicago during the 2011 heat wave period. The two-way nested approach with fine-resolution modelling framework can equip researchers with an integrated simulation setup to capture the full impacts of meteorological and photochemical reactions. The applied method would serve as a basis for future model improvements and parameterization development, fine-resolution dispersion, and photochemical modelling for other geographical locations.

The model performance is evaluated by comparing the simulation results with the observations. Despite the model biases in simulating meteorological and chemical variables, the performance of WRF-Chem is generally consistent with most air quality models (Gilliam et al., 2006; Wu et al., 2008; Wang et al., 2009; Liu et al., 2010; Appel et al., 2012), thus is mostly suited for application of simulating and investigating the effects of urban heat island and its mitigation strategies. The MBA, MAE, and RMSE estimations confirmed the model capabilities. For meteorological components, the WRF-ChemV3.6.1, as configured here, captures well the diurnal variations of 2-m air temperature (MBA ~-0.07 ∘C), overpredicts 10-m wind speed (MBA ~1.65 m/s), overpredicts dew point temperature (MBA ~0.4 ∘C), and underpredicts 2-m relative humidity (MBA $\sim-1.4\%$). For chemical component, the model underpredicts the daily fine particular matters ($PM_{2.5}$) (MBA ~-1.5 µg/m^3) and overpredicts the O_3 concentrations (MBA ~5 ppb). The model underpredicts the NO_2 (~2.5 ppb) and overpredicts particulate sulfate (MBE ~5 µg/m^3) and underpredicts particulate nitrate (MBE ~-4 µg/m^3) and organic carbon (MBE ~-3 µg/m3) in urban areas of aforementioned cities during the 2011 heat wave period. The model tends to perform relatively better in urban, rather than in suburban areas.

Two sets of simulations are conducted with regard to surface modifications: the CTRL scenario and the ALBEDO scenario. With albedo enhancement, the results indicated:

- a decrease in air temperature by 2.3∘C in urban areas and 0.7∘C in suburban areas
- a slight increase in wind speed across the domain
- an increase in relative humidity (3%) and dew point temperature (0.3∘C) in urban areas
- a decrease of $PM_{2.5}$ concentrations by 2.7μg/m^3 in urban areas and 1.4μg/m^3 in suburban areas
- a decrease of O_3 concentrations by 6.3ppb in urban areas and 2.5ppb in suburban areas
- minimal changes in $PM_{2.5}$ subspecies
- a decrease of nitrogen dioxide to 1 ppb in urban areas

The results presented here are episode- and region-specific and thus may not provide a suitable basis for generalization to other circumstances. Overall, the results confirm that for Sacramento in California, Houston in Texas, and Chicago in Illinois, the albedo enhancement is an effective mitigation strategy to reduce the air temperature and improve air quality. The results show that Sacramento and Houston benefit more from increasing surface solar reflectance. These findings are an asset for policymakers and urban planning designers. However, the suggestion is to investigate the effects of other UHI mitigation strategies on urban climate and air quality before making decisions or applying any surface modifications. Another suggestion is to simulate the models with more accurate emission inventories. In addition, a simulation for the entire year is recommended that can reveal more information of the mitigation strategy impacts.

6.7. Applications of a Two-Way Nested Simulation Approach in Urban Climate and Air Quality Studies

A two-way nested approach provides an integrated simulation setup to capture the full impacts of meteorological processes and photochemical reactions in the atmosphere. This approach reduces the uncertainties associated with scale separation and grid resolution. It provides a good understanding of the effects of surface modification strategies on urban climate and air quality. The prepared modeling setup here can assist other researches to investigate the effects of any mitigation strategies in other locations and episodes. In addition, it can be applied to investigate the effects of increasing surface reflectivity on aerosol-radiation-cloud interactions in the atmosphere, which is the other objective of this dissertation. The results of this assessment are presented in the following chapter (Chapter 7). The other application is to estimate the albedo fraction of urban areas and its correlation with air temperature and ozone concentrations. The results of these analyses are presented in Chapter 8.

Chapter 7
Effects of Increasing Surface Reflectivity on Aerosol-Radiation-Cloud Interactions in the Urban Atmosphere

The primary pollutants emitted from natural and anthropogenic sources turn into secondary compounds by photochemical reactions and atmospheric meteorological factors. Aerosols affect the radiative balance of the Earth-Atmosphere system by scattering and absorbing the incoming solar radiation directly and by influencing cloud formation and precipitations indirectly (IPCC 2013; Zhang et al., 2014 and 2008). The aerosols impact cloud properties by convective potential energy such as radiation, relative humidity and wind shear (Fan et al., 2013). The evaporative cooling of water bodies during daytime is recognized to modulate the influence of aerosols on the processes of convective systems (Tao et al., 2011). Aerosols also act as cloud condensation nuclei (CCN) and may impact the life-time, albedo, and precipitation of cloud systems, through a complex interaction between cloud micro-physics and dynamics (Chen et al., 2011; Archer-Nicholls et al., 2015). There are two opposite effects of aerosols on cloud formation and precipitation, due to aerosol radiative properties and CCN potentials: aerosols reduce the downward solar radiation to the ground, decreasing sensible heat fluxes to evaporate water and thus lessening precipitation; or they absorb solar radiation, gain heat, and enhance the formation of convective clouds, thus increasing precipitation (Kluser et al., 2008; Levin and Brenguier, 2009; Koren et al., 2005; Fan et al., 2013). Current understanding of aerosol effects on the radiative budget and hydrological cycle of the climate system is still inadequate at the fundamental level.

Some uncertainties also exist in aerosol estimation because of their heterogeneous distribution and complex interactions with radiation and clouds in the atmosphere (IPCC AR5, 2013).

Aerosols have a significant impact on climate state (Jacobson, 2002; Chung and Seinfeld, 2005; H. Liao et al., 2009) and future climate changes with regard to employment of mitigation strategies (Brasseur and Roeckner, 2005). WRF-Chem is used to combine the nonlinear effects of aerosols and simulate the interaction of aerosols, meteorology, chemistry and radiation in a fully interactive manner (Grell et al., 2005, 2013 and 2014). WRF_Chem has been employed in a wide range of studies and is capable of simulating the feedbacks among various atmospheric processes and meteorological components, air quality and atmospheric interactions (Grell and Baklanov, 2011; Baklanov et al., 2014; Fast et al., 2012; Gao et al., 2011; Qian et al., 2009; Zhang et al., 2010). Saide et al. (2012) and Yang et al. (2011) evaluated the WRF-Chem simulations of aerosol-cloud-precipitation interactions over the Southeast Pacific (SEP) for one month. The comparisons with measurements and satellite data indicated that the model performed reasonably well in predicting aerosols and clouds. Zhang (2008) applied WRF-Chem over eastern Texas in August 2000 to show that the presence of aerosols causes a decrease in temperature by up to 0.18 ℃ near the surface and an increase by up to 0.16 ℃ at the top of planetary boundary layer (~30 km). Zhang et al. (2014) represented a decrease of 0.22–0.59 mm/day in domain-wide mean precipitation over eastern Texas.

Accordingly, radiation parametrization determines the energy balance of the domain. The urban surfaces receive shortwave energy from the sun. Urban surfaces absorb part of the energy, heat the surface and local atmosphere, reflect the rest, and emit longwave radiation. Surface modification will affect the energy balance of the domain. Increasing surface albedo enhances the reflectivity of the urban area and affects the radiation budget, local temperature and cloud formation. But as important as the topic is, the effects of any surface modifications have not been investigated on the aerosol, radiation and cloud interactions in urban areas. Here, the effects of heat island mitigation strategy are investigated on aerosol-radiation-cloud interactions over the Greater Montreal Area. The research presented in this chapter is summarized in the article, "Effects of Increasing Surface Albedo on Aerosol-Radiation-Cloud Interactions in Greater Montreal Area, Canada," submitted to a journal.

7.1. Defining Simulation Domain and Period

The horizontal domain of the simulation is composed of three two-way nested domains covering North America (445 × 338 grids), part of Ontario and Quebec provinces (139 × 124 grids), and the Greater Montreal Area (GMA) (101 × 71 grids) with the horizontal resolution of 12km, 4km and 800m, respectively. The vertical resolution includes 35 vertical layers. Figure 7.1 shows the simulation domains and land use/land cover. The simulation period extended over seven consecutive hottest days during the 2011 heat wave period, from the 17th to 23rd of July. The first 48h of the simulation is disregarded as the spin-up time.
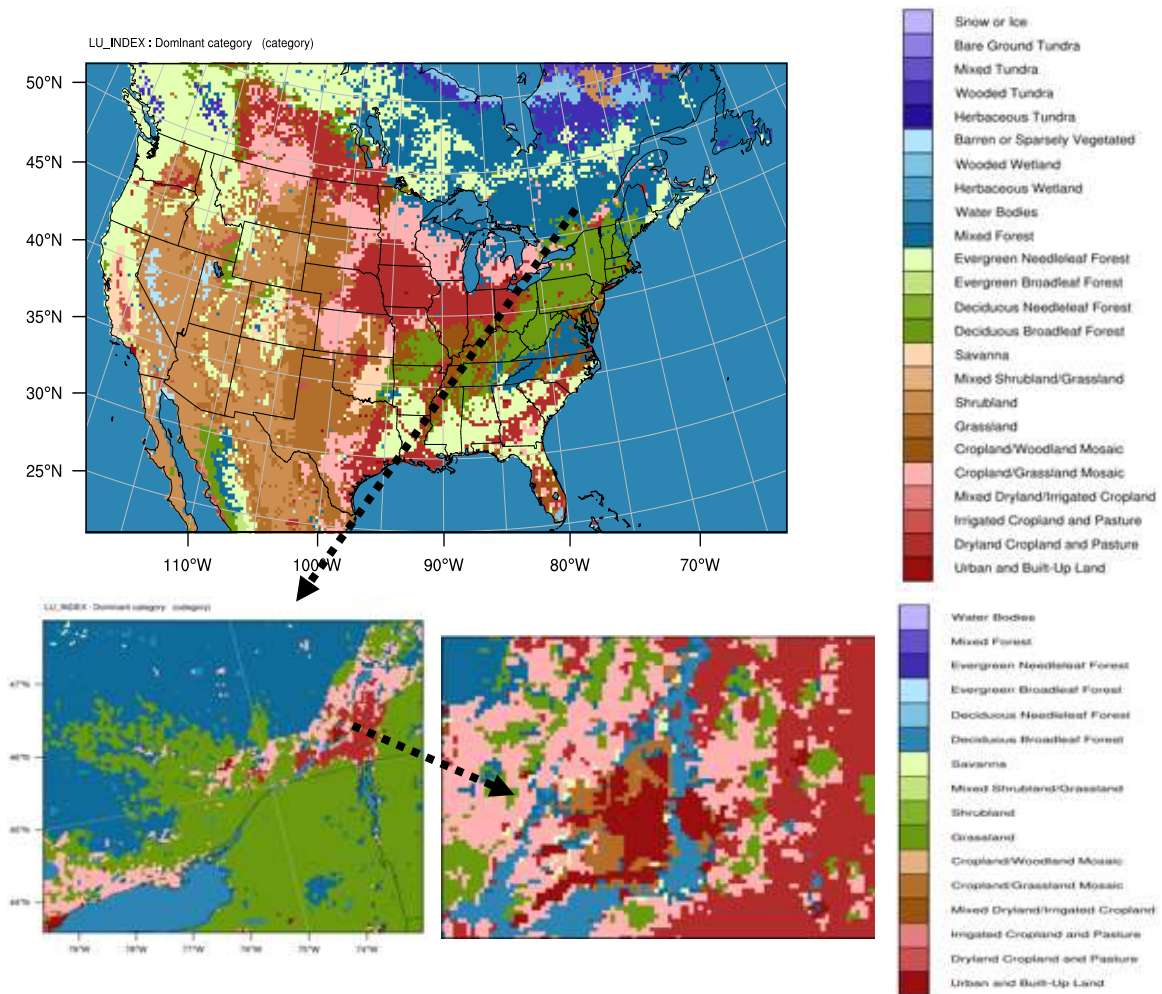
Figure 7.1. The land use/ land cover of the 1st domain over North America (grid size: 12km × 12km), the 2nd domain over Ontario and Quebec provinces (grid size: 4km × 4km) and 3rd domain over Greater Montreal Area (grid size: 800m × 800m)

7.2. Preparation of Input Data for Physical and Chemical Parameterizations

The simulation is conducted with the initial and boundary conditions obtained from the North American Regional Reanalysis (NARR). Land use was derived from the USGS 24-category data

set. The physical and chemical parameterizations are modified to be coupled with the Model for Simulating Aerosol Interactions with Chemistry (MOSAIC) aerosol scheme (Zaveri et al., 2008) and the Carbon Bond Mechanism (CBM-Z) gas phase chemistry scheme (Zaveri and Peters. 1999). Table 7.1 summarized the physical and chemical parametrizations that are used in WRF-Chem

Table 7.1. Selected physical and chemical parameterizations applied in WRF-Chem

Category	Option Used
Microphysics	Morrison double-moment scheme
Radiation Schemes (shortwave & longwave)	RRTMG
Land Surface	NOAH LSM
Planetary Boundary Layer	Mellor-Yamada-Janjic Scheme
Cumulus clouds	Grell3D
Gas-phase Chemistry	CBM-Z
Photolysis	Fast_J
Anthropogenic emissions	US-NEI11
Biogenic emissions	MEGAN
Aerosol scheme	MOSAIC 8-bin
Advection Scheme	Runge–Kutta 3rd order

7.3. Simulation Scenarios to Estimate the Effects of Increasing Surface Reflectivity on Aerosol, Radiation and Cloud Interactions

Four scenarios are defined to separate the impacts of aerosol-radiation interactions from aerosol-cloud interactions. The base scenario represents the processes of meteorological and chemical interactions without considering the aerosol interaction with radiation and cloud, wet scavenging and convective parameterizations (hereafter referred to BASE). In the second, third and fourth simulations, model treatments remain the same as the BASE scenario, but the parameters are activated regarding the aerosol-radiation (as direct effect; hereafter referred to AD-DE), aerosol-cloud (as semi-direct effect; hereafter referred to AC-SDE), and aerosol-radiation-cloud interactions (as indirect effect; hereafter referred to ARC-IDE). In addition, the effects of increasing surface reflectivity are investigated on aerosol-radiation-cloud interactions in the atmosphere. Two sets of simulations, each set consisting of the four aforementioned scenarios, are conducted: CTRL case (UHI effects) and ALBEDO case (increasing surface reflectivity (ISR) effects). Each scenario with albedo enhancement is referred to as ISR. Table 3.19 summarizes these scenarios. The changes are in bold.

Table 7.2. Two sets of simulation: CTRL Cases and ALBEDO Cases. Four sets of scenarios for each case: control simulation with no ARC interactions (BASE), aerosol and radiation interactions as direct effect (AR-DE), aerosol and cloud interactions as semi-direct effect (AC-SDE) and the aerosol-radiation-cloud interactions as indirect effect (ARC-IDE). In ALBEDO cases, each scenario is repeated with regard to Increasing Surface Reflectivity (ISR).

simulations	Scenario	Aerosol-radiative feedback	Aerosol-cloud feedback	Convective parameterization
CTRL Cases	BASE	Off	Off	Off
	AR-DE	**On**	Off	Off
	AC-SDE	Off	**On**	**On**
	ARC-IDE	**On**	**On**	**On**
ALBEDO Cases	ISR-BASE	Off	Off	Off
	ISR-AR-DE	**On**	Off	Off
	ISR-AC-SDE	Off	**On**	**On**
	ISR-ARC-IDE	**On**	**On**	**On**

7.4. Estimation of Aerosol-Radiation, Aerosol-Cloud and Aerosol-Radiation-Cloud Interactions

Radiative flux occurs because of the shortwave radiation reaching the ground and the outgoing longwave radiation and is a combination of scattering, absorption and emission of shortwave and longwave radiation. These estimations split into the balance of incoming shortwave radiation (SW) and outgoing longwave radiation (LW). A set of calculations are defined in Chapter 3 to estimate the radiative budget (RB) over the simulation domain as the difference between the radiation going into the system and the outgoing radiation. For the two scenarios (CTRL and ALBEDO), the radiative balance (ΔRB) is defined based on the differences between their simulation results. As the incoming radiation is the same for all scenarios, the ΔRB is estimated to be equal to the differences in outgoing radiation. The direct, semi-direct and indirect effects of aerosol on radiation budget is also calculated. The aerosol characteristics are assumed to be the same and the sky is assumed to be clear over the domain during the simulation.

Here, the effects of aerosols on the hydrological cycle and of cloud formation on atmospheric stability is minimal, because of the choice of simulation period. It is estimated as the water mixing ratio (Q_{WMR}), which is a gram of water per kilogram of dry air (g/kg) in the atmosphere. The Q_{WMR} is calculated as a combination of the cloud water mixing ratio ($Q_{C_{WMR}}$), rain water mixing ratio ($Q_{R_{WMR}}$) and water vapor mixing ratio ($Q_{V_{WMR}}$) in the atmosphere (g/kg) (Chapter 3).

7.5. Evaluation of Meteorological and Photochemical Model Performance

To evaluate the model performance, the ARC-IDE simulation results are compared with measurements obtained from weather and air quality stations across the GMA during the 2011 heat wave period (21st to 23rd of July). The hourly 2-m air temperature (T2, °C), 10-m wind speed (WS10, m/s) and 2-m relative humidity (RH2, %) are compared with measurements from four weather stations (McTavish (MT), Pierre Elliott Trudeau Intl (PET), St-Hubert (SH), Ste-Anne-de-Bellevue (SAB)). The hourly modelled fine particulate matter (PM$_{2.5}$, μg/m^3), ozone (O$_3$, ppb) and nitrogen dioxide (NO$_2$, ppb) concentrations are compared with measurements from four air quality stations (Decarie Interchange (28), Montreal Airport (66), St-Jean-Baptiste (3), Ste-Anne-de-Bellevue (99)). The mean bias error (MBE), mean absolute error (MAE) and root mean square error (RMSE) of the hourly meteorological parameters (T2 (°C), WS10 (m/s), RH (%)) and chemical components (O$_3$(ppb), PM$_{2.5}$(μg/m^3), NO$_2$(ppb)) are presented in Tables 7.3, 7.4 and 7.5, respectively. Figure 7.2 shows scatterplots of simulated vs. actual measurements of meteorological and chemical variables. The correlation coefficient (R^2) of a linear regression between simulated and measured values are also presented in these figures.

The meteorological performance of the model indicates that the WRF-Chem slightly underpredicts the spatial distribution of 2-m air temperature (MBE= -0.3°C, MAE and RMSE ~1°C), slightly overpredicts 10-m wind speed (MBE= 0.4 m/s, MAE and RMSE ~1m/s), and underpredicts 2-m relative humidity (MBE= -4.3%, MAE= 7% and RMSE=9%). The 2-m air temperature results show a strong correlation (0.85 < R^2 <0.93) with measurements. They show that the model is capable of predicting T2 and the spatial distribution of temperature in urban and rural areas (Figure 7.2-T2). The wind speed is well predicted in urban areas (R^2 = 60) compared to rural areas (R^2 = 40) (Figure 7.2-WS). But the model underpredicts the spatial distribution of relative humidity. This underestimation shows that the microphysics scheme and cloud scheme do not precisely account for the processes of transforming water (rain, vapor, cloud, etc.) and moisture fluxes in the atmosphere. It also shows the model limitation in properly capturing wind speed impacts on water mixing ratio and water content of the air. Figure 7.2-RH shows the correlations between measured and simulated RH range from 0.6 to 0.8.

The chemical component of the model indicates that the WRF-Chem tends to underpredict fine particulate matter (PM$_{2.5}$) (MBE = −0.6 μg/m^3, MAE = 5 μg/m^3 and RMSE = 6.5 μg/m^3), overpredict ozone (O$_3$) (MBE= 3.2 ppb, MAE= 10 ppb, and RMSE=13 ppb), and overpredict the nitrogen dioxide (NO$_2$) (MBE= 1.3 ppb, MAE= 5 ppb, and RMSE=6.3 ppb) concentrations. The

correlation between measured and simulated value shows that the model is capable of predicting air quality parameters reasonably well in urban areas compared to their surroundings. The R^2 of fine particulate matter ranges from 0.5 to 0.7 (Figure 7.2-$PM_{2.5}$). Figure 7.2- O_3 shows the comparison between measurements and simulations of ozone concentrations and indicates a good correlation range from 0.6 to 0.8. The overestimation of O_3 concentrations is due to the NOx and VOCs calculations in emission inventories (US-NEI11 for NOx estimation and MEGAN for VOCs estimation) in the chemistry packages. The NO_2 concentrations are also estimated as one of the precursors in ozone formation. The results show that the model tends to overpredict the nitrogen dioxide and has a poor correlation between measured and simulated value range from 0.4 to 0.5.

Figure 7.3 shows the results of T2, WS10, RH2, $PM_{2.5}$, O_3 and NO_2 comparisons with a weather station (McTavish) and an air quality monitoring station (Decarie Interchange) located near the downtown of the GMA for three days. The model on average slightly underpredicts the particulate matter concentration at night and moderately overpredicts it during the day, but it well captures the morning and evening peaks of $PM_{2.5}$. As for ozone prediction, the model overpredicts its concentrations during the day, but the model accurately captures the peak ozone concentrations. Thus, it shows that the model prediction for ozone is well suited to be compared with the 8-h peak concentration of National Ambient Air Quality Standard (NAAQS), which is also correlated with human health effects. Overall, the performance of WRF-Chem, as configured here, is consistent with most air quality models such as the fifth-generation NCAR/Penn State Mesoscale Model (MM5) and the CMAQ model (Gilliam et al., 2006; Wu et al., 2008; Wang et al., 2009; Liu et al., 2010) in simulating meteorological and chemical variables. Thus, it is well suited for application of simulating and investigating the effects of heat island, and for mitigation strategy regarding aerosols' direct, semi-direct and indirect effects.

Table 7.3. Mean Bias Error (MBE) of T2 (°C), WS10 (m/s), RH2(%) from 4 weather stations: McTavish (MT), Pierre Elliott Trudeau Intl (PET), St-Hubert (SH), Ste-Anne-de-Bellevue (SAB); O_3(ppb), $PM_{2.5}$(µg/m^3), and NO_2(ppb) from 4 air quality stations (Decarie Interchange (DI), Montreal Airport (MA), St-Jean-Baptiste (SJB), Ste-Anne-de-Bellevue (SAB) over GMA during the 2011 heat wave period (21st to 23rd of July)

Variables	Mean Bias Error (MBE)				Average
	MT	**PET**	**SH**	**SAB**	
T2 (°C)	-0.41	-0.34	-0.48	0.10	-0.28
WS10 (m/s)	0.40	0.23	0.70	0.29	0.40
RH2 (%)	-2.83	-6.09	-4.32	-3.81	-4.26
	DI	**MA**	**SJB**	**SAB**	
24-h avg. O_3(ppb)	8.53	-4.04	3.17	5.13	3.19
24-h avg. $PM_{2.5}$(µg/m^3)	0.69	4.90	-1.87	-6.18	-0.62
24-h avg. NO_2(ppb)	0.84	1.11	-5.92	9.43	1.36

Note: The definitions of statistical measurements are as follows Zhang et al. (2006): MBE $= \frac{1}{N}\sum_1^N (C_M - C_O)$, C_M and C_O are modeled and observed concentrations, respectively and N is the total number of model and observation pairs.

Table 7.4. Mean Absolute Error (MAE) of T2 (°C), WS10 (m/s), RH2(%) from 4 weather stations: McTavish (MT), Pierre Elliott Trudeau Intl (PET), St-Hubert (SH), Ste-Anne-de-Bellevue (SAB); O_3(ppb), $PM_{2.5}$(µg/m^3), and NO_2(ppb) from 4 air quality stations (Decarie Interchange (DI), Montreal Airport (MA), St-Jean-Baptiste (SJB), Ste-Anne-de-Bellevue (SAB)over GMA during the 2011 heat wave period (21st to 23rd of July)

Variables	Mean Absolute Error (MAE)				Average
	MT	**PET**	**SH**	**SAB**	
T2 (°C)	0.84	0.88	0.78	1.03	0.88
WS10 (m/s)	0.68	1.02	1.44	0.66	0.95
RH2 (%)	6.79	7.81	5.59	6.47	6.66
	DI	**MA**	**SJB**	**SAB**	
24-h avg. O_3(ppb)	8.85	12.57	7.91	10.12	9.86
24-h avg. $PM_{2.5}$(µg/m^3)	2.84	5.23	5.04	6.33	4.86
24-h avg. NO_2(ppb)	2.16	2.29	6.02	9.44	4.97

Note: The definitions of statistical measurements are as follows Zhang et al. (2006): MAE $= \frac{1}{N}\sum_1^N |C_M - C_O|$ C_M and C_O are modeled and observed concentrations, respectively and N is the total number of model and observation pairs.

Table 7.5. Root mean square error (RMSE) of T2 (°C), WS10 (m/s), RH2(%) from 4 weather stations: McTavish (MT), Pierre Elliott Trudeau Intl (PET), St-Hubert (SH), Ste-Anne-de-Bellevue (SAB); O_3(ppb), $PM_{2.5}$(µg/m^3), and NO_2(ppb) from 4 air quality stations (Decarie Interchange (DI), Montreal Airport (MA), St-Jean-Baptiste (SJB), Ste-Anne-de-Bellevue (SAB) over GMA during the 2011 heat wave period (21st to 23rd of July)

Variables	Root Mean Square Error (RMSE)				Average
	MT	**PET**	**SH**	**SAB**	
T2 (°C)	1.08	1.13	1.10	1.24	1.13
WS10 (m/s)	1.07	1.39	1.90	0.87	1.30
RH2 (%)	9.60	10.16	7.74	8.42	8.98
	DI	**MA**	**SJB**	**SAB**	
24-h avg. O_3(ppb)	10.96	14.48	11.45	14.74	12.91
24-h avg. $PM_{2.5}$(µg/m^3)	3.79	6.59	7.81	7.98	6.54
24-h avg. NO_2(ppb)	3.10	3.33	8.08	11.04	6.38

Note: The definitions of statistical measurements are as follows Zhang et al. (2006): RMSE $= \left[\frac{1}{N}\sum_1^N (C_M - C_O)^2\right]^{1/2}$ C_M and C_O are modeled and observed concentrations, respectively and N is the total number of model and observation pairs

145
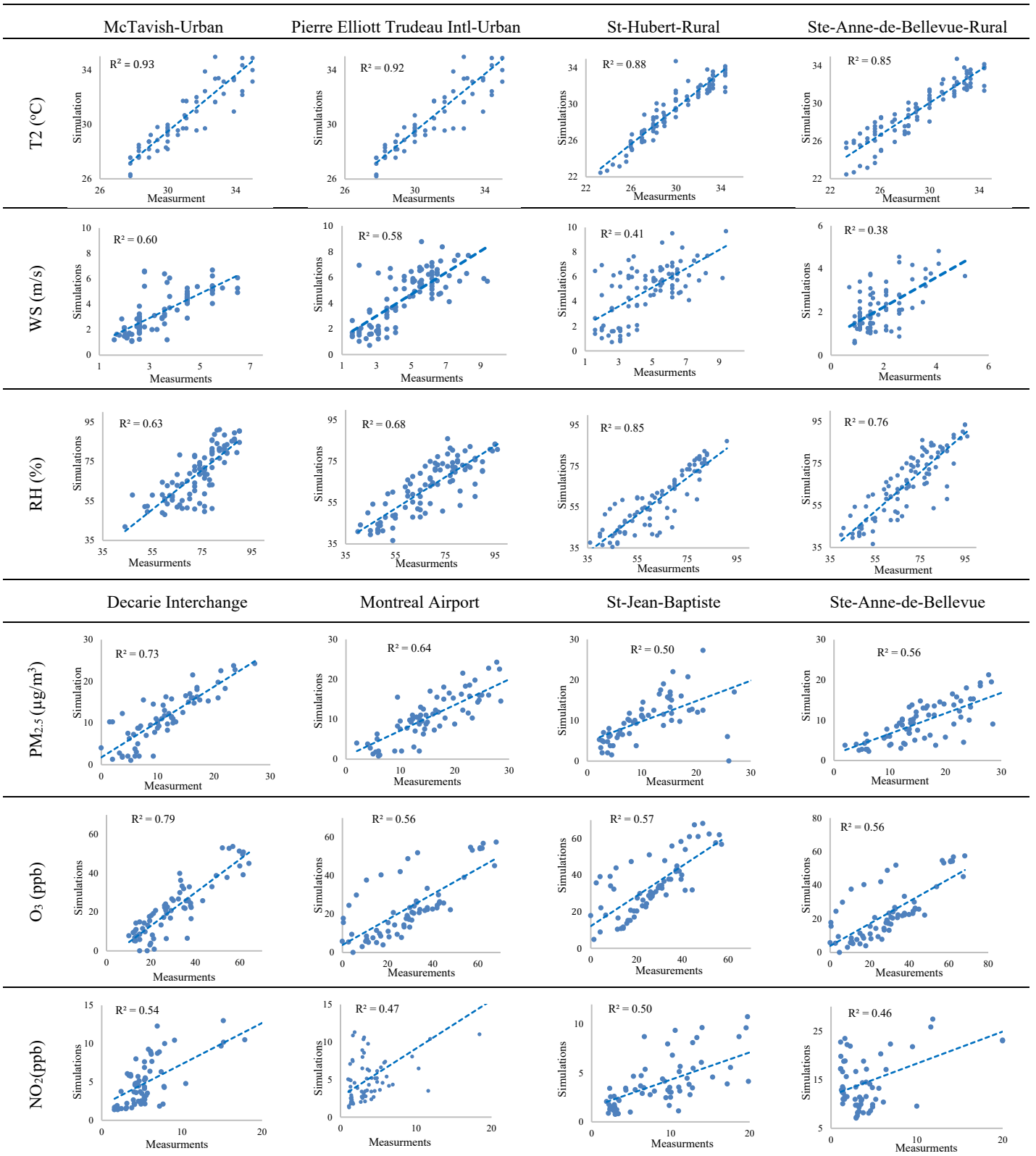
Figure 7.2. Comparison of simulation with measurements of T2 (°C), WS10 (m/s), RH2(%) from 4 weather stations: McTavish (MT), Pierre Elliott Trudeau Intl (PET), St-Hubert (SH), Ste-Anne-de-Bellevue (SAB); and O₃(ppb), PM₂.₅(μg/m³), NO₂(ppb) from 4 air quality stations (Decarie Interchange (DI), Montreal Airport (MA), St-Jean-Baptiste (SJB), Ste-Anne-de-Bellevue (SAB) over the Greater Montreal Area during the 2011 heat wave period (21st to 23rd of July) [the blue dots are measurements and simulations. The dashed blue line indicates the correlation between measurements and simulations (trendline)]

146
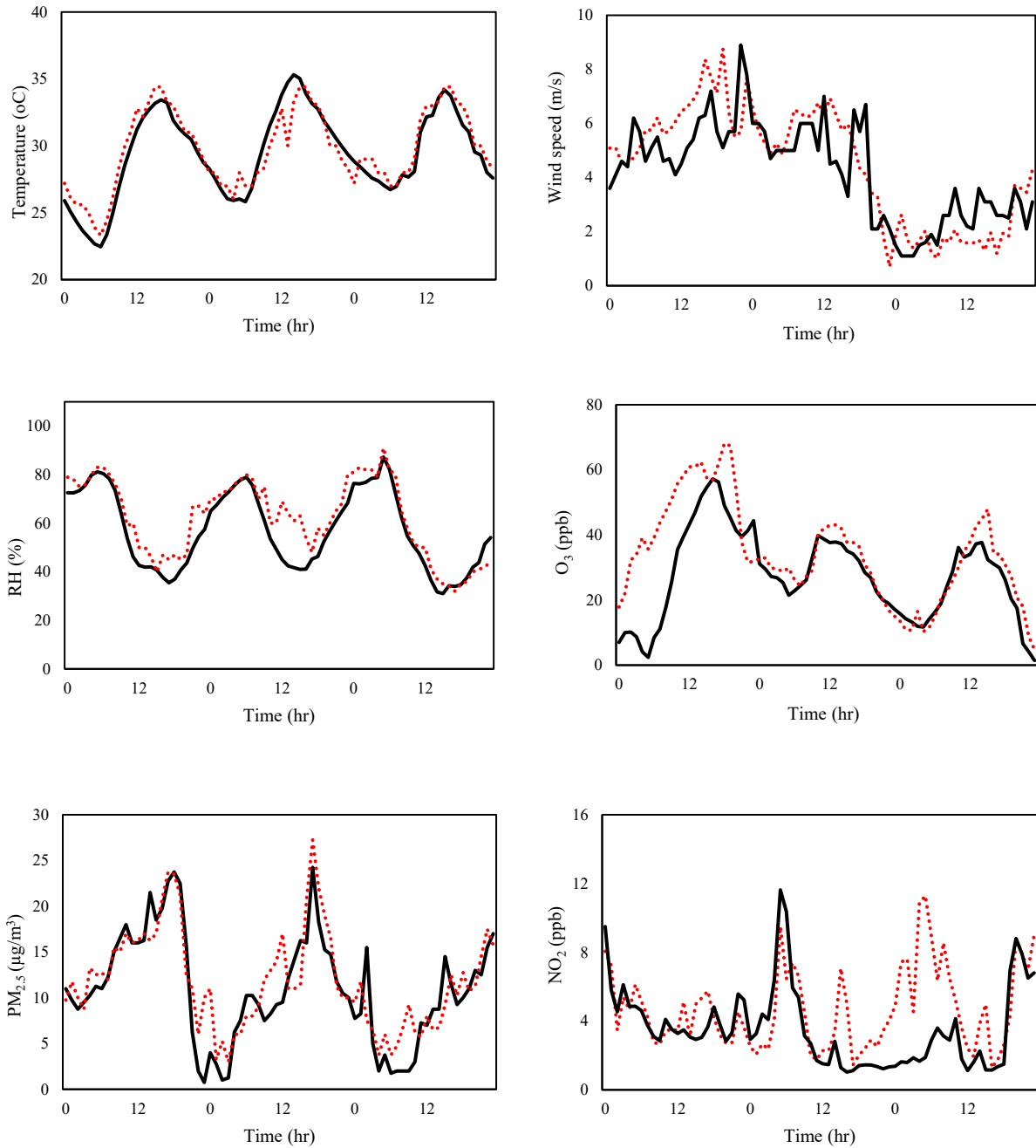
Figure 7.3. Hourly comparison of simulation with measurements of T2 (ºC), WS10 (m/s), RH2(%) from McTavish weather station (MT) and O_3(ppb), $PM_{2.5}$(µg/m^3), and NO_2(ppb) from Decarie Interchange (DI) air quality monitoring station over GMA during the 2011 heat wave period (21st to 23rd of July)[The black solid line shows simulations and the red dashed line shows measurements]

7.6. Effects of Heat Island on Aerosol-Radiation-Cloud Interactions

The simulations are performed during the 2011 heat wave period in the Greater Montreal Area. The effects of heat island are investigated on aerosol, radiation and cloud interactions. The results of four CTRL case simulations including BASE, AR-DE, AC-SDE, and ARC-IDE are analyzed spatially. The radiative balance (RB) and down-welling shortwave radiation at the surface (SW↓) are estimated based on calculations in Chapter 3. The water mixing ratio (WMR) is also calculated as a combination of the cloud water mixing ratio, rain water mixing ratio and water vapor mixing ratio in the atmosphere as grams per kg of dry air (g/kg).

The 2-m air temperature responses vary according to the aerosols' direct and indirect effects. The PBL height changes are closely related to the air temperature change spatially. Table 7.6 summarizes the averaged radiative balance (RB, W m^{-2}), down-welling shortwave radiation at the surface (SW↓, Wm^{-2}), 2-m air temperature (T2, ^{o}C), water mixing ratio (WMR, g/kg), fine particulate matter (PM$_{2.5}$, μg/m^3), and ozone concentrations (O$_3$, ppb) disaggregated as three regions—the North, Center, and South parts of the Greater Montreal Area.

- **Aerosol-Radiation Interactions: Direct Effects**

In general, the direct effects of aerosols are a decrease in radiative balance and thus reduction in the heat absorbed by the surfaces. Aerosol concentrations cause a decrease in shortwave radiation reaching to the ground, whether by scattering or absorbing the incoming solar radiation. Here, the SW↓ reduces by 30Wm^{-2} and thus the RB reduces by almost 15Wm^{-2} across the entire domain. The radiative balance is positive during the daytime and negative at night. The effect of aerosol-radiation indicates that the radiative balance reduces in day and at night in the AR-DE simulation compared to the BASE case simulation.

The 2-m air temperature increases by 0.2^{o}C in the Center of the domain. The increase of air temperature indicates that the aerosols are mostly absorbent because of their sizes (e.g., coarse particulate matters) or compositions (e.g., black carbon). A minimal change in T2 and radiation variables is seen in the Southern part of the GMA. In the North of the domain, a decrease in T2 occurs by 0.4^{o}C. The reduction in T2 indicates that aerosols scatter the solar radiation more and thus cool urban atmosphere. The planetary boundary layer height follows the same changes in temperature: as temperature increases, the PBLH increases and thus the concentration of pollutants across the domain slightly decreases. Here, the PBLH increases by 20m in the Center and decrease by 30m in the Northern parts and decreases slightly in the South region. The water mixing ratio

increases by 0.3g/kg in the Center, whereas it decreases by 0.5g/kg in the North part. The increase in WMR shows that the high temperature causes more evaporation from water bodies in the domains.

In terms of air quality, the aerosol-radiation interactions cause a slight decrease in fine particulate matter concentrations in the South, but reductions by 5 and $3\mu g/m^3$ over the Center and North regions. This reduction owes to an increase in the PBLH. Ozone is a temperature-dependent component, but at most a slight increase is observed across the domains. Figure 5 shows hourly comparisons of air temperature (T2, $^{\circ}$C), relative humidity (RH, %), fine particulate matter (PM$_{2.5}$, $\mu g/m^3$) and ozone (O$_3$, ppb) concentrations with measurements and base case simulations. The hourly comparison of planetary boundary layer height (PBLH, m) and radiative balance (RB, W m^{-2}) of AR-DE and BASE simulations are also presented in Figure 5. The black and yellow solid lines respectively represent the BASE and AR-DE simulations. The red dashed line shows measurements.

- **Aerosol-Cloud Interactions: Semi-Direct Effects**

Considering the effects of clouds and humidity, during the daytime, more incoming solar radiation is absorbed by clouds and water droplets in the atmosphere. The absorption causes changes in radiation balance at the surface. The RB is less during the day and less during the night compared to the base case simulation results. The sky was mostly clear during the simulation period (the 2011 heat wave). Clear sky condition implies slight to minimal changes to radiative budget and downwelling short-wave radiation at the surface. The RB reduces by 10Wm^{-2} over the domain.

The daily 2-m air temperature decreases by 0.2°C and the PBLH shows slight changes. The water mixing ratio also indicates minimal changes. The daily particulate matter concentrations decrease by $3\mu g/m^3$ and the daily ozone concentrations decrease by 2ppb over the entire region, which can be the result of a decrease in temperature. Figure 6 shows the effects of aerosol-cloud interactions on air temperature (T2, $^{\circ}$C), relative humidity (RH, %), fine particulate matter (PM$_{2.5}$, $\mu g/m^3$) and ozone (O$_3$, ppb) concentrations, planetary boundary layer height (PBLH, m) and radiative balance (RB, Wm^{-2}) during the 2011 heat wave period. The black and blue solid lines respectively represent the BASE and AC-SDE simulations. The red dashed line shows measurements.

- **Aerosol-Radiation-Cloud Interactions: Indirect Effects**

To simulate the indirect effects of aerosols, the aerosol-radiation feedbacks, the aerosol-cloud feedbacks and the convective parameterizations are activated. Therefore, the combination of aerosols that scatter solar radiation is estimated with the aerosols that can absorb the solar radiation and emit infrared radiation, thus increasing air temperature, increasing convective parameterization, and increasing latent heat fluxes and cloud formation in the area. Because of the effects of aerosols, water droplets and clouds, less solar radiation ($\sim20Wm^{-2}$) approaches the surface and more longwave radiation is absorbed by particulate matter. Hence, the radiative balance decreases by $25Wm^{-2}$. The 2-m air temperature increases over the Center and North part of the domain by up to $0.5^{\circ}C$ and $0.3^{\circ}C$, respectively. A minimal increase in T2 is also seen in the South area by up to $0.1^{\circ}C$. The PBLH increases by up to 40m in the Center and North and increases by 10m in the South part of the domain. The water mixing ratio slightly increases in the Center and decreases in other part of the Greater Montreal Area.

The aforementioned changes in meteorological parameters impose impacts on every aspect of air quality. They alter photolysis rates and kinetics that lead to changes in chemical transformation. They also change transport and deposition processes. Meanwhile, the changes in solar radiation and temperature affect the NO_2 photolysis rates and hence the formation of O_3 and $PM_{2.5}$ in the atmosphere. This complex interaction also decreases pollutant formation, as expected, because of a reduction in photochemical reactions and temperature caused by ARC interactions. But since the photolysis rate depends on other factors such as albedo and clouds, a dual behavior of pollutant transformation and concentration is seen in the simulations. On the other hand, an increase in planetary boundary layer height leads to a better advection and diffusion of pollutants and decreases their concentrations. The $PM_{2.5}$ shows smaller concentrations by $2\mu g/m^3$, whereas the ozone shows a larger concentration by nearly 2ppb compared to the base case scenario across the entire domain. These conclusions confirm the nonlinear effects of ARC interactions and the effects that aerosols introduce into the atmosphere and weather patterns. Figure 7 shows the effects of aerosol-radiation-could interactions on air temperature (T2, $^{\circ}C$), relative humidity (RH, %), fine particulate matter ($PM_{2.5}$, $\mu g/m_3$) and ozone (O_3, ppb) concentrations, planetary boundary layer height (PBLH, m) and radiative balance (RB, Wm^{-2}) during the 2011 heat wave period. The black and purple solid lines respectively represent the BASE and ARC-IDE simulations. The red dashed line shows measurements.

The results of direct, semi-direct, indirect effects and BASE case simulations are compared with measurements from weather and air quality stations in the GMA during the weekdays

(Tuesday to Friday) of the 2011 heat wave period. Figure 8 shows the comparison of T2 (°C), RH2 (%), O_3 (ppb), and $PM_{2.5}$ ($\mu g/m^3$) with measurements. The AR, AC, ARC, and BASE are presented with yellow, blue, purple, black solid lines, respectively and the measurements are presented with a dashed red line. These comparisons illustrate that the meteorological and photochemical variables can be better predicted in the ARC simulation because the aerosol-radiation, aerosol-cloud and convective parametrizations are activated. This comparison also indicates that the model is well capable of predicting the 2-m air temperature but under-predicts the fine particulate matters and overpredicts the ozone concentrations.

Table 7.6. Summary of meteorological and chemical variable statistics on the 21st of July 2011 heat wave period: radiative balance (RB, W m^{-2}), down-welling shortwave radiation at surface (SW↓, W m^{-2}), T2 (°C), PBLH (m), water mixing ratio (WMR, kg/kg), $PM_{2.5}$($\mu g/m^3$), O_3(ppb) concentrations averaged and disaggregated by regions: North, Center, South over the Greater Montreal Area. Uncertainties (±) show standard deviation across domain.

Scenarios	RB (W m^{-2})			SW↓(W m^{-2})		
	North	Center	South	North	Center	South
BASE	37 ± 35	55 ± 35	30 ± 25	336 ± 20	300 ± 20	330 ± 15
AR-DE	34 ± 30	40 ± 30	26 ± 30	330 ± 15	290 ± 10	300 ± 10
AC-SDE	30 ± 20	45 ± 20	25 ± 20	330 ± 15	300 ± 15	310 ± 10
ARC-IDE	30 ± 25	30 ± 25	22 ± 25	300 ± 10	290 ± 10	300 ± 10
Scenarios	T2(°C)			WMR (g/kg)		
	North	Center	South	North	Center	South
BASE	29.4 ± 0.5	30.4 ± 0.2	30.5 ± 0.3	27 ± 0.5	25 ± 0.6	23 ± 0.2
AR-DE	29.5 ± 0.5	30.7 ± 0.4	30.6 ± 0.5	27 ± 0.7	25 ± 0.5	23 ± 0.7
AC-SDE	29.5 ± 0.4	30.9 ± 0.1	30.8 ± 0.2	26 ± 0.8	25 ± 0.8	22 ± 0.9
ARC-IDE	29.9 ± 0.6	30.9 ± 0.7	30.9 ± 0.7	26 ± 0.9	25 ± 0.7	22 ± 0.7
Scenarios	$PM_{2.5}$($\mu g/m^3$)			O_3(ppb)		
	North	Center	South	North	Center	South
BASE	23 ± 2	28 ± 5	17 ± 3	65 ± 10	66 ± 7	62 ± 10
AR-DE	20 ± 5	23 ± 5	16 ± 4	65 ± 15	66 ± 8	60 ± 10
AC-SDE	20 ± 2	24 ± 2	15 ± 3	62 ± 10	66 ± 2	60 ± 12
ARC-IDE	22 ± 8	25 ± 2	16 ± 5	64 ± 10	66 ± 6	63 ± 10
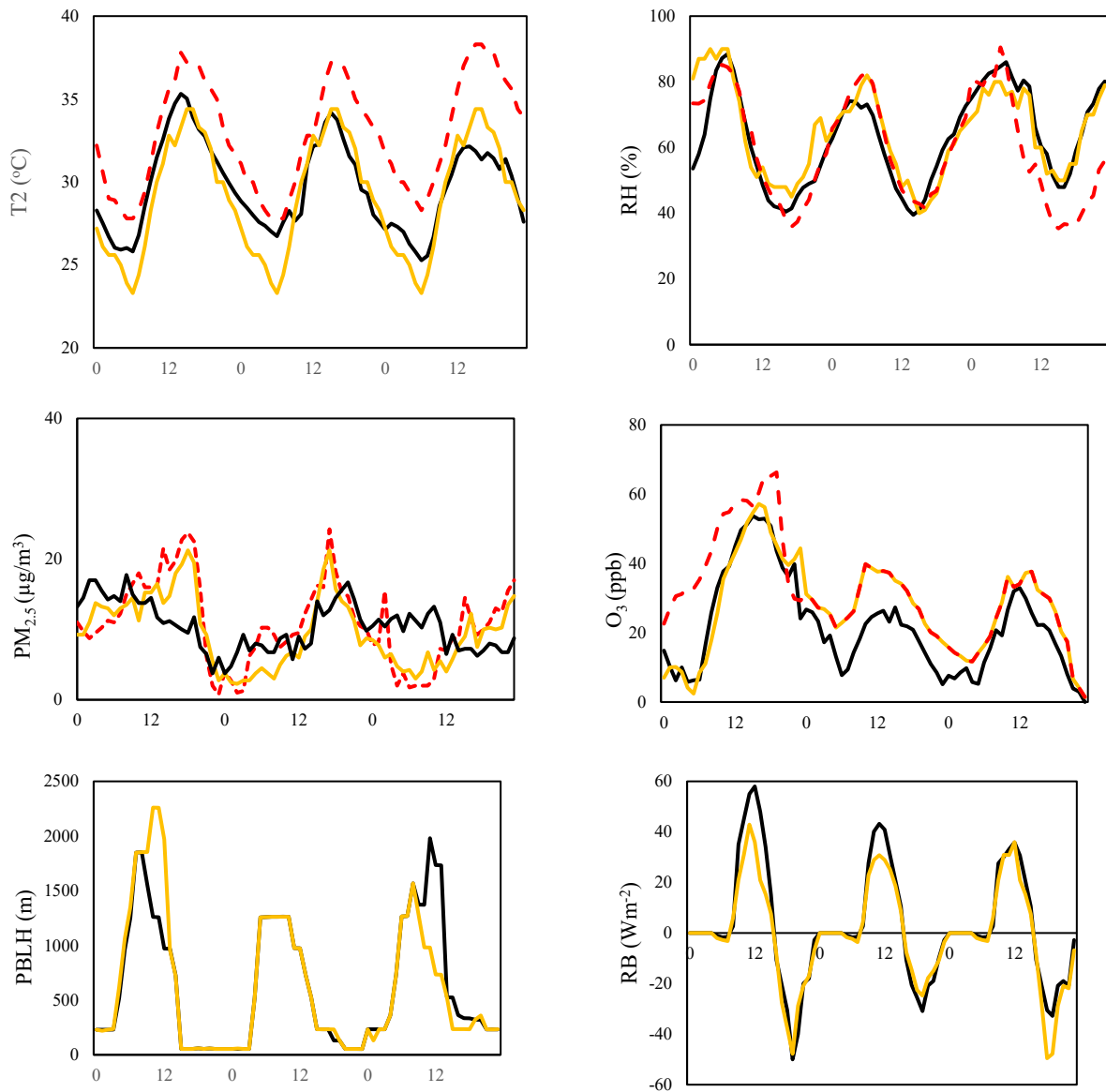
Figure 7.4. Hourly comparison of aerosol-radiation (AR-DE) simulation with base case (BASE) simulation and measurements of T2 (°C), RH2(%), O_3(ppb), $PM_{2.5}$(μg/m³). Hourly comparison of aerosol-radiation (AR-DE) simulation with base case (BASE) simulation of planetary boundary layer height (PBLH, m) and radiative balance (RB, W m⁻²) over GMA during the 2011 heat wave period (21st to 23rd of July) [The black and yellow solid lines respectively represent the BASE and AR-DE simulations. The red dashed line shows measurements]
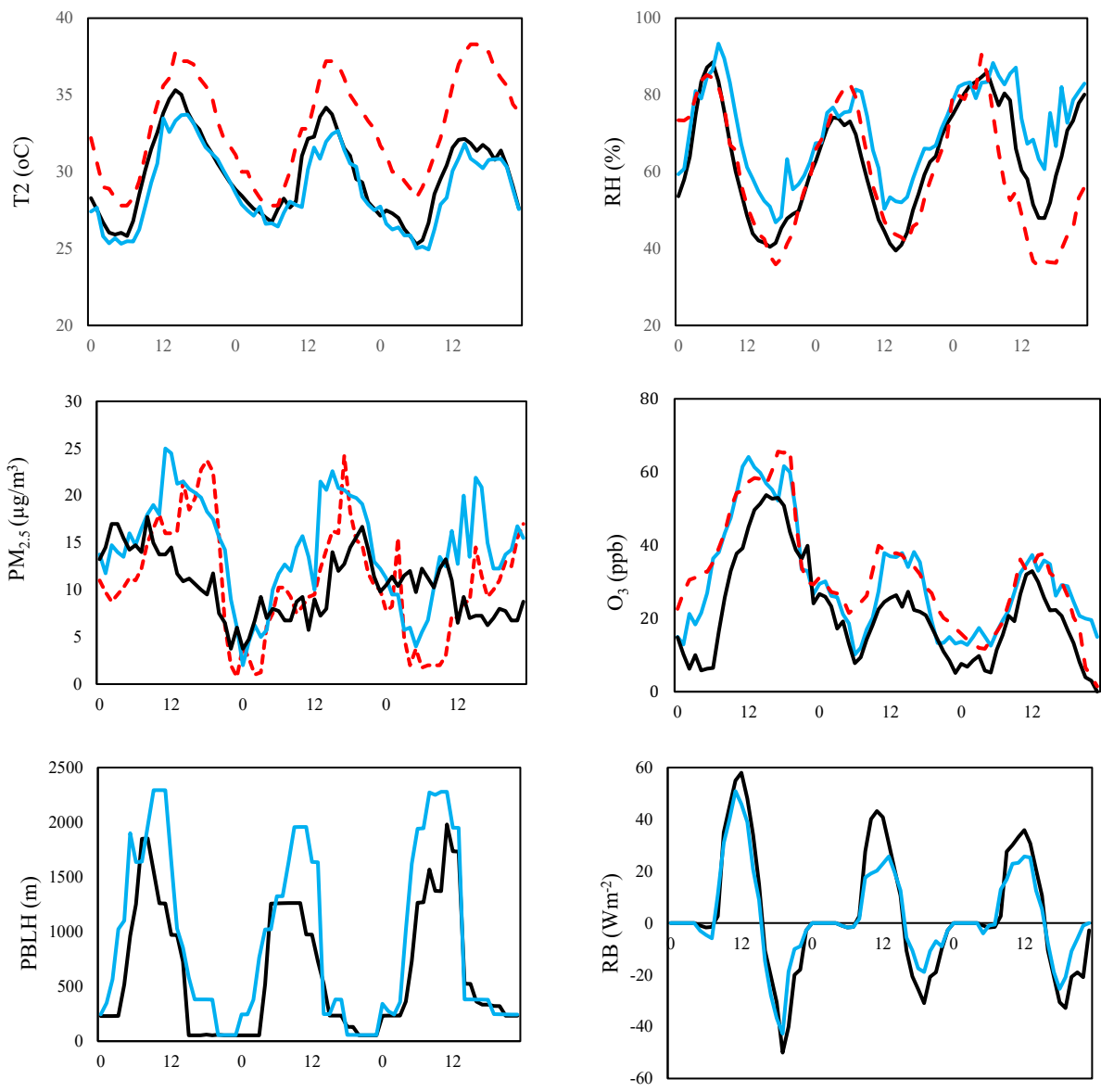
Figure 7.5. Hourly comparison of aerosol-cloud (AC-SDE) simulation with base case (BASE) simulation and measurements of T2 (ºC), RH2(%), O₃(ppb), PM₂.₅(μg/m³). Hourly comparison of aerosol-cloud (AC-SDE) simulation with base case (BASE) simulation of planetary boundary layer height (PBLH, m) and radiative balance (RB, W m⁻²) over GMA during the 2011 heat wave period (21st to 23rd of July) [The black and blue solid lines respectively represent the BASE and AC-DE simulations. The red dashed line shows measurements]
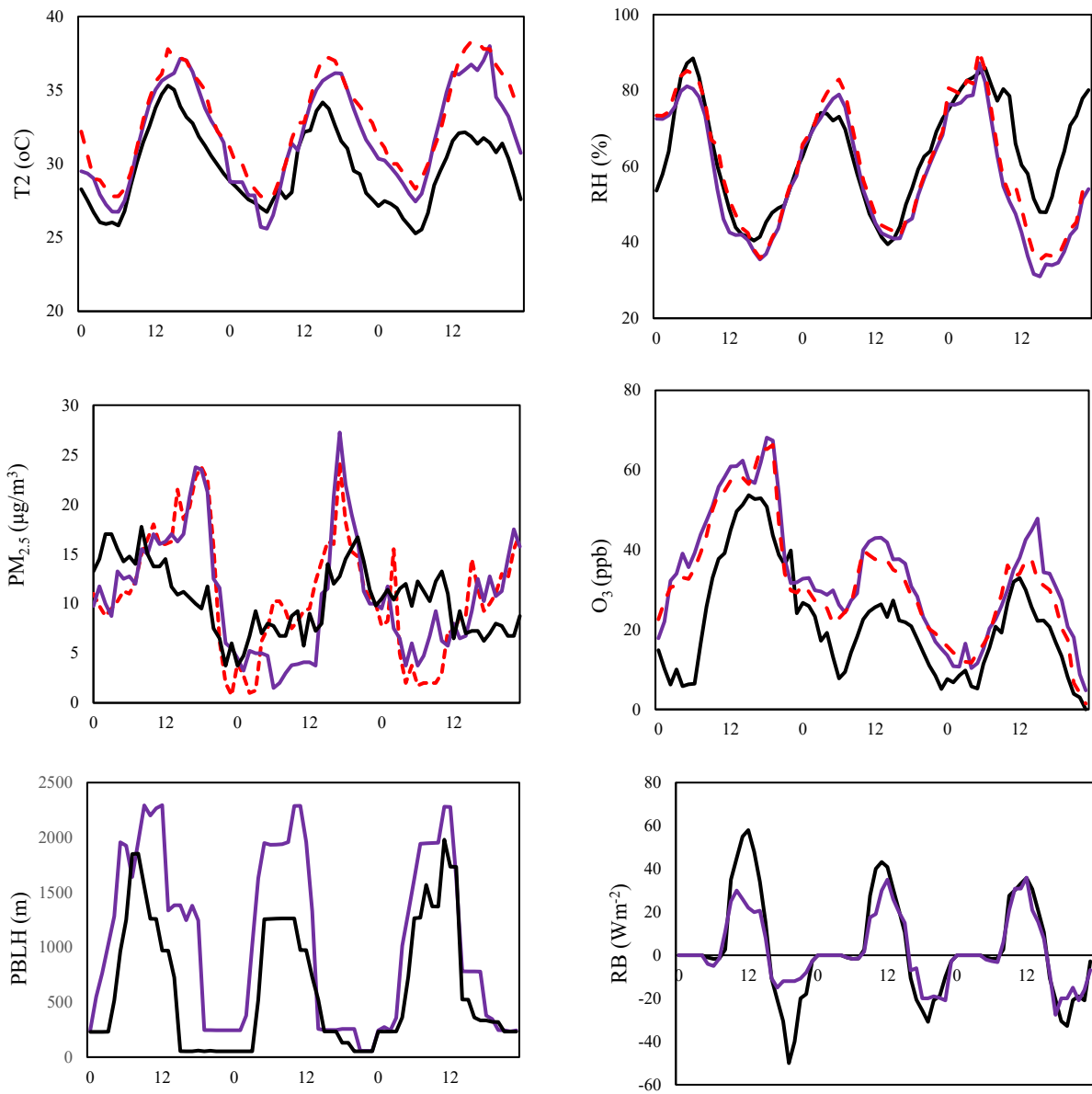
Figure 7.6. Hourly comparison of aerosol-radiation-cloud (ARC-IDE) simulation with base case (BASE) simulation and measurements of T2 (ºC), RH2(%), O_3(ppb), $PM_{2.5}$(µg/m^3). Hourly comparison of aerosol-radiation-cloud (ARC-IDE) simulation with base case (BASE) simulation of planetary boundary layer height (PBLH, m) and radiative balance (RB, W m^{-2}) over GMA during the 2011 heat wave period (21st to 23rd of July) [The black and purple solid lines respectively represent the BASE and ARC-IDE simulations. The red dashed line shows measurements]

154
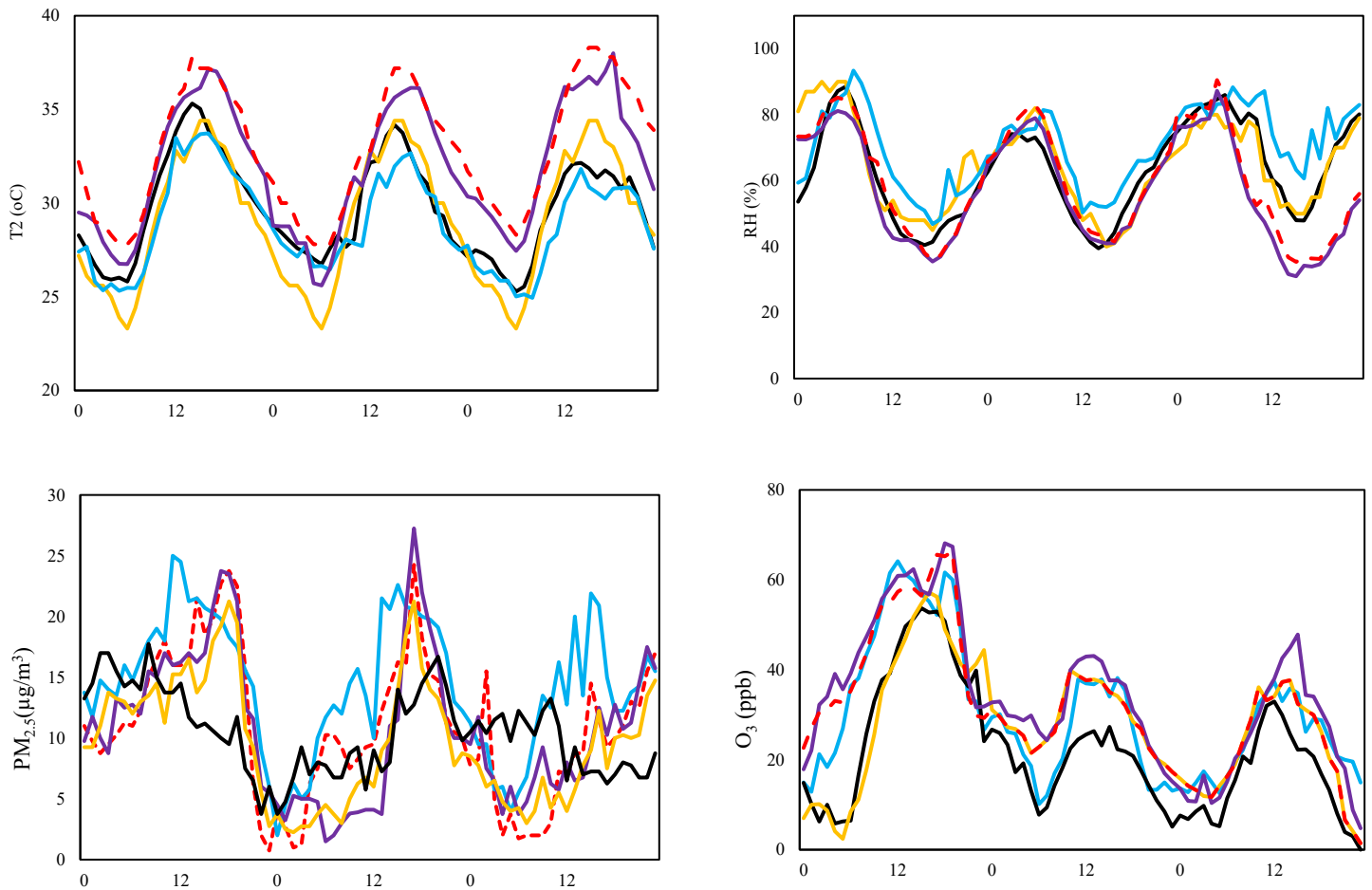
Figure 7.7. The comparison between direct (AR-DE), semi-direct (AC-SDE), indirect (ARC-IDE), and base (BASE) case scenarios of T2(°C), RH2(%), O_3(ppb), $PM_{2.5}$(μg/m^3) with measurements in McTavish station near the center of the GMA. The AR, AC, ARC, BASE is presented with yellow, blue, purple, black solid lines, respectively and the measurements is presented with dashed red line.

7.7. Effects of Increasing Surface Reflectivity (ISR) on Urban Climate, Air Quality and Aerosol, Radiation and Cloud Interactions

The effects of albedo enhancement is analysed on the radiation balance at solar noon (RB, Wm^{-2}), cloud coverage (CC, %), water mixing ratio (WMR, g$_{water}$/kg$_{dry\ air}$), 2-m air temperature (T2, °C), planetary boundary layer height (PBLH, m), ozone (O_3, ppb), fine particulate matters ($PM_{2.5}$, μg/m^3) and nitrogen dioxide (NO_2, ppb) concentrations. Table 8 presents the differences between CTRL and ALBEDO (CTRL−ALBEDO) scenarios in four cases (ISR-BASE, ISR-AR-DE, ISR-AC-SDE, ISR-ARC-IDE) over the North, Center and South part of the Greater Montreal Area during the 2011 heat wave period.

7.7.1. Effects of ISR on Meteorological and Chemical Components

155

Here, the effects of increasing solar reflectivity are presented in the ISR-BASE case simulation, where the radiation and cloud feedbacks are not considered, and convective parameterization is not activated. The simulation results show that albedo enhancement leads to a net decrease in daily 2-m air temperature by up to 0.7°C in the Center and 0.5°C in other parts of the domain during the 2011 heat wave period. The water mixing ratio reduces by 0.2g/kg across Montreal and cloud coverage indicates no change because of albedo increment. The heat island mitigation strategy causes a decline in solar noon radiative balance by almost $20Wm^{-2}$. The planetary boundary layer height lower by 28m in the Center and 20m in the North and South part of Montreal. Decreasing temperature leads to a decrease in planetary boundary layer height, which reduces the advection and diffusion of pollutants. Hence, this phenomenon increases the pollutant concentrations and also assists the O_3 and NO reaction rates to produce NO_2. This is the reason that the ozone concentration is higher in some parts of the domain. On the other hand, by decreasing air temperature, the rate of temperature-sensitive photochemical reaction rates reduces and thus affords a decrease in daily ozone concentrations by nearly 4ppb in the Greater Montreal Area during the heat wave period. Albedo enhancement causes a decline in fine particulate matter by $4\mu g/m^3$ and minimal changes to nitrogen dioxide concentrations.

7.7.2. Effects of ISR on Aerosol, Radiation and Cloud Interactions in the Urban Atmosphere

The effects of albedo enhancement on aerosol and radiation interactions show a slight increase in air temperature by ~ 0.2°C in the Center area and a decrease by the same amount in the other parts of the domain. The reason for these changes is because of the simulation configuration that only the radiation feedback is considered, and the convective parametrization and cloud formation has not been activated. Thus, the results indicate that because of the absorbent components in the Center part of the GMA, although the albedo is increased, but the outgoing longwave radiation from the surface is trapped by atmospheric aerosols. Therefore, without considering the convective parametrizations, the air temperature increases and heats the local atmosphere. An increase in temperature lead to a rise in water mixing ratio by nearly 0.2g/kg in the Center and a decline by the same amount in other part of the domain, but no changes in cloud coverage. Increasing surface reflectivity causes a decrease in radiative balance at solar noon by around $15Wm^{-2}$ across Montreal. Heat island mitigation strategy reduces the planetary boundary layer height across the domain by 10m. Surface albedo modifications cause a decrease in the temperature-dependent photochemical reaction rates in the atmosphere, even though it is minimal. The O_3 (ppb), $PM_{2.5}$ ($\mu g/m^3$), and NO_2

(ppb) concentrations decrease slightly as a consequence of increasing surface reflectivity on aerosol and radiation interactions.

The aerosol and cloud interactions show that albedo enhancement leads to a slight decrease in 2-m air temperature. This occurs because the aerosol-radiation interactions have not been estimated in these simulations. As temperature reduces, the evaporation from water bodies reduces, and thus a decrease in water mixing ratio is expected. But the results show that water mixing ratio behaves differently and increases slightly across the domain. The cloud coverage also rises by 3% across the entire domain. Increasing solar reflectance causes a decrease in radiative balance at solar noon by around $20 Wm^{-2}$. Albedo enhancement causes a decrease in PBLH in a range of 20m in the GMA. The fine particulate matters and ozone concentrations decrease by $1 \mu g/m^3$ and 1ppb in aerosol-cloud (ISR-AC-SDE) simulation, respectively.

Considering the nonlinear and complex interaction of aerosol-radiation-cloud in the atmosphere, the 2-m air temperature decreases by $0.5^{\circ}C$ in the Center and North parts of the domain and $0.3^{\circ}C$ in the Southern area. The water mixing ratio decreases to 0.5 g/kg in the Center and 0.3g/kg in the North and South regions. The cloud coverage declined by 3-5% across the Greater Montreal Area. Albedo enhancement leads to a net decrease in radiative balance at solar noon by $25 Wm^{-2}$ in the Center and $22 Wm^{-2}$ in the Northern and Southern regions. Increasing solar reflectivity imposes a decrease in planetary boundary layer height to 25m and 20m in the Center and other parts of Montreal, respectively. Heat island mitigation strategy affords a decrease in temperature and thus ozone concentrations to almost 3ppb across the entire domain. The fine particulate matter also reduces to about $3 \mu g/m^3$ in the Center and $2 \mu g/m^3$ in other areas during the 2011 heat wave period. The NO_2 concentrations reduces slightly compared to $PM_{2.5}$ and O_3 concentrations across the domain of interest.

Table 8. The differences between CTRL and ALBEDO scenarios of T2 ($^{\circ}C$), RH2(%), O_3 (ppb), $PM_{2.5}$ ($\mu g/m^3$), NO_2 (ppb), NO (ppb) over North, Center and South part of GMA during the 2011 heat wave period

CTRL−ALBEDO	Region	ISR-BASE	ISR-AR-DE	ISR-AC-SDE	ISR-ARC-IDE
Δ RB at noon (Wm^{-2})	North	18	15	20	22
	Center	20	16	21	25
	South	17	17	21	23
Δ Cloud coverage (%)	North	No change	No change	3	3
	Center	No change	No change	3	5
	South	No change	No change	3	3
ΔWMR (g/kg)	North	0.2	0.2	-0.2	0.3
	Center	0.2	-0.2	-0.2	0.5
	South	0.2	0.2	-0.2	0.3
Δ daily T2 ($^{\circ}C$)	North	0.47	0.19	0.25	0.33
	Center	0.67	-0.23	0.25	0.55

	South	0.54	0.21	0.25	0.51
Δ PBLH(m)	North	22	10	20	22
	Center	28	8	23	25
	South	20	10	20	18
24-h avg. O_3(ppb)	North	3.67	0.59	0.74	2.66
	Center	4.41	0.56	0.68	2.76
	South	3.55	0.51	0.57	2.09
24-h avg. $PM_{2.5}$($\mu g/m^3$)	North	3.11	0.98	1.03	2.88
	Center	3.67	0.78	0.54	2.59
	South	3.21	0.60	0.67	1.91
24-h avg. NO_2(ppb)	North	0.19	0.27	0.25	0.28
	Center	0.36	0.18	0.31	0.35
	South	0.13	0.16	0.24	0.23

7.8. Discussion and Limitations of Aerosol, Radiation and Cloud Interactions Assessment

Current understanding of aerosol impacts on the radiative budget and hydrological cycle of the climate system is still inadequate at the fundamental level. Some uncertainties exist in aerosol estimation because of their heterogeneous distribution and complex interactions with radiation and clouds in the atmosphere. Here, a two-way nested approach is applied over the Greater Montreal Area during the 2011 heat wave period. The simulation period is restricted to seven consecutive days during the heat wave event, and hence the short-term response of increasing surface reflectivity is considered. To have a better understanding of aerosol interactions in the atmosphere, it is suggested to perform a simulation over a year to see the seasonal effects as well as rainy and cloudy conditions of these complex nonlinear interactions.

The results of the WRF-Chem simulations, with the meteorological and chemical settings configured here, are in good agreement with measurements, but different settings can also be applied. As with any modeling approaches, there are some issues and caveats to remember when evaluating the simulation outcomes. Some of these concerns relate to the assumptions and fundamental issues during the course of this study—for example, the choice of aerosol scheme, the selection of physical and chemical parametrizations, emission inventories data, and so on. On the other hand, when applying finer resolution grids, the effects of cloud formations and hydrological cycles cannot be captured accurately.

While the simulations illustrate the importance of aerosol-radiation-cloud estimations and the effects of heat island mitigation strategy on these complex interactions, the current study is still subject to a number of limitations. Several issues in model treatments and configurations available for aerosol feedback studies will introduce inaccuracies and uncertainties in model performance.

For example, the MOSAIC aerosol module cannot calculate the estimation of secondary organic aerosols (SOA) accurately and the Fast-J photolysis algorithm disregards the feedbacks of all photochemically-active gases to photolysis. These missing treatments will surely affect the accuracy of aerosol concentrations. In addition, aerosol effects on cloud dynamic feedbacks, hydrological cycle (as precipitation), and convective clouds cannot be fully captured in WRF-Chem, which may cause an underestimation in the indirect effects of aerosols. As mentioned before, seven consecutive days during the 2011 heat wave period is still too short to characterize the long-term variation trend. Nevertheless, this work demonstrates the effects of increasing surface reflectivity on aerosol, radiation and cloud interactions through direct, semi-direct, and indirect effects of aerosols over the Greater Montreal Area and will thus provide a useful foundation upon which future improvements can be identified and focused.

7.9. Effects of Albedo Enhancement on Urban Climate, Air Quality and Aerosol, Radiation and Cloud Interactions in the Urban Atmosphere

The effects of increasing surface reflectivity are investigated on urban climate, air quality and aerosol-radiation and cloud interactions over Greater Montreal Area during the 2011 heat wave period. A two-way nested approach is applied by online coupling of the chemistry package within the solver of the Weather Research and Forecasting model (WRF-Chem). In addition, the WRF-Chem is coupled with a multi-layer of the Urban Canopy Model (ML-UCM) to provide more detail of the effects of surface modifications. This approach simulates the emission, transport, deposition, chemical transformation, and aerosol interactions in the atmosphere. The two-way nested method captures more detailed treatments of urban morphology and responses to heat island mitigation strategies. Therefore, the method estimates the feedbacks between chemistry and meteorological interactions as cloud formation and radiation budget.

The direct, semi-direct and indirect effects of aerosols are analysed. These simulations are conducted with and without convective parameterizations and are performed only with regard to radiation schemes, to separate the instantaneous radiative effects of the aerosol-radiation from aerosol-cloud interactions. The ARC simulation is compared with measurements from weather and air quality monitoring stations. To mitigate the urban heat island impacts, the surface albedo of roofs, walls and grounds increased from 0.2 in CTRL scenario to 0.65, 0.60 and 0.45, respectively, in ALBEDO scenario. The consequences of increasing surface reflectivity are disaggregated spatially for data presentation into three regional subdomains: North, Center, and

South regions of the Greater Montreal Area. The outcomes indicate a decrease in 2-m air temperature, a minimal to slight decrease in water mixing ratio, a decrease in planetary boundary layer height, a decline in radiative budget at solar noon, a decrease in cloud coverage and minimal to slight reductions in ozone, fine particulate matter and nitrogen dioxide concentrations.

Albedo enhancement led to a net decrease in radiative balance at solar noon by 25Wm^{-2} in the Center and by nearly 22Wm^{-2} in the Northern and Southern regions of the Greater Montreal Area during the 2011 heat wave period. The consequences of increasing solar reflectivity on aerosol-radiation-cloud interactions indicated a decrease in 2-m air temperature by 0.5°C in the Center and North parts of the domain and by 0.3°C in the Southern area. The water mixing ratio decreased to 0.5g/kg in the Center and 0.3g/kg in the North and South regions. The cloud coverage declined by 3-5% across the Greater Montreal Area. Increasing urban albedo imposes a decrease in planetary boundary layer height to 25m and 20m in the Center and other parts of Montreal, respectively. Heat island mitigation strategy afforded a decrease in temperature and thus ozone concentrations to 3ppb across the entire domain. The fine particulate matter reduced to about 3μg/m^3 in the Center and 2μg/m^3 in other areas during the 2011 heat wave period. Albedo enhancement causes a decrease in boundary-layer height that reduces the chance of advection and diffusion of pollutants and hence increases the pollutants concentrations. In addition, shallow boundary layer can impose an increase in pollutants reaction rates. Decreasing the contaminates dispersion as well as increasing the chance of chemical reactions result in growing pollutants concentration in some part of the domain. The consequences discussed here are episode and domain specific and may not be applied in generalizing and extrapolating the findings to other times, seasons, or geographical locations.

The effects of increasing surface reflectivity have been investigated on urban climate and air quality. A two-way nested approach is applied in WRF-Chem. This approach simulates the emission, transport, deposition, chemical transformation, and aerosol interactions in the atmosphere. The two-way nested method captures more detailed treatments of urban morphology and responses to heat island mitigation strategies. In addition, the method estimates the feedbacks between chemistry and meteorological interactions as cloud formation, precipitation and radiation budget. However, to what extent the WRF and WRF-Chem results are closer with measurements, a comparison between the meteorological model and photochemical model is required. This comparison indicates the capability of each model in predicting air temperature. In addition, assessing the correlation between albedo enhancement and air temperature illuminates the effects

of this heat island mitigation strategy on urban climate and air quality. These comparisons are presented in the following section with more detail.

7.10. Summary of Simulation Results in terms of Air Temperature Predictions and its Correlation with Albedo Enhancements

The temperature changes because of albedo enhancement are of an interest to urban climate and air quality policymakers. Thus, the performance of WRF and WRF-Chem simulations are also evaluated regarding 2-m air temperature. The WRF and WRF-Chem simulations are compared with measurements. The conclusion of these comparisons is presented in Section 7.10.1. In addition, the correlation between changes in albedo enhancement that impose changes in temperature and ozone concentrations are estimated for three different urban categories (high intensity residential, low intensity residential, and industrial and commercial) in the urban canopy model (UCM). The results of the present study are applied to the Greater Montreal Area (GMA) in Canada. The consequences of increasing surface albedo in three cities—namely, Sacramento (California), Houston (Texas), and Chicago (Illinois) in the USA—are also estimated. These analyses are illustrated in Section 7.10.2.

7.10.1. Air Temperature Prediction in WRF and WRF-Chem

Here, the WRF and WRF-Chem simulations of 2-m air temperature (T2) are compared with measurements (four weather stations (McTavish (MT), Pierre Elliott Trudeau Intl (PET), St-Hubert (SH), Ste-Anne-de-Bellevue (SAB)) across the Greater Montreal Area during the 2011 heat wave period. The mean bias error (MBE), mean absolute error (MAE) and root mean square error (RMSE) are estimated. Table 7.8 summarizes the outcomes. Figure 7.5 compares the T2 of simulations with measurements. The outcomes of WRF-Chem, WRF and measurements are presented by a dashed red line, solid black line and dashed black line, respectively. The comparisons indicate that WRF and WRF-Chem slightly underpredict the 2-m air temperature; though the WRF-Chem outcomes show less error compared to WRF. To perform the WRF-Chem, more efforts are needed in order to select the proper physical parameterizations that can be coupled with proper choice of chemistry packages. In addition, WRF-Chem needs more computational resources to be performed. The estimation of anthropogenic and biogenic emissions is required to be simulated. Table 7.9 summarizes the key features of WRF and WRF-Chem. More details can be found in Chapter 3. Thus, for urban climate simulations, it is suggested to perform the WRF.

But, if the focus of interest is air quality, the WRF-Chem has to be carried out. The WRF-Chem is able to predict the meteorological process and air quality conditions, simultaneously. This is the reason that the WRF-Chem tends to reflect the real atmosphere, and the results have a good agreement with measurements.

Table 7.8. Mean Bias Error (MBE), Mean Absolute Error (MAE) and Root Mean Square Error (RMSE) of T2 (°C) from WRF and WRF-Chem results compared with measurements (McTavish (MT), Pierre Elliott Trudeau Intl (PET), St-Hubert (SH), Ste-Anne-de-Bellevue (SAB)) over GMA during the 2011 heat wave period

Model	Performance	MT	PET	SH	SAB	Average
WRF	MBE	0.07	-0.88	-0.94	0.03	-0.43
	MAE	1.51	1.37	1.30	1.10	1.32
	RMSE	1.91	1.83	1.70	1.47	1.73
WRF-Chem	MBE	-0.41	-0.34	-0.48	0.10	-0.28
	MAE	0.84	0.88	0.78	1.03	0.88
	RMSE	1.08	1.13	1.10	1.24	1.13

The definitions of statistical measurements are as follows Zhang et al. (2006): $MBE = \frac{1}{N}\sum_1^N(C_M - C_O)$, $MAE = \frac{1}{N}$, $RMSE = \left[\frac{1}{N}\sum_1^N(C_M - C_O)^2\right]^{1/2}$, C_M and C_O are modeled and observed concentrations, respectively and N is the total number of model and observation pairs.
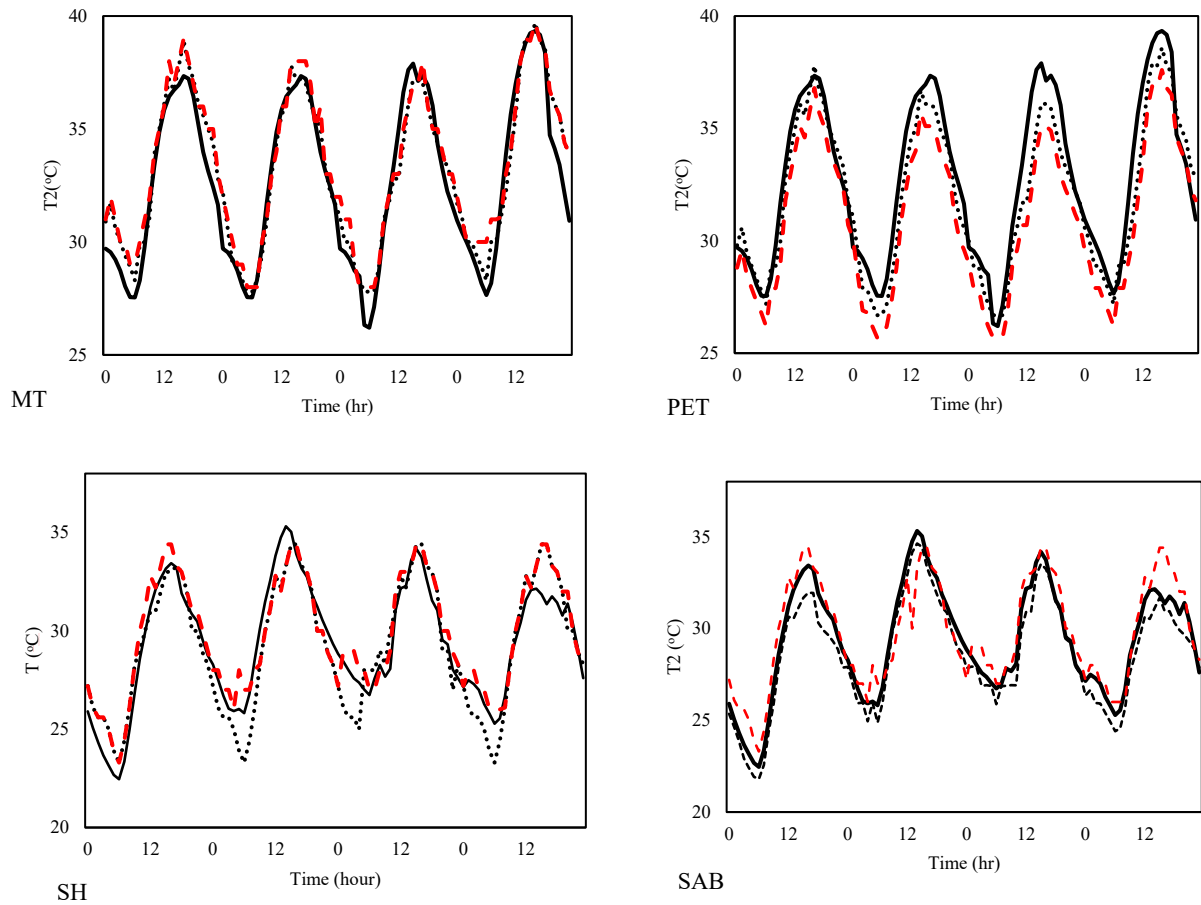
Figure 7.8. The hourly 2-m air temperature (T2, °C) comparisons of WRF results (solid black line) vs. WRF-Chem results (dashed red line) vs. measurements (dashed black line) from four weather stations across the GMA during the 2011 heat wave period (McTavish (MT), Pierre Elliott Trudeau Intl (PET), St-Hubert (SH), Ste-Anne-de-Bellevue (SAB))

Table 7.9. Summary of the WRF and WRF-Chem key features

WRF	WRF-Chem
WRF simulate the advection and diffusion of variables. It has sub-grid scale transport (WRF parameterizations, PBL, convection). WRF can be used for regional and global applications. It has the following capabilities: - Fully compressible nonhydrostatic equations - Complete Coriolis and curvature terms - One-way and Two-way nesting with multiple nests and nest levels - Mass-based terrain-following coordinate - Vertical grid-spacing can vary with height - Four different map-scale factors: (polar stereographic; Lambert-conformal; Mercator; Latitude and longitude - Runge-Kutta 2nd and 3rd order time integration options - Scalar-conserving flux form for prognostic variables - 2nd to 6th order advection options - Monotonic transport and positive-definite advection option for moisture, scalar, tracer, and TKE - Time-split small step for acoustic and gravity-wave modes - Upper boundary absorption and Rayleigh damping & lateral boundary conditions – Full physics options for land-surface, planetary boundary layer, atmospheric and surface radiation, microphysics and cumulus convections	WRF-Chem can be coupled with the WRF. Coupling the WRF with chemistry package enables researchers to simulate chemical processes (transport, deposition, emission, chemical transformation, aerosol interactions, photolysis and radiation) to predict air quality conditions. The component of air quality is consistent with the meteorological ones within the same transport scheme, grid and physics schemes and time steps. It has the following capabilities: -Dry deposition soil/vegetation scheme - Wet scavenging -Biogenic emission estimation - Anthropogenic emission estimation - Gas-phase mechanism assessment - Photolysis estimation - Aerosol estimation - Treatment of chemical reactions, aqueous phase chemistry, gas phase species and aerosols

7.10.2. The Correlation Between Surface Albedo Enhancement and Temperature Reduction

Here, the results of WRF-Chem is presented with more details. The WRF-Chem is coupled with the urban canopy model (UCM), which has three urban categories: 1) low intensity residential (LIR), 2) high intensity residential (HIR) and 3) industrial and commercial (I/C) areas. In each category, building properties are considered to be similar. In addition, the fraction of roofs, pavements, and vegetation in each grid cell is assumed to be constant and the same as other grids in the same urban category. This limitation causes uncertainties in estimating the correlation between the fraction of albedo enhancement and decreasing air temperature and ozone concentrations. But, as the conclusions of these simulations and previous studies reveal, the correlation between decreasing air temperature and increasing surface reflectivity is not because of the size of the city or its population. For instance, Sacramento is nearly one third of Chicago in terms of area and has nearly half the population density; but because of its specific synoptic condition, weather pattern and geographical location the effects of albedo enhancement are significant. Sacramento ranks fifth because of its high ozone concentration. Thus, the effects of reducing air temperature on ozone concentrations are larger compared to other cities. It shows that

UHI mitigation strategies that reduce temperature will improve air quality to some extent. Table 7.10 presents these comparisons.

Table 7.10. The comparisons between our simulation results and the previous one

City	Studies	Results
Sacramento Population= 500, 000 Area= 253 km^2 Population density = 1900/km^2	The simulations: Albedo of roofs, walls, pavements increased by 0.65, 0.6 and 0.45, respectively	T2 decreased by 2.5°C in urban and 0.7°C in rural areas O$_3$ decreased by 8 ppb in urban and 3 ppb in rural areas
	Taha (2008) Albedo increased by 0.11 Vegetation increased by 0.14	T2 decreased by 1.6°C O$_3$ decreased by 10 ppb
	Taha et al., (2015) Albedo of roofs, walls, pavements increased by 0.4, 0.1, and 0.2, respectively	T2 decreased by 2.3°C O$_3$ decreased by 5-11 ppb
Houston Population= 2.3 million Area= 1700 km^2 Population density = 1400/km^2	The simulations: Albedo of roofs, walls, pavements increased by 0.65, 0.6 and 0.45, respectively	T2 decreased by 3°C in urban and 0.8°C in rural areas O$_3$ decreased by 7.2 ppb in urban and 3 ppb in rural areas
	Taha (2003) roof albedo was increased from an average of 0.1 to an average of 0.3; wall albedo was increased from an average of 0.25 to an average of 0.3; pavement albedo was increased from an average of 0.08 to 0.2	T2 decreased by 3.5°C
Chicago Population= 2.7 million Area= 606 km^2 Population density = 4593/km^2	The simulations: Albedo of roofs, walls, pavements increased by 0.65, 0.6 and 0.45, respectively	T2 decreased by 2°C in urban and 0.8°C in rural areas O$_3$ decreased by 5 ppb in urban and 2 in rural areas
	Taha et al., (1999) Roof albedo increased by 0.03 ± 0.05 and vegetative fraction increased by 0.03 ± 0.04.	T2 decreased by 1°C

In previous studies, researchers looked at a simple linear interpolation between the effects of roofs and grounds albedo enhancement on air temperature reduction in urban areas. Linear interpolation means that increasing albedo of roofs and grounds causes a decrease in air temperature in urban areas. But, here in addition to the effects of albedo of roofs and grounds, the effects of albedo of walls are investigated on air temperature. The effects of walls are accounted for in different results and correlation between albedo enhancement and temperature reduction. Because of these factors, the impacts of three urban categories in the urban canopy model are also considered in the following.
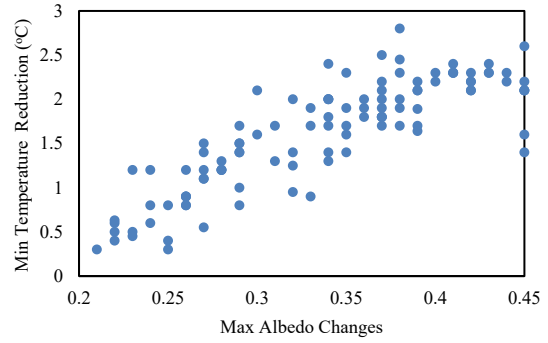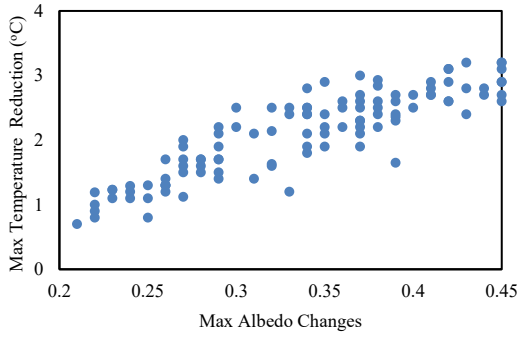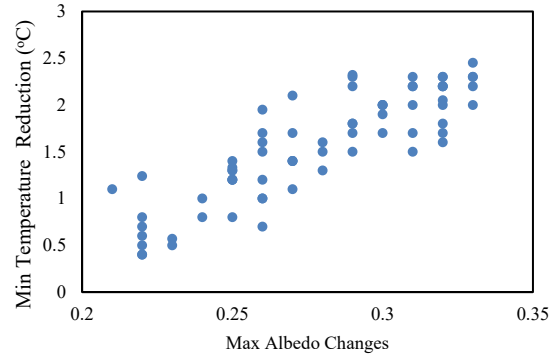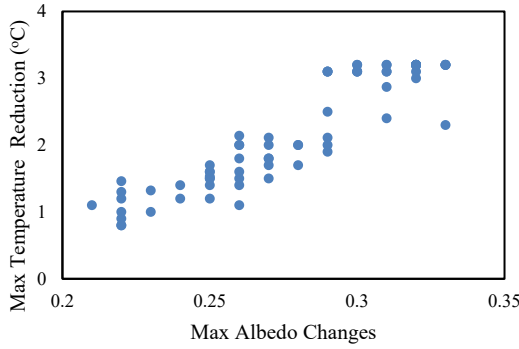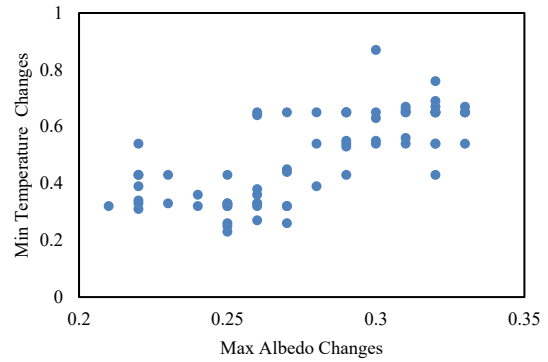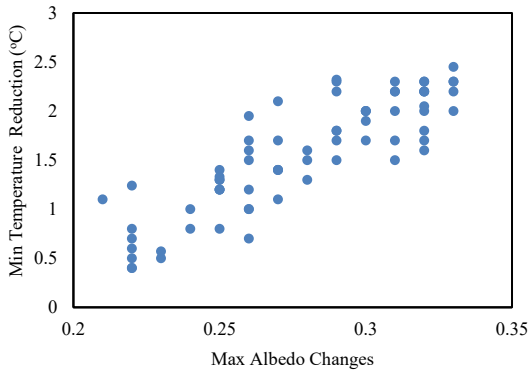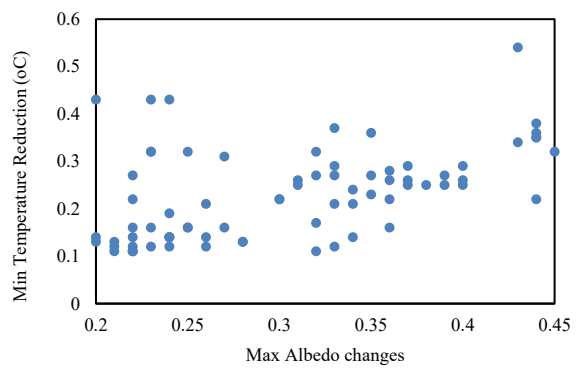
Figure 7.10 shows the inner domains of the simulations. The Google maps of the three urban categories are also presented. The downtown of each city is chosen as the high intensity residential area. The low intensity residential area and industrial/commercial area are selected based on Google map data and satellite pictures. Then the grid that covers each area is considered. Table 7.10 presents the results of the daily average of albedo changes, 2-m air temperature reduction and ozone concentration reduction for Sacramento (36 × 31 grids), Houston (41 × 31 grids), Chicago (36 × 31 grids) with a horizontal resolution of 2.4 km, and for the Greater Montreal Area (GMA) (101 × 71 grids) with the horizontal resolution of 800 m.

Sacramento area is 36 in west-east direction and 31 in south-north direction, each grid is 2.4km×2.4km

Midtown Sacramento- High intensity residential (black box)

Mercy General Hospital- industrial /commercial area (yellow box)

low intensity residential (green box)

166

Houston area is 41in west-east direction and 31 in south-north direction, each grid is 2.4km×2.4km

| High intensity residential (black box) | Downtwon -industrial/commercial area (yellow box) |

low intensity residential (green box)
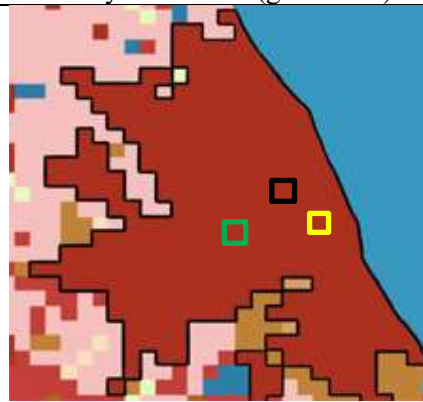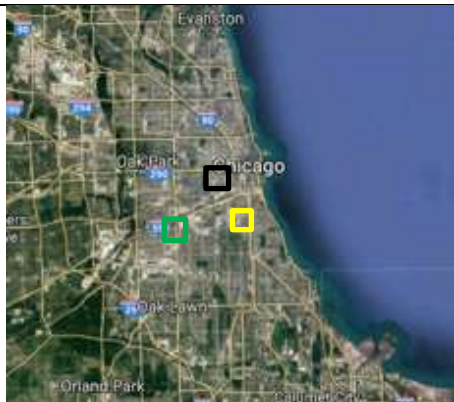
Chicago area is 36 in west-east direction and 31 in south-north direction, each grid is 2.4km×2.4km

High intensity residential (black box)

Industrial/commercial area (yellow box)

low intensity residential (green box)
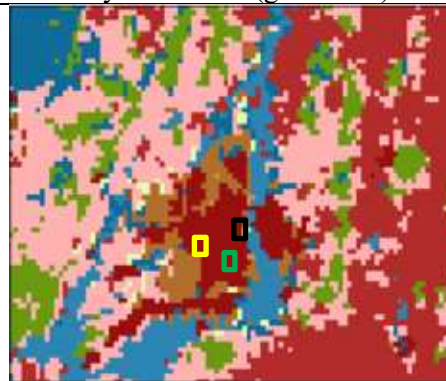
Greater Montreal Area is 145 in west-east direction and 91 in south-north direction, each grid is 0.800km×0.800km
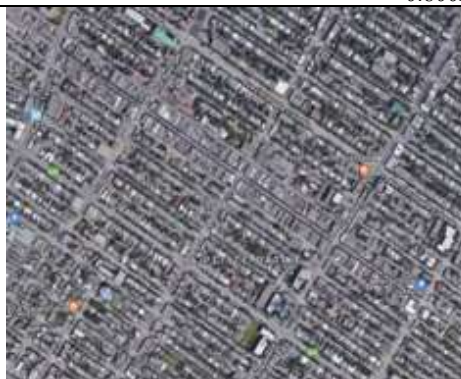
High intensity residential (black box)

Industrial/commercial area (yellow box)

low intensity residential (green box)

Figure 7.10. The land use/ land cover of the inner domains of the 3rd and 4th objectives: Sacramento, Houston, Chicago and Greater Montreal Area and the google map of high intensity residential (HIR), low intensity residential (LIR) and industrial/commercial (I/C) areas. The black, green and yellow boxes refer to HIR, LIR and I/C areas, respectively.

The high intensity residential areas (HIR) are close to downtown and city centers. The effects of albedo enhancement in HIR areas on air temperature and ozone concentrations are nearly twice the low intensity residential (LIR) and industrial/commercial (I/C) areas. But, since the size of each grid in Sacramento, Houston, Chicago is 2.4km × 2.4km, which is relatively large, they do not exactly represent each urban category. For example, on the grid that covers the downtown and midtown of Sacramento, there are also parks, museum and malls, and commercial centers. Figure 7.11 summarizes Table 7.11 with the daily average changes in albedo that induce air temperature reduction and ozone concentration reduction. The black, red and blue bar charts represent the albedo changes, air temperature reduction (°C) and ozone concentration reduction (ppb) due to increasing surface reflectivity in the three urban canopy categories. The left Y-axis shows the air temperature in °C and the right Y-axis shows ozone concentration in ppb. In addition, Figure 7.12 shows the 2-m air temperature reduction related to albedo enhancement in each UCM category (low intensity (LIR), high intensity residential (HIR) and commercial/industrial (I/C) areas) in each city (Sacramento, Houston, Chicago, and Greater Montreal Area). Figure 7.13 presents the changes in ozone concentration reduction because of air temperature reduction in each UCM category in the aforementioned cities.

Figure 7.14 shows the correlation between temperature reduction and albedo changes in the Sacramento area (36 × 31 grids), Houston area (41 × 31 grids), and Chicago area (36 × 31 grids), a the horizontal resolution of 2.4 km, and the Greater Montreal Area (GMA) (101 × 71 grids), with a horizontal resolution of 800 m. The correlation between the effects of albedo enhancement on reducing air temperature is nearly 0.85 for Sacramento and Houston and 0.75 for Chicago and the GMA. Figure 7.15 indicates the effects of decreasing temperature on ozone concentration reduction in the Sacramento area (36 × 31 grids), Houston area (41 × 31 grids), and Chicago area

169

(36 × 31 grids), with s horizontal resolution of 2.4 km, and the Greater Montreal Area (GMA) (101 × 71 grids) with s horizontal resolution of 800 m. Figure 7.15 reveals that ozone concentration depends on temperature. The R^2 is around 0.90 for Sacramento and Houston and 0.70 and 0.60 for Chicago and the GMA, respectively. In addition, Figure 7.16 presents the correlation between ozone concentration reduction and albedo changes in Sacramento, Houston, Chicago and the GMA. The correlation between increasing albedo and decreasing ozone concentration is nearly 0.80, 0.62, 0.55 respectively for Sacramento, Houston and Chicago, with a horizontal resolution of 2.4km, and 0.75 for the Greater Montreal Area, with a horizontal resolution of 800m.

Table 7.11. The average (daily average of simulation period (3 days)) changes of albedo (Fraction), 2-m air temperature reduction (ºC), ozone concentration reduction (ppb) in each UCM categories (low intensity (LIR) and high intensity residential (HIR), commercial/industrial (C/I) areas) in each city (Sacramento, Houston, Chicago, Greater Montreal Area)

Cities	UCM categories	Average albedo changes (Fraction)	Average temperature reduction (ºC)	Average ozone concentration reduction (ppb)
Sacramento	LIR	0.21	0.81	2.98
	HIR	0.33	2.31	7.52
	I/C	0.20	0.89	3.61
Houston	LIR	0.19	0.81	2.85
	HIR	0.27	2.51	7.23
	I/C	0.19	0.80	3.98
Chicago	LIR	0.23	0.75	1.77
	HIR	0.32	1.53	4.23
	I/C	0.19	0.78	2.87
Greater Montreal Area	LIR	0.16	0.82	2.82
	HIR	0.32	1.85	4.81
	I/C	0.15	1.10	1.11
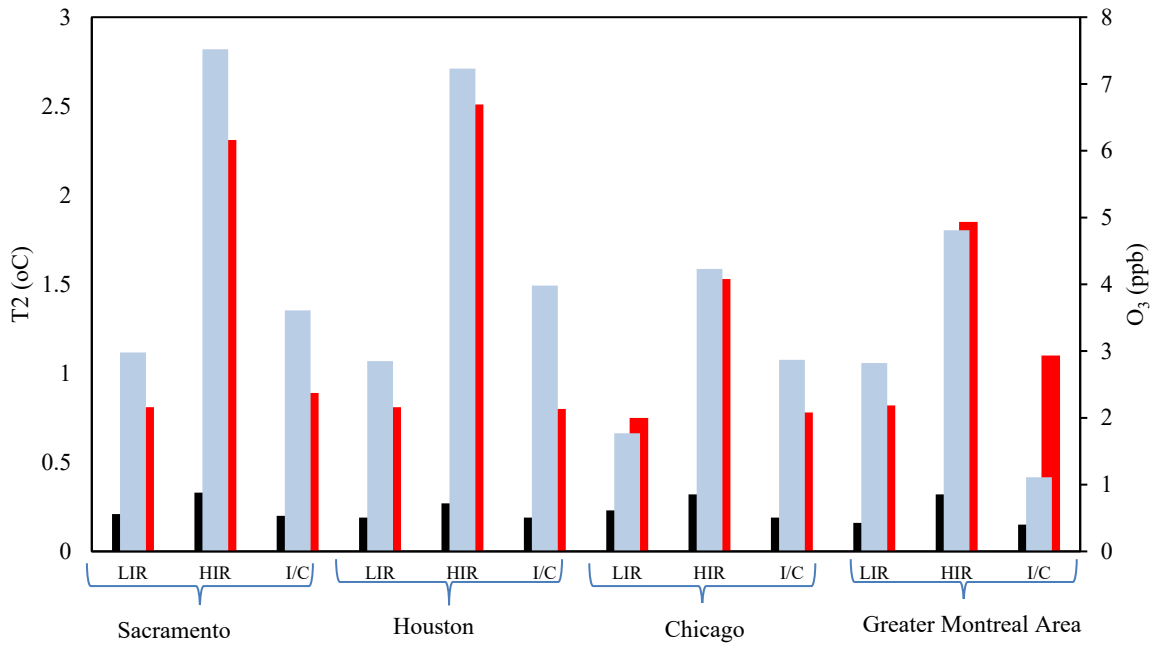
Figure 7.11. The average of minimum and maximum changes of albedo (Fraction, black bars), 2-m air temperature reduction (°C, red bars) and ozone concentration reduction (ppb, blue bars) in each UCM categories (low intensity (LIR) and high intensity residential (HIR), commercial/industrial (I/C) areas) in each city (Sacramento, Houston, Chicago, Greater Montreal Area). The left Y-axis shows the air temperature in °C and the right Y-axis shows the ozone concentration in ppb.
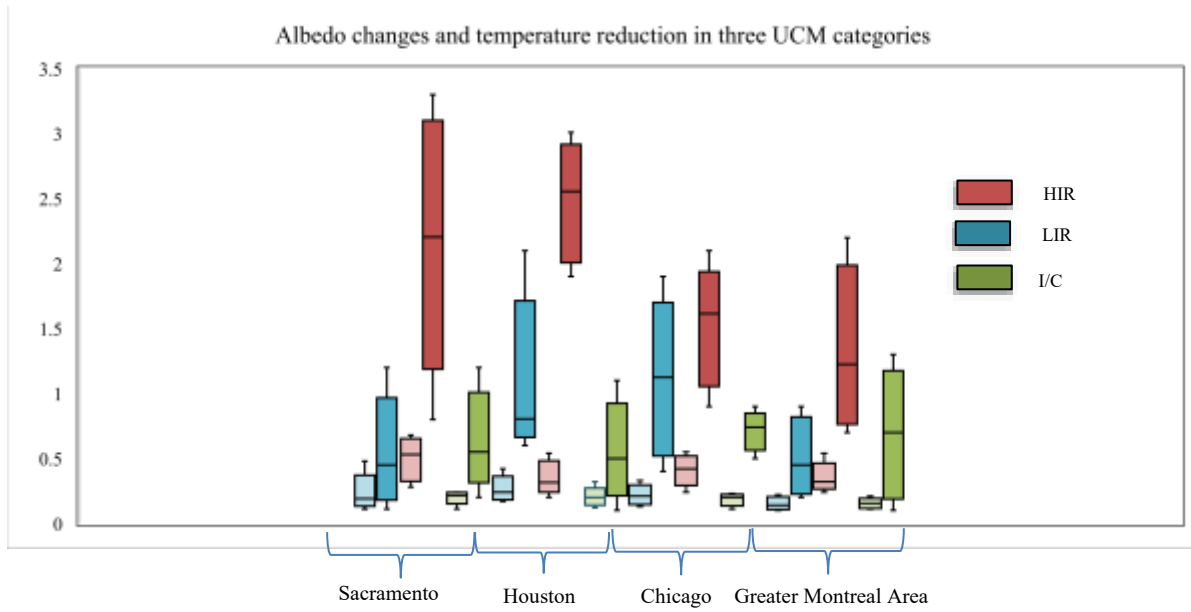
Figure 7.12. The albedo changes (light colors) and 2-m air temperature reduction (ºC-dark colors) in each UCM categories: low intensity (LIR-blue bars), high intensity residential (HIR-red bars) and commercial/industrial (I/C-green bars) areas) ones in each city: Sacramento, Houston, Chicago, and Greater Montreal Area
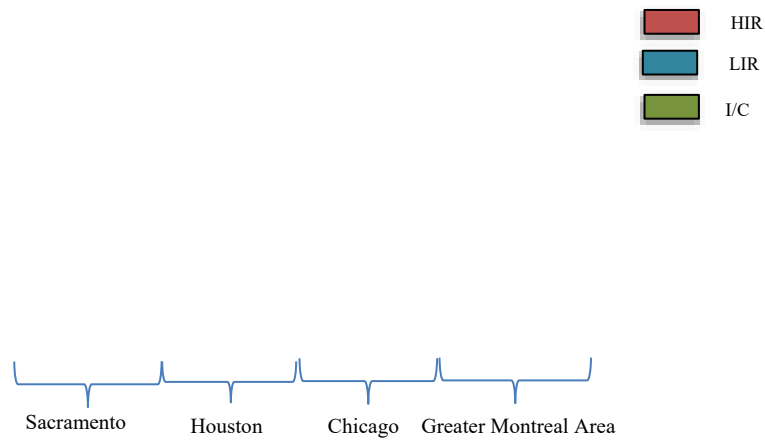
Figure 7.13. The temperature reduction (ºC- light colors) and ozone concentration reduction (ppb-dark colors) in each UCM categories: low intensity (LIR-blue bar), high intensity residential (HIR-red bars), and commercial/industrial (I/C, green bars) areas) ones in each city: Sacramento, Houston, Chicago, and Greater Montreal Area

a- Correlation between temperature reduction in Sacramento, Houston, and Chicago regarding to albedo changes
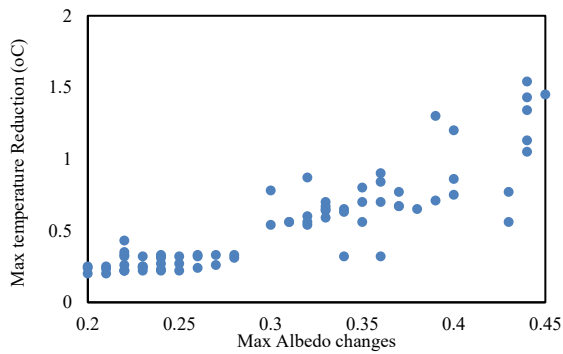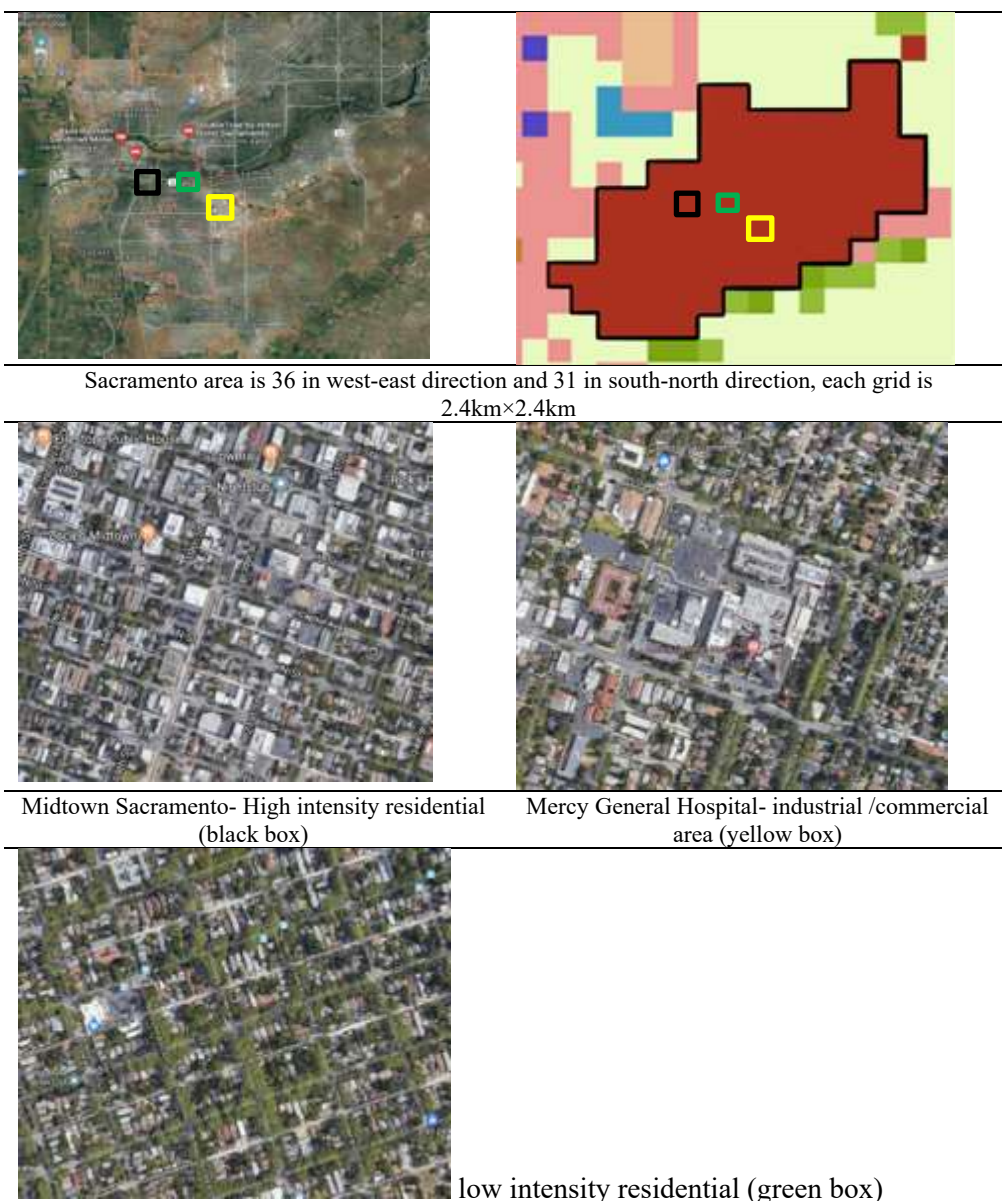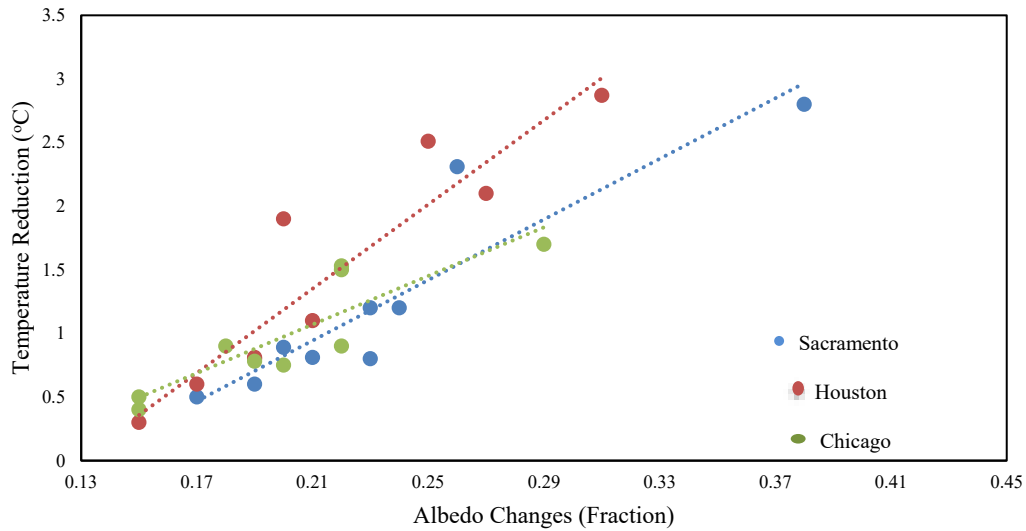

b- Correlation between temperature reduction in Greater Montreal Area regarding to albedo changes
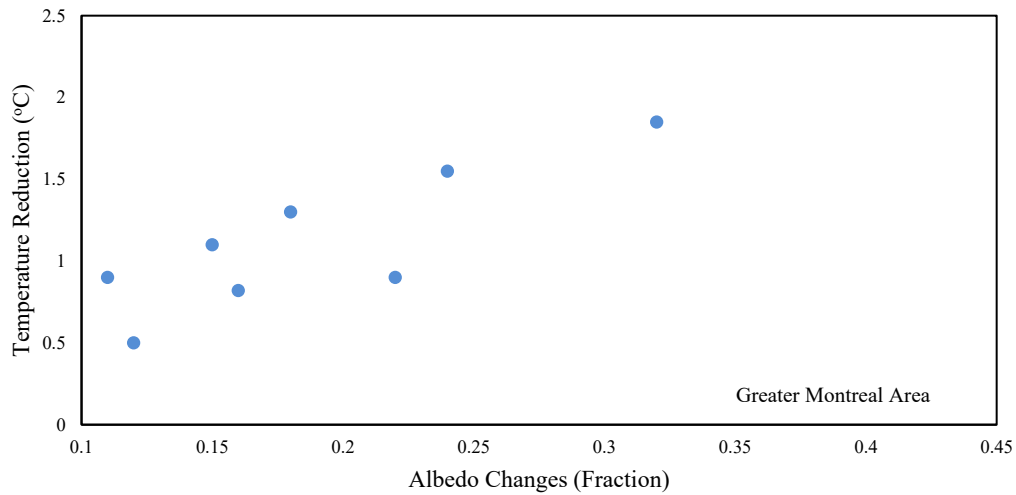
Figure 7.14. The correlation between temperature reduction and albedo changes in (a) Sacramento area (36 × 31 grids), Houston area (41 × 31 grids), and Chicago area (36 × 31 grids) with the horizontal resolution of 2.4km. (b) Greater Montreal Area (GMA) (101 × 71 grids) with the horizontal resolution of 800m.

a- Correlation between ozone concentration reduction in Sacramento, Houston, and Chicago regarding to temperature reduction
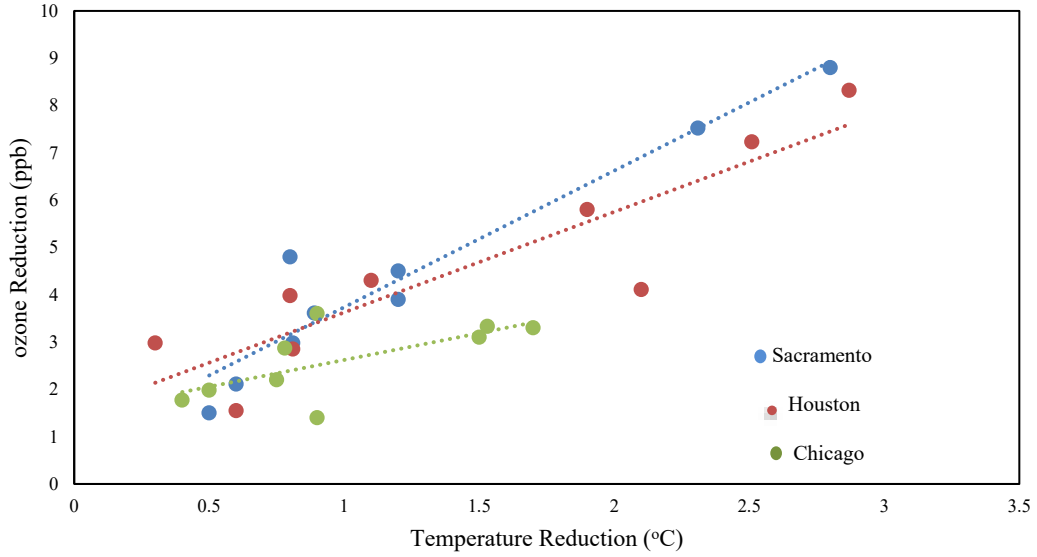
b- Correlation between ozone concentration reduction in Greater Montreal Area regarding to temperature reduction
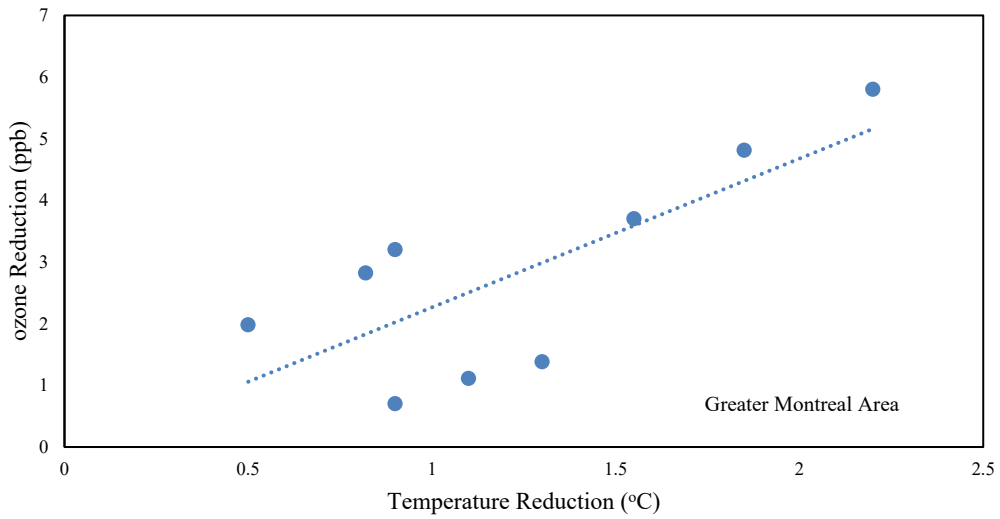
Figure 7.15. The correlation between ozone concentration reduction and temperature reduction in (a) Sacramento area (36 × 31 grids), Houston area (41 × 31 grids), and Chicago area (36 × 31 grids) with the horizontal resolution of 2.4km. (b) Greater Montreal Area (GMA) (101 × 71 grids) with the horizontal resolution of 800m.

a- Correlation between ozone concentration reduction in Sacramento, Houston, and Chicago regarding to albedo changes
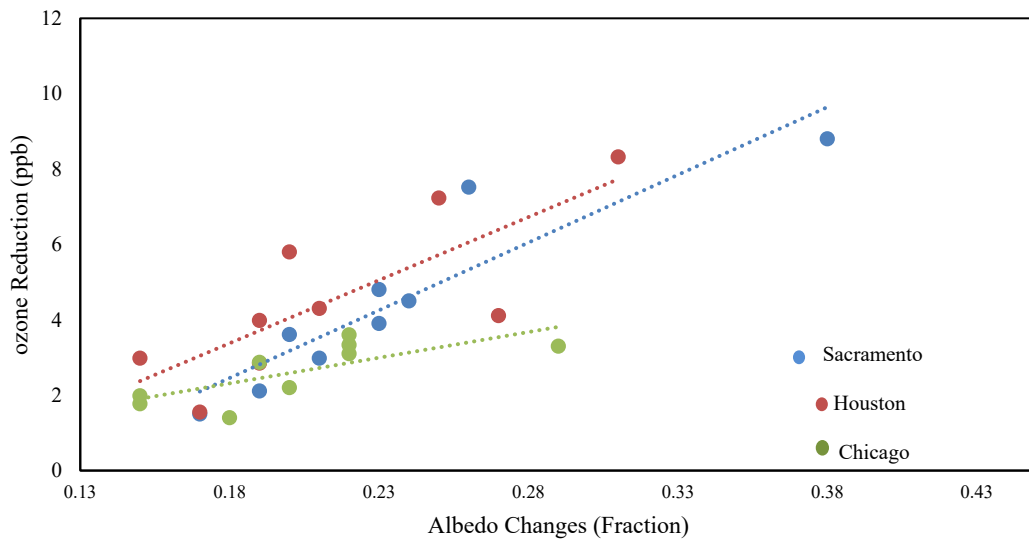
b- Correlation between ozone concentration reduction in Greater Montreal Area regarding to albedo changes
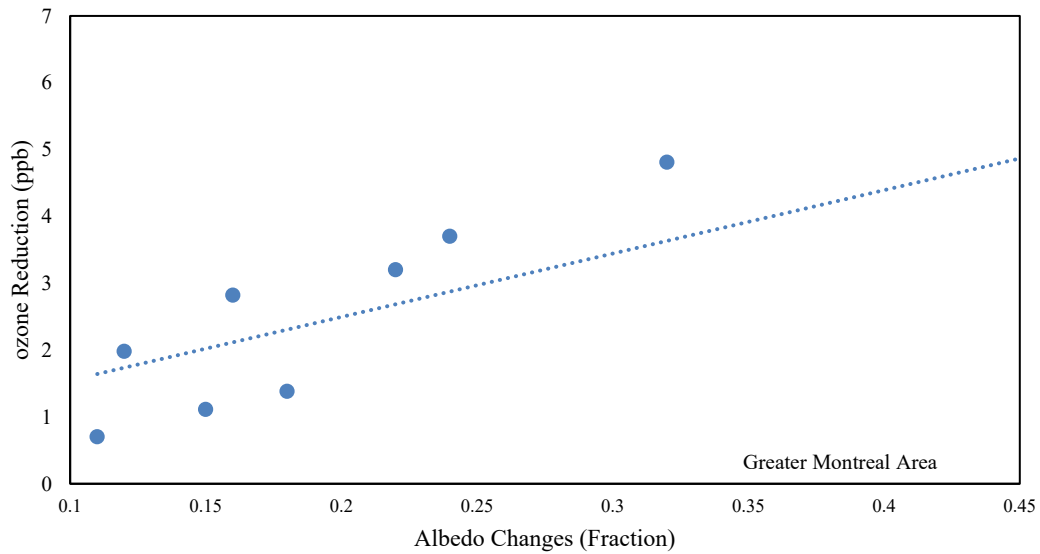
Figure 7.16. The correlation between ozone concentration reduction and albedo changes in (a) Sacramento area (36 × 31 grids), Houston area (41 × 31 grids), and Chicago area (36 × 31 grids) with the horizontal resolution of 2.4km. (b) Greater Montreal Area (GMA) (101 × 71 grids) with the horizontal resolution of 800m.

Chapter 8
Conclusion and Remarks

Surface and air temperatures are typically higher in urban areas compared to their surroundings and form the urban heat island (UHI) phenomenon. UHI increases cooling energy demands, deteriorates air quality, endangers human health, increases mortality and changes the urban ecosystem. To fight the UHI effects, increasing surface reflectivity (ISR) is well-documented as a measurable and repeatable heat island mitigation strategy.

The focus of this research was to investigate the effects of increasing surface reflectivity on urban climate, air quality and heat-related mortality. The goals were accomplished by applying the online numerical Weather Research and Forecasting model coupled with Chemistry (WRF-Chem). WRF-Chem considers a variety of meteorological and physical parameterizations and chemical processes to predict weather and air quality conditions. In addition, a multi-layer of the Urban Canopy Model (ML-UCM) was coupled with the WRF-Chem to represent the urban areas. The models were further modified to accommodate the specific needs of this study and related sensitivity analysis.

A base case scenario (CTRL) was established for each of the objectives identified in the study. The results are compared with measurements obtained from weather and air quality stations across the interested domain. The consequences of ISR were deemed to be reasonable enough, within the episode and scope of the study, to proceed in evaluating the potential impacts of surface modification strategy. Then, the albedo of roofs, walls, and pavements was increased from 0.2 in the CTRL scenario to 0.65, 0.60 and 0.45 in the ALBEDO scenario. The outcomes indicate that albedo enhancement is effective in modifying air temperature, meteorology-sensitive and temperature-sensitive photochemical reaction rates and reducing biogenic and anthropogenic emissions in urban areas. Hence, the effects of increasing surface reflectivity on temperature has significant positive impacts on the rates of production and accumulation of ozone in the polluted boundary layer in urban areas. Albedo enhancement also affects other meteorological and

photochemical fields, modifies weather patterns, and improves air quality and human comfort and health. These effects may vary spatially and temporally.

8.1. Summary of Conclusions

This numerical modeling study was carried out to evaluate the potential meteorological and photochemical impacts of surface modification on urban climate, air quality and heat-related death. The conclusive outcomes of this research regarding the effects of increasing surface reflectivity are summarized in the following:

1st Task: *Develop a platform for urban climate simulation and heat island mitigation strategy.*
Mesoscale models are comprised of physical parameterizations (cumulus, microphysics, planetary boundary layer, radiation, and land-surface) that need to be carefully selected to predict weather conditions. The physical processes can be selected based on the twenty sets of sensitivity analysis. A proper simulation platform is essential to have a better understanding of the effects of UHI and its mitigation strategy on urban climate and air quality for environmental policymakers. The sensitivity of near surface air temperature, wind speed, relative humidity and precipitation to different physical models was evaluated by applying the WRF for Montreal, Canada for the period 9–11 August 2009. The combination of WDM6 (Lim and Hong, 2010), Grell 3D (Grell, 1993; Grell and Devenyi, 2002), MYJ (Janjic, 1994), and RRTMG (Iacono et al., 2008) as microphysics, cumulus, planetary boundary layer, and radiation schemes, respectively, resulted in the least error compared to measurements and thus is suggested as an appropriate platform for urban climate simulations and UHI mitigation strategy. Increasing surface reflectivity was applied and the results indicate a decrease in 2-m air temperature by 0.2 ℃, a slight increase in 10-m wind speed, a decrease in relative humidity by 3%, and a decrease in precipitation by 0.2 mm/day across the domain.

2nd Task: *Investigate the effects of urban heat island and its mitigation strategy on heat-related mortality.*
The proper physical parameterizations were applied to achieve the second goal. The effects of extreme heat events and increasing surface reflectivity were investigated on meteorological parameters (air temperature, wind speed, relative humidity, and dew point temperature), heat stress indices (National Weather Service – Heat Index, apparent temperature, Canadian Humid Index, and Discomfort Index) and heat-related deaths. Heat-related mortality correlations were

developed. The simulation domain was the Greater Montreal Area. The simulation period included two heat wave events in 2005 and 2011. The beneficial contributions of ISR were a decrease in temperature by 0.6 °C, an increase in relative humidity by 2%, an increase in dew point temperature by 0.4 °C, a slight increase in wind speed, and a decrease in heat-related mortality by 3.2%, meaning that nearly seven lives could be saved.

3rd Task: *Develop a two-way nested simulation approach to assess the effects of urban heat island and its mitigation strategy on urban climate and air quality.*

The effects of increasing surface reflectivity were investigated over a larger geographical area (North America) within a nested domain of urban areas (Sacramento in California, Houston in Texas, and Chicago in Illinois) in a two-way nested approach to decrease the uncertainties associated with scale separation and grid resolution. The developed approach provided an integrated simulation setup to capture the full impacts of meteorological and photochemical reactions. WRF-Chem simulated the diurnal variation of air temperature reasonably well, overpredicted wind speed and dew point temperature, underpredicted relative humidity, overpredicted ozone and nitrogen dioxide concentrations, and underpredicted fine particulate matter ($PM_{2.5}$). The performance of $PM_{2.5}$ was a combination of overprediction of particulate sulfate and underprediction of particulate nitrate and organic carbon. Increasing the surface albedo of roofs, walls, and pavements from 0.2 to 0.65, 0.60, and 0.45, respectively, resulted in a decrease in air temperature by 2.3°C in urban areas and 0.7°C in suburban areas; a slight increase in wind speed; an increase in relative humidity (3%) and dew point temperature (0.3°C); a decrease of $PM_{2.5}$ and O_3 concentrations by 2.7μg/m^3 and 6.3 ppb in urban areas and 1.4μg/m^3 and 2.5ppb in suburban areas, respectively; minimal changes in $PM_{2.5}$ subspecies; and a decrease of nitrogen dioxide (1 ppb) in urban areas. Sacramento enjoyed larger reductions in ozone concentration as a result of larger decrease in air temperature because of the heat island mitigation strategy.

4th Task: *Investigate the effects of heat island mitigation strategy on aerosol-radiation-cloud interactions in the atmosphere.*

The effects of albedo enhancement were investigated on aerosol-radiation-cloud (ARC) interactions in a two-way nested simulation approach over the Greater Montreal Area during the 2011 heat wave period. Four sets of simulations with and without aerosol estimations and

convective parameterizations were carried out to explore the direct, semi-direct and indirect effects of aerosols. The albedo enhancement induced a decrease in 2-m air temperature by nearly 0.5 °C in the Center and North part of the domain and a decrease by nearly 0.3 °C in the South part. The relative humidity and water mixing ratio also decreased by 0.5 g/kg and 3%, respectively. Albedo enhancement led to a decrease in ozone concentrations by 2 ppb across the entire domain. Reducing temperature led to a reduction in planetary boundary layer height, which reduced the advection and diffusion of pollutants. Hence, this phenomenon increased the pollutant concentrations and also assisted the O_3 and NO reaction rates to produce NO_2. The fine particulate matter also decreased by nearly 3 $\mu g/m^3$ in the Center and by nearly 2 $\mu g/m^3$ in the other parts of the GMA during the 2011 heat wave period. The NO_2 and SO_2 reductions were much less compared to $PM_{2.5}$ and O_3. An increase of albedo led to a net decrease of radiative flux into the ground and therefore a decrease of convective cloud formation and precipitation.

In addition, here the results of 2-m air temperature in these four tasks are compared with other studies that applied the WRF and WRF-Chem. Table 8.1. shows the root mean square error of these four tasks and previous research. The comparisons indicate that the WRF and WRF-Chem results are generally consistent with the measurements and thus are well reliable to be applied for further investigations.

Table 8.1. Comparisons of 2-m air temperature results (Root Mean Square Error (RMSE)) of the current tasks with previous studies using WRF and WRF-Chem

Study	RMSE of T2
Fallmann et al., 2014	1.7
Salamanca et al., 2012,	1.5
Vahmani & Ban-Weiss. 2016,	3.8
Chen et al., 2013,	1.61
Millstein D. & Menon S., 2011	2.8
Georgescu et al., 2012	1.9
Georgescu et al., 2014	2.5
Zhou Y. et al., 2010	1.1
Fallmann et al., 2014	1.6
Salamanca & Martilli, 2012	1.6
Taha et al., 2015	1.1
Touchaei et al., 2016	1.8
1st task: develop a proper platform for urban climate simulation	1.9
2nd task: effects of albedo enhancement on heat-related mortality	1.6
3rd task: develop a two-way nested simulation approach	1.3
4th task: effects of increasing albedo on aerosol-radiation-cloud interactions	1.1

8.2. Remarks

To conclude, this research demonstrates the potential capacity of the increasing surface reflectivity to mitigate the UHI effects. The consequences of albedo enhancement indicate a decrease in air temperature, a decrease in temperature-dependent photochemical reaction rates and a decrease in heat-related mortality. Accordingly, there are four scientific contributions regarding the effects of urban heat island and its mitigation strategy: 1) a platform is developed for urban climate simulations and heat island mitigation strategy; 2) heat-related mortality calculations are derived to estimate the effects of heat island and its mitigation strategy on human death rate; 3) a two-way nested simulation approach is developed to investigate the effects of UHI and increasing surface reflectivity on urban climate and air quality over a larger geographical area within nested domains of urban areas; 4) the effects of albedo enhancement are investigated on aerosols interactions, radiation budget and hydrological cycles in the atmosphere and at the surface.

The benefits and applications of this research are: developing a comprehensive basis for local and regional climate and air quality simulations; assessing the effects of increasing surface reflectivity on urban climate and air quality in various urban areas; investigating the aerosol estimation in the chemistry package within WRF-Chem; providing more accurate and reliable information for air quality policymakers to improve urban climate and air quality and reduce heat-related mortality during heat wave periods.

The main drawback in investigating the potential impacts of surface modification is that the meteorological and photochemical modeling carries inherent numerical issues, assumptions and limitations that affect the results and hence should be acknowledged. There is a risk to implement this strategy if one only seeks to reduce air temperature, whereas it may also reduce the planetary boundary layer height, increase the ozone and particulate matter concentrations in some parts of the domain, reducing cloud formation and precipitation. Thus, there are some caveats that regulators need to carefully consider prior to albedo enhancement.

8.3. Future Work

Increasing surface reflectivity indicates a promising UHI mitigation strategy to reduce the air temperature and temperature-dependent photochemical reaction rates, and thus to improve urban climate and air quality and reduce heat-related death. However, this research can be even more fruitful if the following recommendations will be considered for future studies:

- Here, the simulations were conducted during the heat wave periods. It is essential to investigate the effects of UHI mitigation strategy over seasonal time spans and on an annual basis. This would provide a more realistic assessment of the long-term effects of UHI and increasing surface reflectivity.
- Comparing other mitigation strategies such as increasing surface vegetation in urban areas with increasing surface albedo. This comparison provides a more beneficial assessments for air quality regulators and policymakers.
- Improve the input data such as emission inventories in terms of biogenic and anthropogenic emissions, and urban morphological data, for future analyses.
- Next, modeling efforts of the UHI and its mitigation strategies should evaluate scenarios based on future-year emission inventories that account for increased urbanization. Future-year controlled emissions should also be applied to scenarios of lower emissions.
- City-specific modeling is needed to account for actual urbanization trends and growth plans that have impacts on local meteorology and air quality.

Modifications and improvements of models (such as photolysis rate estimations and aerosols estimations) may be needed beyond what was achieved in this study to make the application more specific to certain regions and conditions.

References

Akbari H. and Kolokotsa D. 2016. Three decades of urban heat islands and mitigation technologies research. Enbuild. 133: 834-842.

Akbari H. and Touchaei A.G. 2014. Modeling and labeling heterogeneous directional reflective roofing materials. Sol. Energy Mater. Sol. Cells 124: 192-210.

Akbari, H., Bretz, S., Kurn, D.M. and Hanford, J. 1997. Peak power and cooling energy savings of high-albedo roofs. Energy and Buildings, 25, (2) 117-126

Akbari, H., Menon, S. and Rosenfeld, A. 2009. Global cooling: increasing world-wide urban albedos to offset CO2. Climatic Change, 94, (3-4) 275-286

Akbari, H., Pomerantz, M., and Taha, H. 2001. Cool surfaces and shade trees to reduce energy use and improve air quality in urban areas. Solar Energy, 70, (3) 295-310

Akbari, H. and Rose, L.S. Characterizing the Fabric of the Urban Environment: A Case Study of Metropolitan Chicago, Illinois; Report LBNL-49275; Lawrence Berkeley National Laboratory: Berkeley, CA, USA, 2001.

Akbari, H., Rose, L.S. and Taha, H. 2003. Analyzing the land cover of an urban environment using high-resolution orthophotos. Landsc. Urban Plan. 63, 1–14.

Abdul-Razzak, H. and Ghan, S. J. 2002. A parameterization of aerosol activation 3. sectional representation, J. Geophys. Res., 107, 3: 1029-2001

Ackermann, I.J., Hass, H., Memmesheimer, M., Ebel, A., Binkowski, F.S. and Shankar, U. 1998. Modal aerosol dynamics model for Europe: Development and first applications. Atmos. Environ. 32, 2981–2999.

Ahmad, S. and Hashim, N.M. 2007. Effects of soil moisture on urban heat island occurrences: case of Selangor, Malaysia. Humanity & Social Sciences Journal, 2, (2) 132- 138

Ahmadov, R., McKeen, S.A., Robinson, A.L., Bahreini, R., Middlebrook, A.M., de Gouw, J.A., Meagher, J., Hsie, E.-Y., Edgerton, E., and Shaw, S. A. 2012. volatility basis set model for summertime secondary organic aerosols over the eastern United States in 2006. J. Geophys. Res. 117, 06–31.

American Lung Association. 2017. Available online: http://www.lung.org/our-initiatives/healthy-air/ sota/city-rankings/most-polluted-cities.html (accessed on 28 January 2018).

Anderson B.G., and Bell M.L. 2009. Weather-related mortality: how heat, cold, and heat waves affect mortality in the United States. Epidemiology. 20(2): 205–213.

Appel, K.W., Chemel, C., Roselle, S.J., Francis, X.V., Hu, R.-M., Sokhi, R.S., Rao, S.T and Galmarini, S. 2012. Examination of the Community Multiscale Air Quality (CMAQ) model perfor-mance over the North American and European domains. Atmos. Environ. 53, 142–155.

Archer-Nicholls, S., Lowe, D. and Darbyshire, E. 2015. Characterizing Brazilian biomass burning emissions using WRF-Chem with MOSAIC sectional aerosol, Geosci. Model Dev., 8, 549–577

Arnfield, A.J. and Grimmond, C.S.B. 1998. An urban canyon energy budget model and its application to

urban storage heat flux modeling. Energy and Buildings, 27, (1) 61-68

Arnfield, A.J. 2003. Two decades of urban climate research: a review of turbulence, exchanges of energy and water, and the urban heat island. International Journal of Climatology, 23, (1) 1-26

ARW User Guide, 2017. ARW Version 3 Modeling System User's Guide. National Center for Atmospheric Research, Boulder (CO), US.⌞SEP⌟

Åström D.O, Forsberg B. and Rocklöv J. 2011. Heat wave impact on morbidity and mortality in the elderly population: A review of recent studies. Maturitas. 69(2): 99-105.

Baik J. J., Kim. Y. H., and Han J. Y. 2007. Effect of boundary-layer stability on urban heat island induced circulation, Theor. Appl. Climatol., 89, 73–81.

Baklanov, A., Schlünzen, K., Suppan, P. 2014. Online coupled regional meteorology chemistry models in Europe: current status and prospects, Atmos. Chem. Phys., 14, 317–398.

Ban-Weiss G.A., Woods J., Levinson R. 2014. Using remote sensing to quantify albedo of roofs in seven California cities, Part 1: Methods. Sol Energy. 115: 777-790.

Barnard, J. C., Fast, J. D., and Paredes-Miranda, G. 2010. Technical Note: Evaluation of the WRF-Chem "Aerosol Chemical to Aerosol Optical Properties" Module using data from the MILAGRO campaign, Atmos. Chem. Phys., 10, 7325–7340.

Barnett AG., Tong S., Clements AC. 2010. What measure of temperature is the best predictor of mortality? Environ. Res. 110 (6): 604-611.

Basu R, and Samet JM. 2002. Relation between elevated ambient temperature and mortality: a review of the epidemiologic evidence, Epidemiol. Rev. 24: 190–202.

Basu R. 2009. High ambient temperature and mortality: a review of the epidemiologic studies from 2001 to 2008. Enviro Health. 8: 40-48.

Berry R., Livesley S.J., Aye L. 2013. Tree canopy shade impacts on solar irradiance received by building walls and their surface temperature, Build. Environ. 69: 91–100.

Bhati, S. and Mohan, M., 2016. WRF model evaluation for the urban heat island assessment under varying land use/land cover and reference site conditions. Theor. Appl. 16: 94-101

Bianchini, F. and Hewage, K. 2012. How "green" are the green roofs? Lifecycle analysis of green roof materials. Build. Environ. 48, 57-65.

Blonquist, J. M., J. M. Norman, and B. Bugbee. 2009. Automated measurement of canopy stomatal conductance based on infrared temperature. Agricultural and Forest Meteorology 149:1931–1945.

Bond, T. C. and Bergstrom, R. W. 2006. Light absorption by carbonaceous particles: an investigative review, Aerosol Sci. Tech., 39, 1–41.

Bond, T. C., Doherty, S. J., Fahey, D. W. and Forster, P. M. 2013. Bounding the role of black carbon in the climate system: a scientific assessment, J. Geophys. Res.- Atmos., 11, 1–163.

Bornstein, R., and Lin, Q. 2000. Urban heat islands and summertime convective thunderstorms in Atlanta: Three cases studies, Atmos. Environ., 34, 507–516.

Bowler, D.E., Buyung-Ali. L., Knight, T.M., and Pullin, A.S. 2010. Urban greening to cool towns and cities: A systematic review of the empirical evidence. Landscape and Urban Planning, 97, (3) 147-155

Boylan, J. W. and Russell, A. G. 2006. PM and light extinction model performance metrics, goals, and criteria for three-dimensional air quality models, Atmos. Environ., 40, 4946–4959.

Britter, R.E. & Hanna, S.R. 2003. Flow and dispersion in urban areas. Annual Review of Fluid Mechanics, 35, 1: 469-496.

Bunker A., Wildenhain J., Vandenbergh A., Henschke N., Rocklöv J., Hajat S. and Sauerborn R. 2016. Effects of Air Temperature on Climate-Sensitive Mortality and Morbidity Outcomes in the Elderly; a Systematic Review and Meta-analysis of Epidemiological Evidence. EBioMedicine. 6: 258-268.

Bougeault, P., Lacarrere, P., 1989. Parameterization of orography-induced turbulence in a mesobeta-scale model. Mon. Weather Rev. 117, 1872–1890. Environment Canada, (2013).

Chapman, E. G., Gustafson Jr., W. I., Easter, R. C., Barnard, J. C., Ghan, S. J., Pekour, M. S., and Fast, J. D. 2009. Coupling aerosol- cloud-radiative processes in the WRF-Chem model: Investigating the radiative impact of elevated point sources, Atmos. Chem. Phys., 9: 945–964.

Chapman, L. and Thornes, J.E. 2004. Real-Time Sky-View Factor Calculation and Approximation. Journal of Atmospheric & Oceanic Technology, 21, 5: 730-741

Chen F. and Dudhia J. 2001. Coupling an advanced land surface–hydrology model with the Penn State–NCAR MM5 modeling system. Part I: model implementation and sensitivity. Monthly Weather Review, 129: 569-585.

Chen F., Kusaka H., Bornstein R., Ching J., Grimmond C. S. B., Grossman-Clarke S., Loridan T., Manning K.W., Martilli A., Miao S., Sailor D., Salamanca F.P., Taha H., Tewari M., Wang X., Wyszogrodzkia A.A. and Zhang C. 2011. The integrated WRF/urban modelling system: development, evaluation, and applications to urban environmental problems. Int. J. Climatol. 31: 273-288.

Chen H., Oak R., Huang H. and Tsuchiya T. 2009. Study on mitigation measures for outdoor thermal environment on present urban blocks in Tokyo using coupled simulation, Build. Environ. 44: 2290–2299.

Chen, F. and Dudhia, J. 2001. Coupling an advanced land surface–hydrology model with the Penn State–NCAR MM5 modeling system. Part I: model implementation and sensitivity. Mon. Weather Rev. 129, 569–585. [L] SEP

Chen, F. 2011. The integrated WRF/urban modeling system: Development, evaluation, and applications to urban environmental problems, Int. J. Climatol., 31(2), 273–288. [L] SEP

Chen, F., Yang, X. and Zhu, W. 2013. WRF simulations of urban heat island under hot-weather synoptic conditions: The case study of Hangzhou City, China. Atmos. Res. 138, 364–377.

Chen, S.H. and Sun, W.Y. 2002. A one-dimensional time dependent cloud model. J. Meteorol. Soc. Jpn. 80, 99–118. [L] SEP

Chen, Y., Jiang, W.M., Zhang, N., He, X.F., and Zhou, R.W. 2009. Numerical simulation of the anthropogenic heat effect on urban boundary layer structure. Theor Appl Climatol, 97, (1-2) 123-134

Chou, M.D. and Suarez, M.J. 1999. A Solar Radiation Parameterization (CLIRAD-SW) Developed at Goddard Climate and Radiation Branch for Atmospheric Studies; NASA Technical Memorandum NASA/Goddard Space Flight Center Greenbelt: Greenbelt, MD, USA.

Chuang, M.-T., Zhang, Y. and Kang, D. 2011. Application of WRF/Chem-MADRID for real-time air quality forecasting over the southeastern United States. Atmos. Environ. 45, 6241–6250.

Conti S., Meli P., Minelli G., Solimini R., Toccaceli V., Vichi M., Beltrano C. and Perini L. 2005. Epidemiologic study of mortality during the summer 2003 heat wave in Italy. Environ Res 98(3):390–399.

Coutts AM., Daly E., Beringer J. and Tapper NJ. 2013. Assessing practical measures to reduce urban heat: green and cool roofs, Build. Environ. 70: 266–276.

Crouse DL., Peters PA., van Donkelaar A., Goldberg MS., Villeneuve PJ., and Brion O. 2012. Risk of nonaccidental and cardiovascular mortality in relation to long-term exposure to low concern- tractions of fine particulate matter: a Canadian national-level cohort study. Environ Health Perspect 120:708–714.

Csiszar I. and Gutman G. 1999. Mapping global land surface albedo from NOAA AVHRR. Journal of Geophysical Research, 104: 6215–28.

Curriero FC, Heiner KS, Samet JM, Zeger SL, Strug L. and Patz JA. 2002. Temperature and mortality in 11 cities of the eastern United States. Am J Epidemiol. 155: 80–87.

Cusack L., de Crespigny C., Athanasos P. 2011. Heatwaves and their impact on people with alcohol, drug and mental health conditions: a discussion paper on clinical practice considerations. J. Adv. Nurs. 67 (4): 915-922.

Diaz J., Jordan A., García R., Lopez C., Alberdi J., Hernandez E., Otero A. 2002. Heat waves in Madrid 1986-1997: effects on the health of the elderly. Int. Arch. Occup. Environ. Health. 75 (3): 163-170.

Diffenbaugh N.S. and Ashfaq M. 2010. Intensification of hot extremes in the United States. Geophys Res Lett. 37(15): 157-185.

Dudhia, J., 1989. Numerical study of convection observed during the winter monsoon experiment using a mesoscale two-dimensional model. J. Atmos. Sci. 46, 3077–3107.

Duffie, J.A. and Beckman, W.A., 1991. Solar Engineering of Thermal Processes. Wiley and Sons, Inc., Hoboken (NJ), US.

Emeis, S. 2010. Surface-based remote sensing of the atmospheric boundary layer. Series: Atmospheric and Oceanographic Sciences Library, 40: 174pp.

Environment Canada, (2017). [Online: http://climate.weather.gc.ca/].

EPA. 2005. Available online: http://www.epa.gov/ttnchie1/net/2005inventory.html (accessed on 28 January 2017).

Epstein Y. and Moran D.S. 2006. Thermal comfort and heat stress indices. Ind Health. 44(3): 388-398.

Fallmann, J., Emeis, S. and Suppan, P. 2014. Mitigation of urban heat stress - a modelling case study for the area of Stuttgart. DIE ERDE - Journal of the Geographical Society of Berlin, 144, (3-4) 202-216

Fallmann, J., Emeis, S. and Suppan, P. 2013. Mitigation of urban heat stress—A modelling case study for the area of Stuttgart. J. Geogr. Soc. Berl. 144, 202–216.

Fallmann, J., Forkel, R. and Emeis, S. 2016. Secondary effects of urban heat island mitigation measures on air quality. Atmos Environ. 125, 199–211.

Fan, H. and Sailor, D.J. 2005. Modeling the impacts of anthropogenic heating on the urban climate of Philadelphia: a comparison of implementations in two PBL schemes. Atmospheric Environment, 39, (1) 73-84.

Fan, J., Leung, L. R., Rosenfeld, D., Chen, Q., Li, Z., Zhang, J., and Yan, H. 2013. Microphysical effects determine macro-physical response for aerosol impacts on deep convective clouds. P. Natl. Acad. Sci. USA, 110, E4581–E4590.

Fast, J. D., Allan, J., Bahreini, R., Craven, J. and Emmons, L. 2014. Modeling regional aerosol and aerosol precursor variability over California and its sensitivity to emissions and long-range transport during the 2010 CalNex and CARES campaigns, Atmos. Chem. Phys., 14, 10013–10060.

Fast, J. D., Gustafson, W. I., Easter, R. C., Zaveri, R. A., Barnard, J. C., Chapman, E. G., Grell, G. A., and Peck- ham, S. E. 2006. Evolution of ozone, particulates, and aerosol direct radiative forcing in the vicinity of Houston using a fully coupled meteorology-chemistry-aerosol model, J. Geophys. Res., 111, 1– 29.

Fast, J.D., Gustafson, W.I., Jr., Easter, R.C., Zaveri, R.A., Barnard, J.C., Chapman, E.G., Grell, G.A. and Peckham, S.E. 2006. Evolution of ozone, particulates, and aerosol direct radiative forcing in the vicinity of Houston using a fully coupled meteorology-chemistry-aerosol model. J. Geophys. Res. 111, 203–213.

Ferrari, C., Touchaei, A.G., Sleiman, M., Libbra, A., Muscio, A., Siligardi, C. and Akbari, H. 2013. Effect of aging processes on solar reflectivity of clay roof tiles. Adv. Build. Energy Res. 8 (1), 28–40.

Fischer E.M, Oleson K.W. and Lawrence D.M. 2012. Contrasting urban and rural heat stress responses to climate change. Geophy Res Lett 39(3).

Gao, Y., Zhao C., Liu X., Zhang M., and Leung L. R. 2014. WRF-Chem simulations of aerosols and anthropogenic aerosol radiative forcing in east Asia, Atmos. Environ., 92, 250–266.

Gilliam R.C., Hogrefe C. and Rao S.T. 2006. New methods for evaluating meteorological models used in air quality applications. Atmos. Environ. 40: 5073–5086.

Grell G.A. and Devenyi D. 2002. A generalized approach to parameterizing convection combining ensemble and data assimilation techniques. Geophysical Research Letters. 29 (14): 31-38.

Grell, G. A. and Freitas, S. R. 2014. A scale and aerosol aware stochastic convective parameterization for weather and air quality modeling, Atmos. Chem. Phys., 14, 5233–5250.

Grell, G. A., and S. Freitas. 2013. A scale and aerosol aware stochastic convective parameterization for weather and air quality modeling, Atmos. Chem. Phys. Discuss., 13, 23,846–23,893.

Grell, G. and Baklanov, A. 2011. Integrated modelling for forecasting weather and air quality: a call for

fully coupled approaches, Atmos. Environ., 45, 6845–6851.

Grell, G.A. 1993. Prognostic evaluation of assumptions used by cumulus parameterizations. Mon. Weather Rev. 121, 764–787.

Grell, G.A., Peckham, S.E., Schmitz, R., McKeen, S.A., Frost, G., Skamarock, W.C. and Eder, B. 2005. Fully coupled "online" chemistry within the WRF model. Atmospheric Environment, 39, (37) 6957-6975

Grimmond, C.S.B. 1992. The suburban energy balance: Methodological considerations and results for a mid-latitude west coast city under winter and spring conditions. International Journal of Climatology, 12, (5) 481-497

Guenther, A., Karl, T., Harley, P., Wiedinmyer, C., Palmer, P.I. and Geron, C. 2006. Estimates of global terrestrial isoprene emissions using MEGAN (Model of Emissions of Gases and Aerosols from Nature). Atmos. Chem. Phys. 6, 3181–3210.

Guenther, A.B., Jiang, X., Heald, C.L., Sakulyanontvittaya, T., Duhl, T., Emmons, L.K., and Wang, X. 2012. The Model of Emissions of Gases and Aerosols from Nature version 2.1 (MEGAN2.1): an extended and updated framework for modeling biogenic emissions. Geosci.Model Dev., 5, (6) 1471-1492

Guenther, A.B., Zimmerman, P.R., Harley, P.C., Monson, R.K., and Fall, R. 1993. Isoprene and monoterpene emission rate variability: Model evaluations and sensitivity analyses. Journal of Geophysical Research: Atmospheres, 98, (D7) 12609-12617

Guenther, A.B., Jiang, X., Heald, C.L., Sakulyanontvittaya, T.; Duhl, T.; Emmons, L.K.; Wang, X. The Model of Emissions of Gases and Aerosols from Nature Version 2.1 (MEGAN2.1): An extended and updated framework for modeling biogenic emissions. Geosci. Model. Dev. 2012, 5, 1471–1492.

Hajat S., O'Connor M. and Kosatsky T. 2010. Health effects of hot weather: from awareness of risk factors to effective health protection. Lancet. 375(9717): 856–863.

Han, J. and Pan, H., 2011. Revision of convection and vertical diffusion schemes in the NCEP Global Forecast System. Weather Forecast. 26, 520–533.

Hanna A.F., Yeatts K.B., Xiu A., Zhu Z. and Smith R.L. 2011. Associations between ozone and morbidity using the spatial synoptic classification system. Env Health 10 (1):1–15.

Harlan S.L., Brazel A.J., Prashad L., Stefanov W.L. and Larsen L. 2006. Neighborhood microclimates and vulnerability to heat stress. Soc. Sci. Med. 63 (11): 2847-2863.

Harlan S.L. and Ruddell D.M. 2011. Climate change and health in cities: impacts of heat and air pollution and potential co-benefits from mitigation and adaptation. Curr. Opin. Environ. Sustain. 3 (3): 126-134.

Hong B. and Lin B. 2014. Numerical study of the influences of different patterns of the building and green space on microscale outdoor thermal comfort and indoor natural ventilation. Building Simulation. 7: 525-536.

Hong, S., Lim, J.J. 2006. The WRF single-moment 6-class microphysics scheme (WSM6). J. Korean Meteorol. Soc. 42, 129–151.

Hong, S.Y., Dudhia, J., Chen, S.H. 2004. A revised approach to ice microphysical processes for the bulk

parameterization of clouds and precipitation. Mon. Weather Rev. 132, 103–120.⸢⸤SEP⸥

Hooshangi, H., Akbari, H., Touchaei, A.G. 2016. Measuring solar reflectance of variegated flat roofing materials using quasi-Monte Carlo method. Energ. Buildings. 10: 060-073.⸢⸤SEP⸥

Horton D.E., Skinner C.B., Singh D., Diffenbaugh N.S. 2014. Occurrence and persistence of future atmospheric stagnation events. Nat Clim Change Lett. 4: 698-703.

Iacono, M. J., Delamere, J. S., Mlawer, E. J., Shephard, M. W., Clough, S. A., and Collins, W. D. 2008. Radiative forcing by long–lived greenhouse gases: calculations with the AER radiative transfer models. Journal of Geophysical Research, 113, D13103,

IPCC (Intergovernmental Panel on Climate Change). Climate Change 2013: The Physical Science Basis. Contribution of Working Group I to the Fifth Assessment Report of the Intergovernmental Panel on Climate Change, Cambridge University Press, Cambridge, UK and New York, NY, USA, 1535 pp.

IPCC. 2014. Summary for policymakers. In: Climate Change 2014. Impacts, Adaptation, and Vulnerability. Part A: Global and Sectoral Aspects. Contribution of Working Group II to the Fifth Assessment Report of the Intergovernmental Panel on Climate Change. 1-32, New York (NY), USA.

Jacobson, M. Z. 2006. Effects of externally-through-internally-mixed soot inclusions within clouds and precipitation on global climate. The Journal of Physical Chemistry A, 110(21):6860–6873.

Jacobson, M.Z. and Ten Hoeve, J.E. 2011. Effects of Urban Surfaces and White Roofs on Global and Regional Climate. Journal of Climate, 25, (3) 1028-1044

Jandaghian Z., Akbari H. 2018. The Effects of Increasing Surface Albedo on Urban Climate and Air Quality: A Detailed Study for Sacramento, Houston, and Chicago. Climate. 6(2) 19.

Jandaghian Z., Touchaei G.A., Akbari H. 2017. Sensitivity analysis of physical parameterizations in WRF for urban climate simulations and heat island mitigation in Montreal. Uclim. 24: 577-599

Jandaghian, Z., and Akbari, H. 2018. The effects of increasing surface reflectivity on heat-related mortality in Greater Montreal Area, Canada. Uclim. 25: 135-15

Janjic Z. I. 1994. The step–mountain Eta Coordinate Model: Further developments of the convection, viscous sublayer, and turbulence closure schemes. Monthly Weather Review. 122: 927–945.

Janjic Z. I. 2002. Nonsingular implementation of the Mellor–Yamada Level 2.5 Scheme in the NCEP meso model. NCEP Office Note, No. 437.

Janjic, Z.I., 1990. The step-mountain coordinate: physical package. Mon. Weather Rev. 118, 1429–1443.⸢⸤SEP⸥

Janjic, Z.I., 1994. The step–mountain eta coordinate model: further developments of the convection, viscous sublayer, and turbulence closure schemes. Mon. Weather Rev. 122, 927–945.⸢⸤SEP⸥

Jenkins K., Hall J., Glenis V., Kilsby C., McCarthy C., Goodess D., Smith N., Malleson M. 2014. Probabilistic spatial risk assessment of heat impacts and adaptations for London, Clim. Change 124: 105–117.

Jerrett M, Burnett RT, Beckerman BS, Turner MC, Krewski D, Thurston G, et al. 2013. Spatial analysis of

air pollution and mortality in California. Am J Respir Crit Care Med 188(5):593–599.

Jerrett M, Burnett RT, Pope CA III, Ito K, Thurston G, Krewski D, et al. 2009. Long-term ozone exposure and mortality. N Engl J Med 360(11):1085–1095.

Kain, J.S., 2004. The Kain–Fritsch convective parameterization: an update. J. Appl. Meteorol. 43, 170–181.⌊SEP⌋

Kalkstein L., Sailor D., Shickman K., Sherdian S. and Vanos J. 2013. Assessing the health impacts of urban heat island reduction strategies in the District of Columbia. Report DDOE ID#2013-10-OPS, Global Cool Cities Alliance.

Kalkstein L.S., Greene J.S., Mills D. and Samenow J. 2011. An Evaluation of the Progress in Reducing Heat- Related Human Mortality in Major U.S. cities. Natural Hazards 56:113-129.

Kalkstein L.S. and Sheridan S.C. 2003. The Impact of Heat Island Reduction Strategies on Health-Debilitating Oppressive Air Masses in Urban Areas. Phase 1. U.S. EPA Heat Island Reduction Initiative.

Kalkstein L.S. and Valimont K.M. 1986. An evaluation of summer discomfort in the United States using a relative climatological index. Bull. Am. Meteorol. Soc. 67, 842–848.

Kalkstein LS. 1999. A new approach to evaluate the impact of climate on human mortality. Environ Health Perspect 96:145-150.

Kalkstein, L.S. and Valimont, K.M., 1986. An evaluation of summer discomfort in the United States using a relative climatological index. Bull. Am. Meteorol. Soc. 67, 842–848.

Kalnay, E. and Cai, M. 2003. Impact of urbanization and land-use change on climate. Nature, 423, (6939) 528-531

Klüser, L., Rosenfeld, D., Macke, A. and Holzer-Popp, T., 2008. Observations of convective clouds generated by solar heating of dark smoke plumes. Atmospheric Chem- istry and Physics 8, 2833-2840.

Köhler, H. 1936. The nucleus in and the growth of hygroscopic droplets, T. Faraday Soc., 32, 1152–1161.

Koren, I., Kaufman Y. J, Remer L. A., and Martins J. V. 2004. Measurement of the effect of Amazon smoke on inhibition of cloud formation, Science, 303(5662), 1342–1345.

Krayenhoff E.S. and Voogt J.A. 2010. Impacts of urban albedo increase on local air temperature at daily-annual time scales: model results and synthesis of previous work, J. Appl. Meteorol. Climatol. 49: 1634–1648.

Kruger E.L., Minella F.O. and Rasia F. 2010. Impact of urban geometry on outdoor thermal comfort and air quality from field measurements in Curitiba, Brazil. Building & Environment. 46: 621-634.

Kusaka, H., Kondo, H., Kikegawa, Y., and Kimura, F. 2001. A Simple Single-Layer Urban Canopy Model for Atmospheric Models: Comparison With Multi-Layer And Slab Models. Boundary-Layer Meteorology, 101, (3) 329-358

Laden F, Schwartz J, Speizer FE and Dockery DW. 2006. Reduction in fine particulate air pollution and mortality: extended follow-up of the Harvard Six Cities study. Am J Respir Crit Care Med 173(6):667–

672.

Lai, L.W. and Cheng, W.L. 2009. Air quality influenced by urban heat island coupled with synoptic weather patterns. Science of The Total Environment, 407, (8) 2724-2733

Levin, Z. and Brenguier, J.-L. 2009. Effects of pollution and biomass aerosols on clouds and precipitation: observational studies, Chapter 6. In: Levin, Z., Cotton, W.R. (Eds.), Aerosol Pollution Impact on Precipitation: a Scientific Review. Springer, ISBN 978-1-4020-8689-2.

Li, D., Bou-Zeid, E., 2014. Quality and sensitivity of high-resolution numerical simulation of urban heat islands. Environ. Res. Lett. 9: 055-001.

Liao, J., Wang, T., Wang, X., Xie, M., Jiang, Z., Huang, X. and Zhu, J. 2014. Impacts of different urban canopy schemes in WRF/Chem on regional climate and air quality in Yangtze River Delta, China. Atmos. Res. 146, 226–243.

Lim, K.S., Hong, S., 2010. Development of an effective double-moment cloud microphysics scheme with prognostic Cloud Condensation Nuclei (CCN) for weather and climate models. Mon. Weather Rev. 138, 1587–1612.

Lin Y., Colle B. A. 2011. A new bulk microphysical scheme that includes riming intensity and temperature–dependent ice characteristics. Monthly Weather Review, 139: 1013–1035.

Lin Y., Farley R., Orville H. D. 1983. Bulk parameterization of the snow field in a cloud model. Climate and Applied Meteorology, 22:1065–1092.

Lin, Y., Colle, B.A., 2011. A new bulk microphysical scheme that includes riming intensity and temperature-dependent ice characteristics. Mon. Weather Rev. 139, 1013–1035.

Lin, Y., R. Farley, D., and Orville, H. D. 1983. Bulk parameterization of the snow field in a cloud model. J. Clim. Appl. Meteorol., 22, pp. 1065–1092.

Lin, Y., Farley, R. and Orville, H.D. Bulk parameterization of the snow field in a cloud model. J. Clim. Appl. Meteorol. 1983, 22, 1065–1092.

Liou, K.N., 1980. An Introduction to Atmospheric Radiation, 2nd ed. Academic Press, San Diego (CA), US.

Liu, X.-H., Zhang, Y., Olsen, K., Wang, W.-X., Do, B., and Bridgers, G. 2010. Responses of future air quality to emission controls over North Carolina, part I: model evaluation for current-year simulations. Atmospheric Environment 44 (23), 2443-2456.

Liu, Y., Chen, F., Warner, T., & Basara, J. 2006. Verification of a Mesoscale Data- Assimilation and Forecasting System for the Oklahoma City Area during the Joint Urban 2003 Field Project. Journal of Applied Meteorology and Climatology, 45, (7) 912-929

Lynn B H. 2009. A modification to the NOAH LSM to simulate heat mitigation strategies in the New York City metropolitan area J. Appl. Meteorol. Climatol. 48 199–216

Mansell, E.R., Ziegler, C.L. and Bruning, E.C., 2010. Simulated electrification of a small thunderstorm with two-moment bulk microphysics. J. Atmos. Sci. 67, 171–194.

Marta-Almeida, M., Teixeira, J.C., Carvalho, M.J., Melo-Gonçalves, P. and Rocha, M.A. 2016. High resolution WRF climatic simulations for the Iberian Peninsula: Model validation. Phys. Chem. Earth Parts 10: 03-010.

Martel B., Giroux J.X., Gosselin P., Chebana F., Ouarda T.B.M.J., Charron C. 2010. Indicateurs et seuils météorologiques pour les systèmes de veille-avertissement lors de vagues de chaleur au Québec. Québec: Institut national de santé publique du Québec. ISBN 978-2-550-59896-1.

Martilli, A. 2007. Current research and future challenges in urban mesoscale modelling. International Journal of Climatology, 27, (14) 1909-1918

Martilli, A., Clappier, A., and Rotach, M. 2002. An Urban Surface Exchange Parameterisation for Mesoscale Models. Boundary-Layer Meteorology, 104, (2) 261-304

Martilli, A., Grossman-Clarke, S., Tewari, M., and Manning, K. W. 2014. Description of the modifications made in WRF.3.1 and short user's manual of BEP. 24:05-014.

Matsui, H., Koike, M., Kondo, Y., Moteki, N., Fast, J. D., and Zaveri, R. A. 2013. Development and validation of a black carbon mixing state resolved three-dimensional model: aging processes and radiative impact, J. Geophys. Res.-Atmos., 118, 2304–2326

Matzarakis A. and Nastos P.T. 2011. Human-biometeorological assessment of heat waves in Athens. Theor. Appl. Climatol. 105, 99-106.

McGeehin M.A. and Mirabelli M. 2001. The potential impacts of climate variability and change on temperature-related morbidity and mortality in the United States. Environ Health Perspect 109(Suppl 2):185–189.

McMichael A. and Woodruff R.E, Hales S., 2006. Climate change and human health: present and future risks. 367(9513):859-69.

Mesinger F., Dimego G., Kalnay E., Mitchell K., Shafran P.C., Ebisuzaki W., Jovic D., Woollen J., Rogers E., Berbery E. H., EK M.B., Fan Y., Grumbine R., Higgins W., Li H., Lin Y., Manikin G., Parrish D., Shi W. 2006. North American Regional Reanalysis. Bulletin of American Meteorological Society, 87(3): 343–360.

Miao, S. G., Chen. F., Li. Q. C., and Fan S. Y. 2010. Impacts of urban processes and urbanization on summer precipitation: A case study of heavy rainfall in Beijing on 1 August 2006, J. Appl. Meteorol. Climatol., 50, 806–825.

Milbrandt, J.A., Yau, M.K., 2005a. A multimoment bulk microphysics parameterization. Part I: analysis of the role of the spectral shape parameter. J. Atmos. Sci. 62, 3051–3064.

Milbrandt, J.A., Yau, M.K., 2005b. A multimoment bulk microphysics parameterization. Part II: a proposed three-moment closure and scheme description. J. Atmos. Sci. 62, 3065–3081.

Millstein, D., Menon, S., 2011. Regional climate consequences of large-scale cool roof and photovoltaic array deployment. Environ. Res. Lett. 6 (034001).

Misenis, C. and Zhang, Y. 2010. An examination of sensitivity of WRF/Chem predictions to physical parameterizations, horizontal grid spacing, and nesting options. Atmos. Res. 2010, 97, 315–334.

Mlawer, E.J., Taubman, S.J., Brown, P.D., Iacono, M.J., Clough, S.A., 1997. Radiative transfer for inhomogeneous atmospheres: RRTM, a validated correlated-k model for the longwave. J. Geophys. Res. 102, 16663–16682.

Morakinyo. T.E, Balogun. A.A. and Adegun O.B. 2013. Comparing the effect of trees on thermal conditions of two typical urban buildings, Urban Clim. 3: 76–93

Morrison, H., Thompson, G., Tatarskii, V. 2009. Impact of cloud microphysics on the development of trailing stratiform precipitation in a simulated squall line: comparison of one- and two-moment schemes. Mon. Weather Rev. 137, 991–1007.

NCAR. WRF User's Guide. 2016. Mesoscale and Microscale Meteorology Division; National Center for Atmospheric Research (NCAR): Boulder, CO, USA.

NCAR. WRF-CHEM Emission Guide. 2016. National Center for Atmospheric Research (NCAR) and The University Corporation for Atmospheric Research (UCAR): Boulder, CO, USA.

NCAR. WRF-CHEM User's Guide. 2016. WRF-Chem Emissions Guide; National Center for Atmospheric Research (NCAR): Boulder, CO, USA.

Nitschke M., Tucker G.R., Hansen A., Williams S., Zhang Y. and Bi P. 2011. Impact of two recent extreme heat episodes on morbidity and mortality in Adelaide, South Australia: a case-series analysis. Environ. Health 10 (42): 10-42

NOAA. 2001. National oceanic and atmospheric administration changes to the NCEP Meso Eta analysis and forecast system: increase in resolution, new cloud microphysics, modified precipitation assimilation, modified 3DVAR analysis.

O'Neill M.S. and Ebi K.L. 2009. Temperature extremes and health: impacts of climate variability and change in the United States. J Occup Environ Med 51: 13–25.

O'Neill M.S. Zanobetti A. and Schwartz J. 2003. Modifiers of the temperature and mortality association in seven US cities, Am. J. Epidemiol. 157: 1074–1082.

O'Neill M.S., Zanobetti A. and Schwartz J. 2005. Disparities by race in heat-related mortality in four US cities: the role of air conditioning prevalence, J. Urban Health Bull. N. Y. Acad. Med. 82: 191–197.

Oke. TR. 1973. City size and the urban heat island. Atmos Environ 7:769–779

Oke, T.R. 1981. Canyon geometry and the nocturnal urban heat island: Comparison of scale model and field observations. Journal of Climatology, 1, (3) 237-254

Oke, T.R. 1982. The energetic basis of the urban heat island. Quarterly Journal of the Royal Meteorological Society, 108, (455) 1-24

Oke, T.R. 1987. Boundary layer climates, 5 ed. Psychology Press. Oleson, K.W., Bonan, G.B., & Feddema, J. 2010. Effects of white roofs on urban temperature in a global climate model. Geophysical Research Letters, 37, (3) L03701

Oke, T.R. 1997. Urban climates and global environmental change. Applied Climatology: Principles & Practices.New York, NY: Routledge 273-287

Oleson K.W., Bonan G.B. and Feddema J. 2010. The effects of white roofs on urban temperature in a global climate model, Geophys. Res. Lett., 37, 37: 03-21.

Oleson K.W., Bonan G.B., Feddema J. and Jackson T. 2011. An examination of urban heat island characteristics in a global climate model, Int. J. Climatol. 31(12): 02-22

Oliver B., Hoelscher M.T., Meier F., Nehls T., Ziegler F. 2015. Evaluation of the health-risk reduction potential of countermeasures to urban heat islands. Enbuild. 114: 27-37.

Onishi, A., Cao, X., Ito, T., Shi, F. and Imura, H. 2010. Evaluating the potential for urban heat-island mitigation by greening parking lots. Urban Forestry & Urban Greening, 9, (4) 323-332

Pan, H.L., Wu, W.S., 1995. Implementing a mass flux convective parameterization package for the NMC medium range forecast model. In: NMC Office Note, 409.40, pp. 20–233.

Peng R.D., Bobb J.F., Tebaldi C., McDaniel L., Bell M.L., Dominici F. 2011. Toward a quantitative estimate of future heatwave mortality under global climate change. Environ. Health Perspect. 119(5): 701-706.

Pielke, R.A.S., 2002. Mesoscale Meteorological Modeling, 2nd ed. Academic Press, San Diego (CA), US.

Qian, Y., D. Gong, J. Fan, L. R. Leung, R. Bennartz, D. Chen, and W. Wang. 2009. Heavy pollution suppresses light rain in China: Observations and modeling, J. Geophys. Res., 114, D00K02, doi:10.1029/2008JD011575.

Raaschou-Nielsen et al., 2013. Air pollution and lung cancer incidence in 17 European cohorts: prospective analyses from the European Study of Cohorts for Air Pollution Effects (ESCAPE). 10.1016/S1470-2045(13)70279-1.

Rizwan, A.M., Dennis, L.Y.C., and LIU, C. 2008. A review on the generation, determination and mitigation of Urban Heat Island. Journal of Environmental Sciences, 20, (1) 120-128

Rose, L.S., Akbari, H. and Taha, H. 2003. Characterizing the Fabric of the Urban Environment: A Case Study of Greater Houston, Texas; Report LBNL-51448; Lawrence Berkeley National Laboratory: Berkeley, CA, USA.

Rosenfeld, A.H., Akbari, H., Romm, J.J. and Pomerantz, M. 1998. Cool communities: strategies for heat island mitigation and smog reduction. Energy and Buildings, 28, (1) 51- 62

Rosenfeld, D. 2000. Suppression of rain and snow by urban and industrial air pollution, Science, 287(5459), 1793–1796.

Saide, P. E., Spak, S. N., Carmichael, G. R., Mena-Carrasco, M. A., Yang, Q., Howell, S., Leon, D. C., Snider, J. R., Bandy, A. R., Collett, J. L., Benedict, K. B., de Szoeke, S. P., Hawkins, L. N., Allen, G., Crawford, I., Crosier, J., and Springston, S. R. 2012. Evaluating WRF-Chem aerosol indirect effects in Southeast Pa- cific marine stratocumulus during VOCALS-REx, Atmos. Chem. Phys., 12, 3045–3064.

Sakka, A., Santamouris, M., Livada, I., Nicol, F. and Wilson, M. 2012. On the thermal performance of low-income housing during heat waves. Energy Build. 49, 69-77.

Salamanca, F. and Martilli, A. 2012. A numerical study of the Urban Heat Island over Madrid during the DESIREX (2008) campaign with WRF and an evaluation of simple mitigation strategies. International Journal of Climatology, 32, (15) 2372-2386

Salamanca, F. and Martilli, A. 2012. A numerical study of the Urban Heat Island over Madrid during the DESIREX (2008) campaign with WRF and an evaluation of simple mitigation strategies. International Journal of Climatology, 32, (15) 2372-2386

Salamanca, F., Georgescu, M., Mahalov, A., Moustaoui, M. and Wang, M. 2014. Anthropogenic heating of the urban environment due to air conditioning. J. Geophys. Res. Atmos. 119 (10), 5949–5965.

Salamanca, F., Martilli, A. and Yague, C. 2012. A numerical study of the Urban Heat Island over Madrid during the DESIREX (2008) campaign with WRF and an evaluation of simple mitigation strategies. Int. J. Climatol. 32, 2372–2386.

Santamouris M. 2014. Cooling the cities – a review of reflective and green roof mitigation technologies to fight heat island and improve comfort in urban environments, Sol. Energy 103: 682–703.

Santamouris M, Sfakianaki A, Pavlou K. 2010. On the efficiency of night ventilation techniques applied to residential buildings, Energy Build. 42: 1309–1313.

Santamouris M. 2013. Using cool pavements as a mitigation strategy to fight urban heat island – a review of the actual developments, Renew. Sustain. Energy Rev. 26: 224–240.

Savi T, Andri S. and Nardini A. 2013. Impact of different green roof layering on plant water status and drought survival, Ecol. Eng. 57: 188–196.

Schell, B., Ackermann, I.J., Hass, H., Binkowski, F.S. and Ebel, A. 2001. Modeling the formation of secondary organic aerosol within a comprehensive air quality model system. J. Geophys. Res. Atmos. 106: 28275–28293.

Schwarzenbach, R., Gschwend, P., and Imboden, D. 1993. Environmental Organic Chemistry. John Wiley & Sons Inc., New York.

Seinfeld, J.H. and Pandis, S.N. 2012. Atmospheric Chemistry and Physics: From Air Pollution to Climate Change, 2nd ed.; John Wiley & Sons, Inc.: Hoboken, NJ, USA.

Sheridan S. and Kalkstein A. 2009. Trends in heat-related mortality in the United States, 1975–2004. Nat Hazards. 50(1): 145–160.

Sheridan S.C, Kalkstein L.S. 2004. Progress in heat watch-warning system technology. Bull Am Meteorol Soc. 85:1931–1941.

Sheridan S.C. 2002. The redevelopment of a weather-type classification scheme for North America. Int J Climatol 22(1):51–68.

Sherwood S.C. and Huber M. 2010. An adaptability limit to climate change due to heat stress. Proc Nat Acad Sci 107:9552–9555.

Skamarock W.C., Klemp J.B., Dudhia J, Gill D.O., Barker D.M., Duha M.G., Huang X.Y., Wang W. and Powers J.G., 2008. A Description of the Advanced Research WRF Version 3. National Center for

Atmospheric Research: Boulder, CO, USA.

Skamarock, W. C., Klemp, J. B., Dudhia, J., Gill, D. O., Barker, D. M., Wang, W. and Powers, J. G. 2005. A Description of the Advanced Research WRF Version 2. National Center for Atmospheric Research Boulder CO Moseoscale and microscale meteorolgy division.

Skamarock, W.C., Klemp, J.B., Dudhia, J., Gill, D.O., Barker, D.M., Wang, W., Powers, J.G. 2008. A Description of the Advanced Research WRF Version 3; National Center for Atmospheric Research: Boulder, CO, USA.

Smoyer K.E, Rainham D.G. and Hewko J.N. 2000. Heat-stress-related mortality in five cities in Southern Ontario: 1980–1996. Int J Biometeorol. 44: 190–97.

Spanaki, A., Tsoutsos, T. and Kolokotsa, D. 2011. On the selection and design of the proper roof pond variant for passive cooling purposes. Renew. Sustain. Energy Rev. 15 (8), 3523-3533.

Stein, U. and Alpert, P. 1993. Factor separation in numerical simulations. J. Atmos. Sci. 50: 2107–2115. ⌊SEP⌋

Stocker, T.F., Dahe, Q., and Plattner, G.K. 2013. Climate Change 2013: The Physical Science Basis. Working Group I Contribution to the Fifth Assessment Report of the Intergovernmental Panel on Climate Change.Summary for Policymakers.

Stockwell, W.R., Kirchner, F., Kuhn, M., and Seefeld, S. 1997. A new mechanism for regional atmospheric chemistry modeling. Journal of Geophysical Research: Atmospheres, 102, (D22) 25847-25879

Stockwell, W.R., Middleton, P., Chang, J.S., and Tang, X. 1990. The second-generation regional acid deposition model chemical mechanism for regional air quality modeling. Journal of Geophysical Research: Atmospheres, 95, (D10) 16343-16367

Stockwell, W.R., Kirchner, F., Kuhn, M. and Seefeld, S. 1997. A new mechanism for regional atmospheric chemistry modeling. J. Geophys. Res. Atmos. 102, 25847–25879.

Synnefa A., Santamouris M. and Kolokotsa D. 2009. Promotion of cool roofs in the EU—The Cool Roofs Project Second Int. Conf. on Countermeasures to Urban Heat Islands (Berkeley, CA) (available at http://heatisland2009.lbl.gov/docs/ 231120-synnefa-doc.pdf)

Taha H., Akbari H. and Rosenfeld A. 1991. Heat island and oasis effects of vegetative canopies: micrometeorological field-measurements. Theor Appl Climatol. 44:123–38.

Taha H. 1997. Urban climates and heat islands: albedo, evapotranspiration, and anthropogenic heat. Energy Build Spec Issue Urban Heat Islands. 25: 99–103.

Taha H. 2008. Urban surface modification as a potential ozone air-quality improvement strategy in California: A mesoscale modeling study. Bound. Layer Meteorol. 127: 219–239.

Taha H. 2008. Meso-urban meteorological and photochemical modeling of heat island mitigation. Atmos Environ. 42:8795-809.

Taha H., 2009. In Mesoscale and Meso-urban Meteorological and Photochemical Modeling of Heat Island Mitigation in California: Results and Regulatory Aspects Conference on Countermeasures to UHI, Berkeley (CA) USA. ⌊SEP⌋

Taha, H. 1997a. Modeling the impacts of large-scale albedo changes on ozone air quality in the South Coast Air Basin. Atmospheric Environment, 31, (11) 1667-1676 [SEP]

Taha, H. 1999. Modifying a Mesoscale Meteorological Model to Better Incorporate Urban Heat Storage: A Bulk-Parameterization Approach. Journal of Applied Meteorology, 38, (4) 466-473

Taha, H. 2008. Episodic Performance and Sensitivity of the Urbanized MM5 (uMM5) to Perturbations in Surface Properties in Houston Texas. Bound. Layer Meteorol. 127, 193–218.

Taha, H. 2005. Evaluating Meteorological Impacts of Urban Forest and Albedo Changes in the Houston-Galveston Region: A Fine-Resolution (UCP) Meso-Urban Modeling Study of the August–September 2000 Episode; Report Prepared for the Houston Advanced Research Center by Altostratus Inc.; Altostratus Inc.: Martinez, CA, USA.

Taha, H. 2013. Meteorological, emissions, and air-quality modeling of heat-island mitigation: Recent findings for California, USA. Int. J. Low Carbon Technol. 10: 3–14.

Taha, H. 2003. Potential Meteorological and Air-Quality Implications of Heat-Island Reduction Strategies in the Houston-Galveston TX Region; Technical Note HIG-12-2002-01; Lawrence Berkeley National Laboratory: Berkeley, CA, USA.

Taha, H. 2013. Ranking and Prioritizing the Deployment of Community-Scale Energy Measures Based on Their Indirect Effects in California's Climate Zones. Available online: http://www.energy.ca.gov/2011publications/CEC-500-2011-FS/CEC-500-2011-FS-021.pdf (accessed on 28 January 2018).

Taha, H., Chang, S. and Akbari, H., 2000. Meteorological and Air Quality Impacts of Heat Island Mitigation Measures in Three U.S. Cities. LBNL, Berkeley (CA) USA

Taha, H., Konopacki, S., and Gabersek, S. 1999. Impacts of Large-Scale Surface Modifications on Meteorological Conditions and Energy Use: A 10-Region Modeling Study. Theor. Appl. Climatol. 62: 175–185.

Taha, H., Wilkinson, J., Bornstein, R., Xiao, Q., McPherson, G., Simpson, J., Anderson, C., Lau, S., Lam, J. and Blain, C. 2015. An urban–forest control measure for ozone in the Sacramento, CA Federal Non-Attainment Area (SFNA). Sustain. Cities Soc. 21: 51–65.

Tao, W., Simpson, J. and McCumber, M., 1989. An ice–water saturation adjustment. Mon. Weather Rev. 117, 231–235. [SEP]

Tao, W.-K., Shi, J.J., Chen, S.S., Lang, S., Lin, P.-L., Hong, S.-Y., Peters-Lidard, C., Hou, A. 2011. The impact of microphysical schemes on hurricane intensity and track. Asia-Pac. J. Atmos. [SEP]

Tao, Z., Larson, S.M., Wuebbles, D.J., Williams, A. and Caughey, M. 2003. A summer simulation of biogenic contributions to ground-level ozone over the continental United States. J. Geophys. Res. 108-4404. [SEP]

Tessum, C.W., Hill, J.D. and Marshall, J.D. 2015. Twelve-month, 12 km resolution North American WRF-Chem v3.4 air quality simulation: Performance evaluation. Geosci. Model. Dev. 8: 957–973.

Tewari, M., Chen, F., Wang, W., Dudhia, J., LeMone, M.A., Mitchell, K., Ek, M., Gayno, G., Wegiel, J. and Cuenca, R.H. 2004. Implementation and verification of the unified NOAH land surface model in the

WRF model. In: 20th Conference on Weather Analysis and Forecasting/16th Conference on Numerical Weather Prediction, pp.11–15.

Thompson, G., Field, P.R., Rasmussen, R.M. and Hall, W.D. 2008. Explicit forecasts of winter precipitation using an improved bulk microphysics scheme. Part II: implementation of a new snow parameterization. Mon. Weather Rev. 136, 5095–5115. Tiedtke, M., 1989. A comprehensive mass flux scheme for cumulus parameterization in large-scale models. Mon. Weather Rev. 117, 1779–1800.

Thunis, P. and Cuvelier, C. 2000. Impact of biogenic emissions on ozone formation in the Mediterranean area—A BEMA modeling study. Atmos. Environ. 34: 467–481.

Tong, H., Walton, A., Sang, J., and Chan, J.C.L. 2005. Numerical simulation of the urban boundary layer over the complex terrain of Hong Kong. Atmospheric Environment, 39, (19) 3549-3563

Touchaei A.G. and Akbari H. 2013. The climate effects of increasing the albedo of roofs in a cold region. Adv. Build. Energy Res. 7: 186–191.

Touchaei A.G. and Akbari H. 2015. Evaluation of the seasonal effect of increasing albedo on urban climate and energy consumption of buildings in Montreal. Urban Clim. 14: 278–289.

Touchaei, A.G., Akbari, H. and Tessum, C.W. 2016. Effect of increasing urban albedo on meteorology and air quality of Montreal (Canada) - Episodic simulation of heat wave in 2005. Atmos. Environ. 132, 188e206.

Touchaei, A.G. and Wang, Y., 2015. Characterizing urban heat island in Montreal (Canada)—effect of urban morphology. Sustain. Cities Soc. 19, 395–402.

UCAR (University Corporation for Atmospheric Research). GCIP NCEP Eta Model Output. 2005. Available online: http://rda.ucar.edu/datasets/ds609.2/ (accessed on 15 January 2017).

US Census Bureau. Cartographic Boundary Shapefiles Regions. 2013. Available online: https://www.census.gov/geo/maps-data/data/cbf/cbf_region.html (accessed on 10 February 2017).

US Census Bureau. Year-2014 US Urban Areas and Clusters. 2014. Available online: ftp://ftp2.census.gov/geo/tiger/TIGER2014/UAC/ (accessed on 10 February 2017).

US EPA (US Environmental Protection Agency). Air Quality Modeling Technical Support Document for the Regulatory Impact Analysis for the Revisions to the National Ambient Air Quality Standards for Particulate Matter, Research Triangle Park, NC 27711. 2012. Available online: http://www.regulations.gov/ (accessed on 28 January 2018).

US-National Climate Data Centre (NOAA). Available online: https://www.ncdc.noaa.gov (accessed on 28 January 2018).

Vandentorren, S., Bretin, P., Zeghnoun, A., Mandereau-Bruno, L., Croisier, A., Cochet, C., Riberon, J., Siberan, I., Declercq, B. and Ledrans, M., 2006. Heat-related mortality e August 2003 heat wave in France: risk factors for death of elderly people living at home. Eur. J. Public Health 16 (6), 583e591.

Vaneckova P., Beggs P.J. and Jacobson C.R., 2010. Spatial analysis of heat-related mortality among the elderly between 1993 and 2004 in Sydney, Australia. Soc. Sci. Med. 70 (2), 293-304.

Vanos J.K., Cakmak S., Bristow C., Brion V., Tremblay N., Martin S.L. and Sheridan S.S. 2013. Synoptic

weather typing applied to air pollution mortality among the elderly in 10 Canadian cities. Environ Res 126:66–75.

Vanos J.K., Hebbern C. and Cakmak S. 2014. Risk assessment for cardio- vascular and respiratory mortality due to air pollution and synoptic meteorology in 10 Canadian cities. Environ Pollut 185:322–332.

Wan, H. C., Z. Zhong, X. Q. Yang, and X. A. Li. 2013. Impact of city belt in Yangtze River Delta in China on a precipitation process in summer: A case study, Atmos. Res., 125–126, 63–75.

Wang K., Zhang, Y., Jang C.J., Phillips S. and Wang B.Y. 2009. Modelling study of Intercontinental air pollution transport over the Trans-Pacific region in 2001 using the community multiscale air quality (CMAQ) modelling system. J. Geophys. Res. 114, 43-07.

Wang X.Y., Barnett A.G., Yu W., FitzGerald G., Tippett V., Aitken P., Neville G., McRae D., Verrall K. and Tong S. 2012. The impact of heatwaves on mortality and emergency hospital admissions from non-external causes in Brisbane, Australia. Occup. Environ. Med. 69 (3), 163-169.

Williams, D., Elghali, L., Wheeler, R. and France, C. 2012. Climate change influence on building lifecycle greenhouse gas emissions: case study of a UK mixed-use development. Energy Build. 48, 112e126.

World Health Organization (WHO). 2010. International Classification of Diseases, 10th Revision (ICD-10).

WRF User's Guide. 2016. Mesoscale & Microscale Meteorology Division, National Center for Atmospheric Research (NCAR).

Wu S.-Y., Krishnan S., Zhang Y. and Aneja V. 2008. Modelling atmospheric transport and fate of ammonia in North Carolina, part I. Evaluation of meteorological and chemical predictions. Atmos. Environ. 42, 3419–3436.

Wu, L., Su, H., and Jiang, J. H. 2011. Regional simulations of deep convection and biomass burning over South America: 2. biomass burning aerosol effects on clouds and precipitation, J. Geophys. Res., 116, D17209

Wu, S.-Y., Krishnan, S., Zhang, Y. and Aneja, V. 2008. Modelling atmospheric transport and fate of ammonia in North Carolina, part I. Evaluation of meteorological and chemical predictions. Atmospheric Environment 42, 3419-34 SEP

Yahya, K., Wang, K., Gudoshava, M., Glotfelty, T. and Zhang, Y. 2006. Application of WRF/Chem over North America under the AQMEII Phase 2: Part I. Comprehensive evaluation of 2006 simulation. Atmos. Environ. 2015, 155, 733–755.

Yardley J., Sigal R.J., Kenny G.P. 2011. Heat health planning: the importance of social and community factors. Glob. Environ. Change 21 (2), 670-679.

Zanobetti A., Luttmann-Gibson H., Horton E.S., Cohen A., Coull B.A., Hoffmann B., Schwartz J.D., Mittleman M.A., Li Y., Stone P.H., de Souza C., Lamparello B., Koutrakis P. and Gold D.R., 2014. Brachial artery responses to ambient pollution, temperature, and humidity in people with type 2 diabetes: a repeated-measures study. Environ. Health Perspect. 122 (3), 242.

Zanobetti A. and Schwartz J. 2008. Temperature and mortality in nine US cities. Epidemiology 19:563-70.

Zaveri, R. A., Easter, R. C., Fast, J. D., and Peters, L. K. 2008. Model for simulating aerosol interactions and chemistry (MOSAIC), J. Geophys. Res., 113, D132024

Zaveri, R. A. 2013. Development and validation of a black carbon mixing state resolved three-dimensional model: aging processes and radiative impact, J. Geophys. Res.-Atmos., 118, 2304–2326.

Zhang K., Li Y., Schwartz J.D. and O'Neill M.S. 2014. What weather variables are important in predicting heat-related mortality? A new application of statistical learning methods. Environ. Res. 132, 350-359.

Zhang K., Chen Y.H., Schwartz J.D., Rood R.B. and O'Neill M.S. 2014. Using forecast and observed weather data to assess performance of forecast products in identifying heat waves and estimating heat wave effects on mortality. Environ. Health Perspect. 122, 912-918.

Zhang Y., Liu X.H., Olsen K. M., Wang W.X., Do B.A. and Bridgers G. M. 2010. Responses of future air quality to emission controls over North Carolina—Part I: Model evaluation for current-year simulations. Atmos. Environ. 44: 2443–2456.

Zhang, C., Wang, Y. and Hamilton, K. 2011. Improved representation of boundary layer clouds over the southeast pacific in ARW–WRF using a modified Tiedtke cumulus parameterization scheme. Mon. Weather Rev. 139, 3489–3513.

Zhang, F., Wang, J. and Ichoku, C. 2014. Sensitivity of mesoscale modelling of smoke direct radiative effect to the emission inventory: a case study in north- ern sub-Saharan African region, Environ. Res. Lett., 9, 075002.

Zhang, G.J. and McFarlane, N.A. 1995. Sensitivity of climate simulations to the parameterization of cumulus convection in the Canadian Climate Centre General Circulation Model. Atmosphere-Ocean 33, 407–446.

Zhang, Y., Dulière, V., Mote, P.W., Salathé, E.P. 2009. Evaluation of WRF and HadRM mesoscale climate simulations over the U.S. Pacific Northwest. J. Clim. 22, 5511–5526.

Zhang, Y., Fu, R., Yu, H., Dickinson, R. E., Juarez, R. N., Chin, M., and Wang, H. 2008. A regional climate model study of how biomass burning aerosol impacts land–atmosphere inter- actions over the Amazon, J. Geophys. Res., 113.

Zhang, Y., Chen, Y., Sarwar, G., Schere, K. 2012. Impact of gas-phase mechanisms on Weather Research Forecasting Model with Chemistry (WRF/Chem) predictions: Mechanism implementation and comparative evaluation. J. Geophys. Res.

Zhang, Y., Liu, P., Pun, B. and Seigneur, C. 2006. A comprehensive performance evaluation of MM5-CMANQ for the summer 1999 southern oxidant study episode—Part I. Evaluation protocols, databases and meteorological predictions. Atmos. Environ. 40: 4825–4838.

Zhao, Q., Black, T.L. and Baldwin, M.E., 1997. Implementation of the cloud prediction scheme in the eta model at NCEP. Weather Forecast. 12, 697–712.

Zheng, Y., Alapaty, K., Herwehe, J.A., Del Genio, A.D. and Niyogi, D. 2016. Improving high-resolution weather forecasts using the Weather Research and Forecasting (WRF) model with an updated Kain–Fritsch scheme. AMS Journal.

Appendices

Appendix A presents the "namelist.input" of each task of this dissertation. The theory of the aerosol interactions in the atmosphere is presented in Appendix B. Appendix C shows the chart of the National Weather Service – Heat Index (NWS-HI).

Appendix A

A.1. The 1st Task WRF namelist.input

A.1. The 1st Task WRF namelist.input

A sample of the WRF "namelist.input" for the "Sensitivity Analysis of Physical Parameterizations in WRF for Urban Climate Simulations and Heat Island Mitigation in Montreal".

Namelist.input (S01)

```
&time_control
run_days                = 4,
run_hours               = 12,
run_minutes             = 0,
run_seconds             = 0,
start_year              = 2009, 2009, 2009, 2009,
start_month             = 08, 08, 08, 08,
start_day               = 08, 08, 08, 08,
start_hour              = 00, 00, 00, 00,
start_minute            = 00, 00, 00, 00,
start_second            = 00, 00, 00, 00,
end_year                = 2009, 2009, 2009, 2009
end_month               = 08, 08, 08, 08,
end_day                 = 11, 11, 11, 11,
end_hour                = 12, 12, 12, 12,
end_minute              = 00, 00, 00, 00,
end_second              = 00, 00, 00, 00,
interval_seconds        = 21600,
input_from_file         =.true., .true., .true., .true.,
history_interval        = 60, 60, 60, 60,
frames_per_outfile      = 1000, 1000, 1000, 1000,
restart                 = .false.,
restart_interval        = 1440,
write_hist_at_0h_rst = .true.,
io_form_history         = 2,
io_form_restart         = 102,
io_form_input           = 2,
io_form_boundary        = 2,
debug_level             = 500,
io_form_auxinput2    = 2,
/
&domains
time_step               = 54,
time_step_fract_num     = 0,
time_step_fract_den     = 1,
max_dom                 = 4,
s_we                    = 1, 1, 1, 1,
e_we                    = 37, 43, 91, 145,
s_sn                    = 1, 1, 1, 1,
e_sn                    = 22, 34, 61, 91,
e_vert                  = 51, 51, 51, 51,
p_top_requested         = 10000,
```

```
num_metgrid_levels      = 30,
num_metgrid_soil_levels    = 4,
dx                      = 9000, 3000, 1000, 333.333,
dy                = 9000, 3000, 1000, 333.333,
grid_id                   = 1, 2, 3, 4,
parent_id               = 1, 1, 2, 3,
i_parent_start          = 1, 12, 6, 19,
j_parent_start          = 1, 6, 6, 21,
parent_grid_ratio       = 1, 3, 3, 3,
parent_time_step_ratio  = 1, 3, 3, 3,
feedback                = 1,
smooth_option           = 2,
eta_levels = 1.0000, 0.9968, 0.9953, 0.9937, 0.9921, 0.9905, 0.9886, 0.9864, 0.9837, 0.9805, 0.9766, 0.9720,
0.9664, 0.9599, 0.9520, 0.9427, 0.9315, 0.9184, 0.9028, 0.8753, 0.8407, 0.7752, 0.7142, 0.6574, 0.6046, 0.5553,
0.5095, 0.4668, 0.4271, 0.3901, 0.3557, 0.3236, 0.2937, 0.2659, 0.2401, 0.2160, 0.1935, 0.1726, 0.1532, 0.1351,
0.1182, 0.1025, 0.0879, 0.0743, 0.0616, 0.0498, 0.0338, 0.0286, 0.0191, 0.0033, 0.0000,
/
&physics
mp_physics         = 16, 16, 16, 16,
ra_lw_physics      = 4, 4, 4, 4,
ra_sw_physics      = 4, 4, 4, 4,
radt               = 10, 10, 10, 10,
sf_sfclay_physics  = 2, 2, 2, 2,
sf_surface_physics = 2, 2, 2, 2,
sf_urban_physics   = 0, 0, 0, 3,
bl_pbl_physics     = 2, 2, 2, 2,
bldt               = 0, 0, 0, 0,
cu_physics         = 4, 4, 4, 0,
cudt               = 5, 5, 5, 5,
icloud             = 1,
isfflx             = 1,
ifsnow             = 1,
surface_input_source = 1,
maxiens            = 1,
maxens             = 3,
maxens2            = 3,
maxens3            = 16,
ensdim             = 144,
num_soil_layers    = 4,
num_urban_layers   = 5400,
/
&dynamics
w_damping          = 1,
diff_opt           = 1, 1, 1, 1,
km_opt             = 1, 1, 1, 1,
diff_6th_opt       = 0, 0, 0, 0,
diff_6th_factor    = 0.12, 0.12, 0.12, 0.12,
base_temp          = 290.,
damp_opt           = 0,
zdamp              = 5000., 5000., 5000., 5000.,
dampcoef           = 0.2, 0.2, 0.2, 0.2,
khdif              = 0, 0, 0, 0,
kvdif              = 0, 0, 0, 0,
non_hydrostatic    = .true.,  .true.,  .true.,  .true.,
moist_adv_opt      = 1, 1, 1, 1,
scalar_adv_opt     = 1, 1, 1, 1,
```

```
/
&bdy_control
spec_bdy_width        = 5,
spec_zone             = 1,
relax_zone            = 4,
specified             = .true.,  .false.,  .false.,  .false.,
nested                = .false.,  .true.,  .true.,  .true.,
/

      &grib2
       /

&namelist_quilt
nio_tasks_per_group   = 0,
nio_groups            = 1,
```

A.2. The 2nd Task WRF namelist.input

Effects of Increasing Surface Reflectivity on Heat-Related Mortality in Greater Montreal Area, Canada. The WRF name-list is for the 2005 heat wave period. For the 2011 heat wave, the simulation configuration is the same, the date is different, thus the input data.

```
&time_control
run_days            = 0,
run_hours           = 0,
run_minutes         = 0,
run_seconds         = 0,
start_year          = 2005,   2005,   2005,   2005,
start_month         = 07,     07,     07,     07,
start_day           = 08,     08,     08,     08,
start_hour          = 12,     12,     12,     12,
start_minute        = 00,     00,     00,     0,
start_second        = 00,     00,     00,     0,
end_year            = 2005,   2005,   2005,   2005,
end_month           = 07,     07,     07,     07,
end_day             = 12,     12,     12,     12,
end_hour            = 12,     12,     12,     12,
end_minute          = 00,     00,     00,     0,
end_second          = 00,     00,     00,     0,
interval_seconds    = 10800,
input_from_file     = .true.,  .true.,  .true.,  .true.,
history_interval    = 60,     60,     60,     60,
frames_per_outfile  = 1000,   1000,   1000,   1000,
restart             = .false.,
restart_interval    = 1440,
io_form_history     = 2,
io_form_restart     = 2,
io_form_input       = 2,
io_form_boundary    = 2,
debug_level         = 500,
io_form_auxinput2   = 2,
/

&domains
time_step           = 54,
time_step_fract_num = 0,
time_step_fract_den = 1,
max_dom             = 4,
s_we                = 1,  1,  1,  1,
e_we                = 37, 43, 91, 145,
s_sn                = 1,  1,  1,  1,
e_sn                = 22, 34, 61, 91,
e_vert              = 51, 51, 51, 51,
p_top_requested     = 10000,
num_metgrid_levels  = 30,
num_metgrid_soil_levels = 4,
```

```
dx                    = 9000,   3000,   1000,   333.333,
dy                    = 9000,   3000,   1000,   333.333,
grid_id               = 1,      2,      3,      4,
parent_id             = 1,      1,      2,      3,
i_parent_start        = 1,      12,     6,      19,
j_parent_start        = 1,      6,      6,      21,
parent_grid_ratio     = 1,      3,      3,      3,
parent_time_step_ratio = 1,     3,      3,      3,
feedback              = 1,
smooth_option         = 2,
eta_levels = 1.0000, 0.9968, 0.9953, 0.9937, 0.9921, 0.9905, 0.9886, 0.9864, 0.9837, 0.9805, 0.9766, 0.9720,
0.9664, 0.9599, 0.9520, 0.9427, 0.9315, 0.9184, 0.9028, 0.8753, 0.8407, 0.7752, 0.7142, 0.6574, 0.6046, 0.5553,
0.5095, 0.4668, 0.4271, 0.3901, 0.3557, 0.3236, 0.2937, 0.2659, 0.2401, 0.2160, 0.1935, 0.1726, 0.1532, 0.1351,
0.1182, 0.1025, 0.0879, 0.0743, 0.0616, 0.0498, 0.0338, 0.0286, 0.0191, 0.0033, 0.0000,

/

&physics
mp_physics            = 2,      2,      2,      2,
ra_lw_physics         = 4,      4,      4,      4,
ra_sw_physics         = 5,      5,      5,      5,
radt                  = 9,      9,      9,      9,
sf_sfclay_physics     = 2,      2,      2,      2,
sf_surface_physics    = 2,      2,      2,      2,
sf_urban_physics      = 0,      0,      0,      1,
bl_pbl_physics        = 2,      2,      2,      2,
bldt                  = 0,      0,      0,      0,
cu_physics            = 5,      0,      0,      0,
cudt                  = 0,
icloud                = 1,
surface_input_source  = 1,
maxiens               = 1,
maxens                = 3,
maxens2               = 3,
maxens3               = 16,
ensdim                = 144,
num_soil_layers       = 4,

/
&fdda
/

&dynamics
w_damping             = 1,
diff_opt              = 1,      1,      1,      1,
km_opt                = 4,      4,      4,      4,
diff_6th_opt          = 0,      0,      0,      0,
diff_6th_factor       = 0.12,   0.12,   0.12,   0.12,
base_temp             = 290.,
damp_opt              = 0,
zdamp                 = 5000.,  5000.,  5000.,  5000.,
dampcoef              = 0.2,    0.2,    0.2,    0.2,
khdif                 = 0,      0,      0,      0,
kvdif                 = 0,      0,      0,      0,
non_hydrostatic       = .true., .true., .true., .true.,
moist_adv_opt         = 1,      1,      1,      1,
```

```
scalar_adv_opt        = 1,      1,      1,      1,
/


&bdy_control
spec_bdy_width        = 5,
spec_zone             = 1,
relax_zone            = 4,
specified             = .true., .false., .false., .false.,
nested                = .false.,  .true.,  .true.,  .true.,
/


&grib2
/


&namelist_quilt
nio_tasks_per_group   = 0,
nio_groups            = 1,
/
```

A.3. The 3rd Task WRF-Chem namelist.input

The Effect of Increasing Surface Albedo on Urban Climate and Air Quality: A Detailed Study for Sacramento, Houston, and Chicago.

```
&time_control
run_days             = 0,
run_hours            = 0,
run_minutes          = 0,
run_seconds          = 0,
start_year           = 2011, 2011, 2011, 2011,
start_month          = 07, 07, 07, 07,
start_day            = 15, 15, 15, 15,
start_hour           = 00, 00, 00, 00,
start_minute         = 00, 00, 00, 00,
start_second         = 00, 00, 00, 00,
end_year             = 2011, 2011, 2011, 2011,
end_month            = 07, 07, 07, 07,
end_day              = 23, 23, 23, 23,
end_hour             = 00, 00, 00, 00,
end_minute           = 00, 00, 00, 00,
end_second           = 00, 00, 00, 00,
interval_seconds     = 21600,
input_from_file      = .true., .true., .true., .true.,
history_interval     = 60, 60, 60, 60,
frames_per_outfile   = 1000, 1000, 1000, 1000,
restart              = .false.,
restart_interval     = 1440,
write_hist_at_0h_rst = .ture.,
io_form_history      = 2,
io_form_restart      = 2,
io_form_input        = 2,
io_form_boundary     = 2,
auxinput6_inname     = 'wrfbiochemi_<domain>',
auxinput5_inname     = 'wrfchemi_<domain>_<date>',
auxinput5_interval_m = 60, 60, 60, 60,
io_form_auxinput2    = 2,
io_form_auxinput5    = 2,
io_form_auxinput6    = 2,
io_form_auxinput7    = 0,
io_form_auxinput8    = 0,
io_form_auxinput12   = 0,
io_form_auxinput13   = 0,
debug_level          = 500,
auxinput1_inname     = "met_em.d<domain>.<date>",

/

&domains
```

```
time_step              = 72,
time_step_fract_num    = 0,
time_step_fract_den    = 1,
max_dom                = 4,
s_we                   = 1, 1, 1, 1,
e_we                   = 445, 36, 41, 36,
s_sn                     = 1, 1, 1, 1,
e_sn                     = 338, 31, 31, 31,
e_vert                   = 35, 35, 35, 35,
p_top_requested          = 10000,
num_metgrid_levels     = 30,
num_metgrid_soil_levels = 4,
dx                       = 12000, 2400, 2400, 2400,
dy                       = 12000, 2400, 2400, 2400,
grid_id                  = 1, 2, 3, 4,
parent_id                = 1, 1, 1, 1,
i_parent_start           = 1, 35, 272, 221,
j_parent_start           = 1, 181, 187, 71,
parent_grid_ratio        = 1, 5, 5, 5,
parent_time_step_ratio   = 1, 5, 5, 5,
feedback                 = 1,
smooth_option            = 0,
zap_close_levels         = 50,
interp_type              = 1,
t_extrap_type            = 2,
force_sfc_in_vinterp     = 0,
use_levels_below_ground = .true.
use_surface              = .true.
lagrange_order           = 2,
/
sfcp_to_sfcp             = .true.,

/
&physics
mp_physics           = 2, 2, 2, 2,
progn                = 1, 1, 1, 1,
ra_lw_physics        = 4, 4, 4, 4,
swint_opt            = 1,
ra_sw_physics        = 4, 4, 4, 4,
radt                 = 21, 21, 21, 21,
sf_sfclay_physics    = 2, 2, 2, 2,
sf_surface_physics   = 2, 2, 2, 2,
sf_urban_physics     = 0, 3, 3, 3,
bl_pbl_physics       = 2, 2, 2, 2,
bldt                 = 0, 0, 0, 0,
cu_physics           = 3, 3, 3, 3,
icloud               = 1,
ifsnow               = 1,
isfflx               = 1,
surface_input_source = 1,
cu_diag              = 1, 1, 1, 1,
 cudt                = 0,
 surface_input_source = 1,
 num_soil_layers     = 4,
 num_urban_layers    = 5400,
 mp_zero_out         = 2,
```

```
mp_zero_out_thresh     = 1.e-12,
maxiens                = 1,
maxens                 = 3,
maxens2                = 3,
maxens3                = 16,
ensdim                 = 144,
cu_rad_feedback        = .true., .true., .true., .true.,
/

&fdda
/

&dynamics
rk_ord                 = 3,
w_damping              = 1,
diff_opt               = 1, 1, 1, 1,
km_opt                 = 4, 4, 4, 4,
diff_6th_opt           = 0, 0, 0, 0,
diff_6th_factor        = 0.12, 0.12, 0.12, 0.12,
base_temp              = 290.0,
damp_opt               = 0,
zdamp                  = 5000.0, 5000.0, 5000.0, 5000.0,
dampcoef               = 0.2, 0.2, 0.2, 0.2,
khdif                  = 0, 300, 300, 300,
kvdif                  = 0, 300, 300, 300,
non_hydrostatic        = .true., .true., .true., .true.,
moist_adv_opt          = 2, 2, 2, 2,
scalar_adv_opt         = 2, 2, 2, 2,
chem_adv_opt           = 2, 2, 2, 2,
tke_adv_opt            = 2, 2, 2, 2,
time_step_sound        = 4, 4, 4, 4,
h_mom_adv_order        = 5, 5, 5, 5,
v_mom_adv_order        = 3, 3, 3, 3,
h_sca_adv_order        = 5, 5, 5, 5,
v_sca_adv_order        = 3, 3, 3, 3,
/


&bdy_control
spec_bdy_width    = 5,
spec_zone         = 1,
relax_zone        = 4,
specified         = .true.,  .false.,  .false.,  .false.,
nested            = .false.,  .true.,   .true.,   .true.,
/

&grib2
/

&namelist_quilt
nio_tasks_per_group     = 0,
nio_groups              = 1,
/

&chem
 kemit                  = 23,
```

```
chem_opt              = 11, 11, 11, 11,
bioemdt               = 30, 30, 30, 30,
photdt                = 30, 30, 30, 30,
chemdt                = 0, 0, 0, 0,
io_style_emissions    = 2,
emiss_opt             = 3, 3, 3, 3,
emiss_opt_vol         = 0, 0, 0, 0,
chem_in_opt           = 0, 0, 0, 0,
phot_opt              = 2, 2, 2, 2,
gas_drydep_opt        = 1, 1, 1, 1,
aer_drydep_opt        = 1, 1, 1, 1,
bio_emiss_opt         = 2, 2, 2, 2,
ne_area               = 104,
dust_opt              = 2,
dmsemis_opt           = 0,
seas_opt              = 2,
depo_fact             = 0.25,
gas_bc_opt            = 1, 1, 1, 1,
gas_ic_opt            = 1, 1, 1, 1,
aer_bc_opt            = 1, 1, 1, 1,
aer_ic_opt            = 1, 1, 1, 1,
gaschem_onoff         = 1, 1, 1, 1,
aerchem_onoff         = 1, 1, 1, 1,
wetscav_onoff         = 1, 1, 1, 1,
cldchem_onoff         = 1, 1, 1, 1,
vertmix_onoff         = 1, 1, 1, 1,
chem_conv_tr          = 1, 1, 1, 1,
conv_tr_wetscav       = 1, 1, 1, 1,
conv_tr_aqchem        = 1, 1, 1, 1,
biomass_burn_opt      = 0, 0, 0, 0,
plumerisefire_frq     = 30, 30, 30, 30,
have_bcs_chem         = .true., .true.,.true.,.true.,
aer_ra_feedback       = 1,
aer_op_opt            = 1,
opt_pars_out          = 1,
diagnostic_chem       = 0,
chemdiag              = 1,
/
```

A.4. The 4th Task WRF-Chem namelist.input

Effects of increasing surface reflectivity on aerosol-radiation-cloud interaction over Greater Montreal Area during the 2011 heat wave period. The namelist of the ARC simulation is presented.

Namelist. Input WRF-Chem (ARC)

```
&time_control
run_days             = 0,
run_hours            = 0,
run_minutes          = 0,
run_seconds          = 0,
start_year           = 2011, 2011, 2011,
start_month          = 07, 07, 07,
start_day            = 15, 15, 15,
start_hour           = 00, 00, 00,
start_minute         = 00, 00, 00,
start_second         = 00, 00, 00,
end_year             = 2011, 2011, 2011,
end_month            = 07, 07, 07,
end_day              = 23, 23, 23,
end_hour             = 00, 00, 00,
end_minute           = 00, 00, 00,
end_second           = 00, 00, 00,
interval_seconds     = 21600,
input_from_file      = .true., .true., .true.,
history_interval     = 60, 60, 60, 60,
frames_per_outfile   = 1000, 1000, 1000, 1000,
restart              = .false.,
restart_interval     = 1440,
write_hist_at_0h_rst = .ture.,
io_form_history      = 2,
io_form_restart      = 2,
io_form_input        = 2,
io_form_boundary     = 2,
auxinput6_inname     = 'wrfbiochemi_<domain>',
auxinput5_inname     = 'wrfchemi_<domain>_<date>',
auxinput5_interval_m = 60, 60, 60, 60,
io_form_auxinput2    = 2,
io_form_auxinput5    = 2,
io_form_auxinput6    = 2,
io_form_auxinput7    = 0,
io_form_auxinput8    = 0,
io_form_auxinput12   = 0,
io_form_auxinput13   = 0,
debug_level          = 500,
auxinput1_inname     = "met_em.d<domain>.<date>",


/
```

```
&domains
time_step              = 72,
time_step_fract_num    = 0,
time_step_fract_den    = 1,
max_dom                = 3,
s_we                   = 1, 1, 1,
e_we                   = 445, 139, 101,
s_sn                   = 1, 1, 1,
e_sn                   = 338, 124, 71,
e_vert                 = 35, 35, 35,
p_top_requested        = 10000,
num_metgrid_levels     = 30,
num_metgrid_soil_levels = 4,
dx                     = 12000, 4000, 800,
dy                     = 12000, 4000, 800,
grid_id                = 1, 2, 3,
parent_id              = 1, 1, 2,
i_parent_start         = 1, 329, 98,
j_parent_start         = 1, 212, 74,
parent_grid_ratio      = 1, 3, 5,
parent_time_step_ratio = 1, 3, 5,
feedback               = 1,
smooth_option          = 0,
zap_close_levels       = 50,
interp_type            = 1,
t_extrap_type          = 2,
force_sfc_in_vinterp   = 0,
use_levels_below_ground = .true.
use_surface            = .true.
lagrange_order         = 1,
/
sfcp_to_sfcp           = .true.,

/

&physics
mp_physics             = 2, 2, 2,
progn                  = 1, 1, 1,
ra_lw_physics          = 4, 4, 4,
swint_opt              = 1,
ra_sw_physics          = 4, 4, 4,
radt                   = 21, 21, 21,
sf_sfclay_physics      = 2, 2, 2,
sf_surface_physics     = 2, 2, 2,
sf_urban_physics       = 0, 0, 3,
bl_pbl_physics         = 2, 2, 2,
bldt                   = 0, 0, 0,
cu_physics             = 5, 5, 5,
icloud                 = 1,
ifsnow                 = 1,
isfflx                 = 1,
surface_input_source   = 1,
cu_diag                = 1, 1, 1, 1,
 cudt                  = 0,
 surface_input_source  = 1,
 num_soil_layers       = 4,
```

```
sf_urban_physics      = 0, 0, 0, 0,
num_urban_layers      = 5400,
mp_zero_out           = 2,
mp_zero_out_thresh    = 1.e-12,
maxiens               = 1,
maxens                = 3,
maxens2               = 3,
maxens3               = 16,
ensdim                = 144,
cu_rad_feedback       = .true.,.true.,.true.,.true.,


/

 &fdda
/

&dynamics
rk_ord                = 3,
w_damping             = 1,
diff_opt              = 1, 1, 1, 1,
km_opt                = 4, 4, 4, 4,
diff_6th_opt          = 0, 0, 0, 0,
diff_6th_factor       = 0.12, 0.12, 0.12, 0.12,
base_temp             = 290.0,
damp_opt              = 0,
zdamp                 = 5000.0, 5000.0, 5000.0, 5000.0,
dampcoef              = 0.2,  0.2,  0.2,  0.2,
khdif                 = 0, 0, 300,
kvdif                 = 0, 0, 300,
non_hydrostatic       = .true., .true., .true., .true.,
moist_adv_opt         = 2, 2, 2, 2,
scalar_adv_opt        = 2, 2, 2, 2,
chem_adv_opt          = 2, 2, 2, 2,
tke_adv_opt           = 2, 2, 2, 2,
 time_step_sound      = 4, 4, 4, 4,
 h_mom_adv_order      = 5, 5, 5, 5,
 v_mom_adv_order      = 3, 3, 3, 3,
 h_sca_adv_order      = 5, 5, 5, 5,
 v_sca_adv_order      = 3, 3, 3, 3,

/


&bdy_control
spec_bdy_width        = 5,
spec_zone             = 1,
relax_zone            = 4,
specified             = .true., .false., .false., .false.,
nested                = .false.,  .true.,  .true.,  .true.,
/

&grib2
/

&namelist_quilt
```

```
nio_tasks_per_group     = 0,
nio_groups          = 1,
/

&chem
 kemit                  = 23,
 chem_opt               = 10, 10, 10,
 bioemdt               = 30, 30, 30,
 photdt               = 30, 30, 30,
 chemdt                = 0, 0, 0,
 io_style_emissions     = 2,
 emiss_opt             = 3, 3, 3, 3,
 emiss_opt_vol          = 0, 0, 0, 0,
 chem_in_opt            = 0, 0, 0, 0,
 phot_opt              = 2, 2, 2, 2,
 gas_drydep_opt            = 1, 1, 1, 1,
 aer_drydep_opt            = 1, 1, 1, 1,
 bio_emiss_opt             = 1, 1, 1, 1,
 ne_area             = 104,
 dust_opt              = 2,
 dmsemis_opt              = 0,
 seas_opt              = 2,
 depo_fact             = 0.25,
 gas_bc_opt              = 1, 1, 1, 1,
 gas_ic_opt              = 1, 1, 1, 1,
 aer_bc_opt              = 1, 1, 1, 1,
 aer_ic_opt              = 1, 1, 1, 1,
 gaschem_onoff             = 1, 1, 1, 1,
 aerchem_onoff             = 1, 1, 1, 1,
 wetscav_onoff             = 1, 1, 1, 1,
 cldchem_onoff             = 1, 1, 1, 1,
 vertmix_onoff             = 1, 1, 1, 1,
 chem_conv_tr             = 1, 1, 1, 1,
 conv_tr_wetscav            = 1, 1, 1, 1,
 conv_tr_aqchem            = 1, 1, 1, 1,
 biomass_burn_opt             = 0, 0, 0, 0,
 plumerisefire_frq             = 30, 30, 30, 30,
 have_bcs_chem              = .false., .false.,.false.,
 aer_ra_feedback           = 1,
 aer_op_opt             = 1,
 opt_pars_out             = 1,
 diagnostic_chem            = 0,
 chemdiag                = 1,
/
```

Appendix B

B.1. Theory of the Aerosol Interactions in the Atmosphere

The interaction of aerosol particles and clouds formation involve processes on multiple scales. They range from the nucleation of liquid and solid particles on the scale of a few nanometer to the growth of droplets to several micrometers up to the dynamics of cloud systems and the hydrological cycle on the scale of several kilometers. Here, the aerosol interaction with cloud and microphysics in the atmosphere is explained.

B.1.1. Formation of Hydrometeors in the Atmosphere

The nucleation and growth of a liquid or solid particle in the atmosphere can be described by thermodynamic theory. The thermodynamic state of a system can be defined by one of its thermodynamic potentials. The Gibbs free energy G is commonly used to describe the thermodynamics of phase changes. For a mixture of n components G is calculated by:

$$G = \sum_{l=1}^{n} \mu_l n_l$$

where μ_l is the chemical potential and n_l is the number of moles of component l. The formation of water droplet (wd), from water vapor (wv) is determined by the change in G:

$$\Delta G = G_{wd} - G_{wv} = n_w(\mu_w - \mu_v) + \pi D^2 \sigma_{wv}$$

where σ_{wv} is the surface tension of water vapor interface and represent the amount of energy needed to increase the surface by one-unit area. Assuming water vapor is an ideal gas, μ_v can be expressed as a function of water vapor pressure e (Seinfeld and Pandis, 2006).

$$\mu_v = \mu_v^o + RT ln \frac{e}{e^o}$$

Where R is the universal Gas constant, T is the temperature and μ_v^o is the standard chemical potential defined at $e^o = 1013.25$hpa. The ratio $\frac{e}{e^o}$ is saturation ratio as S. For S=1 the water vapor is in chemical equilibrium. For S<1, the Gibbs free energy change is positive, but for S>1 a maximum G exists.

B.1.2. Diffusional Growth of Aerosol Particles

The diffusional growth of aerosols particles is based upon the droplets in thermodynamic equilibrium with surrounding humid air. Pruppacher and Klett in 1997, calculated this diffusional growth.

$$\frac{dD}{dt} = \frac{\Lambda}{D} (S - S_{eq})$$

where $\Lambda = 4 \left(\frac{\rho_w RT}{e^0 D_v' M_w} + \frac{l_{w,v}\rho_w}{k_a T} \left(\frac{l_{w,v} M_w}{TR} - 1 \right) \right)^{-1}$, k_a is the thermal conductivity of air and $l_{w,v}$ is the evaporation latent heat. The diffusivity of water vapor in the air onto the droplet D_v' is based on the size of the droplet and is calculated by Fukuta and Walter in 1970:

$$D_v' = \frac{D_v}{1 + \frac{2D_v}{a_c D}\sqrt{\left(\frac{2\pi M_w}{RT}\right)}}$$

Where D_v is the diffusivity of water vapor in air neglecting non-continuum effects and a_c is the accommodation coefficient that expresses the probability of a water vapor molecule remaining in the liquid phase upon collision (Seinfeld ad Pandis, 2006). If $S > S_{eq}$ the droplet will grow by condensation of water vapor and if $S < S_{eq}$ the droplet will shrink by evaporation until $S = S_{eq}$. In order to calculate the growth of specific aerosol particle both S and S_{eq} have to be understood.

B.1.3. Nucleation of Ice Crystals

Based on temperature, saturation and available aerosol particles in the atmosphere, ice crystals can nucleate in various ways. The direct nucleation of ice crystals from the gas phase is negligible in the atmosphere. Therefore, the formation of ice crystals requires the freezing of water droplets or solid particles on which ice crystals can nucleate. Freezing of water drops without the presence of solid aerosol particles is referred to as homogeneous freezing and does not perform at temperatures above -33ºC (Fletcher et al., 1962). If solid particles are present, ice crystals can form at higher temperatures, which is referred to as heterogeneous freezing. At temperatures lower than ~ -20ºC, ice crystal is found to nucleate on the surface of insoluble aerosol particles. This process is referred to as deposition freezing. If the air is saturated with respect to water ice crystals can be formed with the help of insoluble particles at temperatures up to ~ -10ºC. Condensation freezing is when ice crystals can form simultaneously with the condensation of water on a solid particle.

Immersion freezing refers to the liquid phase that already surrounds a solid particle. Contact freezing is collision of a super cooled drop with a solid particle.

B.2. Aerosol impact on cloud properties

The initial number concentration of clouds droplets is determined by the activation of aerosol particles and the homogeneous and heterogeneous freezing involving aerosol particles. Therefore, the optical properties of clouds and the efficiency of the microphysical processes in clouds are based on the aerosol population present during the cloud formation.

The optical properties of clouds are modified by aerosol particles. The simple case of sunlight crossing a single cloud layer is presented here to highlight the physical principles of the interaction of aerosol particles with the optical properties of a cloud (Petty, 2004,). Following Beer's law, the transmittance of a cloud layer is calculated by:

$$t_c = e^{-\tau_c/\mu}$$

where τ_c is the optical depth of the cloud and μ is the cosine of the solar zenith angle. The optical depth is defined as:

$$\tau_c = \int_{Z_{cb}}^{Z_{ct}} \beta_{e,c}(Z)dz$$

where $\beta_{e,c}$ is the extinction coefficient, z is the vertical coordinate in m, Z_{cb} and Z_{ct} are the height of the cloud base and cloud top, respectively. The extinction coefficient of a monodisperse cloud can be calculated by:

$$\beta_{e,c} = N_c Q_e \pi r^2$$

where Q_e is the ratio of extinction cross section and geometrical cross section know as the extinction efficiency, N_c the number concentration of cloud droplets. For the radiation transfer in the atmosphere $\beta_{e,c}$ is applied in the numerical simulations.

Radiation transfer is not a one-dimensional issue, since most of the solar radiation is scattered multiple times before it reaches the surface. To account for these affects additional information about the scattering angles and the contribution of absorption to the extinction has to be understood. In WRF as a three-dimensional atmospheric numerical model, direct solar radiation and diffusive scattered radiation is distinguished. To simplify the problem of three-dimensional

scattering, a two-stream approximation is usually used for the diffusive part of the atmospheric radiation. Thereby, the upwelling and down welling part of the diffusive radiation in an atmospheric column are assumed to be isotropic in each hemisphere. The radiation transfer in an atmospheric column can then be treated as a one-dimensional problem and can be described by the extinction coefficient, the single scattering albedo, which is defined as the scattering fraction of the extinction coefficient, and the asymmetry parameter, which can be interpreted as the average of the cosine of the scattering angle for a high number of scattering events (Petty, 2004). All parameters are a function of wavelength and in case of clouds, they depend on the size distribution of hydrometeors in the cloud.

On the other hand, the formation of rain is very complicated and cannot be explained by the diffusional growth of cloud droplets to the size of rain drops, because it would need several hours with a sufficient high supersaturation. Therefore, the growth of cloud droplets to the size of rain drops is dominated by another process, namely the collision and coalescence of the droplets. The increase in mass of a single cloud drop $m_c^{/}$ with diameter D_c, falling through a population of smaller drops with diameter $D_c^{/}$ and mass $m_c^{/}$, can be calculated by the volume the drop is falling through times the number concentration of smaller drops $N_c^{/}$:

$$\frac{dm_c^{/}}{dt} = \frac{1}{4} \pi (D_c + D_c^{/})^2 (|W^{sed} - W^{sed/}|) m_c^{/} N_c^{/} = K_c(D_c, D_c^{/}) m_c^{/} N_c^{/}$$

where W^{sed} and $W^{sed/}$ are the fall velocities of the drops and $K_c(D_c, D_c^{/})$ is the collection kernel of two drops falling with different fall velocities and is calculated by:

$$K_c\left(D_c, D_c^{/}\right) = \frac{1}{4} \pi (D_c, D_c^{/})^2 E(D_c, D_c^{/}) |W^{sed} - W^{sed/}|$$

Smaller cloud droplets will grow slower in comparison to larger particles and for droplets smaller than 10μm the collision efficiency is negligible. Therefore, aerosol particles can strongly modify the growth of cloud droplets to rain drops.

B.3. Numerical Description of Aerosol Particles

To investigate the aerosol-radiation-cloud interactions in the atmosphere, a numerical model at a specific scale is required to evaluate the physical, chemical and aerosol dynamical processes

during a specific period of time. Aerosols are particles with various chemical compositions suspended in the air and can be described by a continuous size distribution as a function of the particle diameter:

$$n_N(D_p) = \frac{dN}{dD_p}$$

To describe chemical and physical processes related with the atmospheric aerosol in numerical model systems efficiently, the size distribution of the aerosol particles is separated in individual overlapping modes, depending on the size and chemical composition of the particles (Whitby and McMurry, 1997). Each mode is approximated by a log- normal size distribution function (Whitby, 1978) with constant chemical composition:

$$n_{N,l}(D_p) = \frac{1}{D_p} \frac{N_l}{ln\sigma_l \sqrt{2\pi}} \exp\left(- \frac{ln^2 \left(D_p / D_{p,l} \right)}{ln^2 \sigma_l} \right)$$

Where n is the number concentration of particles in mode l, σ_l is the geometrical standard deviation of mode l, and $D_{p,l}$ the median diameter of the particles in mode l. The size distribution function and the total number concentration of aerosol particles can be calculated by:

$$n_{N,l}(D_p) = \sum_l n_{N,l}(D_p)$$

To simulate the temporal evolution of $n_{N,l}(D_p)$ in the atmosphere, one has to simulate the temporal evolution of $n_{N,l}$, σ_l , and $D_{p,l}$. For processes like advection and diffusion the differential equations for σ_l and $D_{p,l}$ cannot be solved directly (Whitby and McMurry, 1997). Therefore, the equations in the model are formulated for integral moments of $n_{N,l}(D_p)$. The k-th moment Mkx of the size distribution of mode l is defined as:

$$M_k^l = \int_0^\infty D^k n_{N,l}(D_p) dD_p$$

The moments are directly related to integral quantities of the aerosol population by:

$$N_l = \int_0^\infty n_l(D_p)\mathrm{d}D_p = M_0^l$$

$$O_l = \pi \int_0^\infty D_p^2 n_l(D_p)\mathrm{d}D_p = \pi M_2^l$$

$$V_l = \frac{\pi}{6}\int_0^\infty D_p^3 n_l(D_p)\mathrm{d}D_p = \frac{\pi}{6}M_3^l$$

$$m_l = \frac{\pi}{6}\rho_p \int_0^\infty D_p^3 n_l(D_p)\mathrm{d}D_p = \frac{\pi}{6}\rho_p M_3^l$$

Where O_l is the surface concentration, V_l the volume concentration, and m_l the mass concentration of mode l. To fully determine $n_{N,l}(D_p)$, three moments of the log-normal size distribution function are needed. To derive a numerically feasible solution of the resulting equation system, σ_l is held constant for each mode. The temporal evolution of $n_{N,l}(D_p)$ is calculated by solving the Reynolds-averaged balance equations of N_l and m_l, which are given by (Doms, 2011; Jacobson, 2005).

$$\frac{\partial}{\partial t}y_t = -\nabla.(vy_1) + \nabla.F_{y1} + \frac{\partial}{\partial z}(w_1 y_1) + S_{y1}$$

The first, second, third and fourth terms refer to advection, turbulence, gravitational sedimentation, and microphysical processes, respectively. These terms are calculated during the simulation to estimate the ARC interactions in the atmosphere.

B.4. Aerosol Schemes in WRF-Chem

Currently, there are four aerosol schemes available to be performed in the chemistry package of the WRF: Model for Simulating Aerosol Interactions with Chemistry (MOSAIC); Georgia Tech/Goddard Global Ozone Chemistry Aerosol Radiation and Transport Model (GOCART) (Chin et al., JGR, 2000); Modal Aerosol Dynamics Model for Europe (MADE) (Ackerman et al., 1998); Modal Aerosol Model (MAM). Table C.1 presents and compares these models.

Table C.1. Available aerosol schemes to be coupled with chemistry package
in WRF to evaluate the ARC interactions

Categories	MOSAIC	GOCART	MADE	MAM
Aerosol size distribution	Sectional	Bulk	Modal	Modal
SO_4^{--}	✓	✓	✓	✓
NH_4^{-}	✓	✓	✓	✓
NO3	✓		✓	✓
Organics	✓		✓	
Soot	✓		✓	
Sea salt	✗	✓	✓	
Mineral dust	✗	✓	✓	
Interaction with radiation	✓	✓	✓	Only RRTMG
Interaction with clouds	✓	✓	✓	Only resolved clouds (Sc)
Gas phase chemistry	MOZART[3]	RADM[1]	RADM[1]	CBMZ[4]
Aerosol chemistry	VBS[4]	✗	SORGAM[2]	✗
Highlights	- Sectional scheme for 4 or 8 bins - IA[6], OA[7] & SOA[8]	- Size information available only for dust & sea salt - No SOA	- 3 log-normal modes - IA, OA & SOA	- 3 or 7 log-normal modes - IA, OA, SOA

1. Regional Acid Deposition Model Version
2. Secondary Organic Aerosol Model
3. Model for Ozone & Related chem. Tracer
4. Volatility Basis Set
5. Carbon-Bond Mechanism Version Z)
6. Inorganic Aerosol
7. Organic Aerosol
8. Secondary Organic Aerosol

Accordingly, the MOSAIC as the sectional aerosol estimation and MADE as the modal one, are the most proper aerosol models to be applied in these simulations. In the following section, a brief description of these two aerosol schemes are pointed out.

B.4.1. The MOSAIC aerosol mechanism

The Model for Simulating Aerosol Interactions and Chemistry (MOSAIC) mechanism is a sectional scheme, with 4 or 8 a set of discrete size bins (Zaveri et al., 2008). MOSAIC carries five inorganic ions, with three organic matter and even secondary organic aerosols. All chemical components within each size bin are assumed to be internally mixed (Zaveri et al., 2008). Some uncertainties in the model representation have been recognized in previous studies as aerosol composition, size distribution and optical properties that would probably affect the result in radiative forcing predictions as well (Matsui et al., 2013; Kodros et al., 2015).

Within MOSAIC, each aerosol chemical component has its challenges in calculating refractive index, especially in terms of the most absorbing particle, Black Carbon (BC) (Barnard et al., 2010). The overall complex refractive index is calculated for each bin using a mixing rule (Maxwell-Garnett mixing rule) to approximate the internal structure of the aerosol particles (Bond et al., 2006; Bond and Bergstrom, 2006; Barnard et al., 2010; Matsui et al., 2013). Mie calculations are used to calculate the intermediate optical properties for each bin, which are summed over size bins to give the bulk extinction coefficient (BEC), scattering coefficient (SC), single scattering albedo (SSA = SC /BEC) and asymmetry factor (g). Each of these variables are functions of the size parameter ($x = \frac{2\pi r}{\lambda}$) where λ is the light wavelength and r is the wet radius at the centre of the aerosol bin (Fast et al., 2006). A full description of the optical property calculations is given by Fast et al. (2006) and Barnard et al. (2010).

The activation of cloud condensation nuclei is the key process in simulating aerosol–cloud interactions. Aerosols become activated as soon as the environmental supersaturation in the air entering the cloud `s process and formation. The Köhler et al. (1936) theory describes the equilibrium state of an aerosol particle, assumed to be an aqueous salt solution, with ambient water vapour. Figure C.1 shows the Köhler Curve.
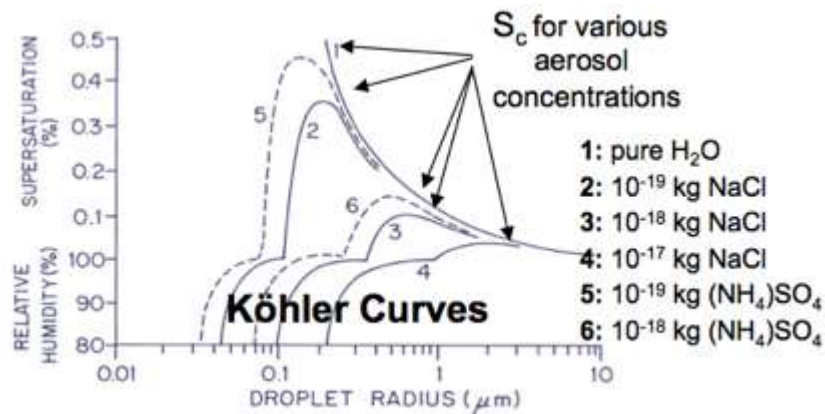

Figure C.1. Köhler Curves (After Jerome Fast, 2014)

When an aerosol particle becomes activated to form a cloud droplet termed as critical supersaturation (SC). The activation fraction is calculated based on mass, number of each bin and aerosol composition using the methodology of Abdul-Razzak and Ghan (2002). The primary driver of cloud droplet activation is the vertical velocity (W): air parcels with higher W reach higher maximum supersaturations (Smax). All particles with Sc < Smax will be activated, whereas those with Sc > Smax remain un-activated within clouds and are known as interstitial aerosols (Chapman

et al., 2009). The number and mass fraction of activated CCN in each aerosol bin can be calculated by comparing Smax with Sc at the sectional limits of each bin (Abdul-Razzak and Ghan, 2002). WRF-Chem carries six diagnostic variables showing the concentration of particles that can potentially activate at given supersaturations of 0.02, 0.05, 0.1, 0.2, 0.5 and 1% as CCN0.02, CCN0.05, CCN0.1, CCN0.2, CCN0.5 and CCN1.0, respectively.

To investigate the indirect effects the cloud activation scheme needs to be coupled with a double-moment microphysical parameterisation that involve both number and mass loadings for hydrometeors. The double-moment Morrison et al. (2005, 2009) parameterisation has been coupled with MOSAIC aerosol (Yang et al., 2011). One of the main sinks of particulate mass is wet scavenging of interstitial and activated aerosol (Slinn, 1984). Wet removal causes the aerosol particles to be deposited out of the atmosphere, without the possibility of resuspension and evaporation (Yang et al., 2015).

In deep convective clouds, secondary activation of aerosol has been observed (Heymsfield et al., 2009) and modelled (e.g. Segal et al., 2003; Yang et al., 2015), whereby further interstitial aerosol particles are activated above cloud base due to supersaturation not being fully offset by droplet growth, as hydrometeors are scavenged in the cloud column. This is a process unrepresented in the current model setup, as the Abdul-Razzak and Ghan (2002) parameterisation assumes all activation at cloud base. If secondary activation were included in the model, it would primarily act to increase the efficiency with which aerosol is scavenged from cloud and reduce the amount of aerosol transported to the mid and up- per troposphere (Yang et al., 2015). However, representing this process is challenging on this scale of the model, without bin microphysics or fully resolved updraft velocities. Use of the aerosol-aware Kain–Fritsch parameterisation (Berg et al., 2015) could enable consideration of this process in parameterised clouds for future studies.

B.4.2. The MADE Aerosol Mechanism

The Modal Aerosol Dynamics Model for Europe (MADE; Ackermann et al. 1998) presents the aerosol population by log-normal size distribution functions, so-called modes, and represent the aerosol dynamic processes like the Brownian coagulation of small particles. Five modes represent sub-micron particles consisting of sulphate, ammonium, nitrate, organic compounds, water, and soot in a range of mixing states and sizes where interact with anthropogenic emissions of particles and gases through coagulation where the size distributions overlap. These modes enable the

explicit simulation of soot aging in the atmosphere (Riemer et al., 2004, 2003). Sea salt and mineral dust particles are represented by three modes for different size ranges in each case. The emissions of sea salt and mineral dust particles are calculated online in the model as a function of atmospheric state, e.g. 10 m-wind speed, and friction velocity, and surface properties, such as sea surface temperature, soil type, and soil moisture (Lundgren, 2010; Stanelle et al., 2010).

Appendix C

National Weather Service – Heat Index (NWS-HI)

The heat index is a measure of how hot it feels when relative humidity is factored in with air temperature. To find the heat index, one can check the air temperature first and then the relative humidity. For example, is the air temperature is 96°F and the relative humidity is 65%, the heat index is 121°F, meaning how hot it feels. The red area without numbers indicates extreme danger. The National Weather Service will initiate alert procedures when the heat index is exceed 105-110 °F for at least two consecutive days.

Temperature (°F)

Relative Humidity (%)	80	82	84	86	88	90	92	94	96	98	100	102	104	106	108	110
40	80	81	83	85	88	91	94	97	101	105	109	114	119	124	130	136
45	80	82	84	87	89	93	96	100	104	109	114	119	124	130	137	
50	81	83	85	88	91	95	99	103	108	113	118	124	131	137		
55	81	84	86	89	93	97	101	106	112	117	124	130	137			
60	82	84	88	91	95	100	105	110	116	123	129	137				
65	82	85	89	93	98	103	108	114	121	128	136					
70	83	86	90	95	100	105	112	119	126	134						
75	84	88	92	97	103	109	116	124	132							
80	84	89	94	100	106	113	121	129								
85	85	90	96	102	110	117	126	135								
90	86	91	98	105	113	122	131									
95	86	93	100	108	117	127										
100	87	95	103	112	121	132										